Universität Hamburg

Doctoral Thesis

Ultracold Rydberg dimers: a toolbox for quantum dynamics, vibronics, and precision spectroscopy

Dissertation

zur Erlangung des Doktorgrades

an der Fakultät für Mathematik, Informatik und Naturwissenschaften, Fachbereich Physik

der Universität Hamburg

vorgelegt von

Rohan Srikumar

Geboren in Kerala, Indien

Hamburg

2026

Gutachter/innen der Dissertation:	Prof. Dr. Peter Schmelcher Prof. Dr. Peter Schauß
Zusammensetzung der Prüfungskommission:	Prof. Dr. Peter Schmelcher Prof. Dr. Peter Schauß Prof. Dr. Ludwig Mathey Dr. Juliette Simonet Dr. Tim Laarmann
Chairperson of the Examination Committee:	Prof. Dr. Ludwig Mathey
Datum der Disputation:	20.10.2026
Vorsitzender Fach-Promotionsausschusses PHYSIK:	Prof. Dr. Johannes Haller
Leiter des Fachbereichs PHYSIK:	Prof. Dr. Markus Drescher
Dekan der Fakultät MIN:	Prof. Dr.-Ing. Norbert Ritter

To my late grandparents. . .

Abstract

This cumulative thesis investigates the dynamical and spectral properties of Ultralong-range Rydberg molecules (ULRM), a peculiar form of quantum matter bound through the low-energy scattering between a Rydberg electron and nearby ground-state perturbers. Particularly, our focus lies on trilobite and butterfly molecules, featuring a Rydberg electron with high orbital angular momentum ℓ that undergoes S-wave and P-wave scattering with the perturber, respectively. Their internal structure is usually studied within the confines of the Born-Oppenheimer approximation, wherein the constituent electronic and nuclear configurations can be treated as separate. While the adiabatic stationary states of these molecules have been examined with much scrutiny, their dynamic and nonadiabatic features were left relatively unexplored. Consequently, this thesis aims to further our understanding of ULRM, by exploring the role of nonadiabatic effects and dynamical effects, while also investigating the underlying spin-dependent electron-atom scattering channels. The results of these investigations are published as a series of articles, whose contents can be broadly classified into three different yet overlapping themes.

The first theme catalogues our study of various nonadiabatic phenomena occurring in the spectra of the ULRM, as a result of the breakdown of the Born-Oppenheimer approximation. We use both Landau-Zener based semi-classical calculations, and exact two-channel vibronic spectral calculations to locate and study the nonadiabatic stabilization and decay of molecular states. In ^{23}Na dimers, we investigate the effects of avoided crossings between the trilobite and energetically nearby $\ell = 2$ quantum defect state, and discover above-threshold resonance states, without an adiabatic equivalence. We also observe nonadiabatic localization effects in the radial probability density of vibronic states. In ^{87}Rb dimers, we were able to recognize and understand the observation of high-lying trilobite states, stabilized against decay to the P-wave butterfly state via avoided crossings, through nonadiabatic surface hopping. In both cases, we find that the nonadiabatic coupling strengths and their spectral influence is highly dependent on the principal quantum number n, of the Rydberg electron.

The second theme explores the internal quantum dynamics of the ULRM, describing the motion of nuclear wavepackets in the adiabatic PECs. For appropriate n-values, we find that pure trilobite potentials feature an oscillatory structure that can act as a molecular diffraction grating, by backscattering incedent wavepackets with appropriate initial conditions. We study the phenomena using Fourier analysis, and propose a pump-probe scheme that utilizes vibrational states in low-ℓ potentials, to experimentally resolve the diffraction effect. As an extension, we also study the effects of including the P-wave butterfly states into our model, and find that nonadiabatic interactions can stabilize the propagating diffraction pattern against shape resonance-induced decay pathways. Our work also explores other exciting dynamical effects, like multi-well interference patterns, exhibited by the time-evolving molecule.

Our final theme of research is centered around the precision spectroscopy of bound ULRM states, combining state-of-the-art numerical and experimental methodology. A high-precision spectroscopic study of the binding energies of these molecules reveal the spin structure, and scattering phase shifts of the electron-atom scattering problem in extremely low energies, typically inaccessible to free electrons. We exploit the predominant S-wave nature and the deep potential energy structure of the trilobite molecule to directly access the electron-atom scattering channel and extract the corresponding scattering lengths with great sensitivity. Moreover, we are also able to observe and characterize for the first time, bound singlet P-wave states of the ULRM, a critical intermediary step in the creation of ultracold anions and two-component neutral plasmas.

Zusammenfassung

Diese kumulative Dissertation untersucht die dynamischen und spektralen Eigenschaften von ultralangreichweitigen Rydberg-Molekülen (ULRM), einer besonderen Form quantenmechanischer Materie, die durch die Niederenergie-Streuung zwischen einem Rydberg-Elektron und nahegelegenen Störstellenatom im Grundzustand gebunden wird. Der Fokus liegt auf Trilobite- und Schmetterlingsmolekülen, in denen ein Rydberg-Elektron mit hohem Bahndrehimpuls ℓ, S- oder P-Wellenstreuung mit einem Störer erfährt. Durch die Born-Oppenheimer-Näherung lässt sich die innere Struktur typischerweise abbilden, indem die elektronischen und nuklearen Freiheitsgrade isoliert behandelt werden. Während die adiabatischen stationären Zustände dieser Moleküle eingehend untersucht wurden, blieben ihre dynamischen und nicht-adiabatischen Eigenschaften vergleichsweise unerforscht. Diese Dissertation zielt daher darauf ab, unser Verständnis von ULRM zu vertiefen, indem sie die Rolle nicht-adiabatischer und dynamischer Effekte untersucht sowie die zugrundeliegenden spinabhängigen Elektron-Atom-Streukanäle analysiert. Die Ergebnisse dieser Untersuchungen sind als eine Reihe von Artikeln veröffentlicht, deren Inhalte sich grob in drei verschiedene, aber überlappende Themenbereiche einteilen lassen.

Der erste Themenbereich umfasst unsere Untersuchung verschiedener nicht-adiabatischer Phänomene in den Spektren der ULRM, die durch den Zusammenbruch der Born-Oppenheimer-Näherung entstehen. Wir verwenden sowohl Landau-Zener-basierte semiklassische Berechnungen als auch exakte Zwei-Kanal-Vibrospektralberechnungen, um die nicht-adiabatische Stabilisierung und den Zerfall molekularer Zustände zu lokalisieren und zu untersuchen. In ^{23}Na-Dimeren untersuchen wir die Auswirkungen von vermiedenen Kreuzungen zwischen dem Trilobite-Zustand und dem energetisch nahegelegenen $\ell = 2$-Quantendefektzustand und entdecken Resonanzzustände oberhalb der Schwelle, die nicht durch die adiabatische Näherung beschrieben werden können. Wir beobachten außerdem nicht-adiabatische Lokalisierungseffekte in der radialen Wahrscheinlichkeitsdichte vibronischer Zustände. In ^{87}Rb-Dimeren konnten wir die Beobachtung hochliegender Trilobite-Zustände erkennen und verstehen, die durch vermiedene Kreuzungen mittels nicht-adiabatischem Oberflächenspringen gegen den Zerfall in den P-Wellen-Schmetterlingszustand stabilisiert werden. In beiden Fällen stellen wir fest, dass die nicht-adiabatischen Kopplungsstärken und ihr spektraler Einfluss stark von der Hauptquantenzahl n des Rydberg-Elektrons abhängen.

Der zweite Themenbereich erforscht die innere Quantendynamik der ULRM und beschreibt die Bewegung nuklearer Wellenpakete in den adiabatischen Potentialkurven. Für geeignete n-Werte stellen wir fest, dass reine Trilobite-Potentiale eine oszillatorische Struktur aufweisen, die als molekulares Beugungsgitter wirken kann, indem sie einfallende Wellenpakete mit geeigneten Anfangsbedingungen rückstreut. Wir untersuchen dieses Phänomen mithilfe der Fourier-Analyse und schlagen ein Pump-Probe-Schema vor, das Schwingungszustände in Potentialen mit niedrigem ℓ nutzt, um den Beugungseffekt experimentell aufzulösen. Als Erweiterung untersuchen wir auch die Auswirkungen der Einbeziehung der P-Wellen-Schmetterlingszustände in unser Modell und stellen fest, dass nicht-adiabatische Wechselwirkungen das sich ausbreitende Beugungsmuster gegen formresonanzinduzierte Zerfallswege stabilisieren können. Unsere Arbeiten untersuchen auch weitere interessante dynamische Effekte, wie Mehr-Mulden-Interferenzmuster, die das zeitlich entwickelnde Molekül aufweist.

Der abschließende Forschungsschwerpunkt widmet sich der Präzisionsspektroskopie gebundener ULRM-Zustände und kombiniert aktuelle numerische und experimentelle Methoden. Eine hochpräzise spektroskopische Untersuchung der Bindungsenergien dieser Moleküle offenbart die Spinstruktur und die Streuungsphasenverschiebungen des Elektron-Atom-Streuproblems bei extrem niedrigen Energien, die für freie Elektronen typischerweise unzugänglich sind. Wir nutzen den vorherrschenden S-Wellen-Charakter und die tiefe Potentialenergiestruktur des Trilobite-Moleküls, um direkt auf

den Elektron-Atom-Streukanal zuzugreifen und die entsprechenden Streulängen mit hoher Empfindlichkeit zu extrahieren. Darüber hinaus können wir erstmals gebundene Singulett-P-Wellen-Zustände der ULRM beobachten und charakterisieren – einen entscheidenden Zwischenschritt bei der Erzeugung ultrakalter Anionen und zweikomponentiger neutraler Plasmen.

Contents

Abstract v

Zusammenfassung vi

List of Publications x

Units and Abbreviations xii

List of Tables and Figures xiii

1 Introduction 1

2 Theoretical framework 9
- 2.1 A primer on Rydberg atoms . . . 9
  - 2.1.1 Quantum defect structure of alkali atoms . . . 10
  - 2.1.2 Rydberg wavefunctions of alkali atoms . . . 11
  - 2.1.3 Fine structure of alkali Rydberg atoms . . . 13
  - 2.1.4 Photoexcitation and radiative lifetimes . . . 15
- 2.2 Molecular structure and vibronic spectra . . . 17
  - 2.2.1 Diatomic Hamiltonian and nonadiabatic coupling terms . . . 18
  - 2.2.2 Born-Oppenheimer approximation . . . 19
  - 2.2.3 Onset of nonadiabaticity . . . 20
  - 2.2.4 The diabatic transform . . . 21
- 2.3 Quantum wavepacket dynamics . . . 23
  - 2.3.1 Adiabatic dynamics . . . 24
  - 2.3.2 Nonadiabatic dynamics . . . 25

3 Ultralong-range Rydberg molecules 27
- 3.1 Binding mechanism: electron-atom scattering . . . 27
- 3.2 Electronic states and potentials . . . 32
  - 3.2.1 Perturbative analysis . . . 33
  - 3.2.2 Exact diagonalization . . . 35
- 3.3 Spin interaction effects . . . 38
- 3.4 Green's function approach . . . 44
  - 3.4.1 Basic formulation . . . 44
  - 3.4.2 Spin couplings . . . 47
  - 3.4.3 Comparative analysis . . . 49

3.5 Experimental setup 50

4 Overview of scientific contributions **52**
4.1 Vibronic spectra: theory and observation 52
4.2 Quantum dynamics 56
4.3 Precision spectroscopy of electron-atom scattering 59

5 Scientific Contributions **62**
5.1 Nonadiabatic interaction effects in the spectra of ultralong-range Rydberg molecules 62
5.2 Vibrationally highly excited trilobite molecules stabilized by nonadiabatic coupling 75
5.3 Internal diffraction dynamics of trilobite molecules 83
5.4 Vibronic quantum dynamics of ultralong-range high-ℓ Rydberg molecules . 92
5.5 High Precision Spectroscopy of Trilobite Rydberg Molecules 105
5.6 Observation of spin singlet butterfly Rydberg molecules in an ultracold atomic Rb gas 112

6 Conclusions **122**

A Finite difference methods **126**
A.1 Single channel Schrödinger equation 126
A.2 Multi-channel Schrödinger equation 127

B Complex Absorbing Potentials **129**

Bibliography **131**

Acknowledgements **148**

Declaration of authorship / Eidesstattliche Versicherung **150**

Declaration of Conformity for Printed Copy / Konformitätserklärung für die gedruckte Ausgabe **151**

List of Publications

The dissertation is written as a cumulative thesis is based on the following publications [P1–P6]:

[P1] R. Srikumar, F. Hummel, and P. Schmelcher, *Nonadiabatic interaction effects in the spectra of ultralong-range Rydberg molecules*, Phys. Rev. A **108**, 012809 (2023).

[P2] R. Srikumar, M. Exner, R. Blättner, P. Schmelcher, M. T. Eiles, and H. Ott, *Vibrationally highly excited trilobite molecules stabilized by nonadiabatic coupling*, Phys. Rev. Res. **7**, 043103 (2025).

[P3] R. Srikumar, S. T. Rittenhouse, and P. Schmelcher, *Internal diffraction dynamics of trilobite molecules*, Phys. Rev. A **110**, 062808 (2024).

[P4] F. Giering, R. Srikumar, and P. Schmelcher, *Vibronic quantum dynamics of ultralong-range high-ℓ Rydberg molecules*, Phys. Rev. A **114**, 022813 (2026).

[P5] M. Exner, R. Srikumar, R. Blättner, M. T. Eiles, P. Schmelcher, and H. Ott, *High Precision Spectroscopy of Trilobite Rydberg Molecules*, Phys. Rev. Lett. **134**, 223401 (2025).

[P6] M. Exner, R. Srikumar, R. Blättner, P. Schmelcher, H. R. Sadeghpour, M. T. Eiles, and H. Ott, *Observation of Spin-Singlet Butterfly Rydberg Molecules in an Ultracold Atomic Rb Gas*, Phys. Rev. Lett. **136**, 243002 (2026).

Declaration of personal contributions to the publications

I have contributed to the analytical modeling, numerical simulation, writing, and preparation of all the listed manuscripts, with the help and contribution of all the co-authors, especially the expert supervision of Prof. Peter Schmelcher.

For the work [P1], I performed the analytical modelling, and obtained the numerical results, with technical assistance from Dr. Frederic Hummel. Dr. Hummel also contributed extensively to the early-stage formulation of the project.

The core idea for the project [P3] was first proposed by Prof. Seth Rittenhouse. The calculations and phenomenological analysis were performed by me, with regular discussions with Prof. Schmelcher and Prof. Rittenhouse. The manuscript [P4] is based on research performed by Felix Giering, under my co-supervision (alongside Prof. Schmelcher). Felix performed the numerical calculations himself, whereas I took the theory lead and designed

the research project. We analyzed the results and wrote the manuscript together.

The series of projects [P2, P5, P6] were carried out in collaboration with experimentalists from the group of Prof. Herwig Ott, RPTU Kaiserslautern. Markus Exner and Richard Blättner performed the experiments under the supervision of Herwig Ott. Markus Exner also prepared many of the figures and wrote the experimental parts of all the corresponding manuscripts. I prepared figures and text for the theory part of all the manuscripts alongside Prof. Matthew Eiles. All the co-authors helped in the preparation and alteration of the manuscripts.

The analytical methods used in [P5] were previously developed by Prof. Eiles and Prof. Chris Greene. I developed the code to perform the spin-coupled exact diagonalization calculation myself (based on the analytical model by Prof. Eiles),whereas the code to calculate the spin-coupled Greene's function calculation was developed by Prof. Eiles. The theory team for the project [P6] consisted of Prof. Hossein Sadeghpour, apart from Prof. Schmelcher, Prof. Eiles, and myself. All these co-authors contributed to the writing of the theory section of the manuscript. I performed the numerical calculations presented in the manuscript, with the help of regular discussions with Prof. Sadeghpour and Prof. Eiles.

Units and Abbreviations

All the discussions presented in this dissertation utilize Hartree atomic units [1] (a.u.) unless specified otherwise. Hence we set the electronic charge e, electronic rest mass m_e, and action $\hbar$ to be of unit value. Common conversions used in the thesis includes:

- Unit of length a_0 = 0.529177 $\mathring{A}$ = $5.29177 \times 10^{-5} \mu m$
- Unit of energy E_h = 6.579634 $\times 10^6$ GHz = 27.2114 eV
- Unit of time $\hbar / E_h$ = 2.418 884 $\times 10^{-8}$ nanoseconds.

List of Abbreviations

ULRM	Ultralong-range Rydberg Molecule
BO	Born-Oppenheimer
PEC	Potential Energy Curve
PES	Potential Energy Surface
CI	Conical Intersection
CAP	Complex Absorbing Potential
ED	Exact Diagonalization
FD	Finite Difference
CG	Clebsch-Gordan
TDSE	Time dependent Schrödinger Equation
TISE	Time independent Schrödinger Equation

List of tables and figures

Tables

2.1 Quantum defects (δ_ℓ) of alkali atoms. 10
2.2 Spin-orbit splitted quantum defects $\delta_{\ell j}$ and $\delta'_{\ell j}$ for alkali atoms. 14

3.1 Ground-state polarizability (α_s), and zero energy S-wave scattering lengths for alkali atoms. 29
3.2 Ground-state properties of alkali atoms relevant for hyperfine structure . . . 40

A.1 Coefficients for 10th order central finite difference approximation of the second-derivative operator. 127

Figures

1.1 Electronic probability density plots of the ULRM. 2

2.1 An illustrative sketch of a diatomic ULRM, in the molecular body-fixed frame. 17

3.1 Electron-atom scattering phase shifts for ^{23}Na and ^{87}Rb 30
3.2 The $^3S_1$ (a) and $^3P_{0,1,2}$ (b) phase shifts for ^{87}Rb obtained from different sources. 31
3.3 PECs of the $n = 25$ ULRM, in $\ell = 0$, trilobite and butterfly states. 34
3.4 Adiabatic PECs of the $n = 35$ ^{87}Rb ULRM obtained from ED. 36
3.5 Adiabatic PECs of the $n = 35$ ^{23}Na ULRM obtained from ED. 37
3.6 Adiabatic PECs obtained by diagonalizing varying finite basis sets 38
3.7 Sketch of the internal spin structure of a diatomic ^{87}Rb ULRM. 39
3.8 Adiabatic PECs of the ULRM, and their spin admixture 41
3.9 Adiabatic PECs of the ULRM, and their hyperfine admixture 43

Chapter 1

Introduction

Rydberg physics today, post the era of laser cooling [2–6], is largely characterized by the ambition to introduce and manipulate long-range interactions in ultracold atomic systems. The latter half of the 20th century witnessed the development of many modern techniques to trap and cool neutral atoms to μK temperatures, invoking the desire to systematically construct quantum matter with desirable properties. Within this context, highly excited Rydberg states of matter that allow strong tunable atom-atom interactions were soon recognized to provide an excellent pathway to introduce and control interactions in ultracold systems. The turn of the 21st century came with many landmark works on ultracold Rydberg atoms, like the formulation of the Rydberg blockade effect [7] predicting that van der Waals interaction between two closely spaced atoms in the same Rydberg state can force the double excitation out of resonance, thereby blocking the number of Rydberg excitations from increasing within a specific radius. A second work of profound importance showed that the scattering interaction between a Rydberg electron and nearby ground-state perturbers, can facilitate the existence of long-range bound states in cold-atom ensembles [8]. In their wake, the last two decades saw the emergence of two broad avenues of research in ultracold Rydberg physics: the first one focusing on the interplay between different Rydberg excitations, and the second one focusing on Rydberg atoms interacting with other perturbing entities to form hybrid quantum systems.

Rydberg-Rydberg systems: The blockade effect allowed for the engineering of two-qubit entangling gates between Rydberg atoms, and was followed by another work showing that atom-atom interactions can be tuned via Rydberg dressing [9]. Soon after, the Rydberg anti-blockade regime was discovered [10], where inter-atom interactions can facilitate more excitations in the vicinity of a Rydberg atom, rather than block them. Later, protocols that use förster resonances [11, 12] and resonant dipole-dipole interactions for high-speed entangling operations have also been developed [13, 14]. With the discovery of magic wavelengths [15], atoms could be simultaneously trapped in both ground and Rydberg states. The last two decades have scene large strides in multi-atom interaction engineering with unprecedented control, new efficient measurement protocols, and the ability to trap arrays of atoms in tweezers or optical lattice setups, making neutral atom platforms a primary contender in the race to realize Quantum computers [16, 17]. Rydberg platforms have also been successfully used to simulate topological phases [18–20], and study fundamental many-body physics phenomena. Rydberg excitations in the blockaded regime have also been used favorably in quantum optics

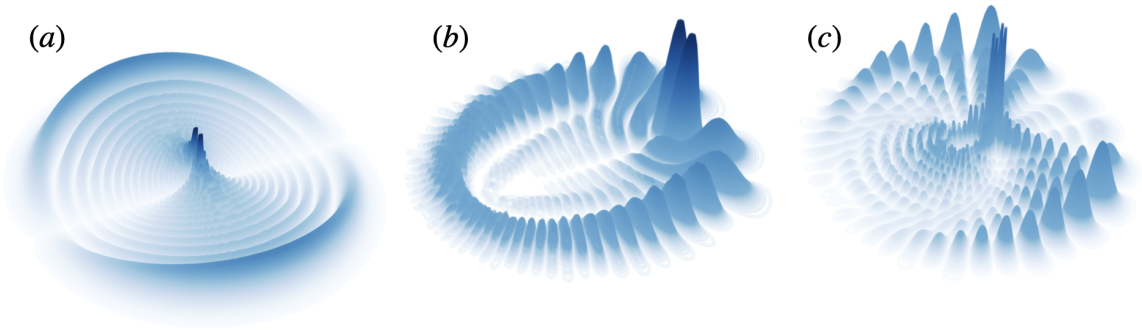


FIGURE 1.1: Illustrative surface plots of the electronic probability density of an $n = 25$ (a) $\ell = 0$, (b) trilobite and (c) butterfly ULRM [8, 43].

setups, to mediate photon-photon interactions [21, 22], to create superatoms [23, 24], and design single-photon sources [25], switches [26, 27], and waveguides [28, 29]. Parallel to the hybrid molecular systems we study in this thesis, Rydberg atoms have also been observed to form bound macrodimer states [30–33] over large distances via state-dependent Rydberg-Rydberg interactions.

Hybrid Rydberg systems: The synthesis of many types of long-range artificial quantum systems are made possible by tailoring the behavior of Rydberg electrons in ultracold gases. The subject of this thesis is the ultralong-range Rydberg molecule (ULRM), a hybrid Rydberg system bound by the attractive scattering of a Rydberg electron off a nearby ground-state atom [8], in a dilute cold-gas. These exotic systems were the first homogeneous diatomic molecule to feature permanent dipole moments of the order of kilodebye, bond lengths of the order of micrometers, properties completely alien to conventional molecules. Soon it was found that interaction of the Rydberg electron with the permanent dipole of the trapped polar molecules, can also be used to coherently control the polar molecule and prepare dipolar superposition states [34] as well as create Rydberg bimolecules. Moreover, Rydberg atoms interacting with trapped cations can also form exotic atom-ion molecules, with even more exaggerated properties [30, 35–37]. The hybrid systems discussed above generally emerge in the dilute gas limit, when the density of the gas is low enough that few-body effects, like molecular formation, takes precedence. At larger atomic densities, studies have explored the effects of a Rydberg impurity in Bose [38–40] or Fermi [41, 42] gases, probing the cross-over from the few to many-body regime, and discovering new quasi-particles like the Rydberg polaron. For the rest of this dissertation, we will exclusively focus on ULRMs, as atom-atom dimers formed in dilute ultracold gases. Exploring the structure and dynamics of these complex systems is an important challenge in the pursuit of controlling quantum matter, but is also an opportunity to understand the fundamentals of atom-atom, atom-ion and atom-electron interactions in the ultra-low energy regime.

For the rest of this dissertation, we will exclusively focus on ULRMs as atom-atom dimers

formed via quantum scattering in dilute ultracold gases, as first theorized in 2000 by Greene et. al [8]. The initial taxonomy of this molecular species was performed on the basis of the orbital angular momentum of the Rydberg electron ℓ, and the electron-perturber scattering partial wave L. Firstly, ℓ determines the electronic state of the Rydberg atom, classifying it into quantum-defect-splitted low-ℓ states that are energetically isolated from the hydrogenic state, and a near-degenerate manifold of high-ℓ states which are indeed hydrogenic. In the low-ℓ case, the weak perturbation does not necessarily change the electronic structure of the Rydberg atom, and the shallow Born-Oppenheimer potentials follow the oscillatory structure of the Rydberg electron's radial probability density. Such low-ℓ molecular states feature binding energies in the order of MHz, and are typically non-polar. However, when the perturber interacts with a high-ℓ manifold, it hybridizes all the different degenerate states to form a highly polar molecular electronic states. The strong interaction creates deep molecular potentials that deviate from the hydrogenic manifold, that supports vibrational states with GHz of binding energies.

Secondly, L determines the behavior of the electron-atom scattering interaction that forms the underlying binding mechanism of the molecule. We describe this interaction by expanding the electron's wavefunction as partial waves centered around the perturber, denoted by angular momentum states. The original work by Greene et al. [8], focussed on the S-wave ($L = 0$) scattering of the electron in a spin-triplet configuration, particularly focusing on the *trilobite molecule*, named so due to the uncanny similarity between its electronic probability density function and a trilobite fossil [44], formed when a high-ℓ Rydberg manifold is strongly perturbed via S-wave scattering. The triplet S-wave scattering features a sufficiently negative scattering lengths, and hence supports an attractive interaction between the Rydberg atom and the ground state atom that allows for binding. The S-wave approximation of the scattering interaction was first thought to be sufficient in describing the properties of ULRM, given the low energy of the scattering electron. However, it was soon found that a shape resonance in the P-wave scattering channel for alkali systems causes a divergence in the electron-atom scattering volume, suddenly increasing the interaction strength between the constituent atoms so that molecular binding is possible. Such shape-resonance induced molecules, that also feature extraordinarily large bond-lengths and dipole moments, were christened *butterfly molecules* as their characteristic electronic probability density plots resemble the wings of a butterfly. Figure 1.1 shows exemplar sketches of the ULRM electronic probability density, illustrating their nomenclature.

These exotic molecular specimens soon garnered interest from ultracold molecular physicists and Rydberg physicists, for their exaggerated properties and rich electronic structure. The trilobite molecule is the first homogeneous dimer that featured dipole moments of the order of $\sim$ kilodebye, with bond-lengths of the order of μm. For comparison, some of the most polar conventional neutral molecules only feature dipole moments $\sim$14 debye [45]. Conventional heteronuclear molecules display permanent electric dipole moments by the

breaking of parity symmetry and mixing of opposite parity states, as is prohibited in their homonuclear counterparts. The high-ℓ ULRM however, becomes a homonuclear exception due to the mixing of near-degenerate opposite parity states due to experimentally relevant field interactions, required to measure the corresponding dipole moments [46]. Moreover, even low-ℓ ULRMs that ideally should have zero permanent dipole moments like their atomic constituent, often exhibit a non-zero permanent dipole due to the admixture with nearby high-ℓ states [47]. In such cases, the influence due to nearby hydrogenic states supersedes the energy difference between opposite parity eigenstates of a pure low-ℓ ULRM. Befittingly, heteronuclear ULRM formed in multi-species atomic gases were also later theoretically predicted [48] and experimentally observed [49, 50].

The initial description of these molecular states only considered the spin-triplet electron-atom scattering channel, as the S-wave spin-singlet scattering interaction was repulsive and did not directly facilitate molecule formation. While this was qualitatively successful, Andersen et al. [51] revealed that the spin-orbit coupling in the Rydberg atom and the hyperfine coupling in the ground-state atom mix the spin-triplet and spin-singlet scattering channels, creating a complex spaghetti of potential energy curves that significantly alters the binding energies, dipole moments, and spin-admixture of molecular states. The mixing of singlet and triplet channels can sometimes produce shallow but attractive potentials with partial spin-singlet character that can indeed hold bound molecular states [52, 53]. Further works showed that the spin-orbit interaction between the total electronic spin and the scattering partial wave L (angular momentum with respect to the perturber) also introduce higher-order corrections to the ULRM spectra [54, 55], that was promptly detected experimentally [56]. The response of ULRMs to external electric and magnetic fields has also been studied in various contexts [57–59], with interesting use cases found in molecular field alignment [60, 61], and creation of giant dipolar states [62].

Experimental observations: The first ULRM was experimentally observed nine years after its prediction, by Bendkowsky et al. [63] in Stuttgart. Their observations featured fully bound vibrational states of low-ℓ Rb dimers in the ns state, with n between 34 and 40. Soon after, they were also able to observe triatomic states of ULRM, as well as quasi-bound states stabilized by internal quantum reflection [64], due to a steep potential drop induced by the P-wave shape resonance. A separate experimental work that followed, also reported the measured lifetimes of ns ULRM in vibrational ground and excited states [65], identifying atom-molecule collisions and internal molecular decay as important mechanisms that supplement the radiative decay rates. All three of these works utilized two photon absorption schemes ($5s_{1/2} \rightarrow 5p_{3/2} \rightarrow ns_{1/2}$) to address the ultracold ^{87}Rb gas and create the low-ℓ ULRM, which were subsequently detected through field ionization [63]. In comparison, a direct photoassociation of trilobite or butterfly molecules would require at least an efficient three-photon absorption scheme to access high-ℓ states. However, it is sometimes the case that high-ℓ molecular states are mixed with low-ℓ states that are energetically nearby, often through

avoided crossings. One can tune these admixtures and energy splittings very well by utilizing an electric field; high-ℓ states are highly polarizable and amenable to manipulation. Keeping this in mind, Booth et al. [47] were able to experimentally produce Cesium trilobite molecules by using an electric field to admix the trilobite state with the energetically nearby s-state (specific to Cesium quantum defect structure), and use standard two-photon absorption techniques to access the ns-admixture in the trilobite state. Very soon, pendular states of ^{87}Rb butterfly molecules were also observed by Niederprüm et al. [66] through a single-photon transition via nearby np-state admixture, whereas mixed trilobite states were photo-excited by Kleinbach et al. [53] via resonant spin-orbit coupling. Finally, direct three-photon excitation of a 'pure' trilobite molecule was experimentally performed by Althön et al. [67] rather recently.

While these experimental studies were initially performed on alkali atoms like ^{87}Rb [63–65] or ^{133}Cs [47, 68, 69], ULRMs formed with divalent Strontium were soon found to be an important and exciting case study [70–72]. Unlike their alkali metal counterparts, bosonic ^{84}Sr does not feature a P-wave shape resonance in the context of electron-atom scattering. Moreover, the lack of hyperfine splitting in ^{84}Sr makes it so that the singlet and triplet scattering channels remain uncoupled, so that the ^{84}Sr ULRM has a much simpler electronic spectrum that features pure trilobite states without the complex spin-couplings present in alkali atoms. Hence, ^{84}Sr provides an ideal testing ground to study the dynamics and structure of trilobite molecules. More recently, ULRMs based on atoms with multiple active valence electrons like Ytterbium [73] and Mercury [74] have been studied, revealing a rich and complex spin structure.

An understanding of the contemporary research field of ULRMs can be efficiently obtained from the series of reviews [75–78] which were documented over the past two decades. The research works presented in this dissertation builds upon this foundation and extends this compendium to include the vibronic structure, quantum dynamical effects, and precision spectroscopy of ULRM.

Thesis contributions: The starting point of all the aforementioned studies is the Born-Oppenheimer (BO) approximation [79], which prescribes the separation of fast-electronic and slow-nuclear motion as a foundational principle in molecular physics. It is through this viewpoint that one talks about the electronic and vibrational substructure of the ULRM as if they are separable entities. However, the BO approximation can break down when the potential energy curves from different electronic states are in close proximity. When the non-adiabatic interaction is strong enough, one can no longer separate the electronic and vibrational modes of a molecule, but rather consider them as coupled *vibronic* degrees of freedom. The exact nature of such interactions depends on the dimensionality of the system.

In one-dimensional systems, like a vibrating diatomic molecule, potential energy curves belonging to electronic states of the same symmetry cannot cross each other, hence forming

an avoided crossing. Such avoided crossings between trilobite, butterfly, and low-ℓ states are commonplace in the potential energy landscape of the ULRM, resulting in nonadiabatic interactions that alter the spectra and lifetimes of the molecule. Earlier works had already discovered the necessary breakdown of adiabaticity due to such avoided crossings, in experiments that looked at ℓ-changing collisions and autodissociation [80]. Interestingly, higher dimensional systems can exhibit what is popularly called a conical intersection (CI), when the potential energy surfaces become degenerate, and the non-adiabatic couplings become singular, causing the complete breakdown of BO physics [81–83]. Found naturally in polyatomic systems, or induced via an external field, CIs can cause ultrafast non-radiative transitions between electronic states [84–87], inducing molecular pre-dissociation and surface hopping at much faster timescales than corresponding radiative processes. Such vibronic processes are vital to the study of many important biomolecular mechanisms, such as photoisomerization [88, 89], photosynthesis [90], as well as photostability and self-repair of DNA under radiation [91, 92]. Additionally, they also cause spontaneous symmetry breaking in the form of Jahn-Teller distortions, affecting the structure and properties of polyatomic systems [93, 94]. Very recently, Hummel et al. [95] formulated the existence of CIs in ULRM dimers by considering the principal quantum number n as a synthetic dimension. This approach allowed us to study how the nonadiabatic interaction effects exhibited by a ULRM change with respect to the internal structure of the constituent Rydberg atom. Similar non-adiabatic effects have also been studied in the context of trapped Rydberg ions [96, 97], Rydberg atom ion molecules [98], and Rydberg bimolecules [99].

However, we find that a systematic theoretical analysis of the vibronic structure of the ULRM were lacking in earlier literature on these dimers. Previous works [80, 95] mainly utilized semiclassical Landau-Zener models to qualitatively understand certain phenomena. The vastly different time-scales and length-scales of the ULRM, highly oscillatory potential energy structure and relatively small level spacings promise unconventional vibronic effects in ULRM, hitherto unexplored using exact quantum mechanics. The works [P1, P2] presented in the thesis, along with that of our collaborators [100, 101], were finally able to initiate a systematic study of non-adiabatic phenomena in ULRMs. In [P1] we highlight the vibronic coupling between electronic states in ^{23}Na dimers. The quantum defect structure of Sodium allows for strong vibronic coupling between trilobite and d-state PECs, while also displaying more prominent energetic alterations to the spectra, in comparison with heavier atoms. We show that the non-adiabatic coupling between the electronic states is heavily dependent on n, and go on to explain this dependency using the concept of CIs in synthetic dimension [95]. We then developed a coupled-channel treatment for calculating the vibronic structure of the ULRM, and compared the obtained spectra for exemplar n-values, that display near-degenerate as well as wide avoided crossings. Here, we predicted the existence of vibronic resonance states that have no adiabatic equivalent, as well as nonadiabatic localization effects that can be qualitatively explained utilizing a Born-Huang model [102–104]. In [P2] we investigate the non-adiabatic stabilization of ^{87}Rb trilobite states against internal molecular

decay, and experimentally verify the existence of predicted non-adiabatic couplings. The internal decay channel here is caused by the avoided crossing between the trilobite and butterfly potential, allowing an adiabatic pathway out of the trilobite PEC. We observe that highly excited vibrational states are stabilized across multiple adiabatic potentials via non-adiabatic surface hopping. We see that the lifetimes (and hence stability) of these states depend highly on the n-value, as predicted in our previous work.

In addition to exciting spectroscopic studies discussed above, there has been increasing interest in the quantum dynamics of long-range molecular systems that feature slow temporal evolution and exaggerated sizes. Recent studies have explored field quench dynamics of ULRM [105], stretching and bending dynamics of ULRM [106], and even dynamical features in charged Rydberg molecules [36, 98]. We find that there is scope to explore many unconventional dynamical effects, not yet analyzed in the previously mentioned works. In [P3] we demonstrate that the electronic potential energy structure of the trilobite molecule can diffract a time-evolving nuclear wavepacket, creating what is effectively a self-diffracting molecule. We perform numerical simulations where a Gaussian initial states with varying widths are allowed to time evolve in trilobite states with appropriate n-values, and explain the observed quantum diffraction effects using a Fourier analysis of the nuclear wavepackets and the trilobite PECs. An exemplar pump-probe scheme that allows for the experimental observation of these dynamical effects is provided, where vibrational ground states in low-ℓ PECs are used as initial and probe states. However, the calculations in [P3] are qualitative in nature and ignore the existence of a shape resonance-induced avoided crossing between the trilobite and butterfly PECs.

Adiabatically speaking, a propagating diffraction pattern should soon decay into the butterfly state via the avoided crossing, only allowing short-term diffraction dynamics. However, we show in [P4] that vibronic coupling between two different adiabatic curves (mixed trilobite-butterfly systems) can indeed stabilize the propagating diffraction pattern against decay into the P-wave channel. We also investigate how the vibronic coupling between the electronic states change as a function of n, and how that manifests as the n-dependency of the observed dynamical phenomena. We further characterize surface hopping between the adiabatic PECs by calculating channel populations as a function of time. Apart from the internal diffraction dynamics, our works [P3, P4] also explore rich multiwell tunneling effects in the highly oscillatory trilobite potentials, for various n-values, in both the adiabatic and non-adiabatic regimes.

Finally, we utilize the recently achieved ability to perform three-photon excitation of high-ℓ molecules by Herwig et al. [67], to access specific electron-atom scattering channels with unprecedented accuracy. In the work [P5], we combine the recently developed spin-coupled Green's function formalism [107] with the state of the art experimental platform, to extract e^-−Rb scattering phase shifts in $^3S_1$ (spin-triplet, L=0) configuration. Conveniently,

trilobite molecules are predominantly $^3S_1$ by nature, and have binding energies of the order of GHz, multiple orders of magnitude higher than the characteristic experimental uncertainties ($\sim$ MHz). Moreover, the Green's function method used circumvents basis-dependent convergence errors that plague other methods that use exact diagonalization of a fermi pseudopotential [108], while also considering the most important angular momentum couplings. This combination allows us to extract e^-–^{87}Rb scattering phases with a relative error of less than one percent, an exciting feat in low-energy regimes.

In the work [P6], we theoretically characterize and report the first experimental observation of the spin-singlet P-wave ULRM (denoted $^1P_1$). These high-ℓ states were photoassociated via three-photon excitation processes, and their identity was validated by comparing the observed dipole moments, signal strengths, binding energies, and splitting to calculated theoretical values. The production of these states realized an important step in the creation of elusive ultracold anions and ultracold neutral plasmas [109] in ^{87}Rb. Creation of these ultracold charged states of alkali atoms has remained a challenge, due to the absence of laser-cooling transitions, and complications in sympathetic cooling techniques [110, 111]. Moreover, ionizing ultracold neutral atoms also comes with its own unique set of problems, primarily induced by the newly produced free photoelectrons [112]. However, the recent proposal to create Heavy Rydberg States (HRS) from $^1P_1$ ULRM [109] bypasses the aforementioned issues, enabling the production of ultracold anions and plasmas. Overall, these experimental collaborations illustrate the ability to create long-range states of desirable spin and angular momentum configuration, using Rydberg mediation.

Outline: The contents of this thesis are organized as follows. Chapter 2 reviews the fundamental theoretical framework required to discuss the physics of Rydberg molecules. Particularly, section 2.1 introduces the basics of Rydberg atoms, with different subsections discussing their internal substructure. Then we lay out the basic molecular physics of the diatomic ULRM in section 2.2, both from an adiabatic and non-adiabatic perspective. The chapter ends with a brief introduction to the topics of quantum dynamics, in single-channel and multi-channel systems. Chapter 3 introduces the object of interest, the ULRM, and proceeds to discuss the underlying binding mechanism, electronic spectra, spin-couplings, and briefly discusses the experimental setup used by our collaborators. We then summarize the core results of our published research in chapter 4, separated into subsections that follow the themes of vibronic spectra, quantum dynamics, and precision spectroscopy. Following this, the scientific contributions themselves are displayed in the order of the discussed themes, in chapter 5. Finally, we conclude the dissertation with a brief summary of our work, along with possible future research directions and outlook in chapter 6.

Chapter 2

Theoretical framework

2.1 A primer on Rydberg atoms

Rydberg atoms are atoms whose valence electron(s) have been excited to a very high principal quantum number n. Considering their orbital size (and dipole moments) that scale with n^2, and their radiative lifetimes that scale wih n^3 [113], these atoms no longer remain constrained to what is deemed as atomic length and time scales. The modern quantum physicist seek their many desirable properties: like their large lifetimes, tunable electromagnetic field sensitivity, and perhaps most importantly the ability to engineer various types of atom-atom interactions. Consequently, they have been established to be a key player in the development of quantum computing and simulation [16, 17, 114–116] platforms, high precision field sensing [117–119], and other frontiers of applied physics research.

Besides their modern relevance and fame, they have inherited a deeper history from the beginnings of atomic and quantum physics. We can start their story from 1890, when Johannes Rydberg proposed an empirical formula [120] that explained the observed spectral lines of simple Hydrogen like elements, hinting at the hidden discrete structure of atoms. This key result sits at the heart of early quantum revolution, inspiring and validating the Bohr's model of atom, and later the fully quantum mechanical formulation of the Hydrogena atom. We now know that Rydberg structure can also be realized in many-electron atoms (or even molecules) by exciting a valence electron to a large n-value. Rydberg states with n upto 300 have been created in a laboratory setting [121], whereas studies with $n \sim 20$ to 50 are ubiquitous in literature today. The electronic structure and collisional properties of these non-hydrogen Rydberg systems were a subject of extensive study across the 1900s [122–126].

The historical relevance of Rydberg states does not stop at the formulation of the quantum theory of atoms; they were instrumental in the Nobel-prize winning experimental works in cavity quantum electrodynamics, enabling the manipulation and non-destructive measurement of individual photons for the first time [127–129]. They also acted as an important laboratory testing grounds for exploring quanum chaos [130–133], acting as a bridge between the quantum and (semi-)classical regimes. With advancements in laser cooling and trapping, Rydberg atoms now take central stage in ultracold physics explorations, like the ULRM. Hence, we must accustom ourselves with the basics of the electronic structure of Rydberg

atoms, atleast for the simplest case of alkali atoms, i.e. atoms with only one valence electron. In this regard, the following sub-sections give a brief overview of the quantum defect structure (Sec. 2.1.1), electronic wavefunctions (Sec. 2.1.2), and radiative properties (Sec. 2.1.4) of alkali atoms.

2.1.1 Quantum defect structure of alkali atoms

Species	ns	np	nd	nf
$Li^{6,7}$	0.3995101	0.04717	0.002129	-
Na^{23}	1.347964	0.855	0.015543	-
Rb^{87}	3.13118	2.65	1.347	0.01652
Cs^{133}	4.049325	3.57	2.47	0.033392

TABLE 2.1: Quantum defects (δ_ℓ) of alkali atoms [48, 55, 113], for $\ell = 0 - 3$, i.e s, p, d and f states without considering the small deviations due to fine-structure and n-dependence. Table 2.2 presents a more meticulous compilation of the data.

When the single valence electron of an alkali atom is sufficiently far away from the inner core (radii $\propto n^2$), the nuclear charge Z is shielded by the Z-1 inner electrons, so that the Rydberg electron experiences an almost Coulombic potential. The deviations from a purely Coulombic model are strongly dependent on the angular momentum ℓ, of the Rydberg electron. In high-ℓ states, the centrifugal barrier prevents the valence electron from penetrating the ionic core. Hence, a high-ℓ Rydberg state is essentially hydrogenic, with the ionic core acting like a $Z = 1$ point charge, causing the valence electron to experience a Coulomb potential.

On the other hand, a Rydberg electron with low-ℓ can still resolve and penetrate the finite-sized ionic core. The consequent deviation of the low-ℓ atomic resonances from hydrogenic energy levels, can be very successfully explained using quantum defect theory. This is done by using a modified non-integer principle quantum number $n^* = n - \delta_\ell$, where δ_ℓ is the quantum defect. Hence, the energy levels of alkali Rydberg atoms can be approximately written as

$$E_{nl} = -\frac{1}{2(n - \delta_\ell)^2} \tag{2.1}$$

in atomic units, while neglecting relativistic and spin corrections. Table 2.1 shows the low-ℓ quantum defects of different alkali atoms, while corresponding $\delta_\ell \sim 0$ for all $l > 3$. Hence all the high-ℓ states together form a quasi-degenerate manifold that mimics the hydrogenic manifold. The low-ℓ states however, are non-degenerate and lowered in energy.

The simplistic model of a Rydberg atom provided above is generally limited to alkali metal species, where the ionic core has a closed shell structure with a stable electronic configuration. This suppresses further electronic excitation of the core, and favors a dominant single-channel quantum defect treatment. However, Rydberg atoms of non-alkali elements have also been

created and studied extensively. In fact, many modern neutral atom platforms for quantum computing utilize divalent Ytterbium [134–138] or Strontium [139, 140] atoms as the basis for their qubits. Unlike alkali metals, their Rydberg states feature a residual low-energy valence electron as part of the ionic core, allowing for different core configurations to exist. Their spectra are typically explained using multichannel quantum defect theory [141–143]. While this is an exciting topic in modern atomic physics, we will limit our focus to the electronic structure of alkali atoms Na^{23} and Rb^{87}, to maintain relevance to the results presented in the thesis.

2.1.2 Rydberg wavefunctions of alkali atoms

Just like its electronic energy levels, the wavefunctions of alkali Rydberg atoms also closely resemble the hydrogen atom wavefunction. The slight, but important variance from its hydrogenic counterpart arises due to the ℓ-dependent core penetration of the valence electron, and polarization effects. The electronic eigenstates are obtained by solving the Schrödinger equation

$$\hat{H}_{Ryd}\phi_{E,\ell}(\mathbf{r}) = E_\ell \phi_{E,\ell}(\mathbf{r})\,, \tag{2.2}$$

$$\hat{H}_{Ryd} = -\frac{1}{2\mu_e}\nabla^2_{\mathbf{r}} + \frac{\ell(\ell+1)}{2\mu_e r^2} + V_\ell(r) \tag{2.3}$$

where μ_e is the reduced mass of the electron-core system i.e. the Rydberg atom, $\mathbf{r} = (r, \theta, \phi)$ are the position coordinates of the Rydberg electron with respect to the ionic core, and $E_\ell = -(n - \delta_\ell)^{-2}/2$ are the quantum defect splitted energies. The electronic wavefunction $\phi_{E,\ell}$ is parametrized by the energy and angular momentum of the electron. The Rydberg atom Hamiltonian $\hat{H}_{Ryd}$ represents an electron moving in an ℓ-dependent central potential V_ℓ, created by the ionic core. Such an effective potential can be modeled as [144]

$$V_\ell(r) = -\frac{Z_\ell(r)}{r} - \frac{\alpha_c}{2r^4}\left(1 - e^{-(r/r_c)^6}\right)\,, \tag{2.4}$$

$$Z_\ell(r) = 1 + (Z-1)e^{-a_1 r} - r(a_3 + a_4 r)e^{-a_2 r}\,, \tag{2.5}$$

where α_c is the static dipole polarizability of the ionic core, Z is the nuclear charge, and r_c depicts the short-range cut-off radius at which the polarization potential is truncated. Z_ℓ is the effective charge experienced by the Rydberg electron, deviating from Z as a function of ℓ and r due to inner electron shielding, and $a_i(\ell)$ are ℓ dependent parameters. The modeling and the parameters are explained in detail in Ref. [144].

Since $V_\ell(r)$ is spherically symmetric, the total wavefunction can be separated into the radial and angular parts [145],

$$\phi_{E,\ell m_\ell}(r, \theta, \phi) = \frac{U_{E,\ell}(r)}{r} Y_{\ell m_\ell}(\theta, \phi) \tag{2.6}$$

where $U_{E,\ell}$ are the energy dependent reduced radial wavefunctions, and $Y_{\ell m_\ell}$ are the angular wavefunctions given by standard spherical harmonics, with m_ℓ being the magnetic quantum number. It is obvious here that the deviation from hydrogenic eigenstates are manifested in the radial wavefunctions, which can be obtained by solving the reduced radial Schrödinger equation

$$\frac{d^2U_{E,\ell}(r)}{dr^2} + 2\mu_e\left[E_\ell - \frac{\ell(\ell+1)}{2\mu_e r^2} - V_\ell(r)\right]U_{E,\ell}(r) = 0 \tag{2.7}$$

for a given energy E_ℓ, obtained from the quantum defects by Eq. 2.1. Since we know the quantum defects for a given species (see Table. 2.1), we can numerically solve Eq. 2.7 using a Numerov integration scheme [146–148] and obtain $\phi_{E,\ell m_\ell}$.

A simpler description of the Rydberg atom wavefunction can be obtained by approximating V_ℓ to be a Coulomb potential, and assuming that the deviation from hydrogen wavefunctions is simply limited to non-integer values of the principal quantum number $n^* = n - \delta_\ell$. The approximation works very well for large r-values, where $Z_\ell \to 1$, and the static core polarization terms are completely overshadowed by the Coulomb term. Then the reduced radial Schrödinger equation becomes,

$$\frac{d^2U_{E,\ell}(r)}{dr^2} + 2\mu\left[E_\ell - \frac{\ell(\ell+1)}{2\mu_e r^2} + \frac{1}{r}\right]U_{E,\ell}(r) = 0\,, \tag{2.8}$$

the radial Coulomb wave equation. The solutions to this equation were a subject of elaborate study in the previous century [149]. We now know that the solutions to Eq. 2.8 that satisfy the necessary boundary conditions (the wavefunction must vanish as $r \to \infty$), can be expressed as [149] :

$$U_{n^*\ell}(r) = \frac{W_{n^*,\,\ell+\frac{1}{2}}\left(\frac{2r}{n^*}\right)}{r\,n^*\sqrt{\Gamma(n^*+\ell+1)\,\Gamma(n^*-\ell)}} \tag{2.9}$$

where $W_{n^*,\,\ell+\frac{1}{2}}$ is the Whittaker-W function [150, 151], and Γ is the gamma function [152]. Note, that we have changed the indexing of the wavefunction from E_ℓ to n^* for the sake of clarity in representation, without losing any relevant information. The Whittaker-W function is not always well-behaved for small r-values; fortunately, the large r-values typical of Rydberg atomic systems render the approximation valid.

For high-ℓ states, the quantum defect vanishes and $n^* \approx n$ becomes an integer. If n and $(2\ell+1)$ are integers, the Whittaker-W function can be written as

$$W_{n,\,\ell+\frac{1}{2}}\left(\frac{2r}{n}\right) = (-1)^{n-\ell-1}\,(n-\ell-1)!\,e^{-r/n}\left(\frac{2r}{n}\right)^{\ell+1} L^{2\ell+1}_{n-\ell-1}\left(\frac{2r}{n}\right)\,, \tag{2.10}$$

where $L^{2\ell+1}_{n-\ell-1}$ are the generalized Laguerre polynomials [152]. Substituting this in 2.9, we obtain

$$U_{n,\ell}(r) = \sqrt{\left(\frac{2}{n}\right)^3 \frac{(n-\ell-1)!}{2n\,(n+\ell)!}}\, e^{-r/n} \left(\frac{2r}{n}\right)^{\ell} L^{2\ell+1}_{n-\ell-1}\left(\frac{2r}{n}\right), \tag{2.11}$$

, i.e. we get back the standard hydrogen-atom wavefunction, as we expect in the high-ℓ case.

The approximate forms of the Rydberg wavefunctions presented here can be very useful when performing qualitative studies, especially since the constituent functions and polynomials are readily available in standard computational mathematics packages like `numpy` and `mpmath`. However, a quantitatively rigorous calculation of the alkali Rydberg wavefunctions must consider the polarization and other finite-size effects of the ionic core (as modeled in Eq. 2.4), and include the fine structure effects due to spin-orbit coupling.

2.1.3 Fine structure of alkali Rydberg atoms

Much like its hydrogenic counterpart, Rydberg atoms also experience the splitting of their eigenstates due to the interaction between the orbital angular momentum and spin. It is often necessary to include the resulting fine-structure in the description of Rydberg states, as the exact quantum defect (and energy) structure, the dipole transition elements, and other radiative properties are noticeably modified. A comprehensive understanding of this spin-orbit coupling mechanism and it's effects on atomic spectra can be found in many standard quantum mechanics and atomic physics textbooks [142, 145, 153, 154]. The spin-orbit coupling term that contributes to the Rydberg atomic Hamiltonian can be written as:

$$\hat{V}_{so} = \alpha_{so} \frac{\boldsymbol{\ell} \cdot \mathbf{s}}{2r^3} \tag{2.12}$$

where $\alpha_{so} \approx \frac{1}{137}$ is the dimensionless fine-structure constant, $\mathbf{s}$ is the spin operator, and $\boldsymbol{\ell}$ is the orbital angular momentum operator. The corresponding magnetic quantum numbers m_s and m_ℓ, i.e. the projection of $\mathbf{s}$ and $\boldsymbol{\ell}$ along the z-axis, are no longer good quantum numbers as the corresponding observables do not commute with $\boldsymbol{\ell} \cdot \mathbf{s}$. Hence we introduce the total angular momentum of the electron $\mathbf{j} = \mathbf{s} + \boldsymbol{\ell}$, and its projection m_j as good quantum numbers in the spin-orbit coupled system [145]. The eigenstates of the total Hamiltonian including V_{so} can be represented as $|n, \ell, s, j, m_j\rangle$ using Dirac notation based on the relevant good quantum numbers of the system. Whereas the eigenstates of the spin-uncoupled system (discussed previously in Sec. 2.1.2) can be represented as $|n, \ell, m_\ell, s, m_s\rangle$, where the Rydberg electron's spin wavefunction is written as $|s, ms\rangle = |\frac{1}{2}, \pm\frac{1}{2}\rangle$ for alkali atoms, so that the allowed values of j are $\ell \pm \frac{1}{2}$.

TABLE 2.2: Quantum defects $\delta_{\ell j}$ and $\delta'_{\ell j}$ dependent on different ℓ, j values in $Li^{6,7}$ [155], Na^{23} [156] and Rb^{87} [157, 158], with data taken from [48, 55]. One can also find the data for K and Cs compiled in [48, 55].

	Li		**Na**		**Rb**	
(ℓ, j)	$\delta_{\ell j}$	$\delta'_{\ell j}$	$\delta_{\ell j}$	$\delta'_{\ell j}$	$\delta_{\ell j}$	$\delta'_{\ell j}$
$(0, 1/2)$	0.3995101	0.0290	1.347964	0.060673	3.1311804	0.1784
$(1, 1/2)$	0.0471835	-0.024	0.855380	0.11363	2.6548849	0.2900
$(1, 3/2)$	0.0471720	-0.024	0.854565	0.114195	2.6416737	0.2950
$(2, 3/2)$	0.002129	-0.01491	0.015543	-0.08535	1.34809171	-0.60286
$(2, 5/2)$	0.002129	-0.01491	0.015543	-0.08535	1.34646572	-0.59600
$(3, 5/2)$	-0.000077	0.021856	0.0001453	0.017312	0.0165192	-0.085
$(3, 7/2)$	-0.000077	0.021856	0.0001453	0.017312	0.0165437	-0.086

Since the total Hamiltonian is diagonal in the $|n, \ell, s, j, m_j\rangle$ basis, the eigenenergies corresponding to each state can be trivially modeled as

$$E_{n\ell j} = -\frac{1}{2(n - \delta_{n\ell j})^2} \tag{2.13}$$

where $\delta_{n\ell j}$ are the experimentally resolved (n, ℓ, j)-dependent quantum defects. The observed n-dependency of these quantum defects can be formulated as

$$\delta_{n\ell j} = \delta_{\ell j} + \frac{\delta'_{\ell j}}{(n - \delta_{\ell j})^2} \tag{2.14}$$

where the measured values of both $\delta_{\ell j}$ and $\delta'_{\ell j}$, are compiled and displayed in table 2.2. The **r**-space representation of these spin-coupled wavefunctions can be readily calculated as

$$\begin{aligned} \phi_{n\ell j m_j} &= \langle \mathbf{r} | n, \ell, j, m_j \rangle \,, && (2.15)\\ &= \sum_{m_\ell, m_s} \langle \mathbf{r} | n, \ell, m_\ell, s, m_s \rangle \langle n, \ell, m_\ell, s, m_s | n, \ell, j, m_j \rangle \,, && (2.16)\\ &= \sum_{m_\ell, m_s} \phi_{n\ell m_\ell} \, C^{j, m_j}_{\ell, m_\ell, s, m_s} && (2.17) \end{aligned}$$

using previously calculated $\phi_{n\ell m_\ell}$ and the appropriate Clebsh Gordon coefficients $C^{j,m_j}_{\ell,m_\ell,s,m_s}$ [153]. Alternatively, one can also obtain $\phi_{n\ell j m_j}$ by numerically solving the Schrödinger equation using Numerov methods, that include the spin-orbit interaction term (Eq. 2.12) represented in the $|n, \ell, j\rangle$ basis, as is done in the `ARC-Alkali Rydberg Calculator` package [159, 160].

We can analyze the fine-structure of Hydrogen to understand how the energy corrections change with respect to (n, ℓ, j). The hydrogenic energy splitting is given by [55, 145]

$$\Delta E_{nj} = -\frac{\alpha^2}{2n^3}\left(\frac{1}{j+\frac{1}{2}} - \frac{3}{4n}\right). \tag{2.18}$$

We see that ΔE_{nj} decreases with both n and j, making the fine-structure splitting more evident for low-ℓ states. However, for $\ell = 0$, there is only one allowed configuration, $j = \frac{1}{2}$. Although eq. 2.18 is derived for the hydrogen atom, alkali atoms also qualitatively show the same behavior. We can see in table 2.2 that the energy difference between different (j, ℓ)-pairs, manifested as the difference in quantum defects, rapidly decrease as ℓ increases. So much so that the splitting is only really evident p states for lighter atoms like Li and Na. In this thesis, we have chosen to include and exclude fine structure effects, depending on the level of accuracy desired in the project. Fine structure effects of Rb^{87} were promptly included in calculations that benchmarked high-precision spectroscopy experiments, whereas projects aimed at qualitative analysis of dynamical and nonadiabatic phenomena excluded such complexities.

In comparison, we completely ignore the hyperfine structure of Rydberg atoms, as the interaction between nuclear magnetic moment and the valence electron are negligible (on the order of kHz) and generally not resolved in laser based spectroscopic methods [161].

2.1.4 Photoexcitation and radiative lifetimes

Rydberg atoms can be efficiently produced by optically exciting a ground-state atom, facilitated by the interaction of the incoming photon (or light field) with the atomic dipole $\mathbf{d} = e\mathbf{r}$. Generally speaking, the transition dipole moment $d_{gn} = \langle g|\mathbf{d}|n\rangle$ from the ground state $|g\rangle$ to an excited Rydberg state $|n\rangle$ scales as n^2 [113], enabling strong light matter interactions and high excitation yields. The alkali atoms of interest have natural ground states desribed as $n_0\, s_{1/2}$, i.e. $j = \frac{1}{2}, \ell = 0$, with n_0 being the principal quantum number of the valence electron. The possible dipole transitions from the $s_{1/2}$ ground states using a monochromatic laser, are limited by dipole selection rules. Hence, one often needs to perform multiphoton transitions to achieve the desired Rydberg levels [162–164]. For example, to excite an Rb^{87} atom to an $18f_{7/2}$ state would require a three photon transition $5s_{1/2} \to 5p_{3/2} \to 5d_{5/2} \to 18f_{7/2}$, using lasers at 780 nm, 776 nm, and 1288 nm [P5, 67].

Apart from the ease of production, Rydberg atoms also feature relatively large lifetimes of the order of microseconds[165–167] to milliseconds [168–170], that allow us enough time to engineer many types of atom-atom interaction [7, 8, 10, 30, 35]. Atomic states in ultracold Rydberg experiments decay by spontaneous radiative emission via dipole transitions to lower energy states. The lifetime of a Rydberg state is obtained by first calculating the total spontaneous decay rate, by summing over all possible decay channels, i.e. summing over the decay rates to all lower energy states that are dipole connected to the initial Rydberg state. Here,

the transitions with the highest frequency (energy difference) contribute most to spontaneous radiative decay [113, 145]. However, the overlap between the radial wavefunctions of the Rydberg atom and the low-lying states (featuring the highest frequency) is minimal. This means that, as the n and ℓ values increases, the decay rates naturally decrease, increasing lifetimes. For low-ℓ states, the radiative lifetimes scale as $\tau \sim (n^*)^3$ [113, 166], facilitating lifetimes of 10s to 100s of microseconds for n =20 to 50. Apart from scaling with respect to n, lifetimes also generally increase with ℓ, due to further reduction in allowed dipole transitions. As an extreme case, circular Rydberg states with $\ell = n - 1$ feature lifetimes on the order of 100s of milliseconds [168–170]. These long-lived circular states have been proposed to be used as qubits in quantum computing and simulation platforms [171, 172], although preparation turns out to be quite difficult, in comparison with their low-ℓ counterparts. In higher temperature experiments, one must also consider stimulated decay due to black-body radiation [113, 173, 174], and various collisional decay mechanisms [113, 126, 175, 176]. The research presented in this thesis however, is perfomed at ultracold $(40 - 150\mu K)$ temperatures where black-body effects are safely ignored.

2.2 Molecular structure and vibronic spectra

In this section we lay down the theoretical framework needed to understand the internal structure and spectra of the ULRM, from a molecular physics perspective. Conventional diatomic molecules feature a wide variety of binding mechanisms, where complex many-body electron-electron interactions need to be considered. Fortunately, the closed-shell inner cores of both alkali atoms, as well as the low-energy scales of the atom-atom interaction, ensure that the inner electrons remain bound to the nuclei. Hence, the binding mechanism can be understood by using only the valence electrons and ionic cores. Figure 2.1 shows an exemplar sketch of an Rb molecular system, where the distance between the cores is given by $\mathbf{R}$, and the coordinate of the Rydberg electron with respect to the core is given by $\mathbf{r}$.

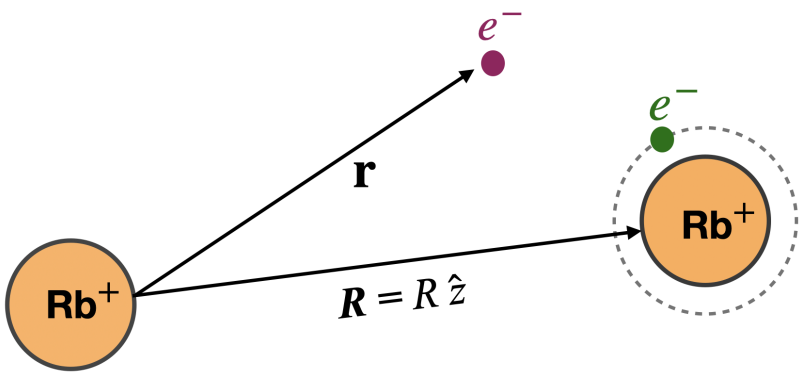


FIGURE 2.1: An illustrative sketch of a diatomic ULRM, in the molecular body-fixed frame.

We can formulate these quantities in the center of mass reference frame of the entire system, decoupling the relative motion and the center of mass motion. The properties of interest are then governed by the relative Hamiltonian [177], only dependent on $\mathbf{r}$ and $\mathbf{R}$. By fixing the coordinate origin at the center of the Rydberg core, and taking the internuclear axis to be always parallel to the z-axis, i.e. $\mathbf{R} = R\hat{z}$, we can describe the system in molecular body-fixed frame of reference [177]. Here, the rotational and translational movements of the center of mass of the molecule, is assumed to be completely independent of its internal degrees of freedom [†] that we seek to investigate. Consequently, the internuclear motion is limited to one-dimensional[†] vibrations along $R\hat{z}$, referred to as R for the rest of this thesis.

[†]The center of mass can only be completely decoupled from the relative Hamiltonian, provided that the potential energy only depends on relative distances between constituent particles. In case there is an external field present, the internal defrees of freedom are coupled to the center of mass motion, and the internuclear motion is not one-dimensional. The work presented in this thesis however, is performed on field-free one-dimensional systems.

2.2.1 Diatomic Hamiltonian and nonadiabatic coupling terms

The internal structure of the diatomic molecule can be analyzed by solving the time independent Schrödinger equation:

$$\hat{H}|\Psi^m(\mathbf{r},R)\rangle = E^m|\Psi^m(\mathbf{r},R)\rangle\,, \tag{2.19}$$

$$\hat{H} = \hat{T}_n + \underbrace{\hat{T}_e + V_e(\mathbf{r}) + V_{ea}(\mathbf{r},R)}_{\hat{H}_{\rm el}(\mathbf{r},R)} + V_{na}(R)\,, \tag{2.20}$$

and obtaining the molecular spectra consisting of the desired eigenstates $|\Psi^m\rangle$ and eigenenergies E^m. Here $\hat{T}_n$ and $\hat{T}_e$ are the nuclear and electronic kinetic energy operators, $V_e(\mathbf{r})$ is the potential experienced by the Rydberg electron due to its ionic core, and $V_{na}(R)$ is the force between the ionic core and the perturbing atom. The interaction between the Rydberg electron and the perturbing atom, given by $V_{ea}(\mathbf{r},R)$, is the only term in the Hamiltonian that depends on both electronic and nuclear coordinates. The one-dimensional nuclear kinetic operator can be written as $\hat{T}_n = -\frac{\partial_R^2}{2\mu_n}$, where μ_n is the reduced mass of the nuclei. Here, both the electron and the nuclei experience similar degrees of Coulombic forces, but they differ massively in their masses, and consequently their velocities. Hence, the electronic coordinates $\mathbf{r}$ are expected to change much faster than their internuclear counterpart, R. One can then isolate $\hat{H}_{\rm el}(\mathbf{r},R)$ as the electronic Hamiltonian that is parametrically dependent on R, and solve it to obtain:

$$\hat{H}_{\rm el}(\mathbf{r},R)|\psi_j(\mathbf{r},R)\rangle = \varepsilon_j(R)|\psi_j(\mathbf{r},R)\rangle\,. \tag{2.21}$$

Here, $|\psi_j(\mathbf{r},R)\rangle$ and $\varepsilon_j(R)$ denote the R-dependent electronic eigenstates and eigenvalues, indexed by j. The exact solutions depend on the nature of V_{ea}, and will be discussed later in this text. Since the electronic eigenstates form an orthonormal and complete basis, one can expand the total molecular wavefunction as

$$|\Psi^m(\mathbf{r},R)\rangle = \sum_j \chi_j(R)|\psi_j(\mathbf{r},R)\rangle\,, \tag{2.22}$$

where $\chi_j(R)$ are the expansion coefficients which portray the mixing of electronic states, as a function of R. This formulation is popularly known as the Born-Oppenheimer expansion [79, 178]. Substituting Eq. 2.22 in the Schrödinger equation 2.20, and integrating out the electronic degree of freedom $\mathbf{r}$, we obtain the coupled-channel vibronic[‡] Schrödinger equation [81]:

$$\left[-\frac{\partial_R^2}{2\mu_n} + V_{na}(R) + \varepsilon_i(R) - E^m\right]\chi_i(R) = \frac{1}{2\mu_n}\sum_j \Lambda_{ij}(R)\chi_j(R)\,. \tag{2.23}$$

[‡]vibronic here denotes the coupled vibrational-electronic degrees of motion

The left hand side of Eq. 2.23 effectively shows the vibrational dynamics of the molecule in a given channel, where $\chi_i(R)$ acts like a potential energy curve (PEC). The right hand side shows how different channels are coupled via the nonadiabatic coupling terms Λ_{ij}:

$$\Lambda_{ij} = 2P_{ij}\partial_R + Q_{ij}\,, \tag{2.24}$$

where P_{ij} and Q_{ij} are derivative couplings of the first and second order, given by:

$$P_{ij}(R) = \langle\psi_i(\mathbf{r},R)|\partial_R|\psi_j(\mathbf{r},R)\rangle_{\mathbf{r}}\,, \tag{2.25}$$
$$Q_{ij}(R) = \langle\psi_i(\mathbf{r},R)|\partial_R^2|\psi_j(\mathbf{r},R)\rangle_{\mathbf{r}}\,, \tag{2.26}$$

where $\langle\rangle_{\mathbf{r}}$ imply that the electronic coordinates $\mathbf{r}$, has been integrated out. The R-dependence of these nonadiabatic terms show how different electronic states are coupled due to the motion of the nuclei.

Note that the mathematical formulation presented above, can also be obtained from publications [P1, 101]. Moreover, a comprehensive understanding of the subject at hand, alongside step-by-step derivations can be obtained from standard textbooks like Ref. [81, 83]. As shown in Ref. [83], it is common to rewrite Eq. 2.23 in matrix form, given by:

$$\left[-\frac{1}{2\mu}(\mathbb{I}\partial_R + \hat{P})^2 + \hat{\varepsilon}(R) + \hat{V}_{ea}(R)\right]\boldsymbol{\chi}(R) = E^m\boldsymbol{\chi}(R)\,, \tag{2.27}$$

where $\hat{P}$ is the first-order coupling operator whose matrix elements are given by Eq. 2.25, $\boldsymbol{\chi}$ is a vector whose entries are each $\{\chi_i\}$, with $\hat{\varepsilon}$ and $\hat{V}_{ea}$ being diagonal operators in this multi-channel indexing. The first term in the Hamiltonian is just the effective kinetic energy operator, whose off-diagonal terms couple different channels of vibrational motion. It is worth noting that $\hat{P}$ is always anti-hermitian, hence P_{ii} is always zero, if the electronic wavefunctions are real-valued. We see in the next sub-section that an exact fully-coupled treatment of the differential equations 2.23 and 2.23, is often unnecessary and unfavourable, as intelligent approximations can greatly reduce the computational expense necessary.

2.2.2 Born-Oppenheimer approximation

Assuming that electronic wavefunctions change with respect to R *adiabatically*, i.e. slowly enough that $\hat{P}$ is almost zero, one can safely ignore the contributions from nonadiabatic terms in the coupled vibronic equations. This adiabatic approximation, first formulated by Robert J. Oppenheimer and Max Born [79], advocates for the complete separation of slow nuclear and fast electronic motion allowing us to independently solve the electronic problem in varying nuclear configurations (parametrized by R in our systems). The multi-channel vibronic equations given by Eq. 2.23 and Eq. 2.27 is then reduced to single-channel vibrational

equations given by:

$$\left[-\frac{1}{2\mu_n}\partial_R^2 + \varepsilon_i(R)\right]\chi_i(R) = E_i^m\chi_i(R)\,. \tag{2.28}$$

Here, $\chi_i(R)$ is a vibrational eigenstate with energy E_i^m that is bound in the adiabatic PEC $\varepsilon_i(R)$. We have safely absorbed V_{ea} into ε_i, as they are both only parametrized by R alone. The total molecular wavefunction can then be written as $\Psi_i^m(\mathbf{r}, R) = \chi_i(R)\psi_i(\mathbf{r}, R)$ with separable electronic and nuclear solutions, effectively truncating the Born-Oppenheimer expansion 2.22 to a single term.

As a next-order approximation, one can consider the correction to the adiabatic potentials due to the nuclear motion, by only including the diagonal terms Λ_{ii} in Eq. 2.23, while still neglecting all off-diagonal elements. Popularly known as the *Born-Huang approximation*[102–104], this effective single-channel treatment gives us the vibrational eigenstates that are bound in a modified potential

$$\varepsilon_i^b(R) = \varepsilon_i(R) - \frac{1}{2\mu_n}\Lambda_{ii}(R) \tag{2.29}$$

$$= \varepsilon_i(R) - \frac{1}{2\mu_n}\langle\psi_i(\mathbf{r}, R)|\partial_R^2|\psi_i(\mathbf{r}, R)\rangle_{\mathbf{r}}\,, \tag{2.30}$$

where one easily recognizes that the diagonal nonadiabatic corrections are first-order perturbations due to the nuclear kinetic energy operator.

The obtained vibrational Schrödinger equations can be solved by numerically using finite difference methods (as explained in A), or by expanding the Hamiltonian in a known set of basis states, and diagonalizing them.

2.2.3 Onset of nonadiabaticity

Both of the aforementioned approximations break down when nonadiabatic couplings become non-perturbative. In the context of traditional molecular physics, sufficiently strong off-diagonal couplings facilitate unique phenomena such as, surface hoppings [179, 180], Jahn-Teller distortions [93, 94], and non-radiative transitions [84–87], with no adiabatic equivalent. Such phenomena are often found in the vicinity of an avoided crossing or conical intersection, when potential energy surfaces (PES) or curves are in close proximity. Of course, the dimensionality of the system dictates how nonadiabatic effects manifest in such a scenario, as dictated by the von- Neumann-Wigner no crossing theorem [181].

To explain briefly, the von Neumann-Wigner theorem [181] states that any two eigenvalues of a Hermitian matrix parametrized by N continuous real degrees of freedom, can only be equal in an $N-2$ dimensional manifold. For one-dimensional diatomic systems like the

one studied here, the eigenvalues of the Hamiltonian parametrized by R cannot be equal. Hence, the adiabatic PECs in different channels $\{\varepsilon_i(R)\}$ cannot cross each other at any R-value. In two-dimensional systems, the associated potential energy surfaces (PES) can be equal in one singular point, denoted as a conical intersection. To understand why the Born-Oppenheimer approximation breaks down near avoided crossings and CIs, we can look at the Hellmann-Feynman form of the derivative coupling [182, 183], given by

$$P_{ij} = \frac{\langle\psi_i|\partial_R \hat{H}_{el}|\psi_j\rangle}{\varepsilon_j(R) - \varepsilon_i(R)}\,, \tag{2.31}$$

for $i \neq j$. We can see from the denominator that, as the two PECs approach each other to form an avoided crossing, the nonadiabatic couplings diverge. In two-dimensions, the partial derivative is replaced by a two-dimensional gradient, and P_{ij} can often be singular or un-defined at the point of conical intersection.

Avoided crossings are ubiquitous in the potential energy landscape of both conventional molecules and ULRM, and the consequent badly-behaved nonadiabatic coupling terms make the numerical solution of the vibronic Schrödinger Eq. 2.27 cumbersome. Fortunately, methods have already been developed, whereby one can change the basis in which the vibronic Hamiltonian is represented in such a way that one no longer needs to directly deal with divergent off-diagonal couplings.

2.2.4 The diabatic transform

In the Born-Oppenheimer basis, the nonadiabatic coupling elements manifest as off-diagonal terms of the kinetic energy operator. By performing a unitary transformation which diagonalizes the kinetic energy matrix, one can circumvent the need to consider these divergent off-diagonal couplings completely. Such a transform would instead introduce off-diagonal terms in the potential energy matrix that are well-behaved, but still account for the couplings between different channels. This is the central idea of *diabatization* [81, 83], the unitary transform is called a diabatic transform, and the resultant basis with diagonal kinetic energy operator is called a diabatic basis. Let $\hat{U}$ be a unitary operator parametrized by R, that acts on the vector of coupled electronic states $\boldsymbol{\chi}$ to produce a new basis vector $\boldsymbol{\chi}^d$, i.e. $\boldsymbol{\chi}^d(R) = \hat{U}(R)\boldsymbol{\chi}(R)$. The vibronic Schrödinger Eq. 2.27 can be rewritten in the transformed basis as:

$$-\frac{1}{2\mu}(\mathbb{I}\partial_R + \hat{P}^d)^2\boldsymbol{\chi}^d(R) + \hat{\varepsilon}^d(R)\boldsymbol{\chi}^d(R) = E^m\boldsymbol{\chi}^d(R)\,, \tag{2.32}$$

where,

$$\hat{\varepsilon}^d = \hat{U}^\dagger\,\hat{\varepsilon}\,\hat{U}\,, \tag{2.33}$$

$$\hat{P}^d = \hat{U}^\dagger(\hat{P}\hat{U} + \partial_R\hat{U})\,, \tag{2.34}$$

are the transformed potential energy operator and derivative coupling operator. The given unitary transform becomes a diabatic transform when the kinetic term in Eq. 2.38 becomes diagonal, i.e. $\hat{P}^d$ vanishes completely. From Eq. 2.33 it is clear that this happens when

$$\partial_R \hat{U} = -\hat{P}\hat{U}\,, \tag{2.35}$$

so that the only off-diagonal terms remaining in Eq. 2.38 is in the diabatic potential energy operator $\hat{\varepsilon}^d$. However, it is not always possible to obtain a consistent general solution to 2.35 in multi-dimensional systems (for example, ULRM in an external field). The geometric phase dependence of the electronic couplings render the diabatization scheme very sensitive to the path of integration around a CI. This prevents us from obtaining a single set of diabatic states that consistently give us accurate vibrational spectra. However, the conventional molecular physics community has performed extensive research on the subject and produced various quasi-diabatization schemes that can perform system-dependent approximate diabatic routines [83].

Thankfully, in one-dimensional systems like the diatomic ULRM, Eq. 2.35 does have an exact and consistent solution, which means that a diabatic transform is always calculable. As a special case, the diabatic transform in a two-channel system has a simple analytical form [184]:

$$\hat{U}(\theta(R)) = \begin{bmatrix} \cos(\theta(R)) & -\sin(\theta(R)) \\ \sin(\theta(R)) & \cos(\theta(R)) \end{bmatrix}\,, \tag{2.36}$$

where $\theta(R)$ is the rotation angle given by

$$\theta(R) = \int_R^\infty P_{12}(x)dx\,. \tag{2.37}$$

Similar closed form solutions for three and four channel solutions can be found elsewhere [101]. For general one-dimensional N-channel systems, one can numerically obtain the solution to Eq. 2.35 by using the split diabatic representation [185]. Once the diabatic transform has been obtained and implemented, the hopefully well-behaved, effective vibronic Schrödinger equation becomes

$$\left[-\frac{1}{2\mu}\mathbb{I}\partial_R^2 + \hat{\varepsilon}^d\right]\boldsymbol{\chi}^d(R) = E^m\boldsymbol{\chi}^d(R)\,, \tag{2.38}$$

diagonalizing which one obtains the eigenvalues and eigenstates (in the diabatic basis) that represent the ULRM spectra. Once the diabatic eigenvectors $\boldsymbol{\chi}^d$ have been calculated, we can transform them back to the adiabatic basis using $\boldsymbol{\chi} = \hat{U}^\dagger\boldsymbol{\chi}^d$. It is often advantageous to treat the system in the adiabatic basis as it grants the reader intuitive clarity, by invoking the Born-Oppenheimer expansion to represent $\Psi^m(\mathbf{r}, R)$. Much like the single-channel case, the diabatic multichannel Schrödinger equation can also be numerically solved using Finite Difference methods as elaborated in the Appendix section A.2, or by utilizing a vibronic

(multichannel) basis set diagonalization is performed in [P1].

2.3 Quantum wavepacket dynamics

Understanding how the quantum states of a molecule change in time is a problem that defines the very heart of quantum chemistry [186–188]. Quantum molecular dynamics helps us to model and understand the very formation of molecules from its atomic constituents through photoassociation [189, 190], decay of molecules via photodissociation[191, 192], different chemical reaction pathways [193, 194], external field responses [195], and the observed spectral signatures of molecular systems [186]. In such simulations, often based on a Born-Oppenheimer perspective, the atomic/ionic cores are modeled as vibrational wavepackets that propagate on potential energy surface(s) or curve(s), exploring a large configuration space while undergoing wave interference effects, tunneling, scattering, and other quantum dynamical phenomena. One generally aims to simulate such wavepacket dynamics by solving the time dependent Schrödinger equation (TDSE), given by

$$i\frac{\partial\chi(t)}{\partial t} = \hat{H}\chi(t)\,. \tag{2.39}$$

In contrast, the time independent Schrödinger equation is used to obtain the stationary states of a molecule, as established in the previous section. When the Hamiltonian is time independent, as is the case in this thesis, the experimentally accessible information about the internal structure of a molecule is obtained from its spectra and cross-sections, primarily explained by its stationary states. However, the TDSE is an initial value problem, characterized by how a given initial configuration or quantum state evolves under a Hamiltonian. Such an approach closely mimics the phenomonology of an actual experiment where the initial state is prepared, time-evolved and then corresponding observable are measured. Both the assortment of possible initial states, and the possible measurement procedures and observables, are constrained by the experimental setup. In such scenarios, the TDSE offers us a simple and elegant equation to solve, that is reflective of its popularity. Of course, a time dependent Hamiltonian often makes the TDSE indispensable, but that is a discussion outside the scope of this thesis.

In this section we first lay down the theoretical minimum to perform adiabatic single-channel wavepacket dynamics in section 2.3.1, explain how a nuclear wavepacket time evolves in a one-dimensional potential energy curve. We then proceed to discuss nonadiabatic, two-channel dynamics in section 2.3.2, analyzing the time evolution of vibronic states in coupled surfaces.

2.3.1 Adiabatic dynamics

Once the electronic Hamiltonian has been solved, the vibrational motion of a molecule within a single adiabatic PEC $\varepsilon(R)$, can be explored by solving the time dependent Schrödinger equation,

$$i\hbar\frac{\partial}{\partial t}\chi(R,t) = \underbrace{\left[-\frac{1}{2\mu_n}\partial_R^2 + \varepsilon(R)\right]}_{\hat{H}_n}\chi(R,t)\,, \tag{2.40}$$

and obtaining the time dependent wavefunction $\chi(R,t)$.

The configuration of the molecule at the beginning of our experiment is represented by the initial wavepacket $\chi(R,t=0)$. For pump-probe style experiments, the initial state is an experimentally accessible eigenstate of the molecule (typically the ground state) residing in a relatively low energy PEC, which is then excited to higher electronic state ensuing new dynamical effects. One can also initialize the wavepacket as a Gaussian, centered at position R_0 with width σ and zero initial momentum, i.e. $\chi(R,t=0) \propto \exp\left[-\left(R-R_0\right)^2/(4\sigma^2)\right]$. This is useful in modeling localized wavepacket scattering and dynamics, given the propensity of harmonic potentials in nature.

The most straightforward way to propagate the initial wavepacket $\chi(R,t=0)$ is by expanding the initial wavefunction in the eigenbasis of the nuclear Hamiltonian, i.e.

$$\chi(R,t) = \sum_k c_k e^{-iE_k t}\chi_k(R), \tag{2.41}$$

where $\chi_k(R)$ are the stationary states of $\hat{H}_n$ with eigenenergies E_k, i.e. $H_n\chi_k(R) = E_k\chi_k(R)$. The coefficients of expansion are then given by the inner-product $c_k = \langle\chi_k(R)|\chi(R,t=0)\rangle$. Of course, such a method necessitates precomputing the spectral decomposition of the Hamiltonian, via exact or approximate diagonalization. In situations where this is not feasible or desirable, we can us finite difference methods like the Crank-Nicolson algorithm [196, 197], or variational methods like $MCTDH$ [198] to simulate wavepacket propagation.

From the time evolving $\chi(R,t)$, we can extract relevant information that corresponds to observables in the laboratory. In typical ultracold molecular experiments, these observables might be the observed molecular spectra (based on photoassociation or field ionization), time dependent probability distribution $|\chi(R,t)|^2$, and time dependent momentum distribution $|\tilde{\chi}(P,t)|^2$. The latter can be obtained by calculating the momentum space wavefunction $\tilde{\chi}(P,t) = \mathcal{F}\{\chi(R,t)\}$ by performing Fourier transformation at each t-value, and is quite useful in analyzing scattering and diffraction effects.

2.3.2 Nonadiabatic dynamics

The dynamics of nuclei cannot always be constrained to a single potential energy curve, as represented in the previous section. As explained in section 2.2, multiple electronic states can be coupled to each other in the vicinity of avoided crossings or CIs, promoting nonadiabatic transitions between different potential curves, such that an exact quantum description of the system necessitates the use of a multichannel TDSE. To avoid dealing with highly singular derivative couplings, we can choose to represent the TDSE in the diabatic basis, as

$$-\frac{1}{2\mu}\partial_R^2 \boldsymbol{\chi}^d + \hat{\epsilon}^d \boldsymbol{\chi}^d(R,t) = i\frac{\partial}{\partial t}\boldsymbol{\chi}^d(R,t)\,, \tag{2.42}$$

much like its time independent counterpart given by Eq. 2.38, with $\boldsymbol{\chi}^d(R,t)$ = $(\chi_1, \chi_2, ..., \chi_N)$ being the time evolving vibronic wavefunction with N-channels, and $\hat{\epsilon}^d$ being the diabatic potential energy operator with off-diagonal terms that couple these channels. In typical simulation routines presented in this thesis, we initialize the wavefunction as a Gaussian wavepacket centered around an $R-$value sufficiently far away from regions where channel couplings are prominent. In such regions, the adiabatic and diabatic PECs coincide, and we can place the wavepacket exclusively in one single-channel and then start the propagation. In exemplar two-channel systems, as studied in [P1, P4], we can initialize the wavepacket $\boldsymbol{\chi^d} = (\chi_1^d,\ \chi_2^d)$ as Gaussian that resides only in the first channel, at $t = 0$:

$$\chi_1^a(R,0) = \frac{1}{(\pi\sigma^2)^{1/4}}\exp\left[-\frac{(R-R_0)^2}{2\sigma^2}\right], \tag{2.43}$$

$$\chi_2^a(R,0) = 0\,. \tag{2.44}$$

As the wavepacket propagates, it can undergo nonadiabatic tunneling and surface hopping effects, which we can study using the time dependent diabatic channel populations

$$p_i^d(t) = \int dR\,|\chi_i^d(R,t)|^2\,. \tag{2.45}$$

Furthermore, we can perform an inverse diabatization transform $\boldsymbol{\chi}^a = U^\dagger\,\boldsymbol{\chi}^d$ to obtain the adiabatic channel populations

$$p_i^a(t) = \int dR\,|\chi_i^a(R,t)|^2 \tag{2.46}$$

which help us understand how the Born-Oppenheimer states are mixed as a function of time. This is particularly useful in analyzing the behavior of vibronic wavepackets in the vicinity of avoided crossings, as they do not manifest in the diabatic basis. Note that the total population

is simply given by the norm of the wavefunction

$$p_{tot}(t) = \sum_i p_i^a(t) = \sum_i p_i^d(t) \tag{2.47}$$

and is invariant of the basis representation, just like the total probability density

$$\rho(R,t) = \sum_i |\chi_i^d(R,t)|^2 = \sum_i |\chi_i^a(R,t)|^2 \,. \tag{2.48}$$

When a propagating wavepacket reaches the endpoints of an R-grid, the enforced boundary conditions can cause the quantum reflection of the wavepacket, leading to interference effects that are numerical artifacts with no physical correspondence. To remedy this, it is customary to use a complex absorbing potential (CAP) [198, 199] that smoothly absorbs the wavepacket before it reaches the grid edge, without affecting the dynamics in the relevant R-range. See Appendix B for a more detailed explanation of Complex Absorbing Potentials. Introduction of a CAP also allows us to simulate the decay of molecular wavefunctions to states outside the relevant Hilbert space. One can simply study the reduction of the total population given by Eq. 2.47, to see how the norm of the wavefunction decreases in time, as more and more population decays due to CAP absorption, such that it simulates molecular decay.

Chapter 3

Ultralong-range Rydberg molecules

In this chapter, we discuss the internal structure of the ultralong-range Rydberg dimers. Previous chapters have reviewed the basic theoretical concepts required to understand the Rydberg atom, as well as the molecular physics of ULRM-like dimers. Now we detail the scattering interaction between the Rydberg atom and ground-state perturber that binds the ULRM, in section 3.1. We then proceed to solve the electronic Hamiltonian to obtain the Born-Oppenheimer potentials and electronic states of the ULRM using perturbative models in section 3.2. At last, we discuss the spin-substructure of the ULRM, and elaborate on the mathematical models used for quantitative research in our works.

3.1 Binding mechanism: electron-atom scattering

Our system consists of two atoms, one of which is excited to a Rydberg state, such that the Rydberg electron undergoes low-energy scattering with the other ground-state atom. A thematic sketch of the model can be found in figure 2.1, accompanied by a detailed discussion of the molecular system in chapter 2.2. Here we continue utilizing the same notation, working in the body-fixed coordinate system so that the Rydberg core is situated at the origin, with the internuclear distance R taken along the z-axis, and position of the Rydberg electron given by $\mathbf{r}$. A rudimentary form of the electronic Hamiltonian that governs the dimer dynamics can be simply written as

$$\hat{H}_{el} = \hat{H}_{Ryd} + V_{ea}(\mathbf{r}, R\hat{z}) + V_{na}(R\hat{z}) \tag{3.1}$$

where $\hat{H}_{Ryd}$ is the Rydberg atom Hamiltonian discussed in chapter 2.1, and V_{ea} is the electron atom scattering potential. The polarization of the perturbing atom due to the Rydberg ionic core induces the polarization potential given by

$$V_{na}(R) = -\frac{\alpha_s}{2R^4}\,, \tag{3.2}$$

where α_s is the static polarizability of a ground-state neutral atom, whose values are given in table 3.1. The R^{-4} dependence of the polarization potential ensure that V_{ea} is only a dominant interaction at shorter ranges like $R \lesssim 100$ atomic units. The long-range tail of the potential is completely negligible at the typical length scales associated with the ULRM ($\gtrsim 1000$ a.u.). An exact quantum mechanical description of an electron scattering with a many-electron heavy atom is cumbersome and complex, due to the complex inner

electron-electron interaction. However, if the electron has very low kinetic energy, V_{na} can be very successfully modeled utilizing a Fermi-pseudopotential approach [122], where the large wavelength of the electron in comparison with the perturber size allows us to represent the electron wavefunction as a finite sum of partial waves centered around the perturber. The scattering interaction then causes phase shifts δ_L in the electron wavefunction, separately for each partial wave L, denoted by the electron angular momentum with respect to the scattering center. At low enough energies, we can assume that only the S-wave term ($L = 0$) contributes to the interaction, so that the Fermi-pseudopotential is given by

$$V_{ea}(\mathbf{r}, R\hat{z}) = V_s(\mathbf{r}, R\hat{z}) = 2\pi a_s(k)\delta(\mathbf{r} - R\hat{z})\,, \tag{3.3}$$

i.e. a contact interaction scaled by the S-wave scattering length $a_s(k)$, defined as

$$a_s(k) = -\frac{\tan(\delta_L(k))}{k}\,. \tag{3.4}$$

Both the phase shift δ_L, and the scattering length a_s depends on the electron momentum k (and thereby its kinetic energy $k^2/2$). A generalization of this formula that includes higher partial waves was developed by Omont [124], which can be written as:

$$V_{ea}(\mathbf{r} - R\hat{z}) = 2\pi \sum_{L=0} (2L+1) \left[-\frac{\tan(\delta_L(k))}{k}\right] P_L\left(\overleftarrow{\nabla}^L_{\mathbf{r}} \frac{\delta(\mathbf{r} - R\hat{z})}{k^L} \overrightarrow{\nabla}^L_{\mathbf{r}}\right)\,, \tag{3.5}$$

where P_L are the Legendre polynomials [152]. The two different arrow directions on the gradient operator is used to show that the left gradient only acts on bra ($\langle|$) vectors, and the right gradient only acts on ket ($|\rangle$) vectors. Note that the first term of the expansion (L=0) reduces back to the S-wave pseudopotential given in Eq. 3.3.

The momentum k of a Rydberg electron in a state $|n, \ell, m\rangle$ can be semiclassically defined as

$$k = \sqrt{\frac{1}{R} - \frac{1}{2(n^*)^2}} \tag{3.6}$$

where $n^* = n - \delta_\ell$, is the quantum defect shifted electronic energy (see section 2.1.1) [†]. There is a noticeable problem with this definition of k, as $R > 2(n^*)^2$ will give us imaginary values for the momentum, and negative values for the kinetic energy. Fortunately, the size of the Rydberg electron orbital, and consequently the relevant range for internuclear distance R, scales with $2(n^*)^2$. Hence in the large R limit where k is ill-defined, there is no scattering interaction between the Rydberg atom and the perturber. Moreover, the internal dynamics of the ULRM, and the typical localized stationary states are limited to much smaller R-values. While the $R \sim 2(n^*)^2$ region poses some conceptual challenges,

[†]The quantum defect δ_ℓ should not be confused with the scattering phase shift δ_L. While the notational ambiguity is unfortunate, the two concepts are very closely related, as they both denote the angular momentum dependent phase shifts in an electronic wavefunction due to low-energy scattering with a perturbing potential.

Alkali Atom	α_s	$a_S^1(0)$	$a_S^3(0)$
Li	164.1	3.7[a], 3.04[b]	-5.66[a], -7.12[b]
Na	162.7	4.2[a], 4.03[b]	-5.9[a], -6.19[b]
K	290.6	0.5[a], 0.47[c]	-15.0[a], -15.4[c]
Rb	319.2	2.03[c], 0.63[d]	-16.9[c], -16.1[d]
Cs	402.2	-4.0[a], -2.4[c]	-25.0[a], -22.7[c]

TABLE 3.1: Ground-state polarizability (α_s) of alkali atoms, as well as the corresponding electron-atom S-wave scattering lengths $a_S^1(k=0)$ and $a_S^3(k=0)$, for the spin-singlet and -triplet configurations, extrapolated to the zero energy limit. All values are expressed in atomic units (a.u.). The displayed data for α_s are taken from Ref. [55, 200, 201], but a more detailed compilation of polarizabilities can be found in Ref. [202]. The zero-energy extrapolation for the scattering length is not theoretically concrete, and hence one finds model-dependent values in the literature that differ from each other. The data for $a_S^1(k=0)$ and $a_S^3(k=0)$ marked a, b, c and d are taken from references [203], [204], [205] and [206], respectively. One can also find other values for $a_S^1(k=0)$ and $a_S^3(k=0)$ from the following references: [48, 78, 206–210]

we can numerically approximate k to be zero, before it becomes imaginary, and successfully simulate the scattering interaction. Typically, the electron momentum range relevant to the binding interaction for ULRM is between $k = 0-0.06$ a.u., corresponding to a kinetic energy of $0-0.05$ eV. The upper limit corresponds to the Ramsaeur-Townsend zero (0.04 eV for Rb^{87}) [8] in the electron-atom scattering potential, beyond which the S-wave scattering length turns positive, no longer facilitating a binding mechanism. In such low-energy ranges, one should only really expect the S-wave scattering interaction to contribute to V_{ea}, so that Eq. 3.3 is all that is needed to understand the binding mechanism. However, the P-wave scattering channel in e^- alkali-atom scattering features a shape-resonance (k = 0.02 to 0.04 a.u. for ^{87}Rb) that causes a rapid rise in the scattering volume, making it a dominant interaction in the binding of alkali ULRM, in the corresponding k-range. Some alkali-earth atoms like bosonic ^{84}Sr does not feature such a P-wave shape resonance, so that a pure S-wave description of the scattering potential is all that is required to understand the ULRM binding mechanism. For alkali atoms, one can then limit Omont's potential to the S- and P-wave terms so that Eq. 3.5 can be reduced to

$$V_{ea}(\mathbf{r} - R\hat{z}) = V_s(\mathbf{r} - R\hat{z}) + V_p(\mathbf{r} - R\hat{z}) \tag{3.7}$$

$$= 2\pi a_S(k)\delta(\mathbf{r} - R\hat{z}) + 6\pi a_P(k)\overleftarrow{\nabla} \cdot \delta(\mathbf{r} - R\hat{z})\overrightarrow{\nabla} \tag{3.8}$$

where the P-wave scattering volume $a_P(k)$ is defined as

$$a_P(k) = -\frac{\tan(\delta_P(k))}{k^3}\,. \tag{3.9}$$

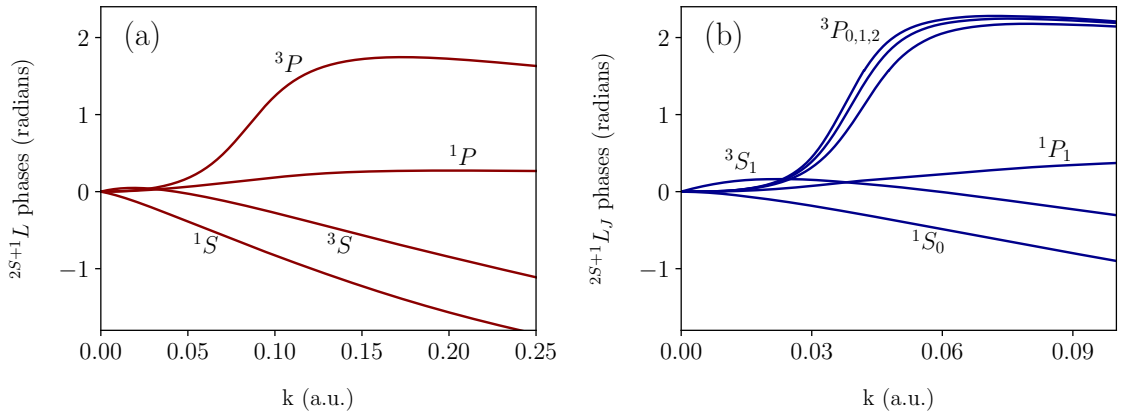


FIGURE 3.1: Electron-atom scattering phase shifts for (a) ^{23}Na [48] and (b) ^{87}Rb [211].

From the above discussion, it is clear that an accurate estimation of $\delta_L(k)$ (or the corresponding $a_L(k)$) in the relevant k-range is necessary to properly model the binding mechanism of the ULRM. Traditionally, one tries to calculate the electron-atom scattering phase shift by solving a two-electron (valence electron and scattering electron) model Hamiltonian via the R-matrix method [141, 143, 212]. A comprehensive discussion of this method is beyond the scope of this thesis, but the reader can find a brief analysis relevant to our work in Ref. [48, 78, 212]. The method considers the interaction between the atomic valence electron and the scattering electron, as well as their individual interaction with the complex ionic core through a dielectronic polarization potential [48, 78, 213]. For light alkali atoms like Li and Na, the good quantum numbers of the system are the scattering angular momentum L and the total spin S_e of the two-electron system. Since we assume that the spin-singlet and spin-triplet subspaces are decoupled, the scattering phase shifts and the scattering lengths discussed above are separately obtained for four different channels (denoted by $^{2S_e+1}L$): ^1S, ^3S, ^1P, and ^3P. Naturally, it follows that the scattering lengths and volumes also depend on these quantum numbers; therefore we can annotate them as $a_L^{2S_e+1}$. For heavier alkali atoms like Rb and Cs, one needs to consider the relativistic spin-orbit coupling $J = L + S_e$ [214, 215], so that we obtain phase shifts and scattering lengths in six different channels ($^{2S_e+1}L_J$): $^1S_0$, $^3S_1$, $^1P_1$, and $^3P_{0,1,2}$. For these elements, the exact energy range for the divergence in the $a_P^3(k)$ scattering volume varies with respect to J.

Figure 3.1 shows the calculated scattering phase shifts for ^{23}Na and ^{87}Rb taken from Ref. [48] and [211]. The absence and presence of spin-orbit splitting in the ^3P channel is dependent on the species displayed. We see that the scattering resonance is unique to the ^3P_J scattering channel, signified by the sudden change in the phase shift that crosses over $\pi/2$ radians (corresponding to a divergence in the scattering volume). The $^1P_1$ scattering

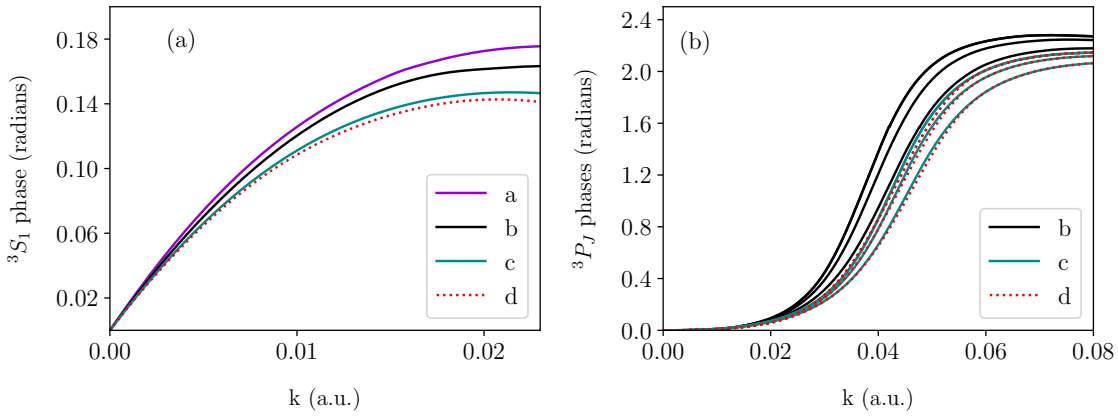


FIGURE 3.2: The $^3S_1$ (a) and $^3P_{0,1,2}$ (b) phase shifts for ^{87}Rb taken from different sources marked by, a: [211], b: [48], c: [216], and d:[P5].

phase shifts might seem to be without interesting structure, as a positive monotonic function of k. However, it allows for attractive scattering and facilitates the binding of a $^1P_1$ ULRM, an important class of molecules. The $^1S_0$ scattering phase on the other hand is largely negative, and only facilitates repulsive interaction at k-scales relevant for ULRM. However, the hyperfine coupling of the ground-state atom mixes the singlet and triplet scattering channels [51, 52], thereby creating shallow but attractive potentials that can hold bound molecular states. Most importantly, the positive $^3S_1$ scattering phase shift (and related $a_S^3(k)$) forms the primary attractive binding mechanism for the ULRM at low-k, until it becomes repulsive (past the Ramsauer-Townsend zero).

Alternatively, one can also find an approximation of $a_S(k)$ (both for spin-singlet and triplet configurations) using a modified effective range theory (MERT) [217, 218], that gives [78]

$$a_S(k) \approx a_S(0) + \frac{\pi\alpha_s}{3}k + \frac{4}{3}a_S(0)k^2\ln(1.23k\sqrt{\alpha_s}) \tag{3.10}$$

$$+ \left(\frac{R_e}{2} + \frac{\pi\sqrt{\alpha_s}}{3} - \frac{\pi\sqrt{\alpha_s}^3}{3(a_S(0))^2}\right)(a_S(0))^2k^2$$

$$- \frac{\pi\alpha_s}{3}k^3\left((a_S(0))^2 + \frac{7\alpha}{117}\right) \tag{3.11}$$

where α_s is ground-state polarizability (given in table 3.1 and Eq 3.2), $a_S(0)$ is the zero energy scattering length, and R_e is an effective range parameter. Within the scope of MERT, both $a_S(0)$ and R_e are adjustable variables that can be used to fit experimental data. Often, earlier works on ULRMs used a linear approximation of Eq. 3.11, that only considered the first two terms,

$$a_S(k) \approx a_S(0) + \frac{\pi}{3}\alpha_s k\,, \tag{3.12}$$

that reproduces the ULRM spectra qualitatively rather well, although it is quantitatively unreliable. But from here, it is clear that $a_S^3(0)$ determines the general scale of the ULRM binding strength. While one might hope to find $a_S^3(0)$ from the aforementioned R-matrix based numerical methods, those models do not converge well at $k = 0$. Hence one must extrapolate the function from non-zero values to obtain $a_S^3(0)$, either by numerical estimate or by empirical extraction. Table 3.1 shows such extrapolated values of both spin-triplet $a_S^3(0)$, and spin-singlet $a_S^1(0)$ taken from different sources [48, 78, 203–210]. Depending on the exact theoretical model or experimental setup used to perform this extrapolation, one can get slightly different values for $a_S(0)$. As expected, the singlet $a_S^1(0)$ is largely positive, whereas the triplet $a_S^3(0)$ is largely negative, indicating repulsive and attractive interactions at the low-k limit.

To conclude, the low-energy behavior of the ${}^3S$ scattering phase, as well as the near-resonant behavior of the ${}^3P$ scattering phase, practically determines the internal electronic structure of the ULRM to a good qualitative approximation. It naturally follows that a precision spectroscopic analysis of the ULRM will give us insights into the exact nature of $a_S^3(0)$ and the P-wave scattering resonance. Figure 3.2 compares the ${}^3S_1$ and ${}^3P_J$ scattering phases obtained via *ab initio* calculations [48, 211] to those extracted from ULRM experiments [P5, 216]. We see that the experimental reconstructions are more similar in structure to each other than to the calculations, providing a valid experimental benchmark. The differences between the plotted data signify inadequacies in the current electron-atom scattering Hamiltonian. While Engels et al. [216] primarily probed anion resonances in the ${}^3P_J$ channel, we were able to extract the ${}^3S_1$ scattering phases using deep trilobite wells, as explained later in this thesis. Together, our works provide the resonance position and low-energy scattering phases that are the key elements in understanding ULRM and electron-atom scattering.

3.2 Electronic states and potentials

Following the discourse on the Born-Oppenheimer approximation, we start our study of the ULRM structure by solving $\hat{H}_{el}$ (Eq. 3.1) parametrized by $R\hat{z} = (R, 0, 0)$ in spherical coordinate. The electronic Hamiltonian can be comfortably represented in the eigenbasis of the constituent Rydberg atomic Hamiltonian $\hat{H}_{Ryd}$, defined as $|n, \ell, m_\ell\rangle$. As discussed in section 2.1.2,

$$\phi_{n\ell m_\ell}(\mathbf{r}) = \langle \mathbf{r}|n, \ell, m_\ell\rangle = \frac{U_{n,\ell}(r)}{r} Y_{\ell m_\ell}(\theta, \phi)\,, \tag{3.13}$$

where $U_{n,\ell}$ is the Hydrogen atom wavefunction for high-ℓ, and the quantum defect wavefunction for low-ℓ.

3.2.1 Perturbative analysis

We first try to solve $\hat{H}_{el}$ by considering the S-wave scattering (Eq. 3.3) to be a perturbation to the Rydberg atom Hamiltonian. Since the contact interaction is only non-zero when $\mathbf{r} = (R, 0, 0)$, and all $m_\ell \neq 0$ states have a node along the internuclear axis ($\theta = 0, \phi = 0$), we can exclusively work in the Σ-subspace where only the states with $m_\ell = 0$ are considered.

For a low-ℓ quantum defect state $|n, \ell, m_\ell\rangle$, we use non-degenerate perturbation theory to obtain the adiabatic potential

$$\varepsilon_{n,\ell}(R) = \langle n, \ell, 0|\hat{V}_s|n, \ell, 0\rangle = 2\pi a_S^3(k(R))\,|\phi_{n\ell 0}(R\hat{z})|^2\,, \tag{3.14}$$

as a perturbation to the atomic energy level, whose oscillatory structure mimics the probability density of the Rydberg electron. This simplistic approach works extremely well in comparison to more elaborate numerical models [8, 219, 220], as long as we limit ourselves to S-wave low-ℓ systems. This is unsurprising, since the strength of the S-wave perturbation is much lesser than the level splitting of the non-degenerate Rydberg levels, so much so that the perturbed eigenstate retains its original $\phi_{n\ell m_\ell}$ form for the most part. Within non-degenerate perturbation theory, the electronic dipole moment of the molecule $\langle n, \ell, m_\ell|e\mathbf{r}|n, \ell, m_\ell\rangle \approx 0$.

On the other hand, the high-ℓ states forming the degenerate n-manifold are heavily mixed by the perturbing interaction. Using textbook degenerate perturbation theory, we obtain the matrix representation of the S-wave pseudopotential (Eq. 3.3)

$$\begin{aligned}\langle\phi_i|\hat{V}_s(R)|\phi_j\rangle &= \langle\phi_i(\mathbf{r})|\,2\pi a_S^3(k(R))\,\delta(\mathbf{r} - R\hat{z})\,|\phi_j(\mathbf{r})\rangle &(3.15)\\ &= 2\pi a_S^3(k(R))\,\phi_i(R\hat{z})\,\phi_j(R\hat{z})\,, &(3.16)\end{aligned}$$

in the high-ℓ atomic basis for a fixed n ($\phi_i, \phi_j \in \{\phi_{n\ell 0} \forall \ell \geq \ell_c\}$) where ℓ_c is the number of non-degenerate quantum defect splitted states. Diagonalizing this matrix will provide us with the adiabatic PECs and electronic eigenstates. But since this perturbation matrix is separable [148], its spectral decomposition contains only one non-zero term, which corresponds to the prominent *trilobite* state

$$\psi_t(\mathbf{r}, R) = \frac{1}{\sqrt{\sum_{\ell\geq\ell_c}^{n-1}|\phi_{n\ell 0}(R)|^2}}\sum_{\ell\geq\ell_c}^{n-1}\phi_{n\ell 0}(R)\,\phi_{n\ell 0}(\mathbf{r})\,, \tag{3.17}$$

and the associated trilobite potential

$$\varepsilon_t(R) = 2\pi a_S^3(k(R))\sum_{\ell\geq\ell_c}^{n-1}|\phi_{n\ell 0}(R)|^2\,. \tag{3.18}$$

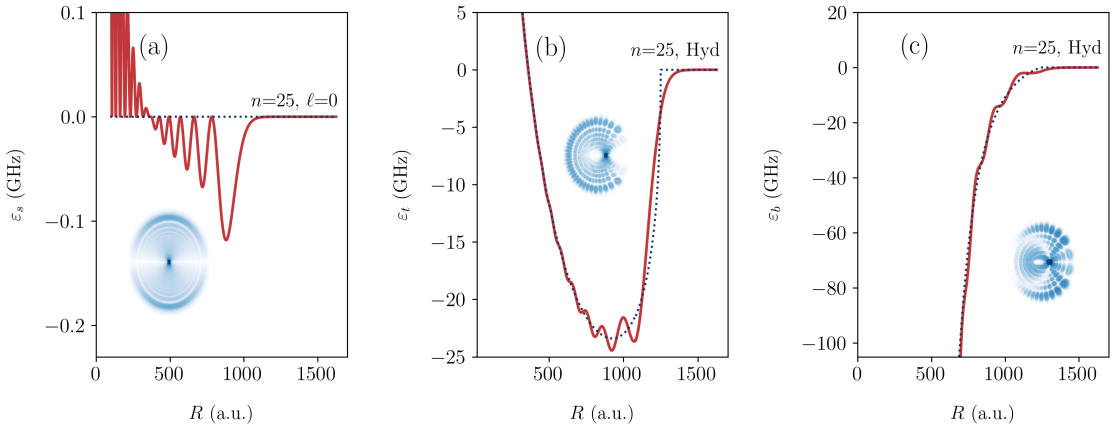


FIGURE 3.3: The potential energy curves of $n = 25$ ULRM, in (a) $\ell = 0$, (b) trilobite and (c) butterfly states. The solid red lines are obtained through first-order perturbation theory, whereas the dotted blue lines in (b) and (c) are obtained using the Borodin-Kazansky approach. The dotted line in (a) signifies the quantum defect splitting. The insets show cylindrical contourplots of the electrons probability density $\rho|\psi(\mathbf{r} = (\rho, z, 0), R = 500a_0)|^2$ [8].

Figure 3.3 (a) and (b) show the potentials corresponding to the ^{87}Rb ULRM in the $n = 25$ s-state and the trilobite state, respectively. The depth of the trilobite potential is several orders of magnitude larger than their low-ℓ counterparts, and is capable of holding 100s of bound molecular vibrational states. Their electronic probability density plot bears a fascinating resemblance to the trilobite fossil [44], explaining its nomenclature.

We can extend our analysis to understand how the P-wave scattering interaction

$$\hat{V}_P = 6\pi a_P^3(k) \overleftarrow{\nabla} \cdot \delta(\mathbf{r} - R\hat{z}) \overrightarrow{\nabla} \tag{3.19}$$

affects the degenerate manifold. This resultant interaction potential is dependent on the gradient of the electron wavefunction in three spatial dimensions: one radial, and two angular. Hence the matrix representation of the scattering Hamiltonian in the Rydberg atomic basis splits into two different subspaces, one with ($m_\ell = 0$) Σ symmetry and the other with ($m_\ell = \pm 1$) Π symmetry [43]. This is because only basis states with $m_\ell = 0$ are perturbed by the radial gradient term, as states with $m_\ell = \pm 1$ have a nodal plane along the internuclear axis. On the other hand, only states with $m_\ell = \pm 1$ are perturbed by the azimuthal and polar gradients, as basis states with $m_\ell = 0$ have a nodal plane perpendicular to the internuclear axis. Performing degenerate perturbation theory on the Σ-subspace like before, we obtain the *butterfly* state

$$\psi_b(\mathbf{r}, R) = \frac{1}{\sqrt{\sum_{\ell \geq \ell_c}^{n-1} |\partial_R \phi_{n\ell 0}|^2}} \sum_{\ell \geq \ell_c}^{n-1} (\partial_R \phi_{n\ell 0})\, \phi_{n\ell 0}(\mathbf{r})\,, \tag{3.20}$$

and the butterfly potential

$$\varepsilon_b(R) = 6\pi a_P^3(k(R)) \sum_{\ell \geq \ell_c}^{n-1} |\partial_R \phi_{n\ell 0}|^2 \,. \tag{3.21}$$

both of which depend on the value of the radial derivative of $\phi_{n\ell 0}$ at $r = R$, given by the notation $\partial_R \phi = \frac{\partial}{\partial r}\phi(r)|_{r=R}$. The states with Π symmetry are decoupled from our system, and generally do not allow bound vibrational states. Moreover, there are no equivalent trilobite or low-ℓ PECs that allow S-wave bound ULRM states in the Π symmetry sector. Hence, for now we focus purely on electronic states and potentials in the Σ subspace, but the reader can see Ref. [148] for a detailed analysis of Π-symmetry states.
Figure 3.3 (c) shows the butterfly PEC $\varepsilon_b(R)$.

Surprisingly, one can obtain the general R-dependence of both the trilobite and butterfly PECs (without the undulations) by using the Borodin-Kazansky model [221]

$$\varepsilon_{bk,L}(R) = \frac{1}{2(n - \delta_L(k(R))/\pi)^2} \,, \tag{3.22}$$

that considers the S-wave and P-wave scattering phase shifts as quantum defects to the Hydrogenic energy level. Focusing only on the S-wave scattering, it is also possible to obtain the anharmonic envelope of the trilobite PEC using a WKB approximation [8, 124] given by

$$\varepsilon_{anh}(R) = \frac{a_s^3(k)}{\pi n^3} \sqrt{\frac{2}{R} - \frac{1}{n^2} - \frac{(\ell_c + 1/2)^2}{R^2}} \,. \tag{3.23}$$

More intricate semi-classical models have also been created, that can further explain the oscillatory structure of these trilobite potentials [222, 223].

Our current mathematical model comes with two clear drawbacks. First, the low-ℓ, trilobite and butterfly states all lie in the same Σ symmetry sector, and hence strongly couple to each other. The von Neumann-Wigner no-crossing theorem [181] necessitates that these potentials should experience level repulsion when they come energetically close to each other. Second, the P-wave scattering volume diverges at the shape-resonance energy, resulting in an unbounded, unphysical potential if not for the level repulsion from neighboring n-manifolds. Hence one cannot accurately represent the P-wave interaction utilizing just one single n-manifold. To resolve these discrepancies, we consider both the S-wave and P-wave interactions together, and try to represent them in a basis set that contains both high-ℓ and low-ℓ states from multiple n-manifolds.

3.2.2 Exact diagonalization

We can obtain the Born-Oppenheimer potentials and the adiabatic electronic states by diagonalizing the matrix representation of $\hat{H}_{el}(R, \mathbf{r})$, in the Rydberg atom basis. Focusing first

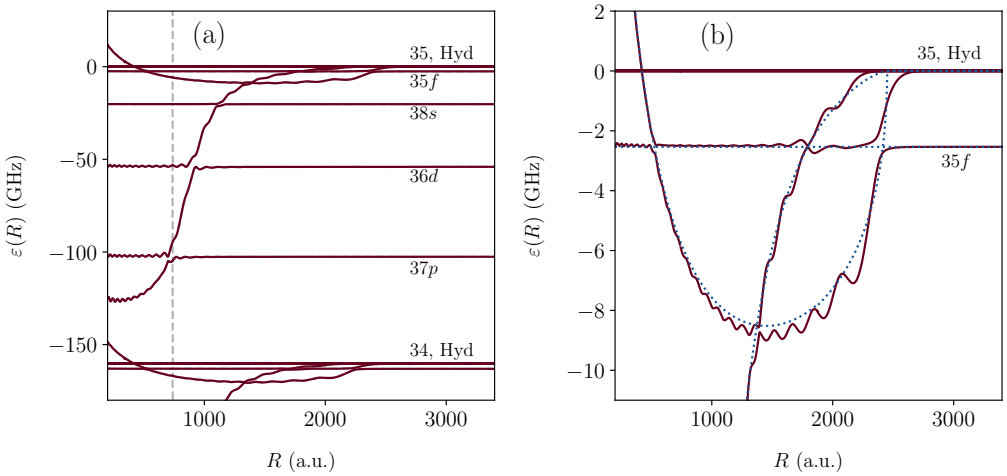


FIGURE 3.4: (a) Adiabatic PECs of the $n = 35$ ^{87}Rb ULRM. The curves are obtained by diagonalizing the Hamiltonian in the $n \in [33, 37]$ finite basis, and the atomic resonances are labeled. The dashed vertical line shows the R-value where the ED method breaks down due to the P-wave resonance. (b) A magnified version that focuses on the trilobite and butterfly potentials, with the blue dotted lines signifying the BK-approach.

on the Σ symmetry sector, the matrix representation can be written as

$$\begin{aligned}[H_{el}]_{ij} &= \langle n_i \ell_i 0 | H_{el} | n_j \ell_j 0 \rangle \\ &= -\frac{1}{2(n_i - \delta_{\ell_i})^2} \cdot \delta_{ij} \; + \; 2\pi a_S^3(k(R)) \phi^*_{n_i \ell_i 0}(R)\, \phi_{n_j \ell_j 0}(R) \\ &\qquad + 6\pi a_P^3(k(R))\, \partial_R \phi^*_{n_i \ell_i 0} \cdot \partial_R \phi_{n_j \ell_j 0}\,. \end{aligned} \tag{3.24}$$

To obtain the ULRM electronic spectrum for a given $n = n_0$, we can use the finite basis set $\{|n_i \ell_i\rangle\}$ that includes all atomic states with energy values between the $n_0 - 2$ and $n_0 + 2$, which we denote as $n_i \in [n_0 - 2, n_0 + 2]$. In doing so one must be careful to consider quantum defect states from higher n-manifolds, that are energetically closer to the n_i-values we consider.

The set of adiabatic potentials that are obtained after diagonalizing $[H_{el}]_{ij}$ in a finite basis are displayed in figure 3.4, for ^{87}Rb. The potential energy landscape shows the trilobite potential, the butterfly potential, quantum defect PECs from different n-manifolds, as well as the avoided crossings between them. As previously explained, the quantum defect structure of ^{87}Rb makes it so that $38s$, $36d$ and $37p$ are the electronic states placed between the $n = 35$ and $n = 34$ manifolds. The dashed vertical line is a computational artifact of the ED method, caused by the diverging P-wave scattering term at the exact resonance value. We also see that the $n = 35$ butterfly curve faces level repulsion against the $n = 34$ hydrogenic manifold, stopping its otherwise uncontrolled decline. Figure 3.4 (b) shows a magnified plot that focuses on the trilobite potential, overlayed with dotted blue lines representing the Borodin-Kazansky

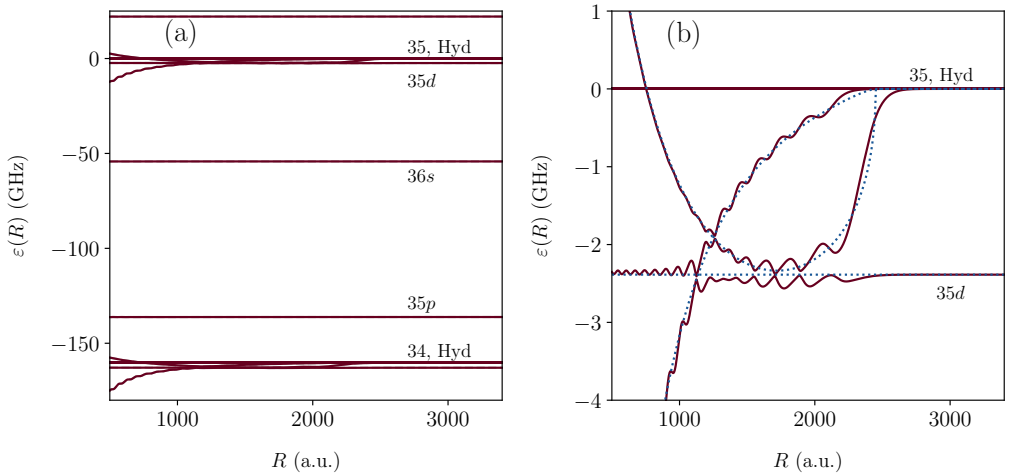


FIGURE 3.5: (a) Adiabatic PECs of the $n = 35$ ^{23}Na ULRM. The curves are obtained by diagonalizing the Hamiltonian in the $n \in [33, 37]$ finite basis, and the atomic resonances are labeled. The P-wave resonance value (where ED breaks down) is outside the R-range plotted, and is not so relevant for ^{23}Na. (b) A magnified version that focuses on the trilobite and butterfly potentials, with the blue dotted lines signifying the BK-approach.

calculation (Eq. 3.22) for the high-ℓ states, as well as the quantum defect splitting for the $35f$-state. The Borodin-Kazansky model very successfully predicts the general potential depth of the adiabatic PECs, and is also able to predict the position of avoided crossings. We see that avoided crossings between trilobite and butterfly PECs happen when $\delta_S(R) \approx \delta_P(R)$, and avoided crossings between high-ℓ and low-ℓ PECs happen when $\delta_{S/P}(k(n, R)) \approx \pi\delta_\ell$. For ^{87}Rb, the trilobite curve primarily crosses with the f-state.

Similarly, figure 3.5 shows the potential energy landscape of the $n = 35$ ^{23}ULRM, primarily highlighting the different quantum defect structure and the different scattering lenths/volumes. Between the $n = 35$ and $n = 24$ manifolds lie the $36s$, $35p$ and $35d$ states with which the butterfly curves admix. The trilobite curve mainly interacts with the $35d$ state, forming an avoided crossing at two different spots. We also see that the trilobite wells are shallower and the P-wave resonance happens at much shorter R-values (implying much larger k-values), as one would expect from figure 3.1. The exact resonance value where a_P diverges, happens at a smaller R-value than what is shown in the figure 3.5, unlike their heavier alkali counterparts. The BK model works extremely well here, predicting the positions of avoided crossings between trilobite, butterfly, and d-state.

The figure 3.6 also shows that the exact energetic positions of the potentials vary with respect to the number n-manifolds used. The BK-curves give us a basis indepedent estimate of the general potential depth, capturing the behavior of a_S and a_P. While the deviations from the BK method generally reduce as we include more and more n-manifolds, complete

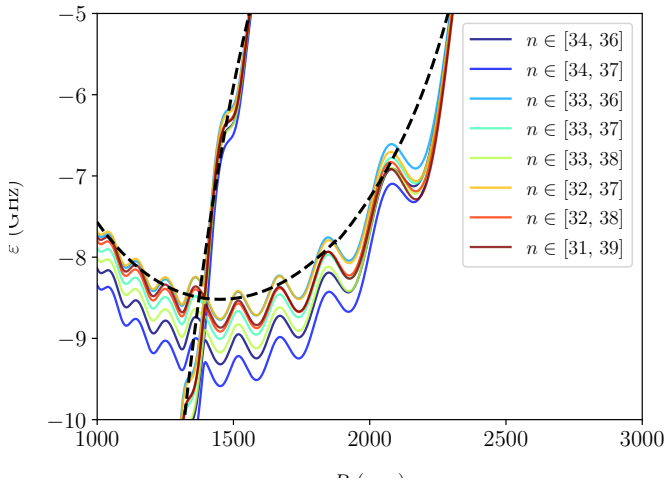


FIGURE 3.6: (a) Adiabatic PECs of the $n = 35$ ^{87}Rb ULRM, obtained by diagonalizing the Hamiltonian in varying $n \in [n_{min}, n_{max}]$ finite basis. The dashed lines correspond to Borodin Kazansky approximation.

convergence is out of sight. Even though one could hope to achieve convergence by indefinitely increasing the number of n-manifolds, the size of the Hamiltonian matrix increases rapidly beyond what is computationally practical (further worsened by considering various spin interactions). This non-convergent behavior during finite basis diagonalization, is well understood as a result of the bare dirac delta form of the pseudopotential, and the unphysical P-wave scattering volume near the resonance [108]. One can resolve this problem and obtain convergent results beyond first-order perturbation theory, by either utilizing regularized delta potentials [108], or by using a Green's function approach [211, 224] to obtain the electronic spectra. While these methods provide a necessary benchmark for high precision spectroscopic studies (like our works [P5, P6]), qualitative analysis of ULRM can be performed very well with exact diagonalization [P1–P3]. Moreover, diagonalization also directly provides the electronic wavefunctions (not just PECs) from which we can calculate dipole moments, transition strengths and non-adiabatic couplings, none of these being trivial from a Coulomb Green's function approach. However, there are plenty of scenarios where the neglectance of fine and hyperfine structure qualitatively alters the ULRM spectra [53, 56, 225]. So the next section discusses the internal fine and hyperfine structure of the ULRM with practical detailing.

3.3 Spin interaction effects

In this section, we lay out the theoretical framework for diatomic ULRMs, that goes beyond a minimalist description and introduce the various angular momentum coupling schemes involved. A comprehensive discussion of the spin-coupled Hamiltonian can be found in the original work of Eiles et al. [55], but we will proceed to briefly discuss the system for the sake of completeness. Figure 3.7 illustrates the relevant quantum numbers that together describe

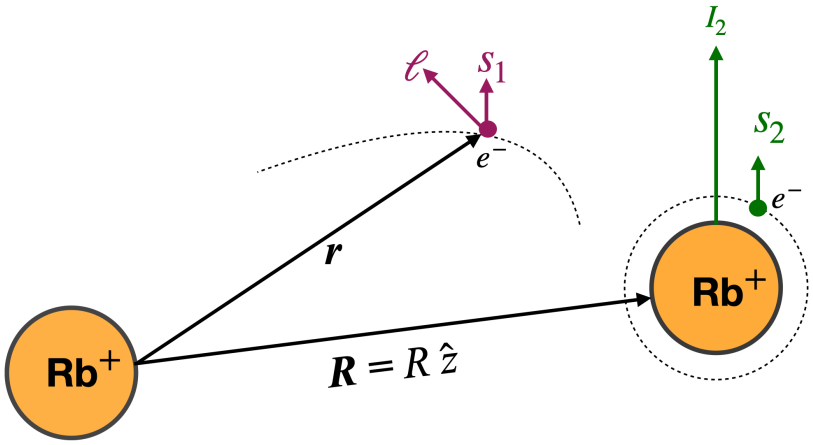


FIGURE 3.7: Sketch of the internal spin structure of a diatomic ^{87}Rb ULRM.

the state of the molecule. The associated electronic Hamiltonian is given by

$$\hat{H}_{el}(\mathbf{r}, R\hat{z}) = \hat{H}^{f}_{Ryd} + \hat{H}_{hf} + \hat{V}_{ea}(\mathbf{r}, R\hat{z}) - \frac{\alpha_s}{2R^4}\,. \tag{3.25}$$

The first term here, is the Rydberg atom Hamiltonian that includes the spin-orbit coupling between Rydberg electron spin s_1 and orbital angular momentum ℓ. As discussed in section 2.1.3, the modified eigenstates of the atomic Hamiltonian are enumerated using the good quantum numbers $|n, \ell, j, m_j\rangle$, where j is the total angular momentum quantum number (corresponding to the operator $\mathbf{j} = \boldsymbol{\ell} + \mathbf{s}_1$), and m_j is its projection along $\hat{z}$. The alteration to atomic energy levels due to fine structure, given by ΔE_{nj} (Eq. 2.18), becomes quite prominent for low-ℓ states, often being comparable to energy scales of the scattering interaction. While the splitting dramatically drops with respect to n^{-3} and j^{-1}, its inclusion becomes necessary to understand various spin mixing effects.

The second term in the Hamiltonian describes the hyperfine coupling between the nuclear spin I_2 and valence electron spin s_2 of the perturbing ground-state atom. The Hamiltonian

$$\hat{H}_{hf} = A\mathbf{I}_2 \cdot \mathbf{s}_2 \tag{3.26}$$

is diagonal in the $|I_2, s_2, F, m_F\rangle$ basis, where F is the hyperfine quantum number corresponding to the operator $\mathbf{F} = \mathbf{I}_2 + \mathbf{s}_2$, and m_F is its projection along the shared z-axis. The associated eigenvalues that determine the hyperfine energy shift are given by [145]

$$E_F = \frac{A}{2}\left[F(F+1) - I_2(I_2+1) - s_2(s_2+1)\right]\,, \tag{3.27}$$

where A is the hyperfine constant. Table 3.2 shows the hyperfine constants, and I_2 for ground-state alkali atoms, confirming that the hyperfine interaction strength is comparable to the scattering interaction strength ($\sim$ GHz). For example, ^{87}Rb has an I_2 = 3/2 and s_2

=1/2, allowing the values $F = 1, 2$. The hyperfine splitting between these two levels is ΔE_F = 6.834 GHz, which is comparable to the depth of the trilobite potential for a large range of n-values. On the other hand, since A scales as n^{-3} we can very easily disregard the hyperfine splitting of the Rydberg atom, as ΔE_F is often of the order of KHz to MHz, depending on ℓ. The hyperfine interaction relies on the electron penetrating the Rydberg core and being close to the nucleus [145], naturally making the interaction a lot weaker for $\ell > 0$. Hence the high-ℓ spectrum of ULRM is unaffected by Rydberg hyperfine structure, while being heavily dependent on the perturber hyperfine structure.

TABLE 3.2: Ground-state properties of alkali atoms relevant for hyperfine structure, with all alkali atoms having s_2=1/2. The data is limited to the most stable isotope of each element from [226, 227].

	^{7}**Li**	^{23}**Na**	^{39}**K**	^{87}**Rb**	^{133}**Cs**
Ground-state configuration	$2s_{1/2}$	$3s_{1/2}$	$4s_{1/2}$	$5s_{1/2}$	$6s_{1/2}$
A (GHz)	0.402	0.886	2.309	3.417	2.298
I_2	3/2	3/2	3/2	3/2	7/2

The spin-dependent pseudopotential $\hat{V}_{ea}$ describes the scattering interaction of the Rydberg electron and perturber, which is described in detail in section 3.1. To revise, the pseudopotential models the contact scattering as a delta function that depends on the distance between the electron and perturber $x = |\mathbf{r} - R\hat{z}|$. This $\delta(x)$ is scaled with respect to the scattering lengths (or volumes) that are specific to the spin and angular momentum configuration of the scattering system, based on the the angular momentum of the Rydberg electron with respect to the perturber $\mathbf{L}$, and the total spin $\mathbf{S}_e = \mathbf{s}_1 + \mathbf{s}_2$. Additionally, heavier alkali atoms display relativistic spin-orbit coupling, so that $\mathbf{J} = \mathbf{L} + \mathbf{S}_e$, and its z-axis projection M_J, are the new good quantum numbers (considering only $\hat{V}_{ea}$). The scattering potential is diagonal in the $|\beta\rangle = |L, S_e, J, M_J\rangle$ basis, and can be expressed as a function of x [55]

$$\hat{V}_{ea}(x) = \sum_{\beta} \frac{(2L+1)^2}{2x^{2(L+1)}}\, \delta(x)\, a_{S_e L J}(k)\, |\beta\rangle\langle\beta|\,, \tag{3.28}$$

being spherically symmetric with respect to the scattering center, i.e. the perturber. Since we limit L to be 0 or 1 (S-wave or P-wave), and alkali diatoms naturally have S_e = 0 or 1 (spin-singlet or spin-triplet), there are six different scattering channels ($^{2S_e+1}L_J$): $^1S_0$, $^3S_1$, $^1P_1$, and $^3P_{0,1,2}$, with M_J taking the values $-J$ to J in each channel. The sum over β considers all of these combinations, with the scattering length for each channel $a_{S_e L J}(k)$ taken from Ref. [48], as explained in section 3.1. Finally, the last term in the total electronic Hamiltonian $\hat{H}_{el}$, is simply a scalar potential that describes the core polarization, and is diagonal with respect to any angular momentum basis.

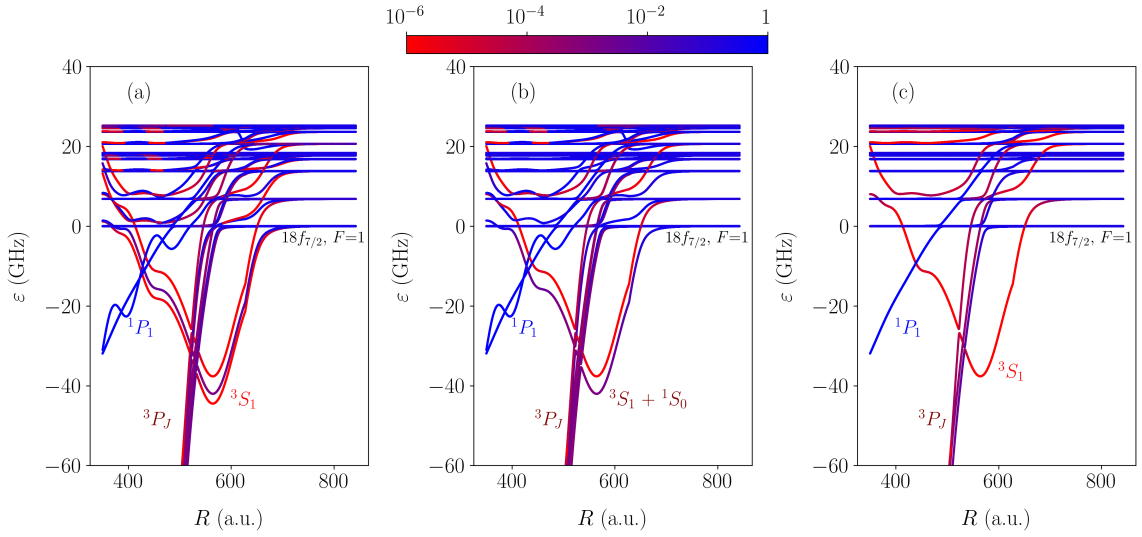


FIGURE 3.8: The adiabatic PECs of the ^{87}Rb $n = 18$ ULRM, calculated for Ω= (a) 1/2, (b) 3/2 and (c) 5/2. The colorbar represents the R-dependent spin-singlet admixture $|\langle\psi_{el}|S_e = 0\rangle|^2$ in the molecular electronic states. The experimentally relevant atomic resonance $18f_{7/2}, F = 1$ is the energy zero. The dominant scattering character $^{2S_e+1}L_J$ of each high-ℓ state is also highlighted.

Since different terms in the total electronic Hamiltonian are diagonal in different basis sets, finding a common basis to represent $\hat{H}_{el}$ is not trivial. The Rydberg atom Hamiltonian conserves n, ℓ, j and $m_j = m_\ell + m_{s_1}$, and the perturber hyperfine term conserves F and $m_F = m_{I_2} + m_{s_2}$. If one is to ignore the scattering interaction $\hat{V}_{ea}$, the non-interacting diatomic Hamiltonian is diagonal in the basis $|n, \ell, j, m_j\rangle \otimes |F, m_F\rangle$. Beyond the dissociation limit ($R > 2n^2$) the flat diatomic potentials can be uniquely identified based on the quantum numbers $|n, \ell, j, F\rangle$. However, the scattering interaction mixes the relevant fine and hyperfine structure, depending on the total spin. It is then pragmatic to use the basis set $|\alpha\rangle = |n, \ell, j, m_j\rangle \otimes |s_2, m_{s_2}, I_2, m_{I_2}\rangle$ to represent the total Hamiltonian, since it automatically diagonalize $\hat{H}_{Ryd}$, while also providing a straightforward implementation of $\hat{H}_{hf}$

$$\begin{aligned}\langle\alpha|\hat{H}_{hf}|\alpha'\rangle &= \langle n, \ell, j, m_j|n', \ell', j', m'_j\rangle \sum_{F,m_F} E_F \langle s_2, m_{s_2}, I_2, m_{I_2}|F, m_F\rangle\langle F, m_F|s'_2, m'_{s_2}, I'_2, m'_{I_2}\rangle \\ &= \delta_{n\ell j m_j, n'\ell' j' m'_j} \sum_{F,m_F} E_F \, C^{F,m_F}_{s_2,m_{s_2},I_2,m_{I_2}} \, C^{F,m_F}_{s'_2,m'_{s_2},I'_2,m'_{I_2}} \,, \end{aligned} \tag{3.29}$$

where E_F is the eigenvalue corresponding to $|F, m_F\rangle$ given by Eq. 3.27, and $C^{F,m_F}_{s_2,m_{s_2},I_2,m_{I_2}}$ are the appropriate Clebsh-Gordon coefficients [153, 154]. The first dirac delta term signifies that $\hat{H}_{hf}$ is diagonal in the Rydberg atom basis.

Representing $\hat{V}_{ea}$ in the selected basis is a more tedious task, as the wavefunction of the Rydberg electron is defined with respect to the ionic core ($\mathbf{r}$) in $|\alpha\rangle$, whereas the electron

wavefunction is defined with respect to the scattering center ($\mathbf{x} = \mathbf{r} - R\hat{z}$) in $|\beta\rangle$. One can translate the scattering interaction from the scattering coordinates to the Rydberg coordinates, using a frame transform $\hat{U}$ whose elements are given by

$$U_{\beta\alpha} = \langle\beta|\alpha\rangle\,, \tag{3.30}$$

so that the matrix representation of $\hat{V}_{ea}$ in $|\alpha\rangle$ basis is simply $\hat{U}^\dagger\hat{V}_{ea}\hat{U}$. Such a frame transformation expands the Ryberg wavefunctions as ($L < 2$) spherical harmonics relative to the position of the perturber, while considering all the spin- angular momentum couplings. The exact derivation of $U_{\beta\alpha}$ is presented in Ref. [55], but here we simply choose to present the final formula

$$U_{\beta\alpha} = \sum_{M_L=-L}^{L} \sqrt{\frac{4\pi}{2L+1}}\, \mathcal{Q}_{n\ell j}^{LM_L} \cdot C^{J,m_j+m_{s_2}}_{L,M_L,S_e,m_j-M_L+m_{s_2}} \tag{3.31}$$

$$\cdot\, C^{j,m_j}_{\ell,M_L,s_1,m_j-M_L} \cdot C^{S_e,m_j-M_L+m_{s_2}}_{s_1,m_j-M_L,s_2,m_{s_2}}\,, \tag{3.32}$$

where $\mathcal{Q}_{n\ell j}^{LM_L}$ takes the form

$$\mathcal{Q}^{00}_{n\ell j} = \sqrt{\frac{2\ell+1}{4\pi}}\,\frac{U_{n\ell j}(R)}{R} \tag{3.33}$$

$$\mathcal{Q}^{10}_{n\ell j} = \sqrt{\frac{2\ell+1}{4\pi}}\,\partial_R\left(\frac{U_{n\ell j}(R)}{R}\right) \tag{3.34}$$

$$\mathcal{Q}^{1\pm1}_{n\ell j} = \sqrt{\frac{(2\ell+1)(\ell+1)\ell}{8\pi}}\,\frac{U_{n\ell j}(R)}{R^2}\,, \tag{3.35}$$

where $U_{n\ell j}$ is the spin-orbit coupled reduced radial wavefunction, so that $\phi_{n\ell j m_j}(R\hat{z}) = \frac{U_{n\ell j}(R)}{R}\,Y_{\ell m_\ell}(0,0)$.

We now know how to represent all the terms of $\hat{H}_{el}$ (Eq. 3.25) in the $|\alpha\rangle = |n,\ell,j,m_j\rangle \otimes |s_2,m_{s_2},I_2,m_{I_2}\rangle$ diatomic basis, considering a finite number of n-manifolds centered around the desired n-value one wants to investigate. As usual, we can diagonalize this Hamiltonian matrix at every R-value to obtain the adiabatic PECs $\varepsilon(R)$ and electronic states $|\psi_{el}(\mathbf{r},R)\rangle$ of the ULRM. Additionally, just like m_ℓ was a good quantum number for the spinless model previously discussed (sec. 3.1), the projection of the total angular momentum $\Omega = m_j + m_{I_2} + m_{s_2}$ is a good quantum number. This splits our Hamiltonian into multiple different symmetry blocks (block diagonal form) where Ω is conserved, greatly reducing the computational effort. As discussed before, the inclusion of only $L < 2$ terms imply that only $|m_\ell| < 2$ or consequently $m_j \leq 3/2$ terms contribute. For ^{87}Rb and lighter alkali metals, $|m_F| = |m_{I_2} + m_{s_2}| \leq 2$, forcing $|\Omega| \leq 7/2$ in steps of 1/2. We separately diagonalize each Ω block to analyze the electronic states and adiabatic PECs allowed by the enforced selection rule.

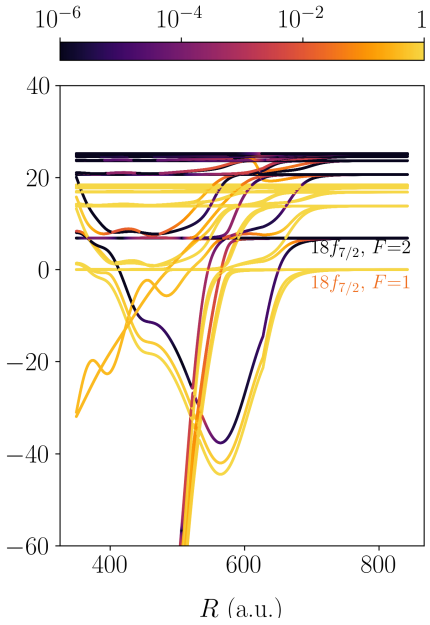


FIGURE 3.9: The adiabatic PECs of the ^{87}Rb $n = 18, \Omega$= 1/2 ULRM colored according to the $F = 1$ hyperfine admixture $|\langle\psi_{el}|F = 1\rangle|^2$ in the corresponding electronic states.

Figure 3.8 shows the calculated Born-Oppenheimer potentials of the ^{87}Rb $n = 18$ ULRM for different values of Ω. To analyze the internal spin structure of these electronic states, we can calculate the expectation values of different angular momentum operators with respect to ψ_{el}. For example, we can calculate the spin-singlet admixture $|\langle\psi_{el}|S_e = 0\rangle|^2$, to see how the triplet and singlet scattering channels are mixed in each ψ_{el}. As shown in figure 3.8, the $\Omega = 1/2$ plots show three different trilobite plots, two originating from the $18f, F = 1$ manifold, and one originating from the $18f, F = 2$ manifold. Two of them show exclusive spin-triplet character, while one of them (shallower PEC from $18f, F = 1$ manifold) has triplet-singlet mixed character. For higher $\Omega = 3/2$, the allowed spin configurations do not permit the pure spin-triplet character, while $\Omega = 5/2$ does not permit any trilobite curve from the $F = 1$ manifold. There is a spaghetti of ^3P_J curves that are predominantly spin-triplet, creating avoided crossings with the trilobite curves. They contain both $M_L = 0$ and $M_L = \pm$ depending on the Ω value. These states correspond to the $(M_L = 0)$ oscillating stairwell potential and the $(M_L = \pm)$ non-oscillating PEC that crosses through it. Since M_L is not a good quantum number, these different butterfly states can form avoided crossings with each other.

Similarly, figure 3.9 shows the PECs of the $\Omega = 1/2$ Rubidium dimer with a color-bar signifying the hyperfine admixture $|\langle\psi_{el}|F = 1\rangle|^2$ in the electronic state. Typical ULRM experiments start with an ultracold cloud in the full hyperfine ground state (eg $5s_{1/2}, F = 1$), and proceeds to photoexcite a Rydberg atom. The photoexcitation does not cause radiative

transitions ($F = 1 \rightarrow F = 2$) in the ground-state atom. However, the electron-atom scattering can mix different F-states. Re-analyzing the three trilobite curves using their F-state character (Figure 3.9), we find that the two pure-triplet trilobite states show either exclusive $F = 1$ or $F = 2$ admixture. The spin-mixed trilobite on the other hand, also show a mixing of the two hyperfine levels. So a standard three-photoexcitation from the $5s_{1/2}, F = 1$ state can directly access the $nf_{7/2}, F = 1$ Rydberg state, only populating the $F = 1$ pure-triplet trilobite and the spin-mixed F-mixed trilobite ($F = 1$ pure-triplet trilobite). In low-ℓ states, electron-atom scattering was used to create remote spin-flips of the hyperfine levels, as well as mediate entanglement between the fine and hyperfine structure of the diatomic system [225]. However, in these high-ℓ molecules the fine structure of Rydberg atoms is rather negligible, compared to the other effects discussed here.

3.4 Green's function approach

3.4.1 Basic formulation

We can solve the electronic Schrödinger equation to obtain the Born-Oppenheimer spectra by utilizing a Green's function based Kirchhoff intergral approach [211, 224], and completely circumvent the finite-basis convergence problem. In line with the adiabatic approximation, the molecular electronic state is obtained separately for each R-value, where the electron's position with respect to the scatterer is given by $\vec{x} = \vec{r} - R\hat{z}$. We start by dividing the electronic coordinate space into two different regions, separated by a very small sphere S centered around the perturber. The sphere encapsulates the electron-atom scattering potential, and its fixed radius $s = |\vec{x}|$ is chosen to be small enough so that the Coulomb potential is essentially constant inside it. In addition, s is large enough that the electron-atom interaction is zero at the sphere surface. Hence, the electron momentum $k = \sqrt{2(E + 1/R)}$ is taken to be a constant across S, so that its wavefunction is a plane-wave of momentum k that undergoes spherically symmetric scattering from the perturber. This allows us to write the wavefunction solution near the surface as

$$\psi_S(k, \vec{x}) = \sum_{L,M_L} B_{LM_L}\, \mathcal{U}_L(k, x)\, Y_{LM_L}(\hat{x})\,, \tag{3.36}$$

$$\mathcal{U}_L(k, x) = \mathcal{J}_L(kx)\cos(\delta_L(k)) \;-\; \mathcal{Y}_L(kx)\sin(\delta_L(k)) \tag{3.37}$$

where $\mathcal{J}$ and $\mathcal{Y}$ are the spherical Bessel functions of the first and second kind [150, 151], L is the scattering partial wave, δ_L is the scattering phase shift, and B_{LM_L} is the expansion constant; we can limit the sum over L, L' to a few terms as $R \gg x, x'$ for ULRMs. The phase shifts used here encodes the electron-atom scattering information, and can be obtained from separate calculations discussed before (Sec. 3.1).

Outside the sphere, the electron only experiences the Rydberg core potential, whose influence can be described by the Green's function

$$G(\vec{r},\vec{r}\,';\nu) = G_{\rm c}(\vec{r},\vec{r}\,';\nu) \,+\, G_{\rm qd}(\vec{r},\vec{r}\,';\nu)\,, \tag{3.38}$$

where $G_{\rm c}$ is the Coulomb Green's function [228] given by

$$G_{\rm c}(\vec{r},\vec{r}\,';\nu) = \frac{\Gamma(1-\nu)}{2\pi|\vec{r}-\vec{r}\,'|}\left[W_{\nu,1/2}(\xi)\partial_\eta M_{\nu,1/2}(\eta) \,-\, M_{\nu,1/2}(\eta)\partial_\xi W_{\nu,1/2}(\xi)\right]\,, \tag{3.39}$$

with $\nu = (-2E)^{-1/2}$ $(E<0)$ denoting the energy-dependent effective principal quantum number, and W, M, and Γ representing the Whittaker-W function, Whittaker-M function [150, 151], and Gamma function [152], respectively. The coordinates $\xi,\eta = (r+r'\pm|r-r'|)/\nu$ follow the convention given in Ref. [107]. The quantum defect correction [107, 229] can be written as

$$\begin{aligned} G_{\rm qd}(\vec{r},\vec{r}\,';\nu) = \frac{\nu}{r\,r'}\sum_{\ell=0}^{\ell_c}\sum_{m_\ell=-\ell}^{\ell} &\frac{W_{\nu,\ell+\frac{1}{2}}\left(\frac{2r}{\nu}\right)W_{\nu,\ell+\frac{1}{2}}\left(\frac{2r'}{\nu}\right)\,Y_{\ell m_\ell}(\hat{r})\,Y^*_{\ell m_\ell}(\hat{r}')}{\Gamma(\nu+\ell+1)\,\Gamma(\nu-\ell)} \\ &\times\frac{\pi\sin(\pi\delta_\ell)}{\sin(\pi\nu)\,\sin\!\left(\pi\nu+\pi\delta_\ell\right)}\,, \end{aligned} \tag{3.40}$$

where δ_ℓ are the ℓ dependent quantum defects, and ℓ_c is the number of non-degenerate quantum defects.

Once the Green's function has been constructed, we can use Kirchhoff integral [230] to obtain the solution to the electronic Hamiltonian (the scattered wavefunction) at any point outside S, as

$$\psi_o(\vec{r},\nu) = -\frac{1}{2}\oint_S\left[G(\vec{r},\vec{r}\,';\nu)\partial_{x'}\psi_o(\vec{r}\,') \,-\, \psi_o(\vec{r}\,')\partial_{x'}G(\vec{r},\vec{r}\,';\nu)\right]s^2\,d\hat{s}\,', \tag{3.41}$$

where $\oint_S s^2\,d\hat{s}\,'$ integrates $\vec{r}\,' = R\hat{z}+\vec{x}\,'$ over the surface of S, and $\partial_{x'}$ is the outward derivative normal to S. This formulation, derived from Green's second indentity, allows us to uniquely evaluate ψ_o outside the surface S if the value of the wavefunction and its derivative at the surface are known. While this is an implicit integral equation, we know that ψ_o has to match the previously defined ψ_S at the surface S; as both the wavefunction value and its normal derivative must be continuous. So we can propagate $\psi_o(\vec{r})$ outwards using the Green's function, from the known values of the wavefunction and its derivative at the surface, for a fixed E and R. To do so we must first be able to express the Green's function and its derivative in perturber-centric coordinates $(\vec{r},\vec{r}\,'\to\vec{x},\vec{x}\,')$. We can expand the Green's function with respect to the perturber position using spherical harmonics to attain

$$G(R\hat{z}+\vec{x},\,R\hat{z}+\vec{x}\,';\,\nu) = \sum_\beta Y_{L'M'_L}(\hat{x})\mathcal{G}_\beta(x,x';\nu)Y^*_{L''M'_L}(\hat{x}\,')\,, \tag{3.42}$$

where β denotes the set of indices (L', L'', M'_L); we use primes to avoid confusion later on. Note that the expansion is diagonal with respect to the good quantum number M'_L. Since $\mathcal{G}_\beta(x, x'; \nu)$ is only dependent on radial distances, the derivative

$$\partial_{x'}\, G(R\hat{z} + \vec{x},\; R\hat{z} + \vec{x}\,'; \nu) = \sum_\beta Y_{L'M'_L}(\hat{x})\partial_{x'}\, \mathcal{G}_\beta(x, x'; \nu) Y^*_{L''M'_L}(\hat{x}\,')\,, \tag{3.43}$$

is rather straightforward to obtain. The exact forms for $\mathcal{G}_\beta$ and $\partial_{x'}\, \mathcal{G}_\beta$ can be found in Ref. [107].

Now we seek to obtain the quantized eigenvalues E parametrized by R, i.e. the potential energy curves $E(R)$. For each R-value, the allowed values of E can be naturally attained by forcing the continuity of the energy dependent wavefunctions $\psi_o(\vec{r}, \nu(E))$ and $\psi_S(k(R, E), \vec{x})$, at the surface S. Matching the inner and outer wavefunctions at S $(\vec{x}, \vec{x}\,' = \vec{s}, \vec{s}\,')$ in the Kirchhoff integral, and expressing all prerequisite terms in the perturber-centric coordinates, we obtain

$$\begin{aligned}
\psi_S(k, \vec{s}) = -\frac{1}{2} \oint_S \sum_\beta Y_{L'M'_L}(\hat{s}) \Big[& \mathcal{G}_\beta(s, s'; \nu) \partial_{s'} \psi_S(k, \vec{s}\,') \\
& - \psi_S(k, \vec{s}\,') \partial_{s'} \mathcal{G}_\beta(s, s'; \nu) \Big] Y^*_{L''M'_L}(\hat{s}\,')\, s^2\, d\hat{s}\,' \\
= -\frac{s^2}{2} \sum_\beta Y_{L'M'_L}(\hat{s}) \Big[& \mathcal{G}_\beta(s, s'; \nu) \left(\oint_S Y^*_{L''M'_L}(\hat{s}\,') \partial_{s'} \psi_S(k, \vec{s}\,')\, d\hat{s}\,' \right) \\
& - \left(\oint_S Y^*_{L''M'_L}(\hat{s}\,') \psi_S(k, \vec{s}\,')\, d\hat{s}\,' \right) \partial_{s'} \mathcal{G}_\beta(s, s'; \nu) \Big]\,.
\end{aligned} \tag{3.44}$$

In the second step we comfortably take $\mathcal{G}_\beta$ and $\partial_{x'}\, \mathcal{G}_\beta$ outside the surface integral, as both functions are spherically symmetric about the perturber, and only dependent on the radial coordinates. After substituting Eq. 3.51 in the right hand side of the previous equation, the integrals over $\hat{s}\,'$ (in parenthesis) filters out terms according to the selection rules of the spherical harmonic functions. Once the angular variables have been integrated out we can conveniently equate the radial terms $s' = s$ at the surface. The expression then reads as

$$\begin{aligned}
\psi_S(k, \vec{s}) = -\frac{s^2}{2} \sum_\beta Y_{L'M'_L}(\hat{s})\, B_{L''M'_L} \Big[& \mathcal{G}_\beta(s, s; \nu)\, \partial_s \mathcal{U}_{L''}(k, s) \\
& - \mathcal{U}_{L''}(k, s) \partial_s\, \mathcal{G}_\beta(s, s; \nu) \Big]\,.
\end{aligned} \tag{3.45}$$

Substituting Eq. 3.51 in the left hand side of the previous equation, and projecting onto an $\langle LM_L|$ channel, i.e. multiplying $Y^*_{LM_L}(\hat{s})$ and integrating over $\hat{s}$ on both sides, we obtain

the set of linear equations

$$B_{LM_L}\mathcal{U}_L(k,s) = -\frac{s^2}{2}\sum_{L''} B_{L''M_L}\Big[\mathcal{G}_{LL''M_L}(s,s;\nu)\,\partial_s\mathcal{U}_{L''}(k,s) - \mathcal{U}_{L''}(k,s)\partial_s\,\mathcal{G}_{LL''M_L}(s,s;\nu)\Big]\,, \tag{3.46}$$

which can be written in the matrix form [211, 224]

$$\sum_{L''} B_{L''M_L}\mathcal{M}_{LL''}(E,R) = 0\,, \tag{3.47}$$

where for a fixed M_L (a conserved quantum number),

$$\mathcal{M}_{LL''}(E,R) = \mathcal{G}_{LL''M_L}(s,s;\nu)\partial_s\mathcal{U}_{L''}(k,s) - \mathcal{U}_{L''}(k,s)\partial_s\,\mathcal{G}_{LL''M_L}(s,s;\nu) + \frac{2}{s^2}\delta_{LL''}\mathcal{U}_L(k,s)\,. \tag{3.48}$$

For a nontrivial solution $B_{LM_L} \neq 0$ to exist, the determinant of $\mathcal{M}(E,R)$ has to be zero. Hence, to find $E(R)$ we scan over E in a grid (parametrizing $\nu(E)$ and $k(E,R)$) and locate the zeros of det($\mathcal{M}(E,R)$), for each posible value of M_L separately. The $E(R)$ obtained should be independent of the exact value of s, given that it is small enough to allow the initial approximation (Coulomb potential is constant across S, and contact interaction is zero along S). To certify this, one generally calculates the PECs for varying s-values, and confirms them to be the same.

3.4.2 Spin couplings

The discussion presented above did not consider the intrinsic spin substructure of the ULRM as revealed in section 3.3, so that the fundamental concept can be established first. We know that a more realistic calculation of the ULRM spectra that can be benchmarked against modern experiments must consider the underlying angular momentum couplings. In fact, older experimental works on ULRM spectroscopy [66, 67, 176, 216] exclusively utilized exact diagonalization methods to analyze their data, instead of the spin-less Kirchhoff integral. This deficit was solved very recently by Eiles et al. [107] as they extended the Kirchhoff integration method to include all the spin couplings in ULRM. Since the basic formulation remains the same as in section3.4.1, we will very briefly summarise the changes to the existing terms that captures the relevant spin coupling effects. A more complete picture can of course be attained from the original text [107].

As explained in section 3.3, the most important spin-interaction terms in the molecular Hamiltonian that one should consider are the hyperfine structure between perturber electronic and nuclear spins, the fine structure of the low-ℓ Rydberg states, and the spin-orbit coupling in the electron-atom scattering interaction. The notations and names used here are consistent with those defined in section 3.3.

Outside the surface S the scattering interaction is zero, conserving the hyperfine quantum numbers of the perturber $|F, m_F\rangle$, the Rydberg atomic states, as well as the orbital angular momentum projection M_L (=m_ℓ). As the Coulomb Green's function only represent the high-ℓ states, one can safely ignore its fine structure, making it diagonal in the $|\alpha\rangle = |s_1, m_{s_1}, M_L;\ F, m_F\rangle$ basis. The quantum defect Green's function on the other hand, pertains to low-ℓ states that exhibit non-negligible fine structure, which we write as

$$G_{\rm qd}(\vec{r},\vec{r}\,';\nu) = \frac{\nu}{r\,r'}\sum_{\ell,j,mj}\frac{W_{\nu,\ell+\frac{1}{2}}\left(\frac{2r}{\nu}\right)W_{\nu,\ell+\frac{1}{2}}\left(\frac{2r'}{\nu}\right)Y_{jm_j}(\hat{r})\,Y^*_{jm_j}(\hat{r}')}{\Gamma(\nu+\ell+1)\,\Gamma(\nu-\ell)} \times\frac{\pi\sin(\pi\delta_{\ell j})}{\sin(\pi\nu)\,\sin\big(\pi\nu+\pi\delta_{\ell j}\big)}\,, \tag{3.49}$$

where $\delta_{\ell j}$ are the j-dependent quantum defects, and $Y_{jm_j}(\hat{r}) = \langle\hat{r}|jm_j\rangle$ are the spinor spherical harmonics. The sum over ℓ runs from 0 to ℓ_c, and the sum over j runs from $|\ell - s_1|$ to $\ell - s_1$ for each ℓ. We can then expand the entire Green's function in the $|\alpha\rangle$ basis so that,

$$G(\vec{r},\vec{r}\,';\nu) = \sum_{\alpha,\alpha'}\delta_{FF'}\delta_{m_F m'_F}\,|\alpha\rangle\langle\alpha'|\,\langle\, s_1 m_{s_1} M_L|G_{\rm qd}(\vec{r},\vec{r}\,';\nu)|s_1 m'_{s_1} M'_L\rangle + \sum_{\alpha}|\alpha\rangle\langle\alpha|\,G_{\rm c}(\vec{r},\vec{r}\,';\nu)\,. \tag{3.50}$$

In the perturber-centric coordinates, the scattered electronic wavefunction can be written as

$$\psi_S(k,\vec{x}) = \sum_\beta B_\beta\,\mathcal{U}_{SLJ}(k,x)\,\langle\beta|\hat{x}\rangle\,, \tag{3.51}$$

$$\mathcal{U}_{SLJ}(k,x) = \mathcal{J}_L(kx)\cos(\delta_{SLJ}(k)) \;-\; \mathcal{Y}_L(kx)\sin(\delta_{SLJ}(k))\,, \tag{3.52}$$

where the index $|\beta\rangle = |LSJM_J; I_2 m_{I_2}\rangle$ represents the electron-atom scattering channels as well as perturber nuclear spin, and δ_{SLJ} are the electron-atom scattering phase shifts in each channel. The scattering interaction is clearly diagonal in this $|\beta\rangle$ basis, and the radial wavefunction in each channel resembles the spherical expansion in Eq. 3.51, with the phase shifts modified by fine structure.

Evaluating the Kirchhoff integral at the surface S by matching the inner and outer wavefunctions with the appropriate coordinate transformation, we get a set of linear equations that can be expressed in matrix form just like Eq. 3.48. The spin-coupled PECs are then obtained by finding the zeros of $\det(\mathcal{M}(E, R))$, for each possible value of the good quantum number $\Omega = M_J + m_{I_2}$ separately.

3.4.3 Comparative analysis

Here we compare the merits and drawbacks of the spin-coupled Green's function approach, when weighed against the spin-coupled Exact Diagonalization approach detailed in section 3.3.

The convergence issues in the diagonalization approach due to the divergent scattering volume and the bare delta form of the pseudopotential (as discussed in Sec. 3.2), unsurprisingly plague the spin-coupled model as well. It is not practical to correctly represent the dirac delta potential in a small enough finite basis that is computationally tractable [108]. Moreover, the Omont form of electron-atom scattering potential is scaled by the P-wave scattering volume which diverges at the shape resonance, forcing the ED method to misbehave.

Fortunately, the Green's functions approach does not directly handle the scattering lengths/volumes or try to resolve the delta potential. The electron-atom scattering phase shifts are directly encoded within the spherical expansions of the scattered wavefunctions around the perturber. The exact form of the short range potential that produces these phases shifts is irrelevant here, as long as δ_{LSJ} is known and V_{ea} remains zero at the surface S. At the P-wave shape resonance, the phase shift merely passes through the value of $\pi/2$ radians (corresponding to an ill-defined a_P^3), but remains well behaved. Hence the potential energy curves obtained are only truly parametrized by δ_{LSJ}, allowing us to extract the phase shifts without any basis-dependent uncertainties. It is also possible to obtain a convergent ULRM spectrum using regularized delta potentials [108], or by generalized local frame-transforms. But these methods should first be extended to include all the relevant spin couplings.

While the Green's function method can be extended to calculate the full electronic wavefunctions (via propagating the wavefunction outwards using Kirchhof's integral) in principle, the exact spin-dependent characterization is highly challenging, and currently undone. So, the exact diagonalization approach is still instrumental in calculating the wavefunctions, dipole moments, spin admixtures, and lifetimes of ULRM; as is obviously necessary in the theoretical analysis of the the observed resonances in our works [P3, P6]. So currently, our workflow includes the utilization of the Green's function calculation to obtain convergent PECs, followed by ED calculations of the wavefunctions, where the phase shifts and basis size is adjusted to match the Green's function result.

3.5 Experimental setup

In this section, we provide a brief synopsis of the experimental methods used by our collaborators to create and study ^{87}Rb ULRM, in the projects [P2, P5, P6]. A comprehensive description of the experimental setup can be found in the thesis of Markus Exner [231].

Preparing the utlracold gas: To begin, an ultracold atomic gas is prepared by using a magneto-optical trap (MOT) [232, 233], that confines the ^{87}Rb vapor using near-resonant radiation pressure. The trap consists of a spatially varying (quadrupolar) magnetic field, combined with an optical molasses [234], i.e. counterpropagating cicularly polarized laser beams along orthogonal axis (created by retroreflection). The laser beams are red-detuned so that an atom moving away from the trap center can absorb a photon propagating in the opposite direction, as the spatially varying zeeman shift drives the transition towards resonance. The counterpropagating photon transfers its momentum to the atom during excitation, reducing its kinetic energy and pushing it back to the trap center (where magentic field is zero and the transition is no longer resonant). The momentum change during radiative decay is in random direction and can be averaged to zero over many cycles, whereas photon absorption and kickback happens only when the atom moves away from the trap center. This creates a damping potential that cools and confines the atom over many cooling cycles. For the ^{87}Rb experiments, the $|5s_{1/2}, F = 2\rangle \leftrightarrow |5p_{3/2}, F = 3\rangle$ transition is used for cooling, with a separate pump laser to ensure a steady population of the initial cooling state [231].

Typically the experimental setup features two different cooling chambers, the first being a 2D-MOT that creates a directed high flux source of cold atoms cooled along two directions. Room temperature ^{87}Rb vapor from a solid metallic source propagates through the 2D-MOT before being loaded into the next chamber, consisting of a 3D-MOT. The 3D-MOT allows for complete spatial confinement, trapping the gas across all three dimensions. Once sufficiently many cooling cycles have elapsed, the pump laser power is reduced and the cooling laser is further deturned, so that atoms are allowed to decay and amass population in the $ket5s_{1/2}, F = 1$ atomic ground-state.

The next step is to transfer the already cooled atomic gas from the 3D-MOT to a crossed optical dipole trap (ODT) [235, 236], to allow further cooling and compression. The 1064 nm ODT laser is far detuned from the nearest atomic transitions ($\sim$ 780 nm), causing a spatially varying AC stark shift [237] that attracts the atoms to the beam center. Unlike the MOT, the ODT does not feature dissipative light forces, and preserves the internal state of the atom. The experiments in Kaiserslautern are able to produce ultracold ^{87}Rb clouds with a temperature $T = 40\mu$K, and density $\rho = 4 \times 10^{13}$ cm^{-3}, in the $|5s_{1/2}, F = 1\rangle$ ground-state.

For the given density, the average interatomic spacing is $\sim (4\pi\rho/3)^{-1/3} \sim 181$ nm. The Rydberg orbital size scale as $2n^2$, with an $n = 25$ state having the orbital size ~ 66 nm, and

an $n = 50$ state having the orbital size ~ 265 nm. Even for the smaller n-values, there is a reasonable probability to find perturber atoms within the Rydberg atom orbit, facilitating the photoexcitation of ULRM. Once the ultracold gas has been prepared, the photoexcitation and detection steps are performed for multiple cycles to gather enough data.

Photoexciting the ULRM: The high-ℓ ULRM states are accessed via their f-state admixture through a three photon excitation scheme. The prepared ultracold ensemble undergoes $|5s_{1/2}\rangle \rightarrow |5p_{3/2}\rangle \rightarrow |5d_{5/2}\rangle \rightarrow |nf_{7/2}\rangle$ using lasers of wavelength 780 nm, 776 nm, and 1276–1288 nm, with the last transition exciting the atom to a desired Rydberg state. Here we note that ODT is designed to trap ground-state atoms and not Rydberg atoms, as they have very different AC stark shifts. While magic wavelength tweezers [15] are widely used to simultaneously trap Rydberg and ground-state atoms in other scenarios, this is not appealing in a ULRM experiment that aims to photoexcite molecules with a wide variety of n-values. Hence, the trapping laser is temporarily turned off before the photoexcitation happens.

State detection: The photoexcited Rydberg atoms and molecules are ionized using a CO_2 laser, and then guided to a reaction microscope using an electric field. The reaction microscope measures the impact position and time of flight of incoming ions, from which we can calculate the initial momentum distribution of the Rydberg core before ionization. We can then selectively look at data corresponding to fragments with zero initial momentum, so as to uniquely detect fully bound stationary eigenstates of the ULRM. However, metastable molecular states can undergo internal decay, consequently undergoing associative ionization or ℓ changing collisions that impart momenta to the nuclei. One can then allow a finite momentum filter with which metastable states with non-zero initial momentum, can also be detected. Hence, spectral signatures that are unique to the finite momentum spectrum belong to short-lived molecular resonances, whereas signatures that are present in the zero momentum spectra belong to stable long-lived states.

Chapter 4

Overview of scientific contributions

This chapter provides a synopsis of the scientific results presented in this dissertation. The publications are classified into the three overlapping themes of vibronic physics, quantum dynamics, and precision spectroscopy. The basic theory and notations required to understand them have already been discussed in chapter 2 and 3. Here we directly discuss the published results and also draw connections between them, while just considering their recent history. The larger context of all the presented studies, is the analysis of these high-ℓ scattering states utilizing conventional molecular physics tools, like vibrational and vibronic spectroscopy, internuclear dynamics, and spin mixing effects. The findings compiled here takes us one step closer to the overarching goal of engineering tailored few body interactions in cold gases, with control over their spin-vibronic structure and internal dynamics.

4.1 Vibronic spectra: theory and observation

There is increasing interest and relevance in the study of non-adiabatic interactions in the ultracold atomic and molecular physics community. The high density of states in Rydberg atoms, with level splittings small enough to be comparable to motional energies, hints that vibronic couplings cannot be ignored in a complete analysis of such systems. They were first shown to manifest in ULRM as modifications to ultracold chemical reaction rates, and were qualitatively analyzed using a Landau-Zener approach [80]. They observed that rates of ℓ-changing collisions and autoionization are altered due to avoided crossings between the trilobite, butterfly, and low-ℓ states, and change rapidly with the n-value of the constituent Rydberg atom. Inspired by this experimental work, a previous collaboration involving our group [95] was able to theoretically explain the phenomenon by considering the internal structure parameter n as a synthetic dimension. It was shown that the electronic structure of a trilobite + f-state ULRM can be solved in a two-dimensional (n, R)-manifold that allows for conical intersections (CIs). One must keep in mind that n is not a continuous degree of freedom; hence, the one-dimensional physical system can only really exhibit avoided crossings. But the synthetic dimension allows us to study how the width of the avoided crossing, and consequently the magnitude of the non-adiabatic coupling changes with respect to n. For n-values in the vicinity of a synthetic CI, the potential energy curves show an almost exact crossing that corresponds to a near singular non-adiabatic coupling. These studies however, only analyzed the electronic structure of ULRM to explain the chemical reaction rates, never

trying to explore the full vibronic structure of the ULRM.

Nonadiabatic interaction effects in the spectra of ultralong-range Rydberg molecules [P1]: This manuscript, alongside Ref. [101] is the first in a series of works that formulated an exact quantum mechanical description of the vibronic structure of the ULRM. Our first investigation focussed on ^{23}Na dimers, as their quantum defect structure supports avoided crossings between the trilobite and $\ell = 2$ d-state. Unlike the Landau-Zener type crossings in Ref. [80, 95], ^{23}Na shows strong mixing between the trilobite and d-states over an extended R-range along 100s of a_0. Moreover, the avoided crossings are positioned relatively close to the minima of the trilobite PEC, so that even the lowest energy bound states are strongly affected by the non-adiabatic coupling to the d-state. This is reflected in the behavior of $\delta_S(k)$ being comparable in size to $\pi\delta_d$ for a large range of R, as explained in section 3.2. Compared to ^{87}Rb dimers the crossing between butterfly and trilobite potentials happen at much smaller R-values in ^{23}Na, allowing us to discount their effects in the qualitative description of low energy vibrational/vibronic states.

We developed a coupled two-channel approach that consists of the trilobite state $|\psi_t\rangle$ and any low-ℓ state $|\phi_{n\ell 0}\rangle$. The electronic Hamiltonian $\hat{H}_{el}$ is then expanded in a restricted two-state basis $\{|\psi_t\rangle, |\psi_d\rangle\}$, and diagonalized to obtain the adiabatic PECs $\varepsilon_\pm$ and electronic states. From the eigenstates we could also obtain the first and second-order derivative couplings. All of the aforementioned calculations were done in a two-dimensional n, R-grid, utilizing Whittaker-W functions to model non-integer n-values. This allowed us to study and confirm the existence of CIs and avoided crossings in synthetic dimensions. Moreover, we were able to predict that avoided crossings become CIs when a radial node of the low-ℓ wavefunction coincides with the (n, R) crossing point, i.e., if $\delta_S(k(n, R)) = \pi\delta_\ell$ and $\phi_{n\ell 0} = 0$ simultaneously. To aid in comparison, we also calculate the Born-Huang spectrum (Eq. 2.29), considering only the diagonal derivative couplings as non-adiabatic perturbations to each adiabatic PEC.

To bypass using such divergent non-adiabatic terms when calculating the vibronic spectrum, one needs to construct a diabatic basis where the off-diagonal kinetic energy terms are transformed away into well-behaved potential energy terms. To this end, we were able to analytically prove that the initial two-state expansion of the Hamiltonian is automatically diabatic by construction, so that the diabatic potential energy operator can be simply written as

$$\hat{\epsilon}_{t\ell} = \begin{bmatrix} \varepsilon_t(R) & C_{t\ell}(R) \\ C_{t\ell}(R) & \varepsilon_\ell(R) + \Delta \end{bmatrix}, \tag{4.1}$$

where the coupling term is derived to be $C_{t\ell}(R) = 2\pi a_S(k(R, n))\phi_{n\ell 0}(R)\sqrt{\sum_{i>\ell_c} |\phi_{ni0}(R)|^2}$, $\varepsilon_t(R)$ is the trilobite PEC, and $\varepsilon_\ell(R)$ is the low-ℓ PEC. Diagonalizing the vibronic Hamiltonian $\hat{T}_n + \hat{\epsilon}_{t\ell}$, using finite difference methods discussed in Appendix A.2, we obtain the

two-channel vibronic spectrum.

For the ^{23}Na dimer, we calculated the coupled trilobite- d-state spectrum for a variety of n-values. Our results highlight two extreme cases, one $n = 48$ case that features two different near-CIs (almost vanishing avoided crossing) in the spectrum, and the other $n = 43$ case that only features a wider avoided crossing. We see that the vibronic spectrum shows significant rearrangement in eigenstate structure, in comparison to Born-Oppenheimer calculations. Most strikingly, the highly non-adiabatic $n = 48$ case shows bound vibronic resonances above the d-state threshold, trapped in between the narrow avoided crossings. These resonances have no adiabatic equivalent, as there are no bound vibrational states in either BO potential that correspond to the resonance energy. To add, the trilobite channel is closed while the d-state channel is open in this energy range. The vibronic couplings then create a Feschbach-style multichannel resonance.

We also observe that all bound vibronic states, irrespective of the n-value, are positively shifted in energy ($\Delta E \sim$ MHz) compared to their adiabatic counterparts. Furthermore, we notice that the radial probability density of the vibronic states exhibits non-adiabatic localization effects in comparsion to the delocalized BO spectra. We promptly explain this utilizing the Born-Huang calculation, as the diagonal non-adiabatic terms add a significant potential barrier between different wells in the trilobite potential. While the behavior of the spectrum near the avoided crossing is intensely affected by the existence or absence of CI, the general localization and non-adiabatic energy shifts are uniform across different n-values. This is unsurprising, as the magnitude of non-adiabatic couplings away from the avoided crossings are quite similar for all n. However, the exact position and width of the avoided crossings still affect the stability of the vibronic resonance states, and also dictate the rates of non-adiabatic transitions as is relevant for ℓ-changing collisions.

The model developed above can be used to analyze the general vibronic coupling between a trilobite and low-ℓ state in any species of ULRM dimers. Moreover, the interaction between any low-ℓ and butterfly state, is a rather straightforward extension. In parallel, our collaborators [101] developed a two-state model that studied the vibronic spectrum of a coupled trilobite-butterfly system $\{|\psi_t\rangle, \psi_b\rangle\}$. This is a conceptually different model, as the pure trilobite and pure butterfly states are not orthogonal to each other, exhibiting strong R-dependent overlap. Nonetheless, they were able to calculate the vibronic spectrum of the trilobite-butterfly model using different approaches and validate their results. Just like the coupled trilobite - low-ℓ system, the coupled trilobite - butterfly system also exhibits multichannel resonances and spectral rearrangement. The existence of CIs between pure trilobite and butterfly PECs can also be predicted by searching for (n, R)-values where the s-state Rydberg wavefunction has a radial node that coincides with the crossing point i.e., if $\delta_S(k(n, R)) = \delta_P(k(n, R))$ and $\phi_{n0} = 0$ simultaneously.

Vibrationally highly excited trilobite molecules stabilized by nonadiabatic coupling [P2]: This experimental collaboration with the group of Herwig Ott reports on the observation of nonadiabatically stabilized resonances in ^{87}Rb dimers. These are the first direct measurements of non-adiabatic spectral signatures in ULRM, verifying the previously established theory [P1, 101, 238].

Particularly, we looked at highly excited vibrational states localized in the trilobite PEC for Rubidium. In ^{87}Rb, the butterfly potentials form an avoided crossing with the trilobite PEC around the trilobite global minima, creating an adiabatic decay pathway for the nuclei. Within the framework of BO-approximation, vibrational states localized in the outer adiabatic potential no longer probes an inner repulsive wall. The nuclei in these potentials roll down the butterfly PEC, eventually undergoing ℓ-changing collisions or autoionization. Therefore, apart from a few stable adiabatic states localized in the undulations of the oscillations of the PEC, one cannot excite high lying adiabatic vibrational states of a trilobite molecule.

However, we are able to unambiguously measure highly excited ($\nu \geq 80$) molecular resonances of an $n = 25$ trilobite molecule, red-detuned from the $25f_{7/2}$ atomic resonance. The measured resonance energies and the vibrational splitting show an excellent match with theoretical calculations performed on an effective trilobite potential, considering an exact diabatic crossing with the butterfly potential. In contrast, measurements for $n = 27$ show no such series of trilobite states, as adiabatically expected.

The observations are very successfully explained by analyzing the n-dependency of avoided crossing using CIs in synthetic dimensions. In fact, despite the added complexity of different spin interactions in the potential energy landscape of the ULRM, we find that the nature of the avoided crossing between trilobite and butterfly states can be very well predicted by a spin-indepedent model [238]. For $n = 25$ we find that the radial node of the s-state wavefunction does indeed (almost) coincide with the crossing point of S-wave and P-wave phase shifts, implying that the n-value finds itself in the vicinity of a conical intersection. The $n = 27$ system bears no such coincidence, featuring a relatively wide avoided crossing. We verified this result by solving the two level system in an (n, R)-grid, obtaining the derivative coupling and avoided crossing width, and confirming the existence (and absence) of CIs near $n = 25$ ($n = 27$). To solidify our results, we were able to calculate the dipole transition strengths (via $nf_{7/2}$) of the high lying trilobite states and successfully match it with observed signal profile. The signal profiles would only match so well if the molecular resonance had the R-dependence of a diabatic trilobite PEC, and not a mixed adiabatic PEC.

In the experiment, Rydberg atoms were excited to the $nf_{7/2}$ state via three-photon absorption with a 3 μs pulse duration, allowing the formation of ULRMs. The Rydberg atoms (and molecules) are then photoionized, and the ions are guided into a reaction microscope. The reaction allows us to reconstruct the momentum of the nuclei before ionization, allowing us to distinguish long-lived stationary states with no momentum, and short lived states with

finite momentum. In the trilobite - butterfly system, vibrational states that are fully localized in either of the adiabatic PECs will essentially have zero momentum before ionization. These states will have clear spectral peaks that appear the same in both zero-momentum and finite-momentum signals. However, high-lying molecular resonances non-adiabatically stabilized across two-channels will have a finite lifetime. So there is a finite population of these states that decay into the butterfly potential, rapidly increasing their momentum. Depending on their resonance widths, their spectrum should be resolvable in a finite momentum signal while being much weaker in the zero-momentum signal.

We use Landau-Zener based semi-classical calculations to theoretically estimate the lifetimes of the $n = 25$ trilobite states to be $\tau \geq 5\mu$s, whereas similar $n = 27$ trilobite states should have $\tau \leq 0.05\mu$s. Since the excitation pulse is only 3 μs long, we can explain that the non-adiabatically stabilized $n = 25$ states are spectroscopically accessible, while $n = 27$ states are not. Additionally, the signal for the non-adiabatic states are only clear in the finite momentum signal, as opposed to adiabatic states which have well resolved zero momentum signal. We also calculate Siegert pseudostates in the adiabatic channel to obtain the vibrational spacing and widths, to concisely exclude the possibility that we were measuring internal reflection states [100]. Since the calculated binding energies, level spacings, signal profiles, and lifetimes explain the observed phenomenon very well, the experimental measurement unmistakably validates the theory of n-dependent stabilization of non-adiabatic resonances in the ULRM.

4.2 Quantum dynamics

As we complete the discussion on the vibrational and vibronic spectra of the ULRM, we shift our focus to dynamical effects that can be found in its time evolution. While stationary states help us understand the general internal workings of the molecule, wavepacket dynamics allows us to simulate how specific initial configurations of the system behave in time. As the limits of coldatom experiments advance at an astonishing pace, it is not unrealistic to expect the ability to curate desired initial states and perform time evolution experiments. For example, Pfau et. al.[36] recently reported the observation of vibrational dynamics of charged Rydberg atom-ion systems, through time resolved ion microscopy. Similar experimental studies of neutral ULRM like the trilobite molecule remains an exciting challenge.

From our studies of the ULRM spectra, we know that the highly oscillatory potential energy landscape with dense level spacing can produce exaggerated long-range vibrational/vibronic states. It is only natural to assume that the time evolution of wavepackets which constitute these states will produce interesting dynamical effects hitherto unseen. Within the large body of literature that discusses the internal structure of ULRM, numerical studies that look into ULRM wavepacket dynamics is sparse [105, 106]. Our works listed below, set out

to fill this gap and simulate the vibrational and vibronic dynamics of high-ℓ ULRM.

Internal diffraction dynamics of trilobite molecules [P3]: First, we present the adiabatic wavepacket dynamics of trilobite ULRM, highlighting the propagating diffraction pattern that emerges as the nuclei time evolve in the trilobite potential. For specific initial state configurations, the oscillatory structures in the trilobite PEC acts as a molecular diffraction grating that backscatters incoming nuclei. We explain the backscattering effect and the necessary conditions that facilitate them using Fourier analysis. As a preliminary work, we only consider single channel dynamics in a pure trilobite state, leaving non-adiabatic extensions due to the interacting butterfly state to the future [P4].

We observe that for high enough n (≥ 50), the trilobite PEC V_t (Eq. 3.18) can be separated into an anharmonic potential well ε_{anh} (Eq. 3.23) overlayed with a chirped oscillatory potential $\varepsilon_{osc} = \varepsilon_t - \varepsilon_{anh}$. Taking the Fourier transform of ε_{osc} we see a clear sideband structure that resembles a diffraction grating with specific periodicity. For $50 \leq n \leq 60$ these sideband structures are centered around the internuclear momentum $K \sim 0.03$ atomic units. From a Bragg scattering perspective, this means that the momentum transferred by ε_{osc} to a traversing wavepacket should be quantized in multiples of the sideband value. Since ε_{osc} is not perfectly periodic, the backscattering has a finite momentum width that changes as the wavepacket traverses, eventually causing the dissipation of the diffraction pattern. Subsequently, we estimated that the wavepackets traversing in the trilobite potential naturally attains the minimum momentum, due to the general potential depth of ε_{anh}. So we performed a series of numerical simulations where we time evolve Gaussian wavepackets $\chi(R, t = 0) \propto \exp\left[-(R - R_0)^2/(4\sigma^2)\right]$ with appropriate initial mean and width, cataloging the onset of propagating diffraction patterns in ULRM under various conditions.

For example, when $n = 55$ the potential minima is around $R_{eq} = 2190$ a.u., so a wavepacket starting around at $R_0 \geq 3000$ a.u. naturally attains the momentum $K \sim 0.06$, undergoing continuous backscattering. The probability density of the time-evolving wavepacket then shows an exquisite diffraction pattern. Similar effects are shown in simulations of a variety of n-values and initial positions. As n increases, the amplitude of ε_{osc} decreases, reducing the contrast of the diffraction pattern. The series of simulations were done with $\sigma = 100$ a.u., comparable to the size of the period of oscillations in ε_{osc}. For a wide range of conditions mentioned in the text, we have successfully simulated and explained a *self-diffracting molecule*, where the electronic structure of the dimer diffracts its own nuclear wavefunction.

Increasing the width of the wavepacket to $\sigma = 300$ a.u., we find a different dynamical effect emerges. The initial wavepacket spans multiple different wells, none of them having localized bound states due to the high n-value (and subsequent shallow ε_{osc}). Hence each well acts as a source emanating wavelets, that interfere with each other to form very narrow localized pulses that are reminiscent of a Dirac comb [239, 240].

Finally, we also propose a possible time resolved pump-probe based experimental scheme that can be used to study these dynamical effects. Mainly, we find that vibrational ground states in low-ℓ PECs have the appropriate R_0 and σ to trigger the diffractive effects. Hence, they can be successfully used as pump states, excited to the trilobite potential via microwave transitions. Depending on the n-value, localized low-ℓ states can also be used as probe states to project the time evolving wavepacket, enabling us to extract a time resolved two-point correlation function (that mirrors the dynamics we wish to study). This methodology conveniently allows us to prepare the initial state, time evolve and observe the probability density all using a single ULRM.

Vibronic quantum dynamics of ultralong-range high-ℓ Rydberg molecules [P4]: This work presents a numerical study of vibronic quantum dynamics in ULRM, by considering a coupled-channel treatment that includes the trilobite and butterfly states. It extends the previously described single channel adiabatic dynamics [P3], by adding the P-wave scattering term, and incorporating the subsequent non-adiabatic couplings as discussed in [P1, P2, 101]. Bridging the two different directions of research, this work is the first to reveal exaggerated vibronic quantum dynamics in ULRM.

Firstly, we continue our investigation of the internal diffraction dynamics using the coupled-channel treatment (with $n \in 54, 60$), to see how non-adiabatic effects change the results of the previous study. In this regard, we first obtain the adiabatic PECs and electronic states by solving the electronic Hamiltonian. As expected, the addition of the P-wave term introduces an adiabatic decay channel via the avoided crossing, potentially destroying the continued propagation of the diffraction pattern. However, we see that the two adiabatic states exhibit extremely large derivative coupling between them, suggesting non-adiabatic stabilization through surface hopping [P2]. As expected the behavior of non-adiabatic coupling is highly n-dependent, with $n = 55$ displaying a near singular derivative coupling (very narrow avoided crossings) and $n = 57$ displaying a relatively weaker coupling (and wider avoided crosing). The two n-values are taken as exemplar cases to perform vibronic dynamics.

We then calculate the diabatic potentials (section 2.2.4), and proceed to construct the diabatic Hamiltonian for propagation (appendix A.2). Importantly, we note that the diabatic PECs deviate from the adiabatic PECs much before the avoided crossing. This is due to the derivative couplings being non-negligible (compared to the level spacing) for an extended R-range away from the crossing. However, for the sake of clarity we choose to initialize the wavefunction at large enough R ($\sim 400o$ a.u.) so that potential behaves like a single channel trilobite. This way we can observe what happens when a well-defined nuclear wavepacket enters a regime of vibronic mixing. Our simulations show that the propagating diffraction pattern is stabilized against adiabatic decay due to surface hopping, for both n-values. We utilize a complex absorbing potential (appendix B) to simulate this internal molecular decay via the adiabatic transition to butterfly potential. By calculating total norm and channel

population, we figure out how the wavefunction decays and switches BO-states as a function of time. Hence, we confirm that n-values which show high non-adiabatic couplings ($n = 55$) display higher surface hopping, and increased stabilization of the propagating diffraction pattern. Additionally, the work also features interesting multi-well tunneling effects that emerge during low-energy oscillations in trilobite ULRM for $45 \leq n \leq 50$.

4.3 Precision spectroscopy of electron-atom scattering

The final theme of scientific contributions we discuss is the high-precision spectroscopy of spin-coupled scattering channels via the ULRM. In these experiment-theory collaborations, momentum resolved spectroscopic data is analyzed and interpreted using a complex theoretical model of the ULRM, while considering all the important spin and angular momentum couplings. In doing so, we aim to access and study electron-atom scattering channels with desired spin configurations (denoted by ${}^{2S_e+1}L_J$), and use them for further research. Particularly, the two works discussed below [P5, P6] present an extensive study of the dimers in ${}^3S_1$ and ${}^1P_1$ scattering channels, respectively.

High Precision Spectroscopy of Trilobite Rydberg Molecules [P5]: The first work studies the fundamental electron-atom interaction problem in the ${}^3S_1$ scattering channel, in low energies not typically accessible through free electrons, through an extensive spectroscopic study of trilobite molecular spectrum. We present the vibrational spectrum for photoassociated trilobite ULRM with $n = 22, 24, 25, 26$ and 27, localized in deep potentials determined by the S-wave scattering length. An accurate measurement of their large binding energies (10-20 GHz), in comparison to the spectroscopic resolution (2-4 MHz) allows us to extract the underlying ${}^3S_1$ phase shift with unmatched accuracy. The seminal work by [216] was the first of its kind to utilize high precision spectroscopy of ULRM to study the electron-atom scattering problem. They successfully obtained detailed data on near-threshold anion states and revealed the fine structure of ${}^3P_J$ scattering channels. Their attempts to extract scattering phase shifts however, came with two major limitations: using finite basis diagonalization to perform calculations, and using shallow low-ℓ potentials to extract data. As discussed in section 3.2.2, the depth of the PEC and the binding energies obtained from finite basis diagonalization do not give convergent results with respect to the number of n-manifolds used. Hence, the phase shifts extracted would be dependent on the external parameter, not giving us quantitatively consistent values for different n. Secondly, the shallow low-ℓ states (~ 100 MHz) limits the achievable accuracy of the extracted phase shifts (for fixed readout error), and also doesn't allow us to selectively access the S-wave scattering channel due to spin-mixing.

In comparison, with the newly established spin-coupled Green's function method [107], we circumvent the convergence issue by directly handling the scattering phase shifts. Moreover, with state of the art three-photon absorption techniques [67], we are able to access deep

high-ℓ states with pure trilobite character. Using the zero-momentum signal from the reactance microscope, we filter out mixed trilobite-butterfly states energetically nearby or above the avoided crossing, obtaining exclusive $^3S_1$ character. By measuring the dipole moment of the vibrational states (via stark broadening) along with the binding energy, we are also able to assign each observed resonance to an exact and unique calculated vibrational state. Once the experimental spectrum was collected, we extracted the new set of phase shifts by adding a ninth-order polynomial to the previously extracted phase shifts [216]. The vibrational spectrum of the molecule could then be calculated, parametrized by only the phase shifts. The polynomials were then varied until the relative error between the experimental and numerical data, averaged over all the assigned eigenstates, was minimized. We show that the chosen n-range 22 to 27, gives us overlapping range for $k(n,R) = \sqrt{2\varepsilon_t(n,R) + 1/R}$ so that we can minimize overfsitting errors in the k-dependent phase shifts $^3\delta_S(k)$.

Our final results show that the binding energies and vibrational splittings from the experimental data can be theoretically reproduced with maximal relative errors of 0.8% and 10%, respectively. This corresponds to an uncertainty of 0.7% in the extracted S-wave phases, providing one of the most accurate estimates of low-energy $e^- - ^{87}$Rb scattering phases to date.

Observation of spin singlet butterfly Rydberg molecules in an ultracold atomic Rb gas [P6]: The final manuscript reports the first ever creation of a long-range $^1P_1$ state in an ultracold Rubidium gas, obtained by photoassociating a singlet butterfly ULRM. These elusive high-ℓ states formed a missing link in the creation of ultracold anions and heavy Rydberg systems [109], and have finally been revealed. The lack of laser cooling transitions in alkali anions, and the unavoidable heating mechanisms (due to free electrons) when ionizing ultracold atoms, makes the production of ultracold neutral plasmas and ultracold anions challenging. However, the $^1P_1$ ULRM allows radiative transitions to the $^1\Sigma$ anionic state, with adequate franck-condon overlap to a stable heavy Rydberg state configuration. This is also the first observation of an almost exclusively spin-singlet ULRM, while previous observations reported on mixed singlet-triplet configurations [52, 241, 242].

We obtained the Born-Oppenheimer potentials and states by diagonalization the full spin Hamiltonian, and benchmarking the PECs against basis size non-convergence, with the Green's function method. The spin-singlet admixture of the electronic states ($|\langle\psi_{el}|S_e = 0\rangle|^2$) was studied to display the $^1P_1$ character of the potentials. Depending on the Ω-value the $^1P_1$ scattering produces an undulating stairwell potential (locally conserving $M_L = 0$), and two non-oscillating PECs ($M_L = \pm$). Our calculations show that the stairwell potential is predominantly of $^1P_1$ character, and can hold multiple stable bound states. Particularly, we calculate that the potential well right below the $nf_{7/2}$ resonance exhibits a reasonably large f-state admixutre, enabling three photon excitation. The experimental group was able to successfully access these states for $n = 18$, after a thorough spectroscopic search. To characterize and ensure that the measured resonance have the $^1P_1$ character, we constructed the

necessary theoretical models to calculate the signal profile, dipole moments, level spacing, and binding energies of the molecules. The numerically obtained results match the observations very well, allowing us to conclude that the long-range $^1P_1$ state has finally been created, and the exact transitions required to reproduce them have been revealed.

Chapter 5

Scientific Contributions

PHYSICAL REVIEW A **108**, 012809 (2023)

Nonadiabatic interaction effects in the spectra of ultralong-range Rydberg molecules

Rohan Srikumar,[1,*] Frederic Hummel,[2,†] and Peter Schmelcher[1,3,‡]

[1]*Zentrum für Optische Quantentechnologien, Fachbereich Physik, Universität Hamburg, Luruper Chaussee 149, 22761 Hamburg, Germany*

[2]*Max-Planck-Institut für Physik Komplexer Systeme, Nöthnitzer Straße 38, 01187 Dresden, Germany*

[3]*The Hamburg Centre for Ultrafast Imaging, Universität Hamburg, Luruper Chaussee 149, 22761 Hamburg, Germany*

(Received 1 February 2023; revised 6 June 2023; accepted 7 June 2023; published 14 July 2023)

Ultralong-range Rydberg molecules (ULRMs) are highly imbalanced bound systems formed via the low-energy scattering of a Rydberg electron with a ground-state atom. We investigate for ^{23}Na the d state and the energetically close-by trilobite state, exhibiting avoided crossings that lead to the breakdown of the adiabatic Born-Oppenheimer (BO) approximation. We develop a coupled-channel approach to explore the nonadiabatic interaction effects between these electronic states. The resulting spectrum exhibits stark differences in comparison to the BO spectra, such as the existence of above-threshold resonant states without any adiabatic counterparts, and a significant rearrangement of the spectral structure as well as the localization of the eigenstates. Our study motivates the use of ^{23}Na ULRMs, as a probe to explore vibronic interaction effects on exaggerated timescales and length scales.

DOI: 10.1103/PhysRevA.108.012809

I. INTRODUCTION

Rydberg atoms are an important player in modern quantum physics due to their unique and extreme properties. Their size and dipole moment scale as n^2, and lifetimes and polarizability scale as n^3 and n^7, respectively, where n is the principal quantum number [1,2]. They offer a state-dependent interaction strength and enhanced sensitivity to electromagnetic fields, rendering them promising platforms for quantum computing [3–7], external field sensing [8–10], detection of polar molecules [11–13], and Rydberg-quantum optics [14–17]. The pioneering article in [18] predicted the formation of ultralong-range Rydberg molecules (ULRMs), as a result of attractive scattering interaction of the Rydberg electron with a ground-state perturbing atom. These exotic bound states feature permanent dipole moments of the order of kilodebye and bond lengths of the order of micrometers, properties which were unheard of in conventional diatomic molecules. However, recent works have also studied other exotic bound molecular systems with exaggerated properties, formed due to different binding mechanisms like the Rydberg macrodimer [19–21] and the Rydberg atom-ion molecule [22–27].

This work is dedicated to the diatomic ULRM, bound as a consequence of low-energy electron-atom s-wave scattering. The scattering mechanism enables the existence of two distinct classes of molecular states [18]. The first type is formed when a Rydberg electron of low angular momentum ($l \leqslant 2$) interacts with the neutral perturber. Molecules of the low-l class exhibit shallow potential wells (approximately 10 MHz) and a very small net electronic dipole moment [28]. The second type is the trilobite class of molecules [29,30], which arise as the high-l hydrogenic manifold is mixed by the ground-state atom [31]. The trilobite molecules exhibit much deeper potential wells (on the order of gigahertz) and a large permanent dipole moment and is responsible for garnering much interest to the field of ULRMs. In addition, the use of higher-order terms in our scattering interaction has also demonstrated the existence of the butterfly state [32,33], which arises as a consequence of p-wave shape resonances. More recently, detailed theoretical models that include higher partial waves of the electron-atom scattering interaction have also been constructed [34]. Starting from its experimental observation in [35], significant progress have been made in the study of ULRMs over the past two decades. This includes its utility, as a probe for spatial correlations in ultracold atomic gases [36], in precision spectroscopy of negative-ion resonance [37], and in the study of Rydberg impurities in ultracold atomic gases [38,39]. Furthermore, the fine and hyperfine structures of these molecules [40–42] as well as their behavior in external electric and magnetic fields have been studied [43–47], and major strides have been made in the experimental exploration of these molecules (see [33,35,37,48–59] for examples of experimental investigations on ULRMs).

One of the important theoretical tools used in the analysis of a ULRM is the well-established Born-Oppenheimer (BO) approximation [60]. As a cornerstone of molecular physics, the BO approximation advocates for the separation of slow nuclear and fast electronic motion, allowing us to independently solve the electronic problem in varying geometrical arrangements of the nuclei, to obtain the so-called adiabatic potential energy curves (PECs). However, there is typically a ubiquity of avoided crossings featured in the PECs of the ULRM and resultingly nonadiabatic interactions potentially leading to the breakdown of the BO approximation are expected. Such a breakdown of adiabaticity can result in the

*rsrikuma@physnet.uni-hamburg.de
†hummel@pks.mpg.de
‡pschmelc@physnet.uni-hamburg.de

 ©2023 American Physical Society

altered spectra and lifetimes of molecular states and even introduce metastable states that are subject to nonadiabatic decay [61]. In the special case of a conical intersection (CI), when the molecular geometry facilitates the degeneracy of two PECs, the nonadiabatic couplings become singular and the adiabatic approximation breaks down completely [62–66]. Recent studies have demonstrated the existence of such CIs in the Rb ULRM, for very specific conditions, when the electron-perturber scattering phase shift divided by π is similar in size to the quantum defect, i.e., $\mu_d \pi \approx \delta_s$ [67]. In the context of traditional molecular physics, CIs play an important role in molecular dynamics as they can cause fast nonradiative transitions between electronic states [68–71], Jahn-Teller distortions [72,73], and surface hoppings [74,75], to name a few examples. The study of nonadiabatic effects in the vicinity of conical intersections has been proven to be necessary for understanding a wide range of natural phenomena such as photostability of DNA [76,77], photoisomerization [78,79], and reaction mechanisms involving photosynthesis [80]. The ULRM, on the other hand, provides us with a platform to explore molecular dynamics in the unique and enormous timescales of microseconds and on length scales of micrometers. Hence, the study of nonadiabatic interaction effects, as well as their contribution to the spectral characteristics in a molecule which features such exaggerated properties, is a challenging and promising direction of research on ULRMs. It is of relevance to mention that recent studies of the Rydberg macrodimer and the Rydberg atom-ion molecule also consider nonadiabatic interaction effects, enabling us to theoretically explore beyond BO physics in multiple exotic Rydberg systems [20,22,81].

In this work we focus on the nonadiabatic interaction between two electronic states in ^{23}Na ULRMs, due to the vibronic coupling between them. The electronic level structure of ^{23}Na leads to avoided crossings and state mixing between the trilobite and the d-state PECs (see [82], for a recent study on vibronic couplings between trilobite and butterfly states). The onset of prominent vibronic interaction effects, as a result of the aforementioned electronic level structure, justifies the choice to study sodium as opposed to heavier atoms. We highlight results for specific n values, with near-degenerate avoided crossings that cause singular vibronic couplings, explained using the concept of CIs in synthetic dimensions. A coupled-channel approach is employed to obtain the vibronic spectra, thereby using the nonadiabatic couplings between the trilobite and d-state PECs. We observe features of vibronic interactions in the underlying spectra including scattering resonance states with no adiabatic counterparts. We also use the single-channel Born-Huang approximation, including the nonadiabatic diagonal corrections without the off-diagonal couplings as a comparative resource. The analysis of vibronic and vibrational spectra is used to justify the necessity of a coupled-channel approach to study the ^{23}Na ULRM.

This work is organized as follows. Section II contains the theory and methodology used throughout this work. Section II A elaborates on the general molecular Hamiltonian and gives insight into the approximations and terminology used to study nonadiabatic couplings. Section II B focuses on the electronic interactions in the ULRM and introduces the electronic states and PECs relevant to our work, before we discuss the specific two-level system and the problem of diabatization in Secs. II C and II D, respectively. The computational tools used as well as the approach to obtain the vibronic spectra are discussed in Sec. III. Section IV features the results and discussion. Section IV is further divided into Sec. IV A, addressing the electronic structure of the ^{23}Na ULRM; Sec. IV B, discussing the nonadiabatic couplings; and Sec. IV C, providing a comparative analysis of the coupled-channel vibronic spectrum and the single-channel approximations. A summary and outlook are presented in Sec. V.

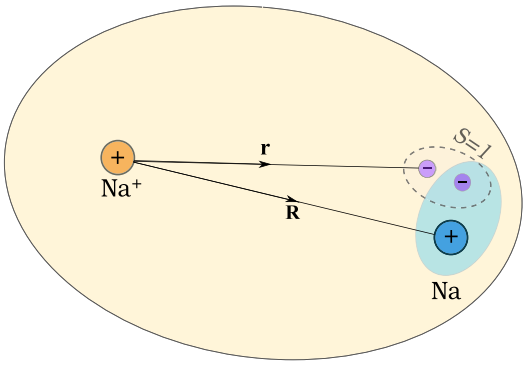


FIG. 1. Sketch of the ^{23}Na ULRM, illustrating the scattering interaction between the Rydberg electron at position **r** and the ground-state atom at position **R**. The triplet nature of the scattering interaction is highlighted.

II. THEORY AND METHODOLOGY

In this section we present the Hamiltonian governing the internal molecular dynamics of the ULRM and the corresponding Schrödinger equation in atomic units. We then proceed to elaborate on the nonadiabatic features of our system and the approximations used to circumvent them. Later we introduce the scattering interaction which forms the binding mechanism of the ULRM and discuss the electronic spectra of the molecule. The focus is then shifted to the interaction between the trilobite and the d state, and the vibronic coupling between them. Finally, we introduce the concept of diabatization and use it in our two-state system as a precursor to obtaining the vibronic spectra.

A. Hamiltonian, adiabatic separation, and nonadiabatic couplings

Our system consists of two ^{23}Na atoms, one in the Rydberg state and the other one in the ground state. Transforming the two-atom system into relative coordinates, **R** is the internuclear vector of the two atoms and **r** is the Rydberg electron position, with the ionic core at the coordinate origin, as depicted in Fig. 1. The Rydberg electrons' interactions with the parent core and the ground-state perturber, as well as the vibrational motion of the diatomic system, are captured in the

molecular single-electron effective Hamiltonian

$$\mathbf{H}_{\rm m} = \frac{\mathbf{P}_{\rm nu}^2}{2\mu} + \underbrace{\frac{\mathbf{p}_{\rm e}^2}{2\mu_{\rm e}} + V_{\rm Ryd}(\mathbf{r}) + V_{en}(\mathbf{R},\mathbf{r})}_{\mathbf{H}_{\rm e}(\mathbf{R},\mathbf{r})}. \tag{1}$$

The first term represents the nuclear kinetic energy $T_{\rm nu}$ along the vibrational degree of freedom, the second term and the third term represent the kinetic energy of the Rydberg electron $T_{\rm e}$ and its interaction with the Rydberg ionic core $V_{\rm Ryd}$, respectively, and the last term V_{en} represents the electron-perturber interaction. In addition, μ and $\mu_{\rm e}$ are the reduced masses of the two nuclei and the electron, respectively. Isolating $\mathbf{H}_{\rm e}(\mathbf{R},\mathbf{r})$ as the electronic Hamiltonian which is parametrically dependent on the internuclear coordinate, we could solve for the corresponding electronic problem. The resulting eigenvalues, i.e., the PECs $\varepsilon_i(\mathbf{R})$ and eigenvectors $\psi_i(\mathbf{R},\mathbf{r})$, depend parametrically on the internuclear coordinates and we have

$$\mathbf{H}_{\rm e}(\mathbf{R},\mathbf{r})\,|\psi_i(\mathbf{R},\mathbf{r})\rangle = \varepsilon_i(\mathbf{R})\,|\psi_i(\mathbf{R},\mathbf{r})\rangle\,. \tag{2}$$

The total molecular wave function can be expanded using the electronic eigenfunctions according to $\Psi_{\rm m}(\mathbf{R},\mathbf{r}) = \sum_i \chi_i(\mathbf{R})\psi_i(\mathbf{R},\mathbf{r})$, known as the Born-Oppenheimer expansion [60,83]. It is an exact representation of the molecular wave function, as the electronic eigenfunctions form an orthonormal and complete basis. Here $\{\chi_i(\mathbf{R})\}$ are the expansion coefficients which portray the $\mathbf{R}$-dependent mixing of electronic states. Inserting this expansion into the molecular Schrödinger equation $\mathbf{H}_{\rm m}\Psi_{\rm m} = E\Psi_{\rm m}$ and integrating out the electronic degrees of freedom, we obtain the coupled-channel time-independent Schrödinger equation (TISE) for the vibrational motion [62]

$$-\frac{1}{2\mu}\nabla_{\mathbf{R}}^2\chi_i(\mathbf{R}) + \varepsilon_i(\mathbf{R})\chi_i(\mathbf{R}) - \frac{1}{2\mu}\sum_j \Lambda_{ij}(\mathbf{R})\chi_j(\mathbf{R}) = E\,\chi_i(\mathbf{R}). \tag{3}$$

Here Λ_{ij} are the nonadiabatic couplings between the nuclear and electronic motions, which can be written as

$$\Lambda_{ij} = 2P_{ij}\nabla_{\mathbf{R}} + Q_{ij}, \tag{4}$$

where $P = (P_{ij})$ and $Q = (Q_{ij})$ are the first- and second-order derivative couplings, defined as

$$P_{ij} = \langle\psi_i(\mathbf{R},\mathbf{r})|\nabla_{\mathbf{R}}|\psi_j(\mathbf{R},\mathbf{r})\rangle\,, \tag{5}$$

$$Q_{ij} = \langle\psi_i(\mathbf{R},\mathbf{r})|\nabla_{\mathbf{R}}^2|\psi_j(\mathbf{R},\mathbf{r})\rangle\,, \tag{6}$$

where angular brackets denote the integration with respect to the electronic degrees of freedom. Here P and Q essentially introduce the coupling between different electronic states ψ_i and ψ_j due to the motion of the nuclei, which in turn affects the vibrational motion of the nuclei. Once the P matrix is obtained, it is straightforward to calculate the second-order coupling using the relation

$$Q_{ij} = \nabla_{\mathbf{R}}P_{ij} + P_{ij}^2, \tag{7}$$

where

$$P_{ij}^2 = -\langle\nabla_{\mathbf{R}}\psi_i(\mathbf{R},\mathbf{r})|\nabla_{\mathbf{R}}\psi_j(\mathbf{R},\mathbf{r})\rangle\,. \tag{8}$$

It is possible to write Eq. (3) in a more compact way, using the complete P matrix as

$$-\frac{1}{2\mu}(\nabla_{\mathbf{R}} + P)^2\boldsymbol{\chi}(\mathbf{R}) + \varepsilon(\mathbf{R})\boldsymbol{\chi}(\mathbf{R}) = E\,\boldsymbol{\chi}(\mathbf{R}), \tag{9}$$

with the vector $\boldsymbol{\chi} = (\chi_i)$, which contains the expansion coefficients, and the diagonal potential energy matrix ε, which contains the corresponding PECs. The nonadiabatic couplings are shown to manifest as off-diagonal terms in the kinetic energy operator for the nuclear vibrational motion.

The BO approximation [60,62–64,83] is used to solve Eq. (3) as a standard approximation, where the nonadiabatic terms are completely neglected, resulting in the decoupling of the molecular vibrational Schrödinger equations governing χ_i to form

$$-\frac{1}{2\mu}\nabla_{\mathbf{R}}^2\chi_i(\mathbf{R}) + \varepsilon_i(\mathbf{R})\chi_i(\mathbf{R}) = E_i\chi_i(\mathbf{R}). \tag{10}$$

Here the total molecular state is simply $\Psi_{{\rm m},i}(\mathbf{R},\mathbf{r}) = \chi_i(\mathbf{R})\psi_i(\mathbf{R},\mathbf{r})$, i.e., the electronic and nuclear motion are adiabatically separated. In addition, $\psi_i(\mathbf{R},\mathbf{r})$ is the adiabatic eigenstate, $\varepsilon_i(\mathbf{R})$ is the adiabatic PEC which describes the electronic motion, and $\chi_i(\mathbf{R})$ is the vibrational wave function on each PEC. These adiabatic states and energy surfaces can be obtained by solving $\mathbf{H}_{\rm e}$ at each fixed nuclear geometry. Equation (10) then describes the vibrational motion of each individual adiabatic potential energy curve. The adiabatic approximation can be justified due to the large differences in masses between the electrons and the nuclei, resulting in very different timescales of their motions. Hence the nuclei are approximated to remain frozen over the course of the electronic dynamics.

In a second approximation, called the Born-Huang (BH) approximation [84–86], we include the diagonal derivative coupling operator Λ_{ii} in Eq. (10),

$$-\frac{1}{2\mu}\nabla_{\mathbf{R}}^2\chi_i(\mathbf{R}) + \varepsilon_i^b(\mathbf{R})\chi_i(\mathbf{R}) = E_i\chi_i(\mathbf{R}), \tag{11}$$

where

$$\varepsilon_i^b(\mathbf{R}) = \varepsilon_i(\mathbf{R}) - \frac{1}{2\mu}\Lambda_{ii}(\mathbf{R}). \tag{12}$$

The Born-Huang approximation still maintains the decoupling between different adiabatic electronic states due to nuclear motion; instead it merely adds a correction to each isolated PEC due to the finite kinetic energy of the nuclei. Hence the BH approximation, much like the BO approximation, results in a single-channel TISE by ignoring the off-diagonal couplings of the coupled-channel TISE (3). The nomenclature used here is based on works in nonadiabatic molecular physics [85,86] and is not to be confused with the notion of a Born-Huang expansion or other potentially ambiguous terminology. Note that P is anti-Hermitian, whereas Q is non-Hermitian. Hence, if the electronic eigenfunctions are real, P_{ii}, the diagonal first-order term vanishes and we obtain $(\Lambda_{ii} = Q_{ii}) \leqslant 0$ [from Eqs. (7) and (8)], thereby causing a purely positive shift in the adiabatic PEC.

Both the Born-Oppenheimer and Born-Huang approximations are valid only when the $\mathbf{R}$ dependence of ψ_i and ε_i is adiabatic, i.e., the change of electronic motion with respect

to **R** is gradual. However, both of these assumptions are broken in the vicinity of an avoided level crossing of two PECs, where the coupling between the electronic states is non-negligible due to a high **R** sensitivity of the electronic states. The strong vibronic coupling effects between the vibrational and electronic states, due to the avoided crossings, can change the spectra and lifetimes of molecules and facilitate surface hopping across the avoided crossing.

B. Electronic interaction

Solving the molecular Hamiltonian for a ULRM first requires the characterization of the electronic interaction between the Rydberg electron and ground-state atom, which perturbs the Rydberg electron wave function via low-energy scattering. We model V_{en}, the interaction potential, using a Fermi pseudopotential [87,88] for s-wave scattering,

$$V_{en}(\mathbf{r},\mathbf{R}) = 2\pi a_s^T(k)\delta(\mathbf{r}-\mathbf{R}), \tag{13}$$

where $a_s^T(k) = a_s^T(0) + \pi\alpha k/3$ is the energy-dependent triplet s-wave scattering length for electron collisions with ground-state atoms, where $a_s^T(0) = -5.9$ is the zero-energy triplet scattering length [89,90] and $\alpha = 162.7$ is the polarizability [91–93]. The wave number k can be semiclassically determined using $k^2 = 2/R - 1/n^2$. The negative triplet scattering length facilitates an attractive interaction capable of binding the two ^{23}Na atoms. A pictorial representation of the interaction is presented in Fig. 1.

The adiabatic electronic Hamiltonian for the ULRM is hence given by $H_e = H_{\mathrm{Ryd}} + V_{en}$, where H_{Ryd} is the Rydberg electron Hamiltonian. The H_e can be diagonalized in the Rydberg-state basis $\{\langle\mathbf{r}|nlm\rangle = \phi_{nlm}(\mathbf{r})\}$, which satisfies the Rydberg atom's TISE

$$H_{\mathrm{Ryd}}\,|nlm\rangle = -\frac{1}{2(n-\mu_l)^2}\,|nlm\rangle\,, \tag{14}$$

where $|nlm\rangle$ is an atomic Rydberg eigenstate. In our case μ_l is the l-dependent quantum defect of ^{23}Na [67,94], which determines the detuning of each quantum-defect state with reference to the hydrogenic state with energy $E_n = -1/2n^2$. It is worth noting that we omit the fine and hyperfine structures of the atomic Rydberg Hamiltonian. These terms may indeed be relevant for specific systems and consequently cannot be ignored if the aim is a comparison with (precise) spectroscopic experimental data. However, our goal is to provide evidence for the vibronic interaction effects primarily and hence we focus purely on the binding interaction, but acknowledge the necessity to introduce further interactions depending on the considered case and species. The spherical symmetry of the Hamiltonian implies that, without loss of generality, the internuclear axis can be taken as the z axis and only $m = 0$ states contribute. The high-angular-momentum states ($n-1 \geqslant l \geqslant 3$ for Na) are approximately degenerate to the hydrogenic manifold due to negligible quantum defects. Degenerate perturbation theory is used to obtain the high-l adiabatic electronic states of H_e,

$$|t\rangle = \frac{1}{T}\sum_{l=3}^{n-1}\phi_{nl0}(R\hat{\mathbf{z}})\phi_{nl0}(\mathbf{r}), \tag{15}$$

where

$$T^2 = \sum_{l=3}^{n-1}|\phi_{nl0}(R\hat{\mathbf{z}})|^2, \tag{16}$$

and the corresponding potential energy curve

$$t(R) = 2\pi a_s^T(k)T^2, \tag{17}$$

which are popularly known as the trilobite state and trilobite PEC [18,31,41]. The low-angular-momentum Rydberg-electron states ($l < 3$) are energetically far detuned from the hydrogenic manifold due to significant quantum defects. Using nondegenerate perturbation theory, we obtain the isolated low-l adiabatic electronic state of H_e,

$$|q\rangle = \phi_{\nu l0}(\mathbf{r}) \tag{18}$$

and the corresponding potential energy curve

$$q(R) = 2\pi a_s^T(k)|\phi_{\nu l0}(R\hat{\mathbf{z}})|^2, \tag{19}$$

where $\nu = n - \mu_l$ is the effective principal quantum number. Note that the low-l molecular electronic state is essentially the Rydberg-electron state, without any R-dependent state mixing. These two PECs, first introduced in [18], are the building blocks of the Rydberg ULRM. The trilobite PECs feature wells which are significantly deeper (on the order of gigahertz) than their low-l counterparts (on the order of megahertz) and can support multiple bound molecular states. These trilobite molecules are extremely polar with a large electric dipole moment $D \approx R - n^2/2\,ea_0$ (a_0 is the length scale in atomic units) as compared to the nonpolar low-l molecules, which can only support a few weakly bound states. This simple perturbative method covers the fundamental properties of Rydberg molecules and it allows us to study the two distinct classes of PECs and analyze the properties of both polar and nonpolar molecules formed by them.

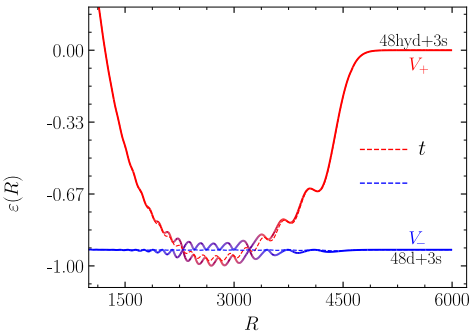
C. Two-level system

As a prototype setup, the nonadiabatic interactions in ^{23}Na ULRMs can be effectively probed by studying the interaction between the trilobite and $l = 2$, i.e., the d quantum-defect state relevant in sodium. We expand H_e in a restricted basis $\{|t\rangle\,, |q\rangle\}$ consisting of the trilobite and d state to obtain

$$V_e = \begin{bmatrix}\langle t|H_e|t\rangle & \langle q|H_e|t\rangle \\ \langle t|H_e|q\rangle & \langle q|H_e|q\rangle\end{bmatrix} = \begin{bmatrix} t & \sqrt{qt} \\ \sqrt{qt} & q+\Delta\end{bmatrix}, \tag{20}$$

where Δ is the energy splitting between the d state with reference to the hydrogenic manifold. Note that the notation used is based on [67], for the sake of continuity and convenience, but the inner product of two eigenstates is summed over coherently without the loss of sign information. The upcoming strategy would be to use the BO approximation and obtain the adiabatic states of the restricted two-level system and utilize them to calculate the nonadiabatic coupling terms. The behavior of these nonadiabatic terms might warrant the necessity to transform our system into a basis where the vibronic spectra can be readily calculated. Moving along our road map, two adiabatic PECs (see Fig. 2) are obtained from the diagonalization

$$V_\pm(R) = \tfrac{1}{2}[t + q + \Delta \pm \sqrt{(t-q-\Delta)^2 + 4qt}], \tag{21}$$


0.00
-0.33
-0.67
-1.00
$\varepsilon(R)$
1500
3000
4500
6000
R
48hyd+3s
V_+
t
V_-
48d+3s

Schrödinger equation is solved without dealing with divergent derivative couplings.

D. Diabatization

The derivative coupling terms, as discussed before, manifest as off-diagonal terms based on the nuclear kinetic energy operator. The idea of diabatization [62,64] is to perform a unitary transformation which diagonalizes the kinetic energy matrix, whereby the need for derivative couplings in solving the vibrational TISE is circumvented. As a result of such a transform, off-diagonal potential energy terms may be introduced in the new basis, which accounts for the vibronic couplings in the diabatic basis. A unitary transformation $\bar{\boldsymbol{\chi}}(R) = U(R)\boldsymbol{\chi}(R)$ would transform the TISE (9) into

$$-\frac{1}{2\mu}(\mathbb{I}\,\partial_R + \bar{P})^2\bar{\boldsymbol{\chi}}(R) + \bar{\varepsilon}(R)\bar{\boldsymbol{\chi}}(R) = E\,\bar{\boldsymbol{\chi}}(R), \tag{26}$$

where

$$\bar{\varepsilon}(R) = U^\dagger\varepsilon(R)U, \quad \bar{P} = U^\dagger(PU + \partial_R U). \tag{27}$$

The transformed derivative coupling matrix vanishes if

$$\partial_R U = -PU, \tag{28}$$

in which case the matrix U represents the diabatic transform, and $\bar{\varepsilon}$ is the diabatic potential energy matrix with off-diagonal terms. While it may not be possible to construct such a unitary transform in all situations, for a two-level system with a single parameter R, such a transformation exists analytically [20,96] where U is a rotation about the angle,

$$\gamma(R) = \int_R^\infty P_{12}(R_1)dR_1. \tag{29}$$

Using the corresponding form of P_{12}, we obtain $\gamma(R) = -\int_R^\infty \theta'(R_1)dR_1 = -\theta(R)$. Hence, the diabatic basis is proven to be the restricted electronic basis $\{|t\rangle, |q\rangle\}$, which was used as the initial ansatz. This gives the diabatic potential matrix

$$\bar{\varepsilon} = \begin{bmatrix} t & \sqrt{qt} \\ \sqrt{qt} & q+\Delta \end{bmatrix}. \tag{30}$$

We have theoretically derived the adiabatic electronic states, nonadiabatic couplings, and the diabatic potential energy curves. What is left is to obtain the vibronic spectrum, by solving the coupled vibrational Schrödinger equations, using the given diabatic potential energy matrix, the elements of which vary as smooth functions of R, devoid of any singularities.

III. COMPUTATIONAL APPROACH: VIBRONIC STRUCTURE

Based on the diabatic PECs, we use a tenth-order finite-difference method [97] to obtain the vibrational wave functions by solving the TISE for each adiabatic PEC. Convergent eigenvalues and wave functions are observed for a grid of $1000\,a_0$–$6000\,a_0$, with a step size of $1a_0$. Convergence of P and Q demands much finer grid steps near the avoided crossings. This is overcome by diabatization; using the smooth diabatic PECs, we obtain a convergent eigenspectrum for the coupled-channel vibronic system for a step size of $1a_0$. Once the diabatic basis is obtained, the coupled-channel vibronic Hamiltonian in the diabatic basis can be represented as

$$H_{\rm m} = \begin{bmatrix} T_{\rm nu} + t(R) & \sqrt{qt}(R) \\ \sqrt{qt}(R) & T_{\rm nu} + q(R) + \Delta \end{bmatrix}, \tag{31}$$

where $T_{\rm nu}$ is the nuclear kinetic energy term acting on each of the diagonal PECs. Solving the TISEs $H_t = T_{\rm nu} + t(R)$ and $H_q = T_{\rm nu} + q(R)$ on the aforementioned grid gives us the eigenspectra $\{E_i^t, |\chi_i^t\rangle\}$ and $\{E_i^q, |\chi_i^q\rangle\}$ corresponding to each diagonal diabatic PEC. We can then expand any eigenvector of $H_{\rm m}$ as

$$\left|\Psi_{\rm m}^j\right\rangle = \sum_{i=0}^{N-1} c_i^j \left|\bar{\chi}_i^t\right\rangle |t\rangle + \sum_{i=0}^{N-1} d_i^j \left|\bar{\chi}_i^q\right\rangle |q\rangle, \tag{32}$$

where

$$H_{\rm m}\left|\Psi_{\rm m}^j\right\rangle = E^j\left|\Psi_{\rm m}^j\right\rangle. \tag{33}$$

Here $\{c^j\}$ and $\{d^j\}$ are expansion coefficients obtained by diagonalizing $H_{\rm m}$ in the diabatic basis and N is the number of vibrational states from each diagonal PEC used for diagonalization. Note that the eigenvector can no longer be separated into well-defined electronic or vibrational parts. However, tracing out the electronic degree of freedom leaves us with the vibrational probability density of $|\Psi_{\rm m}^j\rangle$ along the internuclear axis,

$$P^j(R) = \left|\bar{X}_t^j(R)\right|^2 + \left|\bar{X}_q^j(R)\right|^2, \tag{34}$$

where

$$\bar{X}_t^j(R) = \sum_{i=0}^{N-1} c_i^j\bar{\chi}_i^t(R), \quad \bar{X}_q^j(R) = \sum_{i=0}^{N-1} d_i^j\bar{\chi}_i^q(R). \tag{35}$$

The $P^j(R)$ can be compared to the probability density of the vibrational states in each adiabatic PEC (see Figs. 4 and 5), whereby differences in vibrational motion can be observed between the adiabatic and nonadiabatic cases. To observe electronic-state mixing, we transform the vibronic eigenstate back to the adiabatic basis where $\boldsymbol{X}^j = U^\dagger\bar{\boldsymbol{X}}^j$, where $U^\dagger$ is the inverse-diabatic transform, to obtain

$$\left|\Psi_{\rm m}^j\right\rangle = X_-^j(R)\,|\psi_-\rangle + X_+^j(R)\,|\psi_+\rangle, \tag{36}$$

where $X_\pm$ provides the R-dependent electronic-state mixing due to the nonadiabatic couplings, and

$$p_\pm = \int |X_\pm(R)|^2 dR, \tag{37}$$

which provides the population for the state $|\psi_\pm\rangle$. Color mapping the $P^j(R)$ with the population p_- (see Figs. 4 and 5) is an effective way to visualize both the electronic and vibrational contributions to each vibronic eigenstate. The unbound states above the dissociation threshold suffer box-state behavior due to the fixed boundary conditions we impose and are sensitive to the changes in the boundary-wall position. Hence, only the bound states below the threshold and resonance states above threshold are considered in our analysis. We ensure convergence of these states with respect to variation of both boundary position and grid size.

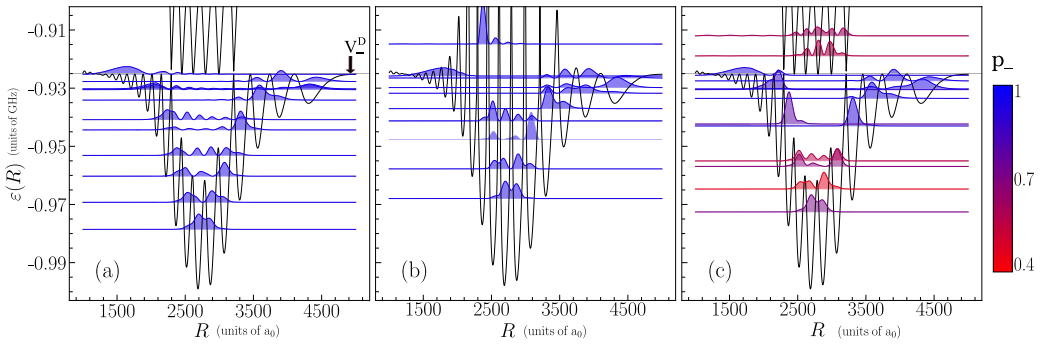


FIG. 4. Eigenspectrum of the ultralong-range sodium molecule for $n = 48$. Selected vibrational energy levels and probability densities of bound states correspond to (a) the V_- Born-Oppenheimer curve, (b) the V_-^b Born-Huang curve, and (c) the coupled-channel nonadiabatic system, with the adiabatic curves plotted for reference. Each vibrational level is color graded according to the electronic contribution by the $|\psi_-\rangle$ state, represented by the population p_-. The dissociation threshold of the V_- PEC, given by $V_-^D = -0.925$ GHz, is presented in (a).

IV. RESULTS AND DISCUSSION

In this section we discuss the electronic and vibronic spectral properties of the sodium ULRM. The principal quantum number $n = 48$ is used to illustrate the structure of the adiabatic PECs and derivative coupling terms, as it is representative of a strong vibronic interaction. We then proceed to discuss the complete vibronic spectra in comparison to the BO and the BH spectra and elaborate on the specific differences between them due to nonadiabatic interaction effects. The vibronic spectrum for $n = 43$ is also discussed, as it features less prominent vibronic coupling when compared to the $n = 48$ case.

A. Electronic structure

Figure 2 features the two-state adiabatic PECs $V_\pm$ determined for $n = 48$ (solid lines). At large R, close to the dissociation limit ($R \sim 4500\,a_0$), the PECs become nearly flat and match the energies of the hydrogenic manifold (V_+) and the d state (V_-), respectively. Inside the Rydberg orbit $R \leqslant 2n^2$, the $|\psi_+\rangle$ electronic state splits off of the hydrogenic manifold, causing the V_+ PEC to descend towards the V_- PEC and form narrow avoided crossings at $R \approx \{2295, 3210\}a_0$, where nonadiabatic couplings become large.

The exchange of the electronic-state character due to state mixing at avoided crossings is given by color grading the adiabatic PECs, with the R-dependent overlap of the adiabatic states with the d state. Corresponding to the mixing of electronic states, the $V_\pm$ PECs split away from $q(R)$ and $t(R)$ for $1700\,a_0 \leqslant R \leqslant 4300\,a_0$. For R values between the avoided crossings, V_- acquires a trilobite character, as is visible from the well structure of the PEC and the low-d-state contribution to $|\psi_-\rangle$. On the other hand, V_+, while being d-state dominant, has a significantly altered well structure. Note that, although $q(R)$ appears to be flat in the relevant energy scale, it does exhibit oscillatory structures of depth less than or equal to 6 MHz, significantly different in depth and structure from V_- for the complete R interval within which potential wells appear. The mixing of electronic states leads to the modification of transition dipole moments, facilitating the excitation of high-l states via two-photon transitions. We remark that the validity of our surfaces $V_\pm$ is confirmed by comparison to numerically obtained adiabatic PECs including atomic Rydberg

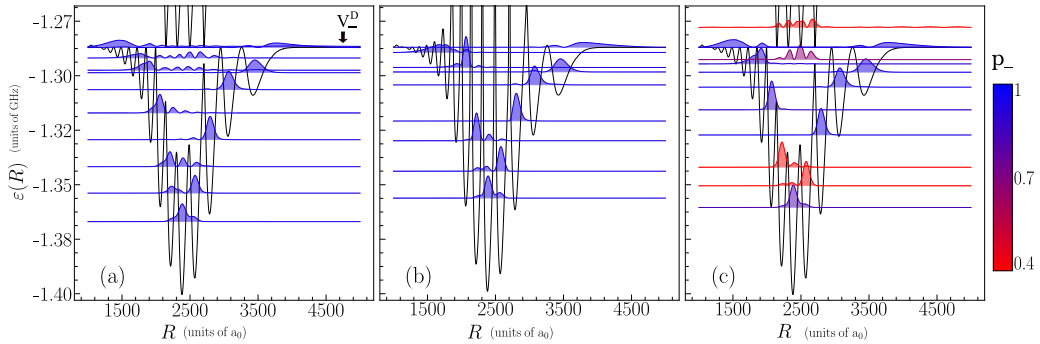


FIG. 5. Eigenspectrum of the ULRM for $n = 43$. Selected vibrational energy levels and probability densities of bound states correspond to (a) the V_- Born-Oppenheimer curve, (b) the V_-^b Born-Huang curve, and (c) the coupled-channel nonadiabatic system, with the adiabatic curves plotted for reference. Each vibrational level is color graded according to the electronic contribution by the $|\psi_-\rangle$ state, represented by the population p_-. The dissociation threshold of the V_- PEC, given by $V_-^D = -1.287$ GHz, is presented in (a).

states belonging to energetically neighboring n manifolds, as well as corresponding quantum-defect split states.

Furthermore, the single-color dashed lines are used to represent the diabatic PECs, corresponding to the trilobite state (red) and the d state (blue). Note that the diabatic curves cross each other at R values corresponding to the avoided crossings. This is expected, as the crossing of diabatic curves, given by the relation $t = q + \Delta$, minimizes the energy gap between the adiabatic PECs to $|V_+ - V_-| = \sqrt{4qt}$ [see Eq. (21)]. Due to the oscillatory nature of the d-state PEC, it is possible that the diabatic curves cross each other near the node of the $|nd0\rangle$ eigenstate. Such a coincidence would result in an extremely narrow avoided crossing, as is illustrated in Fig. 2 for the special case of $n = 48$.

Extending our analysis, if the $t = q + \Delta$ crossing exactly coincides with the node of $|nd0\rangle$, then q vanishes and the adiabatic PECs become degenerate, i.e., $|V_+ - V_-| = 0$. However, the von Neumann–Wigner noncrossing theorem prohibits an exact degeneracy of the PECs corresponding to electronic states of the same symmetry, in single-parameter (determined by R) diatomic systems [98]. We note that the use of the principal quantum number n, as a synthetic dimension [67], allows us to bypass the noncrossing theorem. This is facilitated by using Whittaker Coulomb functions as a replacement for the hydrogenic radial wave functions, for probing noninteger n [99,100]. The two-parameter diatomic system introduces the possibility of forming conical intersections at specific $\{n, R\}$ coordinates. Such CIs would result in complete degeneracy of the adiabatic potentials, representing $\{n, R\}$ values where the diabatic curves cross each other at exactly the node of $|nd0\rangle$. Hence, the width of the avoided crossings and consequently the strength of the nonadiabatic coupling is ascertained to be n dependent, corresponding to the proximity of the $\{n, R\}$ coordinate to a CI.

B. Nonadiabatic coupling

Figure 3 features the nonadiabatic couplings of the two adiabatic electronic states of the ULRM. Since the P matrix is anti-Hermitian, it suffices to analyze P_{12} $(=-P_{21})$ as off-diagonal coupling. Here P_{12} is divided by the reduced mass μ and a_0 so that it can be expressed in units of energy, as represented in Eq. (3). Similarly, Q_{11} and Q_{22} are divided by twice the reduced mass. The nonadiabatic couplings are then expressed in the same energy scale as the adiabatic PECs, allowing to us to compare their relative strengths as they appear in the vibrational TISE [see Eq. (3)] and consequently establish their importance in the calculation of the eigenspectrum.

The derivative off-diagonal coupling for $n = 48$ [see Fig. 3(a)] exhibits two near-singular peaks corresponding to the same R values as the narrow avoided crossings of the underlying PECs. At other R values, P_{12} also exhibits oscillatory structures with smaller amplitude, which are caused by the well structures of V_+ and V_- resulting in an oscillatory potential energy difference between them. The couplings vanish beyond $R > 4500\, a_0$ and $R < 1500\, a_0$, due to a negligible R-dependent state mixing. The second-order nonadiabatic couplings Q_{11} and Q_{22} are both dominated by the contribution from P_{12}, overpowering the derivative term in Eq. (7). Hence both diagonal terms feature near-singular peaks corresponding to the narrow avoided crossings, with negligible strength at other R values, on the displayed scale. The magnitude of the peaks in the nonadiabatic couplings far exceed the energy scale of the adiabatic potential energy curves near the avoided crossing, thereby causing the breakdown of the BO approximation. The strong contribution from the off-diagonal term which dominates the diagonal term implies that the BH approximation is also not applicable. Note that the magnitude and double-peak structure of the nonadiabatic couplings are specific to the $n = 48$ case, which allows the extremely narrow avoided crossings.

To further study the n dependence of nonadiabatic effects, we determine the magnitude of P_{12} over a parameter range of the principal quantum number [see Fig. 3(b)]. The linear structures formed by P_{12} stem from the fact that the length scale of the ULRM, and hence the position of the avoided crossings, scales as n^2. As explained before, these avoided crossings turn into CIs when the trilobite PEC crosses the d-state PEC, exactly at the zero of $|nd0\rangle$. Figure 3(b) features near-singular peaks for specific n values, which corresponds to the existence of such conical intersections accounting for synthetic dimensions. The $n = 48$ case is highlighted, as it is very close to two CIs, which explains the existence of two nearly degenerate avoided crossings and the double-peak structure of nonadiabatic couplings. Other integer n values which are not in the vicinity of a CI also feature prominent but less-peaked derivative couplings which correspond to their respective avoided crossings, which are wider compared to the $n = 48$ case.

C. Vibrational and vibronic spectra

We now perform a comparative analysis of the spectral features of the sodium ULRM, obtained using the BO approximation, the BH approximation, and the coupled-channel Hamiltonian for $n = 48$. Figures 4(a) and 4(b) show the vibrational probability densities of selected bound eigenstates shifted according to their energy eigenvalues calculated using the BO and BH approximations, respectively. Figure 4(c) shows the vibrational probability density of selected bound eigenstates of the coupled-channel Hamiltonian, obtained by tracing out the electronic degree of freedom, shifted according to their energy values. The probability densities are colored according p_-, the population of state $|\psi_-\rangle$. The black lines represent the V_-, V_+ PECs in Figs. 4(a) and 4(c) and the BH corrected V_-^b PEC in Fig. 4(b).

We observe that the vibronic eigenvalues exhibit a significant positive shift in energy when compared to the vibrational eigenvalues obtained using the BO approximation. For $n = 48$, the full vibronic system possesses a ground-state shifted approximately 6 MHz higher in energy than the BO ground state and exhibits negligible energy shifts for bound states near the continuum threshold. The energy gaps between the eigenvalues of the BO system fail to mimic the energy gaps exhibited by the coupled-channel nonadiabatic system. The Born-Huang correction shifts the vibrational ground state approximately 11 MHz higher in energy than the BO ground state, effectively placing it above the first excited state of the BO system and above the ground state of the

coupled-channel system. The higher excited states near the continuum also show significant positive-energy shifts (approximately 4 MHz) between the BO and the BH approximations. The overcorrection in energy values, due to the BH correction, is a result of including only the positive diagonal terms without considering the level repulsion introduced by the off-diagonal terms.

We also observe pronounced differences in the vibrational probability densities obtained within the three models. The vibrational ground state associated with the V_- PEC is delocalized between several wells (2500 a_0–3300 a_0). The ground state belonging to the BH and exact spectra, although similar in density profile, is more localized. Subsequent excited states belonging to the BH and exact spectra, while exhibiting different density profiles, also show more localized behavior. For example, the fourth excited BO state in Fig. 4(a) is delocalized in R over the entire of the V_- PEC at the relevant energy scale. In contrast, the corresponding coupled states presented in Fig. 4(c) exhibit localization in R over the span of a single potential well. Similar effects of localization are also clearly visible in the fifth and seventh excited states of the system. The higher potential barrier introduced between the potential wells by the diagonal BH correction can be viewed as an explanation for vibrational localization in the BH spectrum. However, the vibronic spectrum has a significantly altered probability distribution that is not explained by the diagonal correction alone. Interestingly, the fourth and fifth excited states of the vibronic spectrum are localized in two separate outer wells, allowing them to be nearly degenerate. Note that below the continuum threshold of -0.925 GHz, the BO and BH spectra contain states with purely ψ_- character. Counterintuitively, we observe significant state mixing for the first three excited states of the coupled system, even though they appear to be well localized in the V_- PEC. This indicates strong nonadiabatic couplings between the two closed channels, well below the continuum limit.

A key observation to be made is the existence of nonadiabatic resonance states visible above the V_- dissociation threshold. For energies above -0.925 GHz, the $n = 48$ V_- adiabatic PEC corresponds to an open channel, featuring only continuum states. However, in the complete vibronic picture [Fig. 4(c)], bound states are observed at energies of approximately -0.919 and -0.912 GHz, with significant state mixing (determined by color value). The vibrational probability density of these bound states is localized in the potential energy wells of V_+, but is localized much below the ground state of V_+; hence, it cannot be interpreted to belong to either one of the single channels. The BH spectrum does contain a bound state of energy -0.915 GHz localized in the V_-^b PEC, but this does not compare in energy value or probability density to the aforementioned resonance states. The bound states are hence explained as scattering resonances due to the off-diagonal nonadiabatic coupling between an open channel (limited to V_-) and a closed channel (limited to V_+).

Figure 5 features the vibrational and vibronic spectra, as an extension of the previous case study, for $n = 43$, following the same structure and description as in Fig. 4. The $n = 43$ case is of comparative value, as the system is not in the vicinity of a CI [Fig. 3(b)] as opposed to the $n = 48$ case. The PECs features a much wider avoided crossing ($R \sim 2700\,a_0$) as portrayed in Fig. 5, and the differential couplings, while prominent, are not as peaked as in the $n = 48$ case. The ground states of the BH spectrum and the exact spectrum are shifted by approximately 11 MHz and 6.5 MHz, respectively, relative to the BO ground state. The positive-energy shift due to the nonadiabatic coupling does not vary significantly between the $n = 43$ and $n = 48$ cases. However, the deeper wells of the $n = 43$ PECs ensure that the energy splitting is of less relative importance than for the $n = 48$ case. The first two excited eigenstates of the exact spectrum portray significant state mixing and the nonadiabatic bound states are more localized than the BO states. The BH states near the continuum threshold show lower-energy splitting than the $n = 48$ case, which is associated with the fact that $n = 43$ has a less prominent diagonal correction, due to its less prominent nonadiabatic coupling. Much like the previous case, the vibronic interaction does introduce the radial localization of states for $n = 43$. The fourth, fifth, and eighth excited states of the BO spectrum are all delocalized over multiple wells, in contrast to the corresponding well-localized nonadiabatic states. As a final note in our comparison, a scattering resonance state with no BO or BH counterpart is observed at an energy of approximately -1.278 GHz, well above the continuum threshold of -1.287 GHz.

It is worth noting that although the nonadiabatic couplings are highly n dependent, the behavior of the diabatic curves does not vary significantly over n. Hence the positive-energy shifts (on the order of megahertz), state localization, and existence of resonance states for the exact spectrum are all commonly observed for $30 \leqslant n \leqslant 60$. The pattern of n-dependent singularities [Fig. 3(b)] are also repeated regularly for $30 \leqslant n \leqslant 60$. However, as the energies of the PECs scale as n^{-3}, the contribution of nonadiabatic interaction effects to the complete molecular spectra becomes more important for higher-n values.

V. CONCLUSION AND OUTLOOK

We have investigated nonadiabatic and vibronic interaction effects in the sodium ultralong-range molecule, using the vibronic coupling between states of trilobite and d-state character. The oscillatory nature of the trilobite and d-state PECs, along with the specific quantum defect splitting of sodium, ensures the formation of avoided crossings for a range of n values. We observed that the avoided crossing between the adiabatic PECs introduce significant nonadiabatic couplings that can behave like a singularity for specific n, which is associated with the existence of CIs in synthetic dimensions. Irrespective of the form of the derivative couplings, the exact spectra feature pronounced differences from the BO spectra, including megahertz-scale positive-energy shifts in eigenvalues, localized probability densities, and the existence of scattering resonance states near the avoided crossings, with no adiabatic counterpart. While the Born-Huang correction does partially explain the energy shift and the state localization, it cannot account for the exact spectra and the resonance states. Hence, our results confirm that a coupled-channel approach is necessary to study the vibronic spectra of sodium ULRMs, irrespective of the corresponding principal quantum number n.

A direct extension of our present work would be to include the p-wave scattering terms as well as fine and hyperfine interactions. Inclusion of these terms, although representing a challenge, can help obtain results that are empirically comparable and be further developed to study nonadiabatic effects in spin interacting systems. Nonadiabatic interactions in such systems might give insight into spin-changing and l-changing collision dynamics.

Furthermore, the present study of ULRMs also offers the possibility for research opportunities in nonadiabatic wave-packet dynamics. Notably, the introduction of an electric field breaks the spherical symmetry of the system and facilitates the existence of conical intersections in spatial dimensions. This provides ample opportunity to probe and observe nonadiabatic dynamics near CIs, on timescales of microseconds and distances of the order of micrometers, which are accessible in present-day cold-atom laboratories. Finally, explorations of ULRMs to date have been focusing on heavier molecules formed by the species K, Rb, Cs, and Sr [35,49,53,101]. Here the ability to concoct these molecules allows for a probing of vibronic interaction effects in heavier ULRMs. In addition, corresponding experiments with (ultra)cold sodium clouds would allow one to address the presently investigated ULRMs [102,103]. Hence, we justify the utility of lighter molecules based on Na, as they feature strong nonadiabatic effects and a rich vibronic structure and promote interest in the experimental study of sodium Rydberg molecules.

ACKNOWLEDGMENTS

We acknowledge support from the Deutsche Forschungsgemeinschaft (DFG) within the priority program "Giant Interactions in Rydberg Systems" (DFG SPP 1929 GiRyd Project No. SCHM 885/30-2). R.S. is grateful to Dan Bosworth for beneficial discussions.

[1] T. F. Gallagher, *Rydberg Atoms* (Cambridge University Press, Cambridge, 1994).
[2] N. Šibalić and C. S. Adams, *Rydberg Physics* (IOP, Bristol, 2018).
[3] M. Saffman, T. G. Walker, and K. Mølmer, Rev. Mod. Phys. **82**, 2313 (2010).
[4] M. Saffman, J. Phys. B **49**, 202001 (2016).
[5] A. Browaeys and T. Lahaye, Nat. Phys. **16**, 132 (2020).
[6] D. Bluvstein, H. Levine, G. Semeghini, T. T. Wang, S. Ebadi, M. Kalinowski, A. Keesling, N. Maskara, H. Pichler, M. Greiner, V. Vuletić, and M. D. Lukin, Nature (London) **604**, 451 (2022).
[7] T. M. Graham, Y. Song, J. Scott, C. Poole, L. Phuttitarn, K. Jooya, P. Eichler, X. Jiang, A. Marra, B. Grinkemeyer, M. Kwon, M. Ebert, J. Cherek, M. T. Lichtman, M. Gillette, J. Gilbert, D. Bowman, T. Ballance, C. Campbell, E. D. Dahl *et al.*, Nature (London) **604**, 457 (2022).
[8] J. A. Sedlacek, A. Schwettmann, H. Kübler, R. Löw, T. Pfau, and J. P. Shaffer, Nat. Phys. **8**, 819 (2012).
[9] H. Fan, S. Kumar, J. Sedlacek, H. Kübler, S. Karimkashi, and J. P. Shaffer, J. Phys. B **48**, 202001 (2015).
[10] J. A. Gordon, C. L. Holloway, A. Schwarzkopf, D. A. Anderson, S. Miller, N. Thaicharoen, and G. Raithel, Appl. Phys. Lett. **105**, 024104 (2014).
[11] M. Zeppenfeld, Europhys. Lett. **118**, 13002 (2017).
[12] S. Patsch, M. Zeppenfeld, and C. P. Koch, J. Phys. Chem. Lett. **13**, 10728 (2022).
[13] J. Zou and S. D. Hogan, Phys. Rev. A **106**, 043111 (2022).
[14] O. Firstenberg, C. S. Adams, and S. Hofferberth, J. Phys. B **49**, 152003 (2016).
[15] T. Peyronel, O. Firstenberg, Q.-Y. Liang, S. Hofferberth, A. V. Gorshkov, T. Pohl, M. D. Lukin, and V. Vuletić, Nature (London) **488**, 57 (2012).
[16] O. Firstenberg, T. Peyronel, Q.-Y. Liang, A. V. Gorshkov, M. D. Lukin, and V. Vuletić, Nature (London) **502**, 71 (2013).
[17] A. Paris-Mandoki, C. Braun, J. Kumlin, C. Tresp, I. Mirgorodskiy, F. Christaller, H. P. Büchler, and S. Hofferberth, Phys. Rev. X **7**, 041010 (2017).
[18] C. H. Greene, A. S. Dickinson, and H. R. Sadeghpour, Phys. Rev. Lett. **85**, 2458 (2000).
[19] C. Boisseau, I. Simbotin, and R. Côté, Phys. Rev. Lett. **88**, 133004 (2002).
[20] S. Hollerith, J. Zeiher, J. Rui, A. Rubio-Abadal, V. Walther, T. Pohl, D. M. Stamper-Kurn, I. Bloch, and C. Gross, Science **364**, 664 (2019).
[21] K. R. Overstreet, A. Schwettmann, J. Tallant, D. Booth, and J. P. Shaffer, Nat. Phys. **5**, 581 (2009).
[22] A. Duspayev, X. Han, M. A. Viray, L. Ma, J. Zhao, and G. Raithel, Phys. Rev. Res. **3**, 023114 (2021).
[23] M. Deiß, S. Haze, and J. Hecker Denschlag, Atoms **9**, 34 (2021).
[24] D. J. Bosworth, F. Hummel, and P. Schmelcher, Phys. Rev. A **107**, 022807 (2023).
[25] A. Duspayev and G. Raithel, Phys. Rev. A **105**, 012810 (2022).
[26] N. Zuber, V. S. V. Anasuri, M. Berngruber, Y.-Q. Zou, F. Meinert, R. Löw, and T. Pfau, Nature (London) **605**, 453 (2022).
[27] Y.-Q. Zou, M. Berngruber, V. S. V. Anasuri, N. Zuber, F. Meinert, R. Löw, and T. Pfau, Phys. Rev. Lett. **130**, 023002 (2023).
[28] W. Li, T. Pohl, J. M. Rost, S. T. Rittenhouse, H. R. Sadeghpour, J. Nipper, B. Butscher, J. B. Balewski, V. Bendkowsky, R. Löw, and T. Pfau, Science **334**, 1110 (2011).
[29] D. Booth, S. T. Rittenhouse, J. Yang, H. R. Sadeghpour, and J. P. Shaffer, Science **348**, 99 (2015).
[30] M. A. Bellos, R. Carollo, J. Banerjee, E. E. Eyler, P. L. Gould, and W. C. Stwalley, Phys. Rev. Lett. **111**, 053001 (2013).
[31] N. Y. Du and C. H. Greene, Phys. Rev. A **36**, 971 (1987).
[32] E. L. Hamilton, C. H. Greene, and H. R. Sadeghpour, J. Phys. B **35**, L199 (2002).
[33] T. Niederprüm, O. Thomas, T. Eichert, C. Lippe, J. Pérez-Ríos, C. H. Greene, and H. Ott, Nat. Commun. **7**, 12820 (2016).
[34] P. Giannakeas, M. T. Eiles, F. Robicheaux, and J. M. Rost, Phys. Rev. Lett. **125**, 123401 (2020).
[35] V. Bendkowsky, B. Butscher, J. Nipper, J. P. Shaffer, R. Löw, and T. Pfau, Nature (London) **458**, 1005 (2009).

[36] J. D. Whalen, S. K. Kanungo, R. Ding, M. Wagner, R. Schmidt, H. R. Sadeghpour, S. Yoshida, J. Burgdörfer, F. B. Dunning, and T. C. Killian, Phys. Rev. A **100**, 011402(R) (2019).
[37] F. Engel, T. Dieterle, F. Hummel, C. Fey, P. Schmelcher, R. Löw, T. Pfau, and F. Meinert, Phys. Rev. Lett. **123**, 073003 (2019).
[38] R. Schmidt, H. R. Sadeghpour, and E. Demler, Phys. Rev. Lett. **116**, 105302 (2016).
[39] J. Sous, H. R. Sadeghpour, T. C. Killian, E. Demler, and R. Schmidt, Phys. Rev. Res. **2**, 023021 (2020).
[40] M. T. Eiles and C. H. Greene, Phys. Rev. A **95**, 042515 (2017).
[41] C. Fey, F. Hummel, and P. Schmelcher, Mol. Phys. **118**, e1679401 (2020).
[42] D. A. Anderson, S. A. Miller, and G. Raithel, Phys. Rev. A **90**, 062518 (2014).
[43] I. Lesanovsky, P. Schmelcher, and H. R. Sadeghpour, J. Phys. B **39**, L69 (2006).
[44] M. Kurz and P. Schmelcher, J. Phys. B **47**, 165101 (2014).
[45] F. Hummel, C. Fey, and P. Schmelcher, Phys. Rev. A **99**, 023401 (2019).
[46] F. Hummel, K. Keiler, and P. Schmelcher, Phys. Rev. A **103**, 022827 (2021).
[47] M. Kurz and P. Schmelcher, Phys. Rev. A **88**, 022501 (2013).
[48] J. P. Shaffer, S. T. Rittenhouse, and H. R. Sadeghpour, Nat. Commun. **9**, 1965 (2018).
[49] B. J. DeSalvo, J. A. Aman, F. B. Dunning, T. C. Killian, H. R. Sadeghpour, S. Yoshida, and J. Burgdörfer, Phys. Rev. A **92**, 031403(R) (2015).
[50] J. D. Whalen, S. K. Kanungo, Y. Lu, S. Yoshida, J. Burgdörfer, F. B. Dunning, and T. C. Killian, Phys. Rev. A **101**, 060701(R) (2020).
[51] T. Schmid, C. Veit, N. Zuber, R. Löw, T. Pfau, M. Tarana, and M. Tomza, Phys. Rev. Lett. **120**, 153401 (2018).
[52] T. Niederprüm, O. Thomas, T. Eichert, and H. Ott, Phys. Rev. Lett. **117**, 123002 (2016).
[53] M. Peper and J. Deiglmayr, Phys. Rev. Lett. **126**, 013001 (2021).
[54] D. A. Anderson, S. A. Miller, and G. Raithel, Phys. Rev. Lett. **112**, 163201 (2014).
[55] K. S. Kleinbach, F. Meinert, F. Engel, W. J. Kwon, R. Löw, T. Pfau, and G. Raithel, Phys. Rev. Lett. **118**, 223001 (2017).
[56] M. Schlagmüller, T. C. Liebisch, F. Engel, K. S. Kleinbach, F. Böttcher, U. Hermann, K. M. Westphal, A. Gaj, R. Löw, S. Hofferberth, T. Pfau, J. Pérez-Ríos, and C. H. Greene, Phys. Rev. X **6**, 031020 (2016).
[57] F. Böttcher, A. Gaj, K. M. Westphal, M. Schlagmüller, K. S. Kleinbach, R. Löw, T. C. Liebisch, T. Pfau, and S. Hofferberth, Phys. Rev. A **93**, 032512 (2016).
[58] F. Camargo, J. D. Whalen, R. Ding, H. R. Sadeghpour, S. Yoshida, J. Burgdörfer, F. B. Dunning, and T. C. Killian, Phys. Rev. A **93**, 022702 (2016).
[59] B. Butscher, V. Bendkowsky, J. Nipper, J. B. Balewski, L. Kukota, R. Löw, T. Pfau, W. Li, T. Pohl, and J. M. Rost, J. Phys. B **44**, 184004 (2011).
[60] M. Born and R. Oppenheimer, Ann. Phys. (Leipzig) **389**, 457 (1927).
[61] A. Duspayev, A. Shah, and G. Raithel, New J. Phys. **24**, 053043 (2022).
[62] H. Köuppel, W. Domcke, and L. S. Cederbaum, in *Advances in Chemical Physics*, edited by I. Prigogine and S. A. Rice, (Wiley, New York, 1984), Vol. 57, pp. 59–246.
[63] F. Agostini and B. F. E. Curchod, Wiley Interdiscip. Rev. Comput. Mol. Sci. **9**, e1417 (2019).
[64] M. Baer, *Beyond Born-Oppenheimer: Electronic Nonadiabatic Coupling Terms and Conical Intersections* (Wiley, New York, 2006).
[65] D. R. Yarkony, Rev. Mod. Phys. **68**, 985 (1996).
[66] S. Matsika and P. Krause, Annu. Rev. Phys. Chem. **62**, 621 (2011).
[67] F. Hummel, M. T. Eiles, and P. Schmelcher, Phys. Rev. Lett. **127**, 023003 (2021).
[68] C. Arnold, O. Vendrell, R. Welsch, and R. Santra, Phys. Rev. Lett. **120**, 123001 (2018).
[69] N. Mabrouk, W. Zrafi, and H. Berriche, Mol. Phys. **118**, e1605098 (2020).
[70] T. J. Martinez, Nature (London) **467**, 412 (2010).
[71] H. Köppel, W. Domcke, and L. S. Cederbaum, *Stochasticity and Intramolecular Redistribution of Energy* (Springer Netherlands, Dordrecht, 1987), pp. 217–231.
[72] H. A. Jahn, E. Teller, and F. G. Donnan, Proc. R. Soc. A **161**, 220 (1937).
[73] H. C. Longuet-Higgins, U. Öpik, M. H. L. Pryce, and R. A. Sack, Proc. R. Soc. A **244**, 1 (1958).
[74] M. F. Herman, J. Chem. Phys. **81**, 754 (1984).
[75] M. Barbatti, Wiley Interdiscip. Rev. Comput. Mol. Sci. **1**, 620 (2011).
[76] M. Barbatti, A. J. A. Aquino, J. J. Szymczak, D. Nachtigallová, P. Hobza, and H. Lischka, Proc. Natl. Acad. Sci. USA **107**, 21453 (2010).
[77] H. Kang, K. T. Lee, B. Jung, Y. J. Ko, and S. K. Kim, J. Am. Chem. Soc. **124**, 12958 (2002).
[78] B. G. Levine and T. J. Martínez, Annu. Rev. Phys. Chem. **58**, 613 (2007).
[79] D. Polli, P. Altoè, O. Weingart, K. M. Spillane, C. Manzoni, D. Brida, G. Tomasello, G. Orlandi, P. Kukura, R. A. Mathies, M. Garavelli, and G. Cerullo, Nature (London) **467**, 440 (2010).
[80] L. Hammarström and S. Styring, Philos. Trans. R. Soc. B **363**, 1283 (2008).
[81] S. Hollerith, J. Rui, A. Rubio-Abadal, K. Srakaew, D. Wei, J. Zeiher, C. Gross, and I. Bloch, Phys. Rev. Res. **3**, 013252 (2021).
[82] F. Hummel, P. Schmelcher, and M. T. Eiles, Phys. Rev. Res. **5**, 013114 (2023).
[83] M. Born and K. Huang, *Dynamical Theory of Crystal Lattices* (Oxford University Press, Oxford, 1954).
[84] U. Manthe and H. Köppel, J. Chem. Phys. **93**, 345 (1990).
[85] W. Domcke, D. R. Yarkony, and H. Köppel, *Conical Intersections* (World Scientific, Singapore, 2004).
[86] T. Pacher, L. S. Cederbaum, and H. Köppel, J. Chem. Phys. **89**, 7367 (1988).
[87] E. Fermi, Nuovo Cim. **11**, 157 (1934).
[88] A. Omont, J. Phys. (Paris) **38**, 1343 (1977).
[89] M. T. Eiles, Phys. Rev. A **98**, 042706 (2018).
[90] E. Karule, Phys. Lett. **15**, 137 (1965).

[91] W. F. Holmgren, M. C. Revelle, V. P. A. Lonij, and A. D. Cronin, Phys. Rev. A **81**, 053607 (2010).
[92] J. Mitroy, M. S. Safronova, and C. W. Clark, J. Phys. B **43**, 202001 (2010).
[93] C. R. Ekstrom, J. Schmiedmayer, M. S. Chapman, T. D. Hammond, and D. E. Pritchard, Phys. Rev. A **51**, 3883 (1995).
[94] C. J. Lorenzen and K. Niemax, Phys. Scr. **27**, 300 (1983).
[95] G. A. Worth and L. S. Cederbaum, Annu. Rev. Phys. Chem. **55**, 127 (2004).
[96] Z. Top and M. Baer, Chem. Phys. **10**, 95 (1975).
[97] G. C. Groenenboom and H. M. Buck, J. Chem. Phys. **92**, 4374 (1990).
[98] J. von Neumann and E. P. Wigner, *The Collected Works of Eugene Paul Wigner* (Springer, Berlin, 1993), Pt. A, pp. 291–293.
[99] M. T. Eiles, J. Phys. B **52**, 113001 (2019).
[100] J. Wang and R. Côté, Phys. Rev. Res. **2**, 023019 (2020).
[101] C. Vadla, V. Horvatic, and K. Niemax, Phys. Rev. A **80**, 052506 (2009).
[102] S. Banik, M. G. Galan, H. Sosa-Martinez, M. J. Anderson, S. Eckel, I. B. Spielman, and G. K. Campbell, Phys. Rev. Lett. **128**, 090401 (2022).
[103] T. Świsłocki, M. Gajda, M. Brewczyk, and P. Deuar, Sci. Rep. **11**, 6441 (2021).

PHYSICAL REVIEW RESEARCH **7**, 043103 (2025)

Vibrationally highly excited trilobite molecules stabilized by nonadiabatic coupling

Rohan Srikumar,[1,*] Markus Exner,[2,*] Richard Blättner,[2] Peter Schmelcher,[1,3] Matthew T. Eiles,[4] and Herwig Ott[2,†]

[1]*Zentrum für Optische Quantentechnologien, Universität Hamburg, Luruper Chaussee 149, 22761 Hamburg, Germany*

[2]*Department of Physics and Research Center OPTIMAS, Rheinland-Pfälzische Technische Universität Kaiserslautern-Landau, 67663 Kaiserslautern, Germany*

[3]*The Hamburg Centre for Ultrafast Imaging, Universität Hamburg, Luruper Chaussee 149, 22761 Hamburg, Germany*

[4]*Max Planck Institute for the Physics of Complex Systems, Nöthnitzer Straße 38, 01187 Dresden, Germany*

(Received 21 April 2025; accepted 15 September 2025; published 27 October 2025)

We report on the observation of highly excited ($\nu \sim 100$) vibrational states of a trilobite ultralong-range Rydberg molecule in ^{87}Rb. These states manifest spectroscopically in a regularly spaced series of peaks red-detuned from the $25f_{7/2}$ dissociation threshold. The existence and observed stability of these states require the almost complete suppression of the adiabatic decay pathway induced by the P-wave shape resonance of Rb. This stabilization is predicted to occur only for certain Rydberg levels where the avoided crossing between trilobite and P-wave-dominated butterfly potential energy curves nearly vanishes, allowing the vibrational states to diabatically traverse the crossing with almost unit probability. This is the first direct measurement of beyond-Born-Oppenheimer physics in long-range Rydberg molecules, and paves the way for future experiments to access and manipulate wave packets formed from high-lying vibrational states.

DOI: 10.1103/49ky-d8mm

Efforts to understand and harness ultracold molecules including Rydberg atoms among their constituents are essential to the study of impurity dynamics in ultracold gases [1–10], the design of quantum information storage systems [11], precision measurements of electron-atom interactions [12–16], and the wider study of unorthodox molecular physics and ultracold chemistry [7,17–23]. In particular, ultralong-range Rydberg molecules (ULRMs) composed of a Rydberg atom and a ground-state atom have provoked significant interest due to the possibility that the ground-state atom hybridizes the degenerate Rydberg states of high angular momentum ℓ [24–27]. The resulting molecular states, dubbed trilobites and butterflies depending on the angular momentum (S or P wave, respectively) of the Rydberg electron with respect to the ground-state atom, are highly desirable as they possess enormous dipole moments [28–30] and are more deeply bound than their nonpolar counterparts. The flexibility of the high-ℓ states to adapt to the nuclear geometry makes these states also exciting to investigate in the context of polyatomic systems, ranging from triatomic molecules to Rydberg composites with electronic behavior analogous to solid-state systems [31–38].

Exploiting ULRMs for these promising applications has been hindered by the difficulty of exciting trilobite molecules. Their high-ℓ nature implies a weak dipole coupling to intermediate states, which is overcome either by mixing these states with nonpolar low-ℓ Rydberg states, thus reducing their advantageous properties, or via a three-photon excitation scheme. These approaches have led to the successful observation of low-lying vibrational trilobite states [29,30,39,40]. However, a significant impediment to the creation of vibrationally excited trilobite states is the existence of scattering resonances in the P-wave channel. These introduce avoided crossings between the trilobite potential energy curve (PEC), which possesses a global minima, and the butterfly PEC, which is in this energy range steeply attractive without any stable minima [41,42]. In turn, the inner repulsive wall of the trilobite PECs is destroyed, suppressing higher vibrational excitations (within the framework of the Born-Oppenheimer approximation [43]). Although theoretical calculations have demonstrated the ability of nonadiabatic coupling to modify the binding energies and stability of these states to some extent [44–46], no unambiguous experimental confirmation yet exists for any beyond Born-Oppenheimer effects in ULRM vibrational states.

In this article, we report the experimental detection of highly excited vibrational states of a ^{87}Rb trilobite molecule, which are red-detuned from the $25f_{7/2}$ dissociation threshold. By comparison with the calculated spectrum, we assign vibrational quantum numbers $\nu \gtrsim 80$ to these levels. This assignment only succeeds by treating the trilobite PEC alone, totally neglecting the butterfly interaction. This assumption, consistent with an effective single-channel description that considers an exact diabatic crossing between the trilobite butterfly PEC, is motivated by a recent theoretical model developed to understand the behavior of avoided level

*These authors contributed equally to this work.
†Contact author: ott@physik.uni-kl.de

Published by the American Physical Society under the terms of the Creative Commons Attribution 4.0 International license. Further distribution of this work must maintain attribution to the author(s) and the published article's title, journal citation, and DOI.

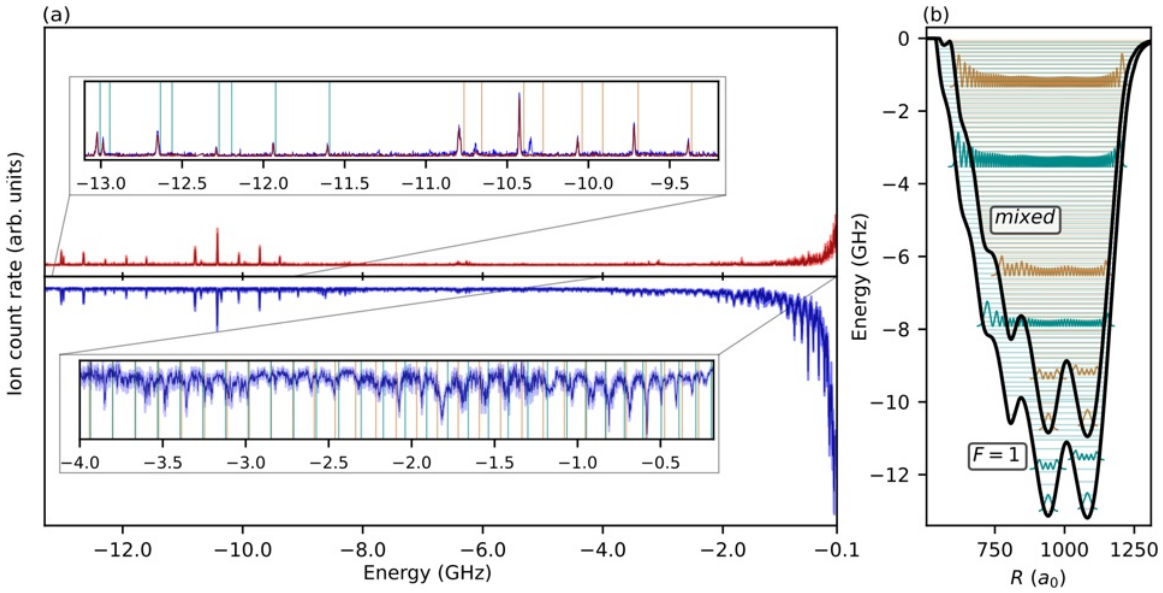


FIG. 1. (a) Ion signal as a function of the detuning from the ^{87}Rb $25f_{7/2}$ atomic state. The red line is the zero momentum signal, whereas the blue line is the full momentum signal. The light-blue (light-red) colored region around the finite (zero) momentum spectra indicates the ion count rate error. The upper inset shows a magnification of the energy range containing the deeply bound trilobite states with the theoretical spectrum overlaid as a stick plot. The lower inset shows a magnification of the spectrum of highly excited vibrational states. The peak heights are scaled linearly in energy to improve visibility. The colored lines mark the positions of the theoretical levels, bound in the two diabatic trilobite PECs shown in panel (b). In panel (b), selected vibrational wave functions are also plotted.

crossings in ULRM [47]. Furthermore, this model predicts that the $n = 27$ PECs behave fully adiabatically, which we confirm experimentally by performing spectroscopy below the $27f_{7/2}$ threshold and finding no signatures of high-lying vibrational states. Our findings, therefore, provide the first direct experimental evidence for strong nonadiabatic coupling in ultralong-range Rydberg molecules.

Figure 1(a) shows the complete vibrational spectrum of a long-range trilobite Rydberg molecule over an energy range stretching from the $25f_{7/2}$ atomic Rydberg line at zero detuning to the bottom of the trilobite potential energy curve at approximately -13 GHz [39]. This spectrum was obtained from an atomic sample of ^{87}Rb atoms at 40 μK and with a peak density of $4e13\,\mathrm{cm}^{-3}$. The atoms are prepared in the $F = 1$ hyperfine ground state in a crossed dipole trap at $\lambda = 1064$ nm. We excite Rydberg nf states through a three-photon excitation scheme at wavelengths of 780, 776, and 1276–1288 nm. Subsequently, we photoionize any Rydberg atoms produced and detect the Rb^+ ions in a reaction microscope. This allows us to spectroscopically distinguish long-lived molecules having zero momentum prior to ionization (red signal) from short-lived states whose decay imparted some finite momentum (blue signal) [48].

The spectral peaks with binding energies deeper than -9 GHz, which have already been reported in Ref. [39], are the signatures of polar trilobite molecules with vibrational states bound in local minima in the deep trilobite potential. We have assigned vibrational quantum numbers up to $v = 5$ in the various potential wells to these peaks [39]. Higher in energy, the signal strength declines rapidly, essentially vanishing from -8 to -4 GHz. The signal resumes from -4 GHz, growing rapidly in strength until the atomic resonance. It is primarily detected in the full momentum spectra, indicating that these states are more short-lived than the deeply bound states. This series is highlighted in the bottom inset, where the peak heights are scaled linearly with energy for easier visualization. Upwards of 30 peaks with a consistent spacing of ∼120 MHz are observed.

The spectroscopic assignment of these peaks is accomplished by comparison of this spectrum with that obtained from theoretical calculations. As in Ref. [39], we have used an approach based on the Coulomb Green's function and incorporating the fine and hyperfine structure of both Rb atoms and all spin-dependent e-Rb scattering channels to compute the PECs [49]. The adiabatic potential energy curves from this calculation are not repulsive at short range; they instead drop steeply due to the effect of the P-wave interaction. Such a potential can still support excited internal reflection states, reflected off of the steep drop [50], but the predicted level spacing (∼230 MHz) and resonance widths (∼260 MHz) are wholly incompatible with the measured spectrum. These internal reflection states, as well as bound vibrational states were calculated using Siegert pseudostates expanded into a basis of B splines [46].

However, the vibrational spectrum of the effectively diabatic trilobite potentials shown in Fig. 1(b) is in very good agreement with the observed series [see the stick spectrum overlaid in the inset of panel (a)]. Here, we emphasize that such a PEC was obtained by considering the crossing between the trilobite and butterfly PECs to be exact. The term "diabatic" as we use it, is limited to the behavior of the avoided crossing and should not be associated with the strict

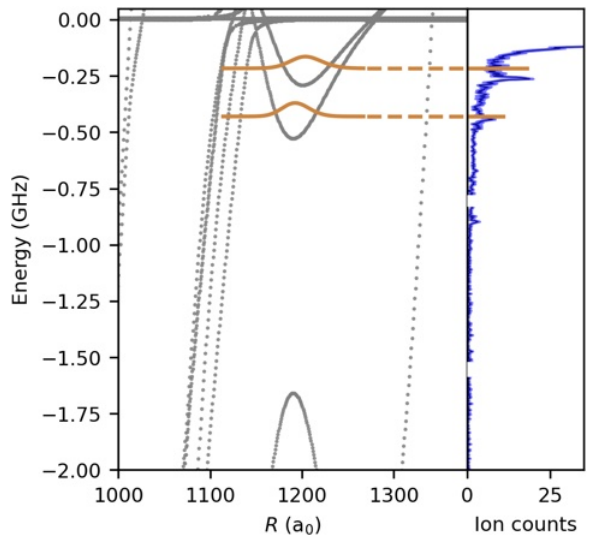


FIG. 2. The molecular spectra and associated potential energy curves near the $27f_{7/2}$ dissociation threshold. The potential energy curves (gray) possess shallow wells that support localized vibrational states (dark orange) in good agreement with the experiment (blue spectrum). The two vibrational states calculated are shown in the orange stick spectrum, with their heights scaled by their respective Franck-Condon factors.

diabatization procedure that necessitates all derivative couplings to be zero (in one-dimensional systems) [44–46]. From this calculation, we identify these peaks as the photoassociation signal of highly excited vibrational states with v in excess of 80.

Remarkably, the opposite is true for $n = 27$, as shown in Fig. 2. The long series of almost equidistant molecular resonances observed for $n = 25$ is completely absent from the experimental spectra for $n = 27$. Only two vibrational peaks are detected. The adiabatic PECs support two quasibound molecular resonances in this same energy range, and their binding energies and line strengths are in good agreement with those observed.

Reference [47] presented a spin-independent model of the trilobite and butterfly molecular system, which predicts this observed behavior. In this model, dynamics in the molecular system follows the two adiabatic potential energy surfaces

$$V_{\pm}(R,n) = \frac{U_{+}(R,n)}{2} \pm \frac{\Delta(R,n)}{2} \tag{1}$$

in the synthetic coordinate space spanned by the internuclear distance R and the principal quantum number n, taken to be a continuous variable. Here, $U_{\pm}(R,n) = U_S(R,n) \pm U_P(R,n)$ are superpositions of the pure S-wave- and pure P-wave-dominated PECs [51], and

$$\Delta(R,n) = \Bigg[[U_{-}(R,n)]^2 + \sqrt{\frac{12\pi \tan\delta_S(k)\tan\delta_P(k)}{k^4}} \left(\frac{u_{n0}(R)}{4\pi R}\right)^4 \Bigg]^{1/2} \tag{2}$$

is the energy gap between adiabatic potential energy surfaces. The energy-dependent scattering phase shifts are $\delta_S(k)$ and $\delta_P(k)$, and $u_{n0}(R)$ is the reduced s-state radial wave function, taken to be the regular Whittaker solution so that it remains valid for arbitrary nonintegral n.

A useful characteristic for the degree of adiabaticity is the Landau-Zener probability for a nonadiabatic transition,

$$P_{\mathrm{LZ}} = \exp(-2\pi\Delta^2/4vs), \tag{3}$$

where $s = |d\Delta/dR|$ is the differential slope at the crossing and $v = \sqrt{2\mu E - \mu(V_+ + V_-)}$ is the semiclassical velocity of the vibrational state. Generally speaking, a purely diabatic treatment requires $P_{\mathrm{LZ}} \to 1$, which is implied by the limit $\Delta \to 0$. We therefore seek the conditions that enable the gap to close. Both terms in Eq. (2) are non-negative, so the gap closes only when both terms simultaneously vanish. As shown in Ref. [47], an application of the spatially generalized Kato's theorem [52,53] leads to the system of equations

$$u_{n0}(R) = 0 \quad \text{and} \quad R = \frac{2n^2}{1 + (k_{SP}n)^2}, \tag{4}$$

where $k_{SP}^2/2 \approx 9\,\mathrm{meV}$ is the energy where the S and spin-orbit-averaged P-wave scattering phase shifts are identical [54].

Figure 3 shows a contour plot of $\Delta(R,n)$ scaled by n^2R for ease of visualization. The marked points indicate where Eq. (4) is satisfied. A Rydberg state whose integer-valued principal quantum number lies close to one of these points will exhibit a strong degree of diabaticity. The horizontal lines show that $n = 25$, along with several higher n values, it comes very close to satisfying these conditions, while $n = 27$ certainly does not. In Figs. 3(b) and 3(c), we compare the adiabatic PECs in this model [Eq. (1), dashed blue lines] with those obtained in the full spin-dependent approach (solid gray) for $n = 25$ and $n = 27$, respectively. These are in excellent agreement regarding both the size of the avoided crossing and the overall depth and structure of the potential curves, confirming the accuracy of this two-level treatment.

Figure 3 shows the calculated P_{LZ} (blue) and lifetimes (red) as a function of energy for $n = 25$ [(Fig. 3(d)] and $n = 27$ [(Fig. 3(e)]. As expected, the former case is extremely diabatic with $P_{\mathrm{LZ}} \sim 1$ almost independent of the velocity. We approximate the lifetime of a molecular state with binding energy E as $\tau(E) = T/(1 - P_{LZ})$, where T is the oscillation period of the vibrational state [55]. For $n = 25$, these are on the order of a few microseconds, comparable with the radiative lifetime. As this approach includes the effect of only a single crossing out of the many seen in Fig. 3, this estimate should be taken as an upper bound on the lifetime [56]. For $n = 27$, the hopping probability is strongly energy-dependent, as now Δ is large enough that the contribution of v in the exponential is important. It does not exceed 60% even for the highest-lying states. The calculated lifetimes are correspondingly short, on the order of a few tens of nanoseconds.

Hence, the n-dependent existence of high-lying vibrational states is directly explained using the n-dependent behavior of the avoided crossing. If this crossing is diabatic, the nonadiabatic effect is the stabilization of highly excited states (no decay). Instead, if the adiabatic PECs display a wide avoid

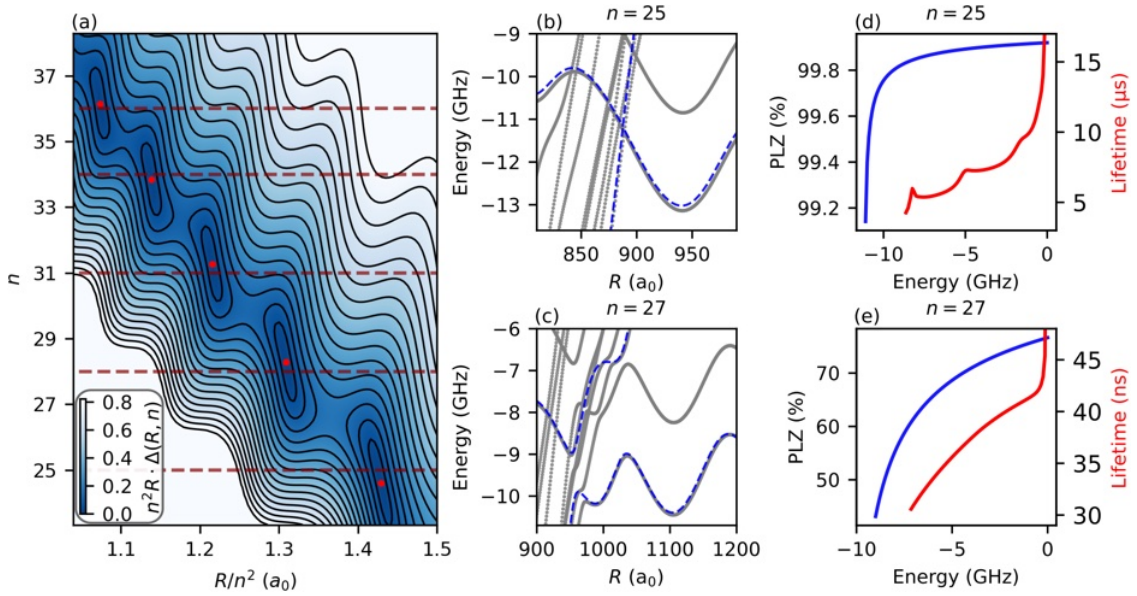


FIG. 3. (a) A contour plot of $n^2R \cdot \Delta(R, n)$ shows the existence of regular intersections in the potential energy surfaces $V_{\pm}(R, n)$. At the dark-blue regions, $\Delta(R, n) \sim 0$, and it exactly vanishes at the marked points where Eq. (4) is satisfied. The horizontal lines highlight n levels that should display a high degree of diabaticity. (a) The adiabatic potential curves calculated via the spin-dependent Green's function method (gray solid line) and the effective two-level model (dashed blue line) are shown for (b) $n = 25$ and (c) $n = 27$. As predicted, the potentials look much more diabatic in the $n = 25$ case, where the avoided crossings nearly vanish. The Landau-Zener crossing probability P_{LZ} (red) between the two adiabatic states, and the associated Landau-Zener lifetimes (blue) are shown for (d) $n = 25$ and (e) $n = 27$.

crossing, the molecule decays adiabatically via the P-wave decay channel (butterfly state) and is subject to complex short-range physics (which includes autoionization to Rb_2^+), as well as l-changing collisions to other quantum defect states [7]. The Landau-Zener treatment can also be understood using the derivative couplings between the electronic states, which are nearly singular for $n = 25$ compared to those for $n = 27$. While a full multichannel quantum calculation would provide a more accurate vibronic spectrum, we are in a regime where spin couplings, contributions from higher scattering partial waves, and uncertainties in the scattering phase shifts all will have a larger effect on the spectrum than deviation from the semiclassical approach used here, which already yields sufficient qualitative insight and a straightforward description of the observed spectra.

Finally, we investigate the observed decline of the signal strength as a function of detuning. Such a decline cannot be based on a change in Landau-Zener probability between states, due to its insensitivity to the semiclassical velocity. We compute the dipole transition element $f_\nu = \int \psi_\nu d(R) \psi_i dR$ of each vibrational state ψ_ν. Here, ψ_i is the initial scattering state of the two atoms and $d(R)$ is the R-dependent electronic dipole transition element. This quantity, proportional to the f-state admixture in the electronic wave function, is shown in the inset of Fig. 4. Both $d(R)$ and the vibrational states are calculated within a model containing only the trilobite potential curve and the f-state PEC. We note that the Franck-Condon principle, strictly taken to just be the overlap of vibrational wave functions, fails to explain the behavior of the experimental signal.

Figure 4 shows the energy dependence of the f_ν (green curve) by connecting its discrete points across the vibrational spectrum. Its behavior is in qualitative agreement with the

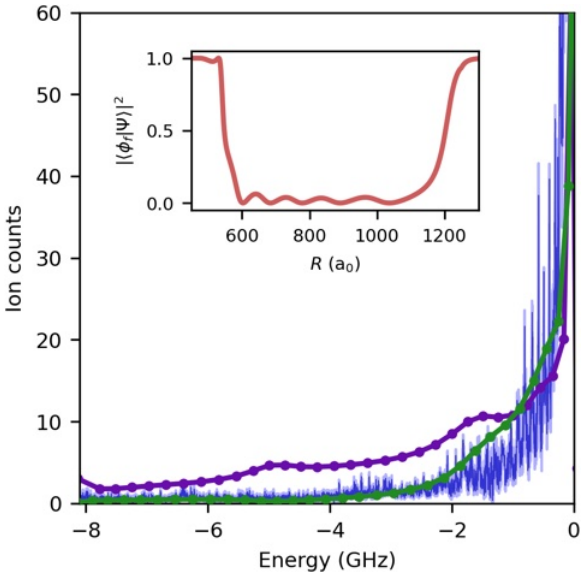


FIG. 4. Energy-dependent Franck-Condon factor calculated neglecting (purple) and including (green) the f-state admixture $|\langle \phi_f | \Psi(R) \rangle|^2$ [proportional to $d(R)$] shown in the inset. Both curves are scaled so that their values are equal at $E = 0$.

peak heights obtained experimentally. The comparison between this curve and the curve plotted in purple, which does not include the transition dipole element $d(R)$, illustrates how the energy dependence of the f_ν is strongly modified by the rapid increase in f-state admixture on the edges of the trilobite well ($R > 1200$ and $R < 600$). As ν increases, the vibrational states extend into these regions of R and therefore couple much more strongly to the initial state.

In conclusion, we have reported the first observation of high-lying vibrational states (up to $\nu = 100$) of trilobite molecules associated with the $n = 25$ Rydberg state. Such states are protected from internal molecular decay since the set of trilobite and butterfly PECs is almost perfectly diabatic for this n. This is not the case in $n = 27$, and such states are subsequently not observed experimentally, confirming the prediction of strongly n-dependent beyond Born-Oppenheimer effect in Ref. [47]. The measured peak positions and line strengths are in excellent agreement with theory, further confirming their assignment to highly excited vibrational states.

Our work reports the first clear evidence of the breakdown of Born-Oppenheimer approximation in the bound states of ULRMs. A further experimental exploration of the other n levels that we have predicted will also behave highly diabatically would provide additional confirmation of the employed theory. These results pave the way toward wave packet creation in the trilobite potential wells [57], manipulation of the avoided crossing and dynamics around it with external fields [58], and further study of nonadiabatic effects in the spectra and dynamics of these molecules.

ACKNOWLEDGMENTS

We would like to thank Max Althön for helpful discussions. This project was funded by the German Science Foundation DFG, Projects No. 460443971 and No. 316211972.

DATA AVAILABILITY

The data that support the findings of this article are not publicly available. The data are available from the authors upon reasonable request.

APPENDIX

1. Experimental methodology

After photoassociation of the molecules in a reaction microscope, we ionize them with a CO_2 laser. The resulting ions are directed via an electric field in Wiley-McLaren configuration to a time- and spatially resolved multichannel plate detector. This allows us to measure the momentum directly before ionization, and hence spectroscopically distinguish the molecules based on their lifetime with respect to internal molecular decay via state-changing collisions. These collisions impart larger momenta to the molecular states, and hence a distinction is made between the signal of stable molecules detected at zero momentum (red) and that of shorter-lived molecules detected with finite momentum (blue) in the spectrum shown in Fig. 1. The finite momentum spectrum contains the zero momentum signal, which implies that a resonance peak uniquely detected in the finite momentum signal, and absent in the zero momentum signal, corresponds to a short-lived molecular resonance (compared to the excitation pulse duration of 3 μs).

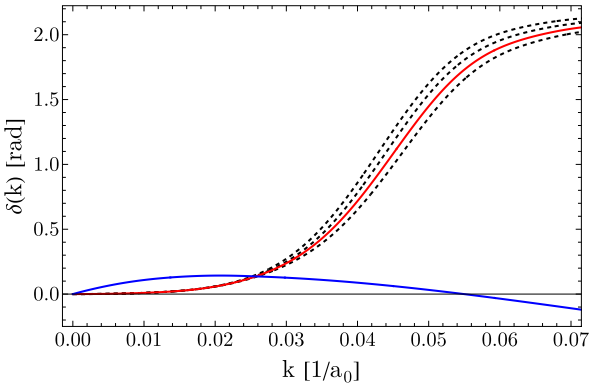


FIG. 5. Phase shifts used in this paper. The $^3S_1$ phase shift (blue) intersects the spin-orbit -averaged ^3P phase shift (red, with dashed black showing the ^3P_J phases) at $k_{SP} = 0.0257$.

2. Two-level model

In this section, we provide additional context and calculations for the diabaticity conditions and modeling used in the main text. We begin with Fig. 5, which shows the $^3S_1$ (blue) and ^3P_J (dashed black) electron-Rb scattering phase shifts across the range of electron momenta relevant here. To keep the diabaticity condition simplest, we consider the ^3P phase shift (red), which is the spin-orbit-averaged result. The S- and P-wave phase shifts are identical at one k value in this energy range, $k_{SP} = 0.0257$.

Next, we compute the trilobite and butterfly potential energy curves for the Rb_2 long-range Rydberg molecule, setting the f-state quantum defect to zero for simplicity and ignoring coupling to the much deeper quantum defect states with $\ell \leqslant 2$. As shown in Refs. [26,47], these potential energy curves are obtained as the eigenvalues of the matrix

$$V = \begin{pmatrix} U_S & C \\ C & U_P \end{pmatrix}, \tag{A1}$$

where $U_S = 2\pi a_S(k) \sum |\phi_{nl0}(R)|^2$ is the "trilobite" potential energy curve and $U_P = 6\pi a_P^3(k) \sum |\frac{d\phi_{nl0}(R)}{dR}|^2$ is the "butterfly" potential energy curve, and $C = \sqrt{12\pi^2 a_s(k) a_p^3(k)} \sum \phi_{nl0}(R) \frac{d}{dR}\phi_{nl0}(R)$ is a coupling element between trilobite and butterfly states. The sums range over all degenerate l levels $3 \leqslant l \leqslant n-1$ and $a_S(k)$, and $a_P^3(k)$ are the S-wave scattering length $-\tan\delta_S(k)/k$ and P-wave scattering volume $-\tan\delta_P(k)/k^3$, respectively. U_S and U_P are separately obtained by diagonalizing the S- and P-wave pseudopotentials,

$$\hat{V}_S = 2\pi a_S(k)\delta^3(\vec{r} - \vec{R}), \tag{A2}$$

$$\hat{V}_P = 6\pi a_P^3(k)\nabla\delta^3(\vec{r} - \vec{R})\nabla, \tag{A3}$$

separately within the degenerate manifold of a single Rydberg n level.

The potential energy surfaces are then given by Eq. (1) in the main text. Equation (2) is derived by evaluating the sums in U_S, U_P, and C in closed form to obtain

$$U_S(R) = \frac{2\pi a_S(k)}{4\pi}[k^2u^2 + u'^2], \tag{A4}$$

$$U_P(R) = 6\pi a_P^3(k)\left(\frac{k^2}{3}\frac{U_S(R)}{2\pi a_S(k)} - \frac{2uu' - u^2/R}{6\pi R^2}\right), \tag{A5}$$

$$C = -\frac{\sqrt{12a_S(k)a_P^3(k)}\pi u^2}{4\pi R^2}. \tag{A6}$$

In these expressions, $u \equiv u_{n0}(R)$ is a short-hand for the reduced radial s-wave Rydberg wave function, and u' is its derivative with respect to R. To evaluate these summations, it is necessary to extend the sum over ℓ to include terms with $0 \leqslant \ell \leqslant 2$. As these terms have only a very small contribution to the total sum, this approximation (equivalent to neglecting the effect of quantum defects) does not affect the accuracy of our conclusions. We now can see the diabaticity requirement (defined as a real or extremely narrow avoided crossing between these potential curves) directly from the Hamiltonian matrix of Eq. (A1). If $C = 0$ simultaneously as $U_S = U_P$, the potential curves will cross. The first condition, from Eq. (A6), holds at any node of the function $u_{n0}(R)$. The second condition can be obtained semiclassically from the Borodin and Kazansky expressions [59], re-derived through a "dressed-ion" picture in Ref. [60],

$$U_S(R) \approx -\frac{1}{2(n - \delta_S(k)/\pi)^2}, \tag{A7}$$

$$U_P(R) \approx -\frac{1}{2(n - \delta_P(k)/\pi)^2}, \tag{A8}$$

and is evidently $\delta_S(k) = \delta_P(k)$. This same condition can be obtained by inserting $u = 0$ into Eqs. (A4) and (A5) and solving for $U_T = U_B$. For the given set of phase shifts [39], the n values that satisfy the aforegiven diabaticity condition will exhibit conical intersections in the (R, n) manifold where $\Delta(R, n) = (V_+ - V_-)(R, n) \to 0$, as seen in Fig. 3.

3. Landau-Zener decay rates and lifetimes

In the main text, we characterize the diabatic effects at the trilobite-butterfly crossing by calculating the Landau-Zener transition probability P_{LZ}, which gives us the probability of nonadiabatic transition between the two adiabatic curves at an avoided crossing. Given that P_{LZ} is the probability that the nuclear wave packet stays in the diabatic trilobite, $P_d = 1 - P_{\mathrm{LZ}}$ is the probability that the nuclei decay down the adiabatic passage each time the wave packet encounters the avoided crossing.

The number of crossing attempts made before time t can be approximated as $n = t/T$, where T is the period of oscillation (given by the inverse of vibrational energy spacing), for $t \gg T$. Hence, the probability that the nuclei remain in the trilobite after $t = nT$ has passed is

$$P(t) = (P_{LZ})^n = (1 - P_d)^{t/T}.$$

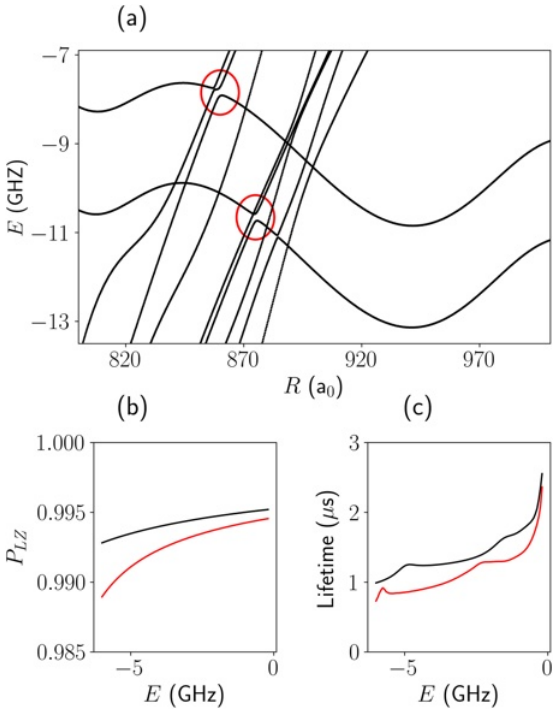


FIG. 6. (a) The adiabatic potential energy curves calculated utilizing the spin-dependent Green's function method (black). The avoided crossings that contribute to molecular decay are highlighted (red). The Landau-Zener crossing probability (b) and the associated lifetimes (c) are calculated and shown separately for the triplet PECs (black) and the mixed PECs (red).

Writing P_d as $1/x$, we get

$$P(t) = (1 - 1/x)^{xt/xT} = ((1 - 1/x)^x)^{(t/Tx)}.$$

In the limit $x \to \infty$, consistent with $P_d \to 0$ (or $P_{LZ} \to 1$), we have then

$$P(t) = e^{-t/Tx} = e^{-t(1-P_{LZ})/T}.$$

Hence, for long time scales ($t \gg T$) and high diabaticity ($P_{LZ} \to 1$), the population of the trilobite state decays exponentially with the rate

$$\Gamma = (1 - P_{LZ})/T,$$

giving us the molecular lifetime

$$\tau = \Gamma^{-1} = T/(1 - P_{LZ}).$$

4. Landau-Zener calculations for the spin-dependent Green's function model

The two-level model used to successfully explain the observed stabilization mechanism neglects the full spin-dependent structure of the ULRM [39,49,61]. The state-of-the-art Green's function model incorporates within its calculations the fine structure of the Rydberg atom, the hyperfine structure of the ground state and the six different electron-atom scattering channels ($^1S_0, ^3S_1, ^1P_1, ^3P_{0,1,2}$) shown in

Fig. 5. Figure 6(a) shows the Born-Oppenheimer potential energy curves of the $n = 25$ ULRM in the energy regime relevant to the avoided crossings. The ^3P_J-shape resonances introduce multiple crossings between the butterfly and trilobite curves, most of which are near exact and does not contribute to an adiabatic decay pathway. However, we do identify one non-negligible avoided crossing between the triplet (mixed) trilobite PEC and the plummeting butterfly curves that presents an adiabatic decay pathway for the molecule in a trilobite state. Figures 6(b) and 6(c) show the probability of nonadiabatic transition and the associated lifetimes calculated separately for the triplet and mixed trilobite state. We see that both the transition probability and the lifetimes are slightly shorter than those computed in the spinless model. The difference can be attributed to the sensitivity of the diabaticity condition to changes in the ^3P_J phase shifts. The spinless model utilizes a spin-orbit-averaged ^3P phase shift (see Fig. 5), whose crossing position with the $^3S_1$ phase shift does not precisely mimic that of $^3P_{0,1,2}$. However, the underlying nonadiabatic physics remains the same with/without the added spin structure. The Landau-Zener crossing probability is still $\gtrsim$0.987 and the associated lifetimes $\sim\mu$s, vastly different from the adiabatic regime exhibited by $n = 27$. Hence, the single-channel diabatic approximation for $n = 25$ retains its validity whether or not the spin structure is included.

[1] R. Schmidt, H. R. Sadeghpour, and E. Demler, Mesoscopic Rydberg impurity in an atomic quantum gas, Phys. Rev. Lett. **116**, 105302 (2016).

[2] J. Sous, H. R. Sadeghpour, T. C. Killian, E. Demler, and R. Schmidt, Rydberg impurity in a Fermi gas: Quantum statistics and rotational blockade, Phys. Rev. Res. **2**, 023021 (2020).

[3] S. Tiwari, F. Engel, M. Wagner, R. Schmidt, F. Meinert, and S. Wüster, Dynamics of atoms within atoms, New J. Phys. **24**, 073005 (2022).

[4] F. Camargo, R. Schmidt, J. D. Whalen, R. Ding, G. Woehl, S. Yoshida, J. Burgdörfer, F. B. Dunning, H. R. Sadeghpour, E. Demler, and T. C. Killian, Creation of Rydberg polarons in a Bose gas, Phys. Rev. Lett. **120**, 083401 (2018).

[5] A. A. T. Durst and M. T. Eiles, Phenomenology of a Rydberg impurity in an ideal Bose-Einstein condensate, Phys. Rev. Res. **6**, L042009 (2024).

[6] F. Engel, S. K. Tiwari, T. Pfau, S. Wüster, and F. Meinert, *In situ* observation of chemistry in Rydberg molecules within a Bose-Einstein-condensate, Phys. Rev. Res. **6**, 033150 (2024).

[7] M. Schlagmüller, T. C. Liebisch, F. Engel, K. S. Kleinbach, F. Böttcher, U. Hermann, K. M. Westphal, A. Gaj, R. Löw, S. Hofferberth, T. Pfau, J. Pérez-Ríos, and C. H. Greene, Ultracold chemical reactions of a single Rydberg atom in a dense gas, Phys. Rev. X **6**, 031020 (2016).

[8] R. Heidemann, U. Krohn, V. Bendkowsky, B. Butscher, R. Löw, and T. Pfau, Rydberg excitation of Bose-Einstein condensates, Phys. Rev. Lett. **100**, 033601 (2008).

[9] K. S. Kleinbach, F. Engel, T. Dieterle, R. Löw, T. Pfau, and F. Meinert, Ionic impurity in a Bose-Einstein condensate at submicrokelvin temperatures, Phys. Rev. Lett. **120**, 193401 (2018).

[10] M. Berngruber, D. J. Bosworth, O. A. Herrera-Sancho, V. S. Anasuri, N. Zuber, F. Hummel, J. Krauter, F. Meinert, R. Löw, P. Schmelcher *et al.*, *In situ* observation of nonpolar to strongly polar atom-ion collision dynamics, Phys. Rev. Lett. **133**, 083001 (2024).

[11] I. Mirgorodskiy, F. Christaller, C. Braun, A. Paris-Mandoki, C. Tresp, and S. Hofferberth, Electromagnetically induced transparency of ultra-long-range Rydberg molecules, Phys. Rev. A **96**, 011402 (2017).

[12] H. Saßmannshausen, F. Merkt, and J. Deiglmayr, Experimental characterization of singlet scattering channels in long-range Rydberg molecules, Phys. Rev. Lett. **114**, 133201 (2015).

[13] F. Engel, T. Dieterle, F. Hummel, C. Fey, P. Schmelcher, R. Löw, T. Pfau, and F. Meinert, Precision spectroscopy of negative-ion resonances in ultralong-range Rydberg molecules, Phys. Rev. Lett. **123**, 073003 (2019).

[14] P. Giannakeas, M. T. Eiles, F. Robicheaux, and J. M. Rost, Generalized local frame-transformation theory for ultralong-range Rydberg molecules, Phys. Rev. A **102**, 033315 (2020).

[15] J. L. MacLennan, Y.-J. Chen, and G. Raithel, Deeply bound $(24D_J + 5S_{1/2})$ ^{87}Rb and ^{85}Rb molecules for eight spin couplings, Phys. Rev. A **99**, 033407 (2019).

[16] M. Peper and J. Deiglmayr, Heteronuclear long-range Rydberg molecules, Phys. Rev. Lett. **126**, 013001 (2021).

[17] M. Deiß, S. Haze, J. Wolf, L. Wang, F. Meinert, C. Fey, F. Hummel, P. Schmelcher, and J. Hecker Denschlag, Observation of spin-orbit-dependent electron scattering using long-range Rydberg molecules, Phys. Rev. Res. **2**, 013047 (2020).

[18] P. Geppert, M. Althön, D. Fichtner, and H. Ott, Diffusive-like redistribution in state-changing collisions between Rydberg atoms and ground state atoms, Nat. Commun. **12**, 3900 (2021).

[19] A. Duspayev, X. Han, M. A. Viray, L. Ma, J. Zhao, and G. Raithel, Long-range Rydberg-atom–ion molecules of Rb and Cs, Phys. Rev. Res. **3**, 023114 (2021).

[20] M. Deiß, S. Haze, and J. Hecker Denschlag, Long-range atom–ion Rydberg molecule: A novel molecular binding mechanism, Atoms **9**, 34 (2021).

[21] T. Niederprüm, O. Thomas, T. Manthey, T. M. Weber, and H. Ott, Giant cross section for molecular ion formation in ultracold rydberg gases, Phys. Rev. Lett. **115**, 013003 (2015).

[22] N. Zuber, V. S. V. Anasuri, M. Berngruber, Y. Q. Zou, F. Meinert, R. Löw, and T. Pfau, Observation of a molecular bond between ions and Rydberg atoms, Nature (London) **605**, 453 (2022).

[23] Y. Q. Zou, M. Berngruber, V. S. V. Anasuri, N. Zuber, F. Meinert, R. Löw, and T. Pfau, Observation of vibrational dynamics of orientated Rydberg-atom-ion molecules, Phys. Rev. Lett. **130**, 023002 (2023).

[24] C. H. Greene, A. S. Dickinson, and H. R. Sadeghpour, Creation of polar and nonpolar ultra-long-range Rydberg molecules, Phys. Rev. Lett. **85**, 2458 (2000).

[25] C. Fey, F. Hummel, and P. Schmelcher, Ultralong-range Rydberg molecules, Mol. Phys. **118**, e1679401 (2020).

[26] M. T. Eiles, Trilobites, butterflies, and other exotic specimens of long-range Rydberg molecules, J. Phys. B: At. Mol. Opt. Phys. **52**, 113001 (2019).
[27] F. B. Dunning, S. K. Kanungo, and S. Yoshida, Ultralong-range Rydberg molecules, J. Phys. B: At. Mol. Opt. Phys. **57**, 212002 (2024).
[28] T. Niederprüm, O. Thomas, T. Eichert, C. Lippe, J. Pérez-Ríos, C. H. Greene, and H. Ott, Observation of pendular butterfly Rydberg molecules, Nat. Commun. **7**, 12820 (2016).
[29] D. Booth, S. T. Rittenhouse, J. Yang, H. R. Sadeghpour, and J. P. Shaffer, Production of trilobite Rydberg molecule dimers with kilo-Debye permanent electric dipole moments, Science **348**, 99 (2015).
[30] M. Althön, M. Exner, R. Blättner, and H. Ott, Exploring the vibrational series of pure trilobite Rydberg molecules, Nat. Commun. **14**, 8108 (2023).
[31] I. C. Liu, J. Stanojevic, and J. M. Rost, Ultra-long-range Rydberg trimers with a repulsive two-body interaction, Phys. Rev. Lett. **102**, 173001 (2009).
[32] C. Fey, J. Yang, S. T. Rittenhouse, F. Munkes, M. Baluktsian, P. Schmelcher, H. R. Sadeghpour, and J. P. Shaffer, Effective three-body interactions in Cs(6*s*)-Cs(*nd*) Rydberg trimers, Phys. Rev. Lett. **122**, 103001 (2019).
[33] M. T. Eiles, C. Fey, F. Hummel, and P. Schmelcher, Triatomic butterfly molecules, J. Phys. B: At. Mol. Opt. Phys. **53**, 084001 (2020).
[34] M. T. Eiles, A. L. Hunter, and J. M. Rost, Ring Rydberg composites, J. Phys. B: At. Mol. Opt. Phys. **53**, 054001 (2020).
[35] M. T. Eiles, A. Eisfeld, and J. M. Rost, Anderson localization of a Rydberg electron, Phys. Rev. Res. **5**, 033032 (2023).
[36] M. T. Eiles, C. W. Wächtler, A. Eisfeld, and J. M. Rost, Topological edge states in a Rydberg composite, Phys. Rev. B **109**, 075422 (2024).
[37] A. L. Hunter, M. T. Eiles, A. Eisfeld, and J. M. Rost, Rydberg composites, Phys. Rev. X **10**, 031046 (2020).
[38] C. Fey, F. Hummel, and P. Schmelcher, Building principle of triatomic trilobite Rydberg molecules, Phys. Rev. A **99**, 022506 (2019).
[39] M. Exner, R. Srikumar, R. Blättner, M. T. Eiles, P. Schmelcher, and H. Ott, High precision spectroscopy of trilobite Rydberg molecules, Phys. Rev. Lett. **134**, 223401 (2025).
[40] K. S. Kleinbach, F. Meinert, F. Engel, W. J. Kwon, R. Löw, T. Pfau, and G. Raithel, Photoassociation of trilobite Rydberg molecules via resonant spin-orbit coupling, Phys. Rev. Lett. **118**, 223001 (2017).
[41] E. L. Hamilton, C. H. Greene, and H. R. Sadeghpour, Shape-resonance-induced long-range molecular Rydberg states, J. Phys. B: At. Mol. Opt. Phys. **35**, L199 (2002).
[42] M. I. Chibisov, A. A. Khuskivadze, and I. I. Fabrikant, Energies and dipole moments of long-range molecular Rydberg states, J. Phys. B: At. Mol. Opt. Phys. **35**, L193 (2002).
[43] M. Born and R. Oppenheimer, Zur quantentheorie der molekeln, Ann. Phys. **389**, 457 (1927).
[44] R. Srikumar, F. Hummel, and P. Schmelcher, Nonadiabatic interaction effects in the spectra of ultralong-range Rydberg molecules, Phys. Rev. A **108**, 012809 (2023).
[45] F. Hummel, P. Schmelcher, and M. T. Eiles, Vibronic interactions in trilobite and butterfly Rydberg molecules, Phys. Rev. Res. **5**, 013114 (2023).
[46] A. A. Durst, M. Simić, N. Abraham, and M. T. Eiles, Nonadiabatic couplings as a stabilization mechanism in long-range Rydberg molecules, Phys. Rev. A **111**, 032811 (2025).
[47] M. T. Eiles and F. Hummel, Kato's theorem and ultralong-range Rydberg molecules, Phys. Rev. A **109**, 022811 (2024).
[48] See Refs. [30,39] and Appendix A 1 for details.
[49] C. H. Greene and M. T. Eiles, Green's-function treatment of Rydberg molecules with spins, Phys. Rev. A **108**, 042805 (2023).
[50] V. Bendkowsky, B. Butscher, J. Nipper, J. P. Shaffer, R. Löw, and T. Pfau, Observation of ultralong-range Rydberg molecules, Nature (London) **458**, 1005 (2009).
[51] See Appendix A 2 for details.
[52] T. Kato, On the eigenfunctions of many-particle systems in quantum mechanics, Commun. Pure Appl. Math. **10**, 151 (1957).
[53] N. H. March, Spatially dependent generalization of Kato's theorem for atomic closed shells in a bare Coulomb field, Phys. Rev. A **33**, 88 (1986).
[54] See Appendix A 2 for more details.
[55] See Appendix A 3 for more details.
[56] See Appendix A 4 for more details.
[57] R. Srikumar, S. T. Rittenhouse, and P. Schmelcher, Internal diffraction dynamics of trilobite molecules, Phys. Rev. A **110**, 062808 (2024).
[58] F. Hummel, K. Keiler, and P. Schmelcher, Electric-field-induced wave-packet dynamics and geometrical rearrangement of trilobite Rydberg molecules, Phys. Rev. A **103**, 022827 (2021).
[59] V. M. Borodin and A. K. Kazansky, The adiabatic mechanism of the collisional broadening of Rydberg states via a loosely bound resonance state of ambient gas atoms, J. Phys. B: At. Mol. Opt. Phys. **25**, 971 (1992).
[60] P. Giannakeas, M. T. Eiles, F. Robicheaux, and J. M. Rost, Dressed ion-pair states of an ultralong-range Rydberg molecule, Phys. Rev. Lett. **125**, 123401 (2020).
[61] M. T. Eiles and C. H. Greene, Hamiltonian for the inclusion of spin effects in long-range Rydberg molecules, Phys. Rev. A **95**, 042515 (2017).

PHYSICAL REVIEW A **110**, 062808 (2024)

Internal diffraction dynamics of trilobite molecules

Rohan Srikumar,[1,*] Seth T. Rittenhouse,[2,3,†] and Peter Schmelcher[1,4,‡]

[1]*Zentrum für Optische Quantentechnologien, Universität Hamburg, Luruper Chaussee 149, 22761 Hamburg, Germany*

[2]*Department of Physics, United States Naval Academy, Annapolis, Maryland 21402, USA*

[3]*Institute of Theoretical Physics, Institute of Physics, University of Amsterdam, Science Park 904, 1098 XH Amsterdam, The Netherlands*

[4]*The Hamburg Centre for Ultrafast Imaging, Universität Hamburg, Luruper Chaussee 149, 22761 Hamburg, Germany*

(Received 5 August 2024; accepted 20 November 2024; published 10 December 2024)

Trilobite molecules are ultralong-range Rydberg molecules formed when a high angular momentum Rydberg electron scatters off of a ground-state atom. Their unique electronic structure and highly oscillatory potential energy curves support a rich variety of dynamical effects yet to be explored. We analyze the vibrational motion of these molecules using a framework of adiabatic wave-packet propagation dynamics and observe that for appropriate initial states, the trilobite potential acts as molecular diffraction grating. The quantum dynamic effects observed are explained using a Fourier analysis of the scattering potential and the associated scattered wave packet. Furthermore, vibrational ground states of the low angular momentum ultralong-range Rydberg molecules are found to be particularly suitable to prepare the relevant wave packets. Hence, we propose a time-resolved pump-probe scheme designed for the realization of the effect in question, and advertise the utilization of a single diatomic Rydberg molecule as a test bed for the study of exaggerated quantum dynamical phenomena.

DOI: 10.1103/PhysRevA.110.062808

I. INTRODUCTION

Ultracold atoms in highly excited Rydberg states have proven to be an outstanding tool in the engineering and control of long-range interactions in atomic, molecular, and optical systems [1–5]. They offer several exploitable features including a highly tunable electronic character which is readily usable for mediating a plethora of atom-atom interaction effects [6–9]. In addition, interactions between a Rydberg atom and a neutral ground-state atom [10] mediated by the Rydberg electron have seen a surge in popularity in the context of engineering and detection of bound molecular states [11,12], ultracold chemical reactions [13], and measurement of spatial correlations [14,15].

Notably, the low-energy scattering of a Rydberg electron off of a ground-state atom can result in the formation of ultralong-range Rydberg molecules (ULRMs), which are bound scattering states that feature massive internuclear proportions [11,16,17]. Three main classes of ULRMs are low-l, trilobite, and butterfly molecules [18,19] classified by the low or high angular momentum l state of the Rydberg electron. In contrast to energetically isolated, quantum defect splitted low-l ULRM, trilobite molecules are formed when the nearly degenerate set of high-l hydrogenic states of a Rydberg electron are hybridized by a scattering neutral atom called a perturber. Butterfly molecules, on the other hand, are formed as a consequence of p-wave shape resonances that exist in the low-energy scattering of an electron with an alkali metal atom [10]. These intriguing systems have undergone numerous theoretical and experimental investigations that explored their electronic and rovibrational spectra [19–30], their responses to external fields [31–35], nonadiabatic effects [36–38], and the complex angular momentum structure they feature [17,39–43]. Recently there has emerged an interest in the dynamics of the constituent nuclei under the influence of these potentials [34,44]. Apart from the neutral trilobite molecule investigated here, nuclear wave-packet dynamics of charged Rydberg molecules have also garnered a great deal of recent interest [45,46].

From the double slit experiment to Bragg scattering of electron from crystal lattices, diffraction and interference effects exhibited by quantum matter have been a matter of significant experimental and theoretical interest from the very inception of quantum mechanics. More recent characterization of similar phenomena includes, among many others, quantum diffraction of confined matter-waves and localized wave packets by time-independent and time-dependent external potentials [47–51]. Here, we propose a system where the electronic potential energy structure of a trilobite molecule mediates the scattering and diffraction of a vibrational wave packet, creating a new approach to observe quantum interference effects in a single diatomic molecular system of huge size.

In this article, we demonstrate that the adiabatic potential energy curves (PECs) of the trilobite molecules form a unique diatomic environment to probe quantum dynamic effects in time and length scales not customarily accessible to conventional molecules. Apart from their exaggerated spatial extent and slow temporal evolution, the trilobite molecules

*Contact author: rsrikuma@physnet.uni-hamburg.de
†Contact author: rittenho@usna.edu
‡Contact author: pschmelc@physnet.uni-hamburg.de

 ©2024 American Physical Society

also feature very high polarizability, extreme sensitivity to electric fields, and a rapidly varying electronic character not reproducible in the dynamics of standard diatomic molecules. A detailed characterization of wave-packet dynamics of a ULRM can provide insight not just into interesting bound vibrational effects, but also low-energy l-changing collision between the ground-state atom and the Rydberg atom [13,52]. The ULRM hence presents itself as a diatomic laboratory capable of performing yet to be explored cold-atom scattering experiments.

In this work we perform numerical simulations of the vibrational wave-packet dynamics of a trilobite molecule as it propagates through the associated trilobite electronic potential. We choose the diatomic ^{87}Rb ULRM as our molecular prototype. We observe that for a range of values of the principal quantum number n, the adiabatic electronic potentials of the ULRM exhibit an undulating structure along the internuclear axis. These potential energy curves can act as a diffraction grating and are backscattering appropriate incident wave packets to form time-propagating multipeak structures. To identify the underlying mechanism, we use a Fourier analysis of the PEC and analyze the behavior of the scattered wave packets in both position and momentum space. We also show that the necessary initial state of the system can be conveniently prepared by the use of advanced optical tweezer setups, or alternatively initialized utilizing the vibrational ground state of low-l ULRM states.

This article is organized as follows. In Sec. II we provide our theoretical framework describing the internal electronic structure of the ULRM [Sec. (II A)], the potential energy landscape, as well as the relevant nuclear dynamics [Sec. (II B)]. In Sec. III we present our numerical results, with Sec. III A highlighting the energetical structure of the trilobite molecule, Sec. III B detailing its vibrational dynamics, Sec. III C addressing potential limitations in the theoretical framework, and Sec. III D detailing the elementary experimental schemes that could be the basis to observe the aforementioned vibrational dynamics. Lastly, our conclusions and future research outlook are provided in Sec. IV.

II. THEORETICAL FRAMEWORK AND METHODOLOGY

We begin by characterizing the electronic interaction between the constituents of our system and model the electronic Hamiltonian for the ULRM. The salient features of the trilobite state are highlighted and their effects on the vibrational dynamics of the ULRM are discussed. We then present the time-dependent Schrödinger equation that governs the internal nuclear dynamics of the ULRM. Throughout our work, the system and the results are presented and analyzed in atomic units (a.u.) unless explicitly mentioned otherwise.

A. Electronic interaction and structure

We consider a system consisting of two ^{87}Rb atoms, one of which is excited to a high-lying Rydberg state, bound to each other via the low-energy scattering of the corresponding Rydberg electron with the ground-state atom. The triplet s-wave scattering of the Rydberg electron off of the ground-state atom facilitates an attractive interaction between the two Rb atoms,

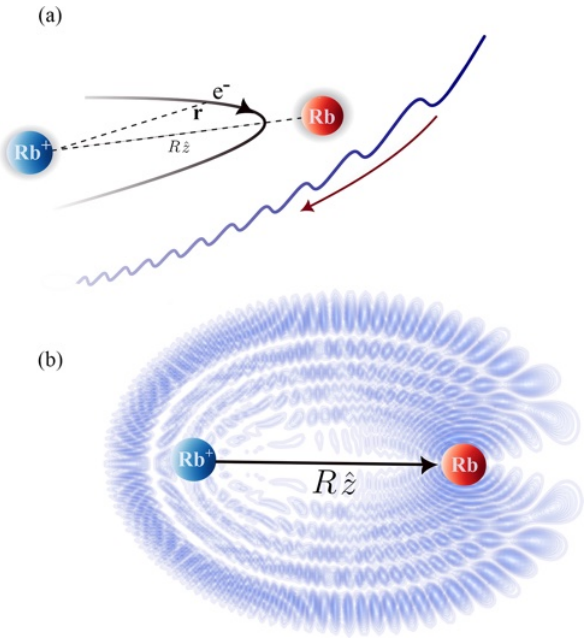


FIG. 1. Illustrative sketch of a trilobite molecule. (a) The binding interaction between the two ^{87}Rb atoms separated by an internuclear vector $R\hat{z}$ (along the z axis) is determined by the low-energy scattering of the excited electron (positioned at $\mathbf{r}$) with the ground-state atom. (b) Characteristic electronic density of a $n = 55$ trilobite state with $R = 4000$ a.u.

which is effectively modeled using a Fermi pseudopotential [10,53] given by

$$V_{en}(\mathbf{r}, \mathbf{R}) = 2\pi a_s^T(k)\delta(\mathbf{r} - \mathbf{R}), \tag{1}$$

where $\mathbf{r}$ and $\mathbf{R}$ are, respectively, the positions of the Rydberg electron and the ground-state atom relative to the positive Rydberg core [as seen in Fig. 1(a)]. Here, $a_s^T(k) = a_s^T(0) + \pi\alpha k/3$ is the low-energy triplet s-wave scattering length for electron-atom collisions, with the zero-energy scattering length $a_s^T(0) = -16.05$ [11,54], the ground-state atom polarizability $\alpha = 319.2$ [55], and the excited electron's wave number k given semiclassically in atomic units as $k^2 = 2/R - 1/n^2$. The singlet scattering interaction, being weaker and repulsive, is safely ignored [11,54]. The adiabatic electronic Hamiltonian for the ULRM is then given by $H_{\text{el}} = H_{\text{Ryd}} + V_{\text{en}}$, with H_{Ryd} describing the Rydberg electron in the potential of its parent ionic core.

For the purpose of this work we extract the Born-Oppenheimer potentials for the ULRMs in the molecular body-fixed frame at the level of perturbation theory. A complete, nonperturbative treatment is possible [40,43], but only creates small quantitative changes and no qualitative change for the results presented here. We express the system in the basis formed by the Rydberg atomic eigenstates $\{\phi_{nlm}(\mathbf{r})\}$ of Rubidium with energies given in atomic units by $E_{nl} = -0.5(n - \mu_l)^{-2}$, where μ_l is the quantum defect [56]. In the body-fixed molecular frame, there is a node along the internuclear axis for all $m \neq 0$ states, which therefore do not

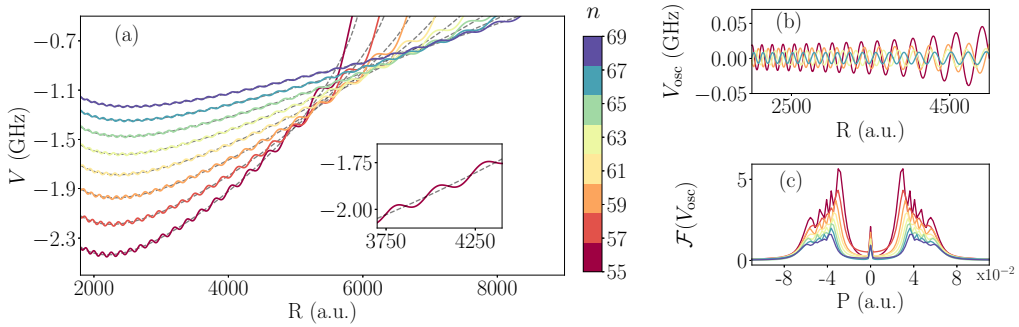


FIG. 2. Potential energy structure of trilobite molecule for ranges of $55 \leqslant n \leqslant 69$ color coded with respect to n. (a) The colored solid lines portray the calculated trilobite potentials V_t for multiple n values, whereas the dotted gray lines plotted in the background represent the approximate curve envelopes V_{anh} (inset magnified to highlight the structure of the PEC). (b) Represents the oscillatory feature of the trilobite potential, defined as V_{osc}, with (c) being the corresponding Fourier transforms $\mathcal{F}\{V_{\text{osc}}\}$.

experience the contact electron-atom interaction of Eq. (1). Rydberg states with lower angular momenta $l < l_{\text{min}}$ ($l_{\text{min}} = 3$ for Rb) are energetically separated due to non-negligible quantum defects. At the level of first-order perturbation theory in V_{en} the related PECs are given by

$$V_l(R) = 2\pi a_s^T(k)|\phi_{n^*l}(R)|^2, \tag{2}$$

where $n^* = n - \mu_l$ is the effective principle quantum number.

The high-l ($l \geqslant 3$) electronic sates create an approximately degenerate manifold of hydrogenic Rydberg states and thus must be treated using degenerate perturbation theory. The resulting PECs are shown for a range of principal quantum numbers in Fig. 2(a) and are given as [11]

$$V_t(R) = 2\pi a_s^T(k) \sum_{l=3}^{n-1} |\phi_{nl}(R)|^2. \tag{3}$$

The corresponding electronic state

$$\psi_t(R, \mathbf{r}) = \frac{1}{T} \sum_{l=3}^{n-1} \phi_{nl}(R)\phi_{nl}(\mathbf{r}), \tag{4}$$

where T is a normalization factor, is commonly referred to as the trilobite electronic state due to its uncanny resemblance to the structure of a trilobite fossil [as seen in Fig. 1(b)]. For large n values, the trilobite PEC can be divided into an anharmonic well overlayed with an oscillatory potential, i.e., $V_t(R) = V_{\text{anh}}(R) + V_{\text{osc}}(R)$. The overall anharmonic envelope is very well represented by the approximation [10,11]

$$V_{\text{anh}}(R) = \frac{a_s^T(k)}{\pi n^3} \sqrt{\frac{2}{R} - \frac{1}{n^2} - \frac{(l_{\text{min}} + 1/2)^2}{R^2}}. \tag{5}$$

At large R values beyond the final well in the PEC, V_{anh} is no longer an accurate envelope of the trilobite potential. However, we will limit our work here to ranges in which it is. In the following work, we will focus on the wave-packet dynamics of the ULRM in the case of trilobite molecules.

Inclusion of important corrections due to p-wave shape resonances, fine structure of the Rydberg atom, hyperfine structure of the ground-state atom, and nonadiabatic interaction effects will undoubtedly produce quantitative changes of the electronic structure and related PEC of the trilobite molecule. However, the interesting dynamical phenomena predicted with the relatively basic approximations used in this work are expected to persist qualitatively in a more accurate treatment. It is also worth mentioning that a heterogenous ULRM [57,58], consisting of an ^{87}Rb Rydberg atom and a ^{84}Sr ground-state atom, exhibits neither a hyperfine structure nor p-wave shape resonances [59,60]. Such a Rb-Sr molecule might be an ideal case to study the dynamical properties of pure trilobite molecules without excess complexities, and can prove useful in the empirical reproduction of phenomena discussed in this work.

B. Vibrational dynamics

To explore the vibrational dynamics of a ULRM in the trilobite state, we solve the corresponding time-dependent Schrödinger equation given at the level of the Born-Oppenheimer approximation by

$$i\hbar \frac{\partial}{\partial t} \chi(R, t) = H_n \chi(R, t), \tag{6}$$

where $\chi(R, t)$ is the time-dependent nuclear wave function representing the radial dynamics of the ULRM along the internuclear axis. The nuclear Hamiltonian H_n is given in atomic units as

$$H_n = -\frac{1}{2\mu} \nabla_R^2 + V_t(R), \tag{7}$$

where the first term is the kinetic energy of the relative motion of the nuclei (with reduced mass μ) and V_t is the trilobite PEC from Eq. (3). We propagate the initial wave packet $\chi(R, t = 0)$ in time via the standard eigenstate expansion, i.e.,

$$\chi(R, t) = \sum_k a_k e^{-iE_k t} \chi_k(R), \tag{8}$$

where $\chi_k(R)$ are the stationary eigenstates of H_n with eigenenergies E_k, i.e., $H_n \chi_k(R) = E_k \chi_k(R)$, and the expansion amplitudes are given by the standard inner product $a_k = \langle \chi_k(R) | \chi(R, t = 0) \rangle$.

Our wave packet is initialized as a Gaussian centered at position R_0 with width σ with zero initial momentum, i.e., $\chi(R, t = 0) \propto \exp[-(R - R_0)^2/(4\sigma^2)]$, and the

time-dependent probability density function $|\chi(R,t)|^2$ is determined. An initially displaced wave packet in the trilobite potential will oscillate back and forth, returning to its initial position, accounting for the anharmonic character of the potential. During this process, it will scatter off the oscillatory portion of the potential, which acts as a diffraction grating, facilitating the backscattering (and forwardscattering) of a time-evolving wave packet. Via the Fourier transform, we also analyze the momentum-space wave function, $\phi(P,t) = \mathcal{F}\{\chi(R,t)\}$, and the oscillatory potential $\mathcal{F}\{V_{\rm osc}(R)\}$ to study and explain such scattering effects in momentum space. In the following we numerically investigate the vibrational dynamics of ULRM in the position and momentum space for different initial state configurations and different principle quantum numbers, using the framework discussed above. The stationary eigenstates of H_n are calculated utilizing a tenth-order finite difference method [61], which are then used to simulate the time-evolving wave packet [Eq. (8)]. Owing to the simplicity of the system, we achieve converged, accurate results with relatively little computational effort. Hence, the results have been calculated with step sizes of $\Delta_R \sim 2$ a.u. and $\Delta_t \sim 0.05$ ns.

III. RESULTS AND DISCUSSION

In this section, we analyze the vibrational dynamics of an oscillating vibrational wave packet in the trilobite molecule. We discuss the potential energy structure of trilobite molecules for multiple n values, highlighting their oscillatory structure as a salient feature. We then proceed to illustrate the probability density plots of a time-propagating Gaussian wave packet as it scatters off an $n = 55$ trilobite potential. The unique dynamical effects that arise as a function of the width and position of the initial wave packet are demonstrated and explained utilizing the Fourier transform of the wave packets and the oscillatory features of the trilobite potential. Finally, prototypical experimental schemes that might be used to observe such dynamical effects are also discussed.

A. Potential energy landscape

The potential energy curves for the principal quantum numbers ranging from $n = 55$ to $n = 69$ are illustrated in Fig. 2(a). The R range is chosen to highlight the oscillatory structure exhibited by V_t. Solid curves represent the trilobite PEC (color coded with respect to n), while dashed lines in the background represent the approximate anharmonic potential $V_{\rm anh}$ according to Eq. (5). Subtracting $V_{\rm anh}$ from the total trilobite potential allows us to isolate the remaining oscillatory part of the trilobite PEC, $V_{\rm osc}$, shown in Fig. 2(b). The potential energy curves exhibit an increasingly shallow envelope and amplitude of oscillation for higher values of n. We also observe a slight increase in the frequency of oscillation for a corresponding increase in n.

Additional insight can be gained by analyzing the oscillatory potential in momentum space through the Fourier transform of $V_{\rm osc}(R)$, $\mathcal{F}\{V_{\rm osc}(R)\}$, the results of which are shown in Fig. 2(c). In momentum-space representation, the potentials exhibit a clear sideband structure that corresponds to its undulating nature in R. For example, the $n = 55$ trilobite state exhibits oscillations in R whose wavelength is approximately 100 a.u., though it does vary, increasing up to $\sim$230 a.u. in the R range considered here. This results in a Fourier spectrum that is strongly peaked at $P = 0.03$ a.u., where P is the radial momentum in the Fourier space. As the oscillations of the PEC deviate from a strict periodic behavior in position space, we observe a broadening of the sideband structures with an overlay of multiple peaks in Fourier space. Note that the Fourier transform is performed using a truncated range of R values ranging from $R = 1300$ to 4500 a.u. This corresponds to the range of internuclear separations probed by the oscillating wave packet. The extremes of the position of the peak of the wave packet are determined by the classical turning points of the system in the trilobite potential when the wave packet is started from rest displaced to one side. The usage of such a limited grid in position space restricts the accuracy of the Fourier analysis and invariably contributes to further broadening of the sidebands and the exact positions of the multiple peaks. Finally, the n dependence of the amplitude of oscillations of the PEC, as discussed before, is also reflected in the n dependence of the amplitude and position of the sidebands in Fig. 2(c).

B. Vibrational dynamic effects

Onset of wave-packet diffraction. We begin by performing a series of dynamical simulations of the ULRM's nuclear wave packet initialized in a Gaussian state centered around different values of R, in an $n = 55$ trilobite PEC. The wave packets are constructed such that the width of the corresponding probability density exhibits a standard deviation of 100 a.u., which is comparable in size to the wavelength of the oscillations in the trilobite potential. Figure 3 illustrates the probability density functions of the time-evolving wave packet, in the position space [Figs. 3(a) and 3(b)] and momentum space [Figs. 3(c) and 3(d)]. The position of the initial state determines the total energy of the time-evolving wave packet, thereby putting an upper bound on the magnitude of radial momentum probed by the nuclei during its dynamics. A Gaussian state centered around $R_0 = 2400$ a.u. [Figs. 3(a) and 3(c)], i.e., relatively close to the equilibrium internuclear distance ($R_{\rm eq} \sim 2190$ a.u.), performs low-energy oscillations around $R_{\rm eq}$ with complex multiwell interference effects. Interestingly, a further increase in the total energy of the wave packet, achieved by having its initial position extended to $R_0 = 3000$ a.u, [Figs. 3(b) and 3(d)], exhibits the onset of a clear multiple-peak structure that resembles a time-propagating diffraction pattern. The emergence of these unique interference patterns is explained by focusing on the momentum picture. Oscillations that achieve lower momentum are not able to probe the clear sideband structure of the trilobite potential exhibited by its oscillatory features [as seen in Fig. 3(e)]. Hence, they only display very faint forward- and backscattering peaks that are quickly dispersed in the course of time. However, oscillations as portrayed in Fig. 3(d) quite clearly achieve higher momentum beyond the sideband structures [as seen in Fig. 3(f)], thereby showing clear signs of forward- and backscattering in the momentum picture. Such an explanation treats the oscillatory structure of the trilobite potential as a diffraction grating in momentum space.

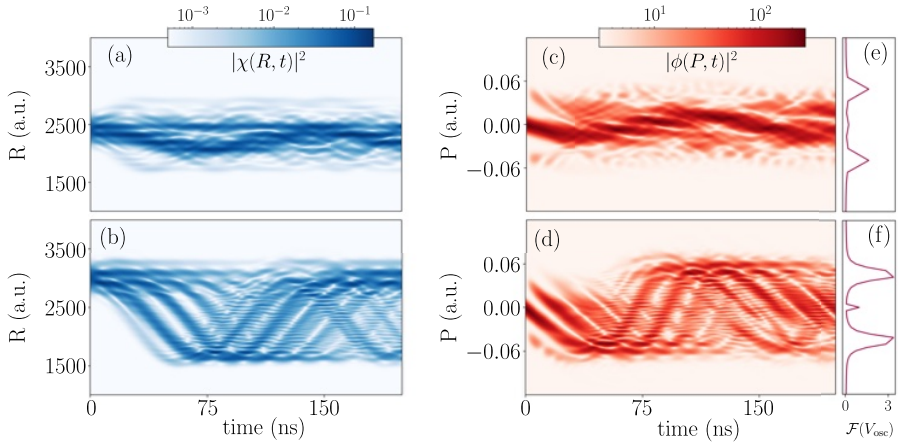


FIG. 3. Onset of wave-packet diffraction. Probability density plots $|\chi(R,t)|^2$ and $|\phi(P,t)|^2$ of the wave-packet scattering off an $n = 55$ trilobite potential, in the (a) and (b) position and (c) and (d) momentum representation. The initial state is a Gaussian wave packet of characteristic width 100 a.u., centered around (a) $R_0 = 2400$ and (b) $R_0 = 3000$ a.u. with the corresponding momentum representation presented in (c) and (d), respectively. (e) and (f) The corresponding Fourier transform of $V_{\rm osc}(R)$ probed by each of the wave packets.

Internal diffraction dynamics. To emphasize the phenomena discussed above, we analyze the vibrational dynamics of a ULRM with an initial Gaussian wave packet centered at $R_0 = 4000$ a.u. again with a width of 100 a.u. As discussed earlier, increasing R_0 farther away from $R_{\rm eq}$ further increases the momentum probed by the wave packet, allowing it to clearly probe the momentum sideband structure of the potential as it scatters off the PEC. Hence, following the trend from the previous simulations (with $R_0 = 2400$ and 3000 a.u.), we see that initializing the wave packet with $R_0 = 4000$ a.u. facilitates repeated coherent backscattering as the wave packet traverses through the PEC. The resulting time-dependent probability density is shown in Fig. 4(a). In this case, the system samples enough of the oscillatory potential to constantly undergo forward- and back scattering, producing a train of almost evenly spaced side peaks. The origin of this behavior becomes apparent in the momentum-space probability density shown in Fig. 4(b). Here, the initial momentum space wave packet scattering off the oscillatory potential produces adjacent scattered peaks corresponding to the momentum of the peak of the Fourier transform. Figure 4(c) shows time slices of the momentum probability density function at different times, showing peaks separated in momentum by around ~ 0.03 a.u., approximately the peak of the sidebands seen in the momentum representation of the PEC in Fig. 2(c). The resulting fragmented wave-train structure in momentum space exhibits a clear and coherent multipeak structure, reminiscent of that observed in waves scattering from a diffraction grating. Apart from the diffraction effects, we also notice that the probability density plots in Fig. 4(a) (marked by the arrows) exhibit sustained population near the initial state of the wave packet, which we denote as "stickiness." This is a result of a large overlap of the initial wave packet with eigenstates that are localized around a well near the initial position [see Fig. 4(d)]. Figure 4(d) shows the vibrational probability densities of eigenstates that participate in the wave-packet dynamics as well as the initial wave packet (cyan) for reference. These localized states (purple) have a large overlap with the initial wave packet and exhibit a vibrational splitting around ∼46 MHz, as opposed to the delocalized states (gray) exhibiting a vibrational splitting of

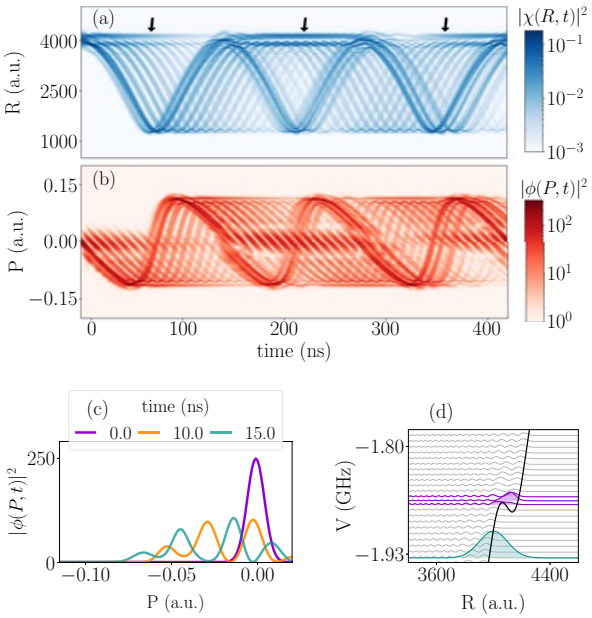


FIG. 4. Probability densities $|\chi(R,t)|^2$ and $|\phi(P,t)|^2$ of the wave packet scattering off an $n = 55$ trilobite potential, in the (a) position and (b) momentum representation. The initial state is a Gaussian wave packet of width 100 a.u., centered around $R_0 = 4000$ a.u. The arrows mark the stickiness of the wave packet discussed in the text. (c) Time slices of $|\phi(P,t)|^2$, illustrating the backscattering undergone by the propagating wave packet. (d) The probability densities of the molecular eigenstates, with the localized states responsible for the initial "stickiness" highlighted (purple) near the initial Gaussian (cyan).

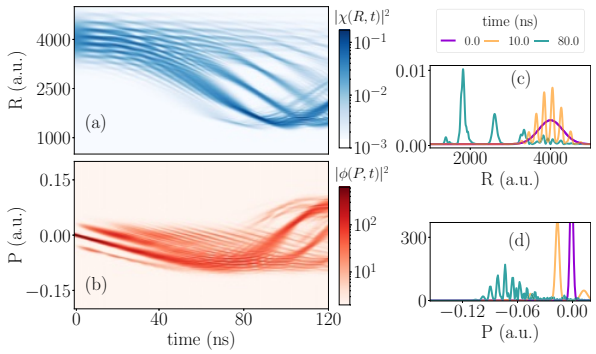


FIG. 5. Interference effects in the scattering of a wide wave packet. Probability densities $|\chi(R,t)|^2$ and $|\phi(P,t)|^2$ of the wave packet scattering off an $n = 60$ trilobite potential are shown in the (a) position and (b) momentum representation. The initial state is a Gaussian wave packet of width 300 a.u., centered around $R_0 = 4000$ a.u. Time slices of $|\chi(R,t)|^2$ and $|\phi(P,t)|^2$ illustrating key stages of evolution are shown in (c) and (d), respectively.

∼67 MHz. Part of the wave packet evolves with the time scales associated with the localized states (∼210 ns), which are noticeably larger than the time scale of the anharmonic oscillation (∼150 ns), thereby exhibiting said stickiness. Due to the limited amount of eigenstates involved, this particular phenomena continues to occur for even larger values of t ($\gtrsim$ 400 ns), retaining its spatial localization periodically, similar to a quantum revival. However, the propagating diffraction pattern is continuously scattered off of a band of varying frequencies, diminishing the chance of a complete quantum revival in finite time.

Wave-train propagation. The aforementioned time-propagating interference effects are dependent on the width of the nuclear wave packet. Above, we used an initial state whose width was of comparable size to the wavelength of the oscillations of the PECs. A spatially very narrow wave packet does not experience the interference effects seen above, and primarily performs anharmonic oscillations, with dispersion enabled by the undulating structure of the PEC. On the other hand, a wave packet that is spatially considerably wider than the wavelength of the oscillations in V_t will show dynamical phenomena distinct from those discussed above. Figure 5 illustrates the dynamics of an initial Gaussian wave packet centered at $R_0 = 4000$ a.u. propagating in the $n = 60$ trilobite curve. The $n = 60$ trilobite features an oscillatory potential with a comparatively smaller wavelength than that of $n = 55$. The initial state is constructed with a width of 300 a.u., several times larger than the well separation distance of V_t. Hence, at $t = 0$ the wave packet spans multiple wells of the trilobite potential. During the initial time dynamics each well of the PEC acts as a source, creating a multipeaked fragmented wave packet with each peak localized at a different well, as portrayed in the $t = 8$ ns time slice shown in Fig. 5(c). Later in the course of the dynamics, these individual wave packets emanating from different wells interfere with each other, forming very narrow localized pulses [$t = 80$ ns, Fig. 5(c)] that are isolated from each other. The widths of these narrow peaks do not conform to the size of the initial wave packet, and are dependent on the scattering potential in which the wave packet propagates. Their formation can be explained by considering the momentum space picture shown in Fig. 5(b). Here, we see that an extremely narrow initial wave packet in momentum space undergoes constant backscattering to form an approximately equidistant train of sharp peaks in P-space [$t = 80$ ns, Fig. 5(d)], loosely reminiscent of a Dirac comb [62,63]. The Fourier transform of such a structure exhibits a pulse-train behavior such as that observed above. As a final note, for higher n values, both the amplitude of oscillations V_{osc} and the general anharmonic envelope V_{anh} of the trilobite PEC becomes considerably more shallow. Hence, the momentum range probed by the wave packet and the magnitude of backscattering it experiences are reduced, thereby resulting in a diminished diffraction pattern.

C. Limitations of the theoretical framework

We have ignored the effects of p-wave shape resonances and spin structure in our analysis. Inclusion of the p-wave scattering term would result in a more complex PEC structure that features avoided crossings between trilobite and butterfly curves near R_{eq}. These avoided crossings would substantially alter the long-time dynamics of the wave packet as it traverses through the full potential energy landscape. This might lead to the introduction of vibronic decay, surface hopping, diabatic stabilization, and several other nonadiabatic effects. Recent works have explored the spectral features of such systems [36–38] and have shown that nonadiabatic effects are of increasing importance at higher n values (like $n \gtrsim 55$) [45]. However, our present work is a proof of methodology meant to bring attention and interest to the study of wave-packet dynamics of trilobite molecules. Furthermore, while the p-wave shape resonances will substantially alter the long time-scale dynamics, the initial time dynamics should still qualitatively exhibit the diffractive effects discussed. Also, one can mitigate the complexity introduced by spin structure to some extent by careful preparation and state selection of the hyperfine state of the ground-state atom. Moreover, the hyperfine splitting of the PECs introduced by ground-state ^{87}Rb remains around ∼ 6.8 GHz while the depth of the trilobite potentials scale as n^{-3} with increasing n. At high enough n values, for example, $n \gtrsim$ 55, the rather large energetic separation between the different hyperfine states can be utilized to select and probe a single PEC. Of course, it is important to note that these complications can be eliminated by selecting a different ground-state perturbing atom, such as Sr, which has no low-energy, p-wave electron-atom resonances and lacks any hyperfine structure.

D. Prototypical experimental setup

The numerical simulations considered have been focusing on the time evolution of Gaussian wave packets. Experimentally one can utilize an optical tweezer setup [64,65] which confines two ground-state Rb atoms in separate harmonic potentials. The width and position of the initial Gaussian wave packet can be tuned through the depth of the optical traps and the separation between the two traps, respectively. Employing a multiphoton excitation of an individual atom to the trilobite state while simultaneously turning off the confinement

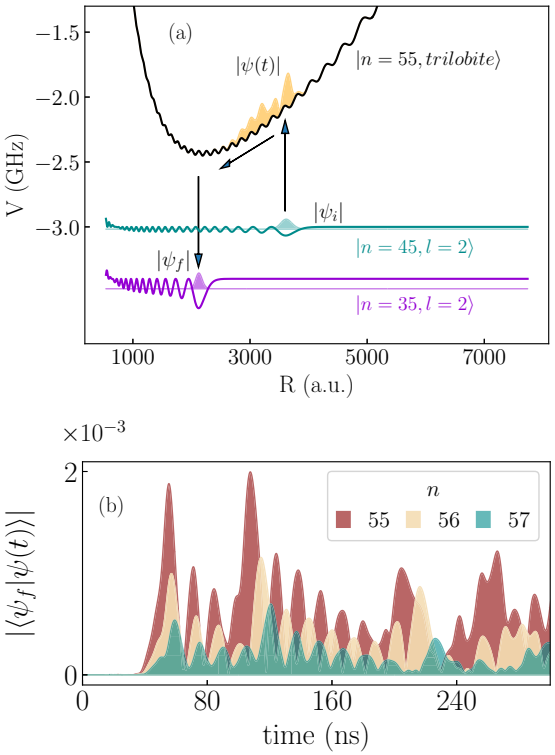


FIG. 6. Pictorial scheme of the suggested pump-probe experiment. (a) The vibrational ground state of the $|n = 45, l = 2\rangle$ ULRM is pumped to the $n = 55$ trilobite potential and subsequently propagates therein. Following a time lag, the wave packet is projected onto the desired $|n = 35, l = 2\rangle$ probe state. (b) Observable time-resolved correlation function calculated for multiple n values using the given setup. For each $|n, trilobite\rangle$ PEC, the pump and probe states are selected to be $|n - 10, l = 2\rangle$ and $|n - 20, l = 2\rangle$, respectively, where $n \in \{55, 56, 57\}$.

potential creates the desired initial state of the ULRM. Such a scheme, although straightforward, is difficult to accomplish in practice utilizing standard optical tweezers. Optical setups with finite laser waists cannot probe the nanometer-scale confinement required to prepare motional states whose dimensions are of the order of ∼100 a.u. Advancements in cold atom trapping employing the integration of plasmonic tweezers that facilitate nanoscale confinement may be one future option to circumvent this problem [66–68].

With this in mind, let us propose an alternate experimental scheme that utilizes a time-resolved pump-probe methodology to monitor dynamical effects in real time. The basic idea is to utilize lower-lying low-l ULRMs to create the initial state and as a probe to monitor the system. Figure 6(a) illustrates a prototypical example of the proposed scheme. The initial state preparation is accomplished by a two-photon transition to the Gaussian-like vibrational ground state of the $|n = 45, l = 2\rangle$ ULRM state. The vibrational ground states for different principle quantum numbers feature a convenient range of mean positions and widths, providing the necessary flexibility needed to observe the dynamical effects we seek. They can also be conveniently used as a probe state localized near a range of desired R values. Similar pump-probe schemes utilizing low-l Rydberg states were also utilized in the study of ion-atom scattering recently [69,70]. As an example, the ULRM is excited from the $|n = 45, l = 2\rangle$ state to the $n = 55$ trilobite electronic state using a microwave pump pulse, utilizing f-state admixture of the high-l molecule [30]. The microwave excitation is fast enough to consider it projective, preserving the vibrational wave packet as the initial state that propagates in the trilobite potential. A time-delayed probe pulse then enables us to project the time-evolving wave packet onto a $|n = 35, l = 2\rangle$ probe state and obtain the timeresolved correlation function. Figure 6(b) shows the predicted result of this proposed experiment for three different n values. In each case the $|n - 10, l = 2\rangle$ pump state is excited to the $|n, trilobite\rangle$, with $|n - 20, l = 2\rangle$ being the probe state. The state selection is done to facilitate comparable propagation times and correlation functions, as seen in Fig. 6(b). The train of evenly spaced diffraction peaks produced by scattering of the wave packet from the trilobite potential is observed as a series of peaks in the time-resolved correlation function. Note that the amplitudes of the correlation function, which carries the phase information of the diffraction pattern, decrease with increasing n. Although not a systematic study of the n dependence of the diffraction effect, the decrease in amplitude of the correlation function is consistent with our analysis that higher n values exhibit reduced backscattering and consequently display diminished diffraction effect. Rather conveniently, the temporal resolution achieved here is only limited by the time delay between the pump and probe pulses and their respective widths, both being finely tunable in the nanosecond regime. In comparison, direct spatiotemporal imaging as achieved in state-of-the-art ion microscopes [71,72] limits the resolution to the order of ∼100 nm and ∼10 ns, rendering the desired phenomenon challenging to observe. Moreover, recent advances in the construction of long-range molecular potentials with tunable electronic character [73] allow the possibility of engineering initial and probe states that can be optically excited to a trilobite state of choice. Note that although the theoretical description of a pump-probe scheme is rather straightforward (and abundant in conventional molecular physics), a corresponding experimental realization of the scheme in ultracold systems is not without due challenges [69,70]. But, within the scope of this work the pump-probe framework allows for the initial state preparation, time propagation, and observation of quantum interference and diffraction effects all encompassed within a single molecular system.

IV. CONCLUSION AND OUTLOOK

We have investigated intriguing wave-packet interference effects that unfold in the nuclear dynamics of a single diatomic trilobite ULRM. The internuclear potential landscape mediated by the Rydberg electron exhibits rapid oscillatory features similar to those of a diffraction grating. We observe that trilobite molecules with nuclear wave-packet widths comparable to that of the characteristic wavelength of the PEC, propagating with high enough initial energy, will undergo backscattering as a consequence of its own electronic

structure. An elementary Fourier analysis of the propagating wave packet and the potential energy landscape explains the observed phenomena, with semiquantitative detail. The self-diffraction phenomena exhibited by these molecules can be readily observed by an appropriate time-resolved pump-probe scheme. Conveniently, the necessary initial state preparation is accessible via the vibrational ground state of, e.g., lower-lying $l = 2$ ULRM states. Hence, we suggest that the ULRM can be functionally used as a single molecular laboratory for observing cold-atom dynamics on exaggerated time and length scales. The behaviors we predict within the simplified description used here should persist qualitatively in the full system and should be readily observable experimentally.

Our work provides new windows of opportunity for the study of dynamical behavior of ultralong-range Rydberg molecules. An immediate extension of our work, featuring the inclusion of p-wave shape resonances of Rb and the consequent introduction of vibronic couplings in the system, offers a new pathway to study multichannel dynamical effects in cold-atom systems. The high-l nature of the trilobite and butterfly configurations exhibiting large dipole transition elements might give rise to a plethora of dynamical effects not usually observed in standard atomic or molecular systems. Furthermore, the massive dipole moment of the trilobite state (and the butterfly state) [18,74,75] can be skillfully exploited by the introduction of an external electric field. This opens the possibility of new explorations in wave-packet dynamics near conical intersections [52], dynamics near pendular states [19], and the coherent control of ULRM to achieve rovibrational state engineering.

ACKNOWLEDGMENTS

We are grateful for the financial support granted by the German Research Foundation (DFG) through the priority program "Giant Interactions in Rydberg Systems" (DFG SPP 1929 GiRyd project SCHM 885/30-2).

[1] T. Wilk, A. Gaëtan, C. Evellin, J. Wolters, Y. Miroshnychenko, P. Grangier, and A. Browaeys, Phys. Rev. Lett. **104**, 010502 (2010).
[2] M. Zeppenfeld, Europhys. Lett. **118**, 13002 (2017).
[3] H. Busche, P. Huillery, S. W. Ball, T. Ilieva, M. P. A. Jones, and C. Adams, Nat. Phys. **13**, 655 (2017).
[4] S. T. Rittenhouse and H. R. Sadeghpour, Phys. Rev. Lett. **104**, 243002 (2010).
[5] J. Vaneecloo, S. Garcia, and A. Ourjoumtsev, Phys. Rev. X **12**, 021034 (2022).
[6] E. Urban, T. A. Johnson, T. Henage, L. Isenhower, D. D. Yavuz, T. G. Walker, and M. Saffman, Nat. Phys. **5**, 110 (2009).
[7] S. Weber, C. Tresp, H. Menke, A. Urvoy, O. Firstenberg, H. P. Büchler, and S. Hofferberth, J. Phys. B: At. Mol. Opt. Phys. **50**, 133001 (2017).
[8] T. Amthor, C. Giese, C. S. Hofmann, and M. Weidemüller, Phys. Rev. Lett. **104**, 013001 (2010).
[9] L. Béguin, A. Vernier, R. Chicireanu, T. Lahaye, and A. Browaeys, Phys. Rev. Lett. **110**, 263201 (2013).
[10] A. Omont, J. Phys. France **38**, 1343 (1977).
[11] C. H. Greene, A. S. Dickinson, and H. R. Sadeghpour, Phys. Rev. Lett. **85**, 2458 (2000).
[12] C. Fey, J. Yang, S. T. Rittenhouse, F. Munkes, M. Baluktsian, P. Schmelcher, H. R. Sadeghpour, and J. P. Shaffer, Phys. Rev. Lett. **122**, 103001 (2019).
[13] M. Schlagmüller, T. C. Liebisch, F. Engel, K. S. Kleinbach, F. Böttcher, U. Hermann, K. M. Westphal, A. Gaj, R. Löw, S. Hofferberth, T. Pfau, J. Pérez-Ríos, and C. H. Greene, Phys. Rev. X **6**, 031020 (2016).
[14] J. D. Whalen, S. K. Kanungo, R. Ding, M. Wagner, R. Schmidt, H. R. Sadeghpour, S. Yoshida, J. Burgdörfer, F. B. Dunning, and T. C. Killian, Phys. Rev. A **100**, 011402(R) (2019).
[15] S. K. Kanungo, Y. Lu, F. B. Dunning, S. Yoshida, J. Burgdörfer, and T. C. Killian, Phys. Rev. A **107**, 033322 (2023).
[16] V. Bendkowsky, B. Butscher, J. Nipper, J. P. Shaffer, R. Löw, and T. Pfau, Nature (London) **458**, 1005 (2009).
[17] C. Fey, F. Hummel, and P. Schmelcher, Mol. Phys. **118**, e1679401 (2020).
[18] E. L. Hamilton, C. H. Greene, and H. R. Sadeghpour, J. Phys. B: At. Mol. Opt. Phys. **35**, L199 (2002).
[19] T. Niederprüm, O. Thomas, T. Eichert, C. Lippe, J. Pérez-Ríos, C. H. Greene, and H. Ott, Nat. Commun. **7**, 12820 (2016).
[20] J. P. Shaffer, S. T. Rittenhouse, and H. R. Sadeghpour, Nat. Commun. **9**, 1965 (2018).
[21] Y. Lu, J. D. Whalen, S. K. Kanungo, T. C. Killian, F. B. Dunning, S. Yoshida, and J. Burgdörfer, Phys. Rev. A **106**, 022809 (2022).
[22] O. Thomas, C. Lippe, T. Eichert, and H. Ott, J. Phys. B: At. Mol. Opt. Phys. **51**, 155201 (2018).
[23] M. A. Bellos, R. Carollo, J. Banerjee, E. E. Eyler, P. L. Gould, and W. C. Stwalley, Phys. Rev. Lett. **111**, 053001 (2013).
[24] W. Li, T. Pohl, J. M. Rost, S. T. Rittenhouse, H. R. Sadeghpour, J. Nipper, B. Butscher, J. B. Balewski, V. Bendkowsky, R. Löw, and T. Pfau, Science **334**, 1110 (2011).
[25] D. A. Anderson, S. A. Miller, and G. Raithel, Phys. Rev. Lett. **112**, 163201 (2014).
[26] K. S. Kleinbach, F. Meinert, F. Engel, W. J. Kwon, R. Löw, T. Pfau, and G. Raithel, Phys. Rev. Lett. **118**, 223001 (2017).
[27] F. Böttcher, A. Gaj, K. M. Westphal, M. Schlagmüller, K. S. Kleinbach, R. Löw, T. C. Liebisch, T. Pfau, and S. Hofferberth, Phys. Rev. A **93**, 032512 (2016).
[28] B. Butscher, V. Bendkowsky, J. Nipper, J. B. Balewski, L. Kukota, R. Löw, T. Pfau, W. Li, T. Pohl, and J. M. Rost, J. Phys. B: At. Mol. Opt. Phys. **44**, 184004 (2011).
[29] M. Deiß, S. Haze, and J. Hecker Denschlag, Atoms **9**, 34 (2021).
[30] M. Althön, M. Exner, R. Blättner, and H. Ott, Nat. Commun. **14**, 8108 (2023).
[31] I. Lesanovsky, P. Schmelcher, and H. R. Sadeghpour, J. Phys. B: At. Mol. Opt. Phys. **39**, L69 (2006).
[32] M. Kurz and P. Schmelcher, J. Phys. B: At. Mol. Opt. Phys. **47**, 165101 (2014).
[33] F. Hummel, C. Fey, and P. Schmelcher, Phys. Rev. A **99**, 023401 (2019).
[34] F. Hummel, K. Keiler, and P. Schmelcher, Phys. Rev. A **103**, 022827 (2021).

[35] M. Kurz and P. Schmelcher, Phys. Rev. A **88**, 022501 (2013).
[36] F. Hummel, P. Schmelcher, and M. T. Eiles, Phys. Rev. Res. **5**, 013114 (2023).
[37] R. Srikumar, F. Hummel, and P. Schmelcher, Phys. Rev. A **108**, 012809 (2023).
[38] A. A. T. Durst, M. Simić, N. Abraham, and M. T. Eiles, arXiv:2408.14919.
[39] F. Hummel, C. Fey, and P. Schmelcher, Phys. Rev. A **97**, 043422 (2018).
[40] M. T. Eiles and C. H. Greene, Phys. Rev. A **95**, 042515 (2017).
[41] D. A. Anderson, S. A. Miller, and G. Raithel, Phys. Rev. A **90**, 062518 (2014).
[42] T. Niederprüm, O. Thomas, T. Eichert, and H. Ott, Phys. Rev. Lett. **117**, 123002 (2016).
[43] C. H. Greene and M. T. Eiles, Phys. Rev. A **108**, 042805 (2023).
[44] C. Fey, M. Kurz, and P. Schmelcher, Phys. Rev. A **94**, 012516 (2016).
[45] A. Duspayev and G. Raithel, Phys. Rev. A **105**, 012810 (2022).
[46] Y. Q. Zou, M. Berngruber, V. S. V. Anasuri, N. Zuber, F. Meinert, R. Löw, and T. Pfau, Phys. Rev. Lett. **130**, 023002 (2023).
[47] C. Brukner and A. Zeilinger, Phys. Rev. A **56**, 3804 (1997).
[48] A. Goussev, Phys. Rev. A **85**, 013626 (2012).
[49] G. Kälbermann, J. Phys. A: Math. Gen. **34**, 6465 (2001).
[50] M. Moshinsky, Phys. Rev. **88**, 625 (1952).
[51] A. Zecca, Eur. Phys. J. Plus **126**, 18 (2011).
[52] F. Hummel, M. T. Eiles, and P. Schmelcher, Phys. Rev. Lett. **127**, 023003 (2021).
[53] E. Fermi, Nuovo Cim. **11**, 157 (1934).
[54] C. Bahrim and U. Thumm, Phys. Rev. A **61**, 022722 (2000).
[55] R. W. Molof, H. L. Schwartz, T. M. Miller, and B. Bederson, Phys. Rev. A **10**, 1131 (1974).
[56] W. Li, I. Mourachko, M. W. Noel, and T. F. Gallagher, Phys. Rev. A **67**, 052502 (2003).
[57] J. D. Whalen, S. K. Kanungo, Y. Lu, S. Yoshida, J. Burgdörfer, F. B. Dunning, and T. C. Killian, Phys. Rev. A **101**, 060701(R) (2020).
[58] M. Peper and J. Deiglmayr, Phys. Rev. Lett. **126**, 013001 (2021).
[59] B. J. DeSalvo, J. A. Aman, F. B. Dunning, T. C. Killian, H. R. Sadeghpour, S. Yoshida, and J. Burgdörfer, Phys. Rev. A **92**, 031403(R) (2015).
[60] F. Camargo, J. D. Whalen, R. Ding, H. R. Sadeghpour, S. Yoshida, J. Burgdörfer, F. B. Dunning, and T. C. Killian, Phys. Rev. A **93**, 022702 (2016).
[61] G. C. Groenenboom and H. M. Buck, J. Chem. Phys. **92**, 4374 (1990).
[62] A. Córdoba, Lett. Math. Phys. **17**, 191 (1989).
[63] S. A. Diddams, L.-S. Ma, J. Ye, and J. L. Hall, Opt. Lett. **24**, 1747 (1999).
[64] N. Schlosser, G. Reymond, I. Protsenko, and P. Grangier, Nature (London) **411**, 1024 (2001).
[65] A. M. Kaufman, B. J. Lester, and C. A. Regal, Phys. Rev. X **2**, 041014 (2012).
[66] M. Mildner, A. Horrer, M. Fleischer, C. Zimmermann, and S. Slama, J. Phys. B: At. Mol. Opt. Phys. **51**, 135005 (2018).
[67] Y. Zhang, C. Min, X. Dou, X. Wang, H. P. Urbach, M. G. Somekh, and X. Yuan, Light Sci. Appl. **10**, 59 (2021).
[68] K. B. Crozier, Light Sci. Appl. **8**, 35 (2019).
[69] T. Schmid, C. Veit, N. Zuber, R. Löw, T. Pfau, M. Tarana, and M. Tomza, Phys. Rev. Lett. **120**, 153401 (2018).
[70] A. Duspayev, X. Han, M. A. Viray, L. Ma, J. Zhao, and G. Raithel, Phys. Rev. Res. **3**, 023114 (2021).
[71] N. Zuber, V. S. V. Anasuri, M. Berngruber, Y. Q. Zou, F. Meinert, R. Löw, and T. Pfau, Nature (London) **605**, 453 (2022).
[72] C. Veit, N. Zuber, O. A. Herrera-Sancho, V. S. V. Anasuri, T. Schmid, F. Meinert, R. Löw, and T. Pfau, Phys. Rev. X **11**, 011036 (2021).
[73] T. Klas, J. Bender, P. Mischke, T. Niederprüm, and H. Ott, Phys. Rev. A **108**, L021301 (2023).
[74] M. I. Chibisov, A. A. Khuskivadze, and I. I. Fabrikant, J. Phys. B: At. Mol. Opt. Phys. **35**, L193 (2002).
[75] D. Booth, S. T. Rittenhouse, J. Yang, H. R. Sadeghpour, and J. P. Shaffer, Science **348**, 99 (2015).

PHYSICAL REVIEW A **114**, 022813 (2026)

Vibronic quantum dynamics of ultralong-range high-ℓ Rydberg molecules

Felix Giering, Rohan Srikumar, and Peter Schmelcher
Zentrum für Optische Quantentechnologien, Universität Hamburg, Luruper Chaussee 149, 22761 Hamburg, Germany

(Received 17 March 2026; accepted 16 July 2026; published 13 August 2026)

We investigate the nonadiabatic quantum dynamics of ultralong-range Rydberg molecules using a vibronically coupled two-channel treatment. The two channels are composed of coupled trilobite and butterfly electronic states, formed as a result of S-wave and P-wave scattering of high angular momentum Rydberg electrons with perturbing ground state atoms. Within the Born-Oppenheimer treatment, the P-wave scattering channel introduces an adiabatic decay pathway that affects the stability and lifetimes of trilobite states. Our numerical results show that the vibronic coupling is dependent on the principal quantum number n, and for certain n there is nonadiabatic stabilization against internal molecular decay, facilitating previously studied dynamical effects in pure trilobite molecules. Apart from the internal diffraction effect caused by the backscattering of vibrational wavepackets from the trilobite potential, we also observe interesting multiwell tunneling effects during low-energy oscillations for a range of n values. Our work serves to highlight the fact that the unique vibrational coordinate dependent electronic structure of these polar molecules, along with high-level densities, promises many exciting dynamical effects.

DOI: 10.1103/j7qc-6fww

I. INTRODUCTION

Long-range synthetic molecules formed by engineering Rydberg excitations in ultracold atomic gases present an exciting frontier in few-body quantum physics research [1–11], exhibiting properties not associated with traditional molecular systems. Of recent fame are the exemplar trilobite and butterfly molecules, formed when a Rydberg atom with high electronic angular momentum (ℓ) undergoes S-wave and P-wave scattering from a nearby ground state atom (perturber), respectively [1,2]. They feature exceptionally high dipole moments [12,13] and micrometer scale bond lengths and have been found useful in precision spectroscopy [14,15], prospective preparation of ultracold neutral plasmas [16], and measuring three-body correlations [17,18]. Moreover, these ultralong-range Rydberg molecules (ULRMs) [19–21] offer a great test bed to study unique and exaggerated quantum dynamics [22–24], and external field interactions [25–27]. Recent numerical simulations show that nuclear wavepackets propagating through the undulating trilobite potential energy curves (PECs) undergo backscattering, thereby creating an internal diffraction effect wherein the electronic structure of the dimer diffracts its own radial motion [24], a phenomenon unobserved in standard molecular physics.

The traditional approach to study the quantum dynamics of ULRMs is through the use of the Born-Oppenheimer (BO) approximation [28]. However, recent studies show that nonadiabatic effects are ubiquitous in such systems, mainly due to avoided crossings introduced by high-ℓ states, as well as the high density of electronic states that are not energetically well separated [29,30]. Such avoided crossings can be highly singular, sometimes forming conical intersections, when the principal quantum number n of the Rydberg atom is taken as a synthetic dimension [31,32]. In alkali ULRMs, the P-wave butterfly potential induces an avoided crossing to the trilobite and low-ℓ potentials, introducing an adiabatic decay pathway. This affects the lifetimes of bound ULRM states [33], while also allowing for internal quantum reflection [34]. Recent experimental observations of highly excited nonadiabatic resonances stabilized against internal adiabatic decay [35] confirm the necessity to go beyond single channel BO approximation to accurately model these molecules. Apart from atom-atom ULRMs, there is also an increasing interest in the study of nonadiabatic phenomena arising in other long-range Rydberg systems, like Rydberg atom-ion molecules [36], macrodimers [4,37], Rydberg bimolecules [38], and trapped Rydberg ion systems [39,40].

The multichannel wavepacket dynamics in ULRMs remains largely unexplored. The authors of previous works have mainly utilized Landau-Zener based semiclassical analysis [31,41,42], or limited themselves to spectral calculations [29,30,35,43]. An exact quantum dynamical study will be able to validate previous semiclassical approximations, as well as point out why and where they fail. Moreover, it can confirm whether or not previously simulated single channel dynamical effects, like the internal diffraction of vibrational wavepackets in the trilobite potential [24], are suppressed due to nonadiabatic effects. In conventional molecules vibronic dynamics facilitate many well documented phenomena like ultrafast nonradiative transitions [44–46], surface hoppings [47,48], and predissociation [49,50], which are not explainable by adiabatic physics. In atom-ion scattering, vibronic dynamics

Published by the American Physical Society under the terms of the Creative Commons Attribution 4.0 International license. Further distribution of this work must maintain attribution to the author(s) and the published article's title, journal citation, and DOI.

is also necessarily included in studies of charge exchange collisions [51], but highly polar ULRMs, with large bond lengths and high-level densities, could exhibit new vibronic dynamical effects that are not seen in regular molecules or scattering processes.

In this work we study the dynamics of ^{87}Rb dimers, in coupled trilobite and butterfly configurations using a two-channel treatment that considers the mixing of nuclear and electronic motion. A comprehensive theoretical study of this system, which looks at the structure of electronic states and nonadiabatic couplings as a function of n, develops diabatization strategies to work around singular couplings, and calculates the molecular vibronic spectra, has already been presented [29]. Here we perform wavepacket dynamics, with vibrational Gaussian states initialized in the trilobite PEC, radially far off from any avoided crossings. As the wavepackets probe the avoided crossing, we see the onset of n-dependent nonadiabatic transitions between different PECs. We use the probability distribution function in position and momentum representations, as well as the evolution of different electronic state populations, to characterize vibronic effects for each n. For some n, the propagating diffraction effect is conserved against internal molecular decay due to nonadiabatic stabilization. We also present here a unique multiwell tunneling phenomenon due to low-energy oscillations around the minima of the trilobite potential. For a range of n values, these trilobite curves exhibit bound vibrational states localized between multiple wells, near the potential minima, allowing unique interference effects in their low-energy dynamics. In comparison, trilobite PECs with much smaller n values ($\leqslant$30) primarily exhibit low-energy dynamics confined to a single well. The calculations presented here neglect the fine and hyperfine structure of the constituent atoms for the sake of ease. Inclusion of the spin couplings would necessitate a more complex multichannel treatment, relevant to future studies.

This work is organized as follows. Section II presents the theoretical and computational framework, introducing the general molecular Hamiltonian and nonadiabatic couplings in Sec. II A, discussing the specific electronic interactions in the ULRM in Sec. II B, and describing the two-channel vibronic dynamics in Sec. II C. Section III presents the results of our numerical simulation, starting from the potential energy structure in Sec. III A, the two-channel wavepacket dynamics in Sec. III B, and multiwell tunneling effects in Sec. III C. The conclusions and outlook of our work are given in Sec. IV.

II. THEORETICAL AND COMPUTATIONAL FRAMEWORK

We begin by formulating the molecular Hamiltonian and the corresponding time-dependent Schrödinger equation which allows us to study the internal molecular dynamics of ULRM. We then discuss the Born-Oppenheimer approximation, the emergence of nonadiabatic couplings between BO adiabatic electronic states, and the associated diabatization procedure which is crucial for constructing a smooth multichannel representation. Subsequently, we highlight the electronic structure of the ULRM and the calculation of adiabatic states and PECs. Finally, we establish the two-channel vibronic system and describe the numerical propagation scheme, where complex absorbing potentials are employed to avoid artificial reflections at the grid boundaries.

A. Molecular Hamiltonian and nonadiabatic couplings

We start by considering two ^{87}Rb atoms, one of which is excited to the Rydberg electronic state. Let us define R as the internuclear separation between the ionic core and the neutral atom (taken along the z axis, with the Rydberg core at the origin), and $\mathbf{r}$ as the coordinate of the Rydberg electron with respect to the Rydberg core. The internal molecular dynamics (in atomic units) in the body-fixed frame is then governed by the time-dependent Schrödinger equation

$$i\frac{\partial}{\partial t}\Psi_m(\boldsymbol{r};R\boldsymbol{e}_z,t)=\hat{H}\Psi_m(\boldsymbol{r};R\boldsymbol{e}_z,t), \tag{1}$$

with Ψ_m being the molecular wavefunction and $\hat{H}$ the molecular Hamiltonian given by

$$\hat{H}=-\frac{\nabla_R^2}{2\mu}-\frac{\nabla_r^2}{2}+V_{\mathrm{Ryd}}(\boldsymbol{r})+V_{\mathrm{ea}}(\boldsymbol{r};R\boldsymbol{e}_z) \tag{2}$$

where μ is the reduced mass of the system. The first two terms of the Hamiltonian describe the kinetic energy operators corresponding to the nuclei and the Rydberg electron, respectively. Moreover, $V_{\mathrm{Ryd}}(r)$ represents the interaction between the Rydberg electron and the ionic core and $V_{\mathrm{ea}}(\mathbf{r};R)$ accounts for the interaction between the Rydberg electron and the perturbing ground state atom. The last three terms of Eq. (2) separately form the electronic Hamiltonian $H_{\mathrm{el}}(\mathbf{r};R)$. Solving the electronic Schrödinger equation parametrized by R yields

$$H_{\mathrm{el}}(\boldsymbol{r};R)\,\psi_i(\boldsymbol{r};R)=V_i(R)\,\psi_i(\boldsymbol{r};R), \tag{3}$$

where $V_i(R)$ are the adiabatic potential energy curves and $\psi_i(\boldsymbol{r};R)$ are the corresponding electronic states. Since $\{\psi_i\}$ forms a complete orthonormal basis (commonly known as the Born-Oppenheimer basis), any given molecular wavefunction can be expanded as $\Psi_m=\sum_i \chi_n(R)\psi_i(\boldsymbol{r},R)$ [52]. Here $\chi_i(R)$ are the R-dependent expansion coefficients that represent the nuclear wavefunction.

Inserting this Born-Oppenheimer expansion in Eq. (2), integrating out the electronic states, and rearranging the terms, we get the multichannel Schrödinger equation

$$-\frac{1}{2\mu}(\nabla_R+\hat{P})^2\boldsymbol{\chi}+\hat{V}\boldsymbol{\chi}=i\frac{\partial}{\partial t}\boldsymbol{\chi}, \tag{4}$$

where $\boldsymbol{\chi}$ is a vector of all χ_n, $\hat{V}$ is a diagonal operator containing all V_n, and $\hat{P}$ is the first order nonadiabatic coupling operator whose matrix elements are given by

$$P_{ij}(R)=\int \psi_i(\boldsymbol{r};R)\partial_R\psi_j(\boldsymbol{r};R)d\boldsymbol{r}. \tag{5}$$

The P-matrix elements appear as off-diagonal terms in the nuclear kinetic energy operator, effectively coupling different adiabatic electronic channels. Note that a more elaborate discussion on derivative couplings can be found in our previous works [29,30], and methodical derivations that show how to obtain Eq. (4) from Eq. (2) are discussed in standard textbooks [53,54]. In the Born-Oppenheimer approximation, the nonadiabatic term $\hat{P}$ is completely ignored, resulting in decoupled single channel equations that describe the nuclear

dynamics of the molecule. This framework provides a natural first description of ultralong-range Rydberg molecules, where the diatomic system time-evolves in a given potential energy curve defined by its time-independent electronic state.

However, nonadiabatic couplings become particularly pronounced near avoided crossings of the adiabatic PECs. Our previous works highlight such cases where a nonadiabatic treatment of the ULRM was necessary due to the presence of avoided crossings [29,30,55]. In such regions the BO approximation breaks down due to singular or rapidly varying couplings, and the adiabatic basis becomes ill suited for describing nuclear dynamics. To remedy this, it is advantageous to perform a basis transformation such that the nuclear kinetic couplings are replaced with off-diagonal potential terms. Given that Eq. (4) is invariant under unitary transformations, any $\hat{U}_d$ which satisfies the condition $\nabla \hat{U}^d = -\hat{P}\hat{U}^d$ will force the derivative couplings to become zero, and is commonly known as a diabatic transform [53,56]. This allows us to rewrite Eq. (4) as

$$-\frac{1}{2\mu}\nabla_R^2 \boldsymbol{\chi}^d + \hat{V}^d \boldsymbol{\chi}^d = i\frac{\partial}{\partial t}\boldsymbol{\chi}^d, \tag{6}$$

where $\boldsymbol{\chi}^d = \hat{U}^d \boldsymbol{\chi}$ are called the diabatic states and the constituents of $\hat{V}^d = \hat{U}_d^\dagger \hat{V} \hat{U}_d$ are called diabatic PECs. In the general case of polyatomic molecules, $\hat{U}^d$ is not uniquely defined and approximate path-dependent diabatization schemes are used to perform vibronic dynamics. Fortunately, if the system is one dimensional (like a diatomic molecule) one can always find a unique diabatization scheme numerically, although this becomes computationally demanding with increasing number of highly coupled channels. Furthermore, in the simplest description of a vibronic system, i.e., a two-channel system with a single parameter R, the diabatic transform is a basic unitary rotation where the rotation angle is given by

$$\theta(R) = \int_R^\infty P_{12}(R_1) dR_1. \tag{7}$$

With the two-channel diabatic framework established, the next step is to specify the electronic interactions responsible for binding in ultralong-range Rydberg molecules.

B. Electronic interaction

The electronic Hamiltonian for the ULRM is given by $H_{\rm el} = H_{\rm Ryd} + V_{\rm ea}$, where $H_{\rm Ryd}$ describes the Rydberg atom and $V_{\rm ea}$ describes the low-energy electron-atom scattering interaction. The S-wave and P-wave scattering can be modeled using Fermi-type pseudopotentials [57,58] such that

$$V_{\rm ea}(\boldsymbol{r}; R) = 2\pi a_S(k)\delta(\boldsymbol{r} - R\boldsymbol{e}_z) + 6\pi a_P(k)\nabla_r \delta(\boldsymbol{r} - R\boldsymbol{e}_z)\nabla_r, \tag{8}$$

with a_S and a_P denoting the energy-dependent S-wave scattering length and P-wave scattering volume, respectively (scattering length taken from [15]). The electron wave number k can be semiclassically approximated by $k = (2/R - 1/n^2)^{1/2}$, where n is the principal quantum number of the Rydberg excitation. In the spin triplet configuration, both a_S and a_P have negative values, facilitating an attractive interaction and binding the molecule. The unperturbed Rydberg electron states $\{\phi_{n\ell m}\}$ are described by the principal and angular momentum quantum numbers (n, ℓ, m), respectively. Since the internuclear axis is taken to be along the z axis, only atomic states with $m = 0$ contribute. They form the eigenbasis of the electronic Rydberg Hamiltonian with the corresponding energies $E_{n\ell} = -(n - \delta_\ell)^{-2}/2$, with δ_ℓ denoting the ℓ-dependent quantum defect [59]. In rubidium the low angular momentum states ($\ell \leqslant 3$) exhibit finite quantum defects, energetically shifting them away from the near-degenerate hydrogenic manifold of high-ℓ states. These low-ℓ states form shallow PECs allowing a few bound states. The high-ℓ states, however, are hybridized by the perturber, resulting in deep potentials that can hold hundreds of bound states. The most prominent of these high-ℓ states are the so-called trilobite and butterfly molecules, split from the hydrogenic manifold due to S-wave and P-wave electron-atom scattering.

Recent works have already characterized the vibronic structure of the coupled trilobite-butterfly system, successfully showing the impact of these avoided crossings in the calculated and observed spectra [29,35]. If one is to ignore the quantum defect structure and limit the system to a single hydrogenic n manifold, one can analytically derive a coupled two-channel model based on the pure trilobite and butterfly wavefunctions,

$$\psi_t(\boldsymbol{r}; R) = \frac{1}{\sqrt{\sum_\ell |\phi_{n\ell 0}(R)|^2}} \sum_\ell^{n-1} \phi_{n\ell 0}(\boldsymbol{r})\phi_{n\ell 0}(R) \tag{9}$$

$$\psi_b(\boldsymbol{r}; R) = \frac{1}{\sqrt{\sum_\ell |\partial_R \phi_{n\ell 0}(R)|^2}} \sum_\ell^{n-1} \phi_{n\ell 0}(\boldsymbol{r})\partial_R\phi_{n\ell 0}(R), \tag{10}$$

respectively. However, since the above given states are not orthogonal to each other, expanding the electronic Hamiltonian in the $\{|\psi_t\rangle, |\psi_b\rangle\}$ basis is not straightforward, and does not guarantee the validity of the formalism presented in Sec. II A. Fortunately, since $V_{\rm ea}$ is a rank-2 operator, its image space can be spanned by any constituent pair of linearly independent wavefunctions. Recently, it was shown that [32] one can utilize a semiunitary transform to project the matrix representation of $V_{\rm ea}$ in the hydrogen atom basis to a perturber spherical basis, following which one obtains the potential energy operator

$$V = \begin{pmatrix} V_t & V_c \\ V_c & V_b \end{pmatrix}, \tag{11}$$

where $V_t = 2\pi a_S(k) \sum |\phi_{n\ell 0}(R)|^2$ and $V_b = 6\pi a_P(k) \sum |\partial_R \phi_{n\ell 0}(R)|^2$ are the trilobite and butterfly PECs, and $V_c = \sqrt{12\pi^2 a_S(k) a_P^3(k)} \sum \phi_{n\ell 0}(R)\partial_R\phi_{n\ell 0}(R)$ is the coupling between them [32,35]. We will obtain the two channel adiabatic PECs and electronic states by diagonalizing the above given matrix. However, it is already clear that the coupled trilobite-butterfly system exhibits conical intersections at (n, R) coordinates, when $V_t = V_b$ and $V_c = 0$ simultaneously. The first condition is roughly fulfilled when the S-wave and P-wave scattering phases are equal [60], and the second condition is fulfilled when the hydrogenic ns state has a node at R (derived using Coulomb summation rules [61,62]). This model was used to successfully predict the n-dependent behavior of the avoided crossing width and the derivative

coupling element, which in turn affected the experimentally observed stability of nonadiabatic resonance states [35]. However, in view of performing exact quantum dynamics, we do not utilize this hydrogenic approximation. Our numerical model considers the quantum defect structure of low-ℓ states, and is not limited to a single n manifold. The electronic spectra and nonadiabatic couplings exhibited by such a model have also been discussed comprehensively in Ref. [29]. This work is exclusively focused on extending these studies by performing vibrational dynamics simulations in the coupled butterfly-trilobite configuration.

Here we mention that the state of the art Green's function methods [63] provide a more accurate description of the electronic structure of the ULRM; however, they do not allow for the calculation of the electronic states and their couplings so far. Moreover, spin-orbit and hyperfine interactions [64,65] are neglected in our model so that a two-channel treatment becomes possible. Fortunately, recent works show that a simple spinless two-channel system can already explain observed nonadiabatic phenomena in ULRMs very well [35]. Hence we choose to focus only on the two-channel case relevant for the trilobite-butterfly interaction, which is well justified when the dynamics is dominated by a pair of energetically isolated states with localized coupling, while all other channels remain weakly interacting and well separated. As a first study we choose to focus on a two-channel model that includes the primary nonadiabatic correction to the dynamics, introduced by the avoided crossing between trilobite and butterfly states. For comparison, the nonadiabatic couplings obtained using a three-channel model are discussed in Appendix B.

C. Computational approach: Two-channel vibronic dynamics

We start by obtaining the adiabatic PECs and the corresponding electronic wavefunctions for a given n by diagonalizing the electronic Hamiltonian within a finite Rydberg basis $\{\phi_{n'\ell'0}\}$ that includes all states with $n' \in \{n-2, n+2\}$. Then we proceed to calculate the diabatic transform and the diabatic PECs for the two-channel trilobite-butterfly system. The initial nuclear wavepacket is a Gaussian function in the first adiabatic channel, i.e., $\boldsymbol{\chi}^a = (\chi_1^a,\ \chi_2^a)^T$, with

$$\chi_1^a(R,0) = \frac{1}{(\pi\sigma^2)^{1/4}} \exp\left[-\frac{(R-R_0)^2}{2\sigma^2}\right], \tag{12}$$

$$\chi_2^a(R,0) = 0. \tag{13}$$

Initializing the wavepacket in the adiabatic basis allows us to populate the trilobite or butterfly state selectively, which is made difficult in the diabatic basis due to strong mixing of electronic states. The adiabatic wavefunction is then transformed into the diabatic basis via $\boldsymbol{\chi}^d(R, t=0) = \hat{U}(R)\,\boldsymbol{\chi}^a(R, t=0)$. We then propagate $\boldsymbol{\chi}^d(R,t)$ using the diabatic Schrödinger equation given by Eq. (6).

Time propagation of the wavepacket is performed using the Crank-Nicolson scheme [66,67], which provides stable and unitary time evolution. The second derivative is evaluated using finite differences of tenth order [68], ensuring high numerical accuracy even for small grid spacings. In our simulations, we use a grid spacing of $\Delta R \approx 1 a_0$ and a time step of $\Delta t \approx 0.001$ ns, chosen such that the energy scale of the system is well resolved [69]. Quantum reflection at the grid boundaries can lead to unphysical interference in the wavepacket dynamics. To prevent this, we employ a complex absorbing potential (CAP) [70,71] that smoothly absorbs the wavefunction near the grid edge and thus simulates the molecular decay due to the open channel nature of our system. See Appendix A for more details on the CAP implementation.

At every time step the total probability density is calculated to be

$$\rho(R,t) = \left|\chi_1^d(R,t)\right|^2 + \left|\chi_2^d(R,t)\right|^2, \tag{14}$$

and the diabatic channel populations are calculated to be

$$p_i^d(t) = \int dR\, \left|\chi_i^d(R,t)\right|^2. \tag{15}$$

One can perform an inverse diabatization transform $\boldsymbol{\chi}^a = U^\dagger\,\boldsymbol{\chi}^d$ to obtain the adiabatic channel populations

$$p_i^a(t) = \int dR\, \left|\chi_i^a(R,t)\right|^2 \tag{16}$$

which help us understand how the electronic states are mixed as a function of time due to vibronic dynamics. Due to the CAP the time evolution is no longer unitary and the total population

$$p_{\text{tot}}(t) = \sum_i p_i^a(t) = \sum_i p_i^d(t) \tag{17}$$

does not maintain unit value, as the wavefunction is absorbed at the end of the grid. Note that the total probability density $\rho(R)$ as well as the total population p_{tot} are basis-independent quantities and hence invariant under the diabatization transform. To understand the scattering effects in the two-channel problem, one can use the Fourier transform to calculate the momentum space wavefunction $\tilde{\chi}(P,t) = \mathcal{F}[\chi(R,t)]$ in each channel, and consequently obtain the total momentum space probability distribution $\tilde{\rho}(P,t) = |\tilde{\chi}_1(P,t)|^2 + |\tilde{\chi}_2(P,t)|^2$, where P is the momentum of the nuclear wavepacket. In the next section, we numerically investigate the vibronic dynamics of the ULRM within the context of internal diffraction dynamics, multiwell tunneling effects, and nonadiabatic decay.

III. RESULTS AND DISCUSSIONS

In the following section, we discuss the results of our numerical simulations. We start with the adiabatic and diabatic potential energy curves as well as the nonadiabatic couplings in the coupled trilobite-butterfly system. We then study the multichannel internal diffraction effect, and analyze the n-dependent nonadiabatic corrections by studying the probability density functions of the evolving wavepacket as well as the population dynamics. Finally, we unravel multiwell tunneling effects in the low-energy oscillations around the minima of the trilobite potential.

A. Potential energy structure

We start with a brief review of the electronic structure of a high-ℓ ULRM. Figure 1 shows the adiabatic PECs for an $n = 55$ ULRM obtained by diagonalizing the electronic Hamiltonian, with the exemplary n value being ideal for observing

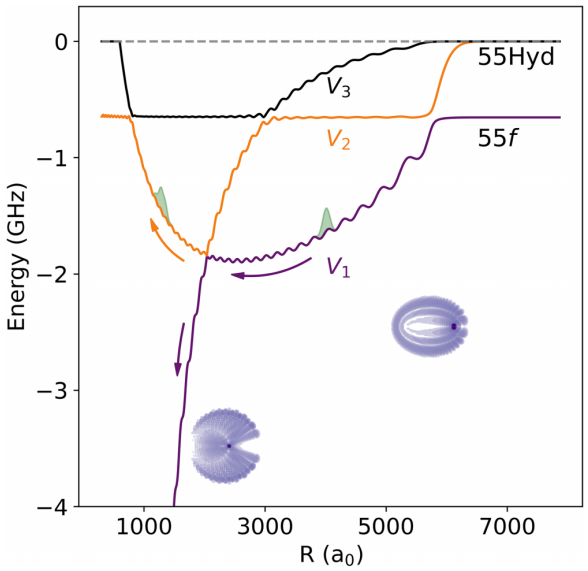


FIG. 1. The Born-Oppenheimer potentials of the $n = 55$ ULRM, obtained by solving the electronic Schrödinger equation. The adiabatic potentials are highlighted as V_1 (violet), V_2 (orange), and V_3 (black), whereas the gray dashed curves show the unperturbed hydrogenic manifold. The wavepackets and arrows are used to illustrate the possible trajectories of a time-evolving nuclear wavefunction. The probability density plots of $\psi_1(\mathbf{r}, R)$ (corresponding to the PEC V_1) calculated at $R = 1400a_0$ and $R = 4880a_0$, portray the change of electronic structure from trilobite to butterfly states as R changes.

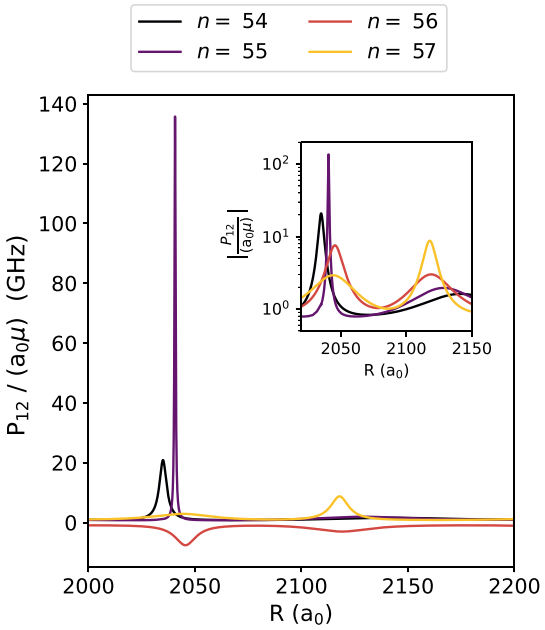


FIG. 2. The first order derivative coupling element $P_{12}/(\mu a_0)$ as a function of the internuclear distance R, for varying n values. The inset depicts the magnitude of P_{12} with log scaling of the y axis.

internal diffraction effects. The adiabatic PECs relevant to the two-state model are highlighted in color (V_1 as blue and V_2 as red), whereas states corresponding to the gray adiabatic curves are not considered in further calculations. When the perturber is radially outside the Rydberg atomic orbital ($R \geqslant 2n^2$), the adiabatic potentials V_1 and V_2 energetically coincide with the unperturbed $55f$ quantum defect state and the high-ℓ hydrogenic state, respectively. At smaller R values the S-wave scattering hybridizes the hydrogenic manifold, introducing an avoided crossing between the trilobite PEC and the $\ell = 3$ PEC, forming the V_1 potential. Here, we choose to focus only on the two highlighted curves as a first approximation. Without the P-wave interaction, V_1 would be a pure trilobite curve with the structure of an anharmonic envelope overlaid with an oscillatory potential [24]. However, the P-wave shape resonance induces a steeply descending butterfly potential that forms a narrow avoided crossing between V_1 and V_2. After the avoided crossing V_1 adiabatically acquires the P-wave character, eventually causing internal molecular decay due to autoionization or ℓ-changing collisions [41]. However, we know that a narrow avoided crossing enhances the vibronic coupling terms, enabling the nonadiabatic transition from V_1 to V_2, possibly offering a stabilizing mechanism against internal molecular decay. The adiabatic electronic probability density plots of $\psi_1(\mathbf{r}, R)$ calculated sufficiently before and after the avoided crossing show how ψ_1 adiabatically changes from trilobite to butterfly configuration.

Figure 2 shows the nonadiabatic coupling P_{12} between the selected states ψ_1, ψ_2 for the selected range of n. We scale P_{12} by $1/(\mu a_0)$ to analyze the energy contribution of the nonadiabatic coupling term as it appears in the Hamiltonian, in GHz units. We see that the derivative coupling strongly depends on n, displaying an order of magnitude difference between the most nonadiabatic ($n = 55$) and most adiabatic ($n = 57$) cases. This is highlighted in the inset, where the y axis is log scaled to simultaneously show the smaller structures in energy. From a semiclassical perspective, the absolute value of the P_{12} at the avoided cross massively impacts the probability that nuclei perform a nonadiabatic jump, i.e., Landau-Zener (LZ) transition from ψ_1 to ψ_2. However, we already see from the inset that the calculated derivative couplings do not form a Lorentzian curve, as is typical in LZ transitions. This is because the level spacing and the derivative coupling elements are comprised of hybridized atomic wave fuctions and their derivatives [29], creating an oscillatory non-Lorentzian structure. The standard Landau-Zener theory on the other hand assumes a linear crossing with a well-defined constant velocity. This is clearly not what happens in low-energy dynamics of ULRMs, where the time-evolving wavefunction probes highly oscillatory potential energy curves and nonadiabatic couplings. Surprisingly, the nonadiabatic transition rates for high-energy dynamics (when the wavefunction starts from the dissociation threshold), is qualitatively very well predicted by the LZ model (see [35]). This could be because high-lying states and their momentum $k(R)$ can be reasonably approximated semiclassically, and their rapidly changing wavefunctions allow a WKB style representation, and probes the crossing with a well-defined velocity. Even so, the standard Landau-Zener theory does not give us exact

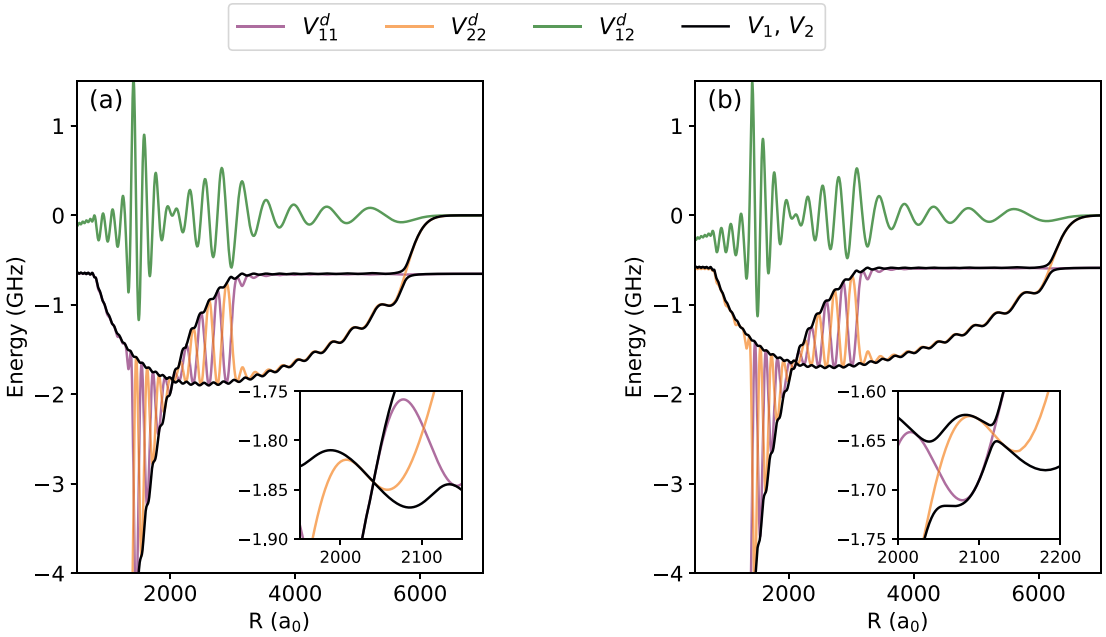


FIG. 3. The adiabatic and diabatic PECs of the (a) $n = 55$ and (b) $n = 57$ ULRMs are shown, with the corresponding insets showcasing a magnified plot of the avoided crossing. The black curves are the adiabatic potentials (V_1, V_2) and the colored curves are the diagonal (V^d_{11}, V^d_{22}) and off-diagonal (V^d_{12}) terms of the diabatic potential energy operator.

time-evolving wavefunctions, as we aim to study here. It is of course possible that an exact multichannel calculation which involves the degenerate manifolds reproduces the semiclassical result, but for now we continue presenting the results of our two-channel study.

Figures 3(a) and 3(b) show the diabatic PECs and the adiabatic PECs (solid black curves) for $n = 55$ and $n = 57$, respectively. Primarily, we see that the highly oscillatory (diagonal) diabatic PECs start deviating from their adiabatic counterparts, far away from the avoided crossing ($>1000a_0$). This is accompanied by the off-diagonal potentials acquiring large nonzero values away from the avoided crossing. Moreover, we see that the global structure of the diabatic curves looks reasonably similar between $n = 55$ and $n = 57$, despite a large difference in the magnitude of derivative couplings. However, the magnified plots (insets of Fig. 3) do show that adiabatic PECs exhibit a narrow near-exact crossing for $n = 55$, and a wider avoided crossing for $n = 57$. This validates the large difference in the magnitude of P_{12} for the two n values. To summarize, the nonadiabatic couplings and the diabatic potentials of the two-channel system deviate considerably from traditional molecular physics, or Landau-Zener models. A more detailed analysis of the vibronic couplings between trilobite and butterfly potentials can be found elsewhere (see Ref. [29]). Note that the exact structure of the diabatic potentials varies considerably depending on the number of channels used in diabatization. In reality, the highly polar electronic states are nonadiabatically coupled to other quantum defect states, as well as the quasidegenerate manifold. To explain higher dynamics spanning the entire potential depth, one would need to incorporate higher quantum defect states and the unperturbed high-ℓ manifold into a multichannel model. Fortunately, the internal diffraction dynamics we probe requires relatively lower kinetic energies [24]. Since we see that the nonadiabatic couplings are still maximal at the avoided crossing, a two-channel model that considers the avoided crossing should give us a reliable semiquantitative model for the problem at hand.

B. Two-channel wavepacket dynamics

We begin our simulation of the wavepacket dynamics, by initializing the nuclear wavefunction as a Gaussian state in the V_1 adiabatic PEC, corresponding to the ψ_1 electronic state. The initial position and width of the Gaussian are taken to be so that the ensuing dynamics display internal diffraction effects. This is because the oscillatory structure of the trilobite potential acts as a diffraction grating in momentum space. The anharmonic envelope of the pure trilobite PEC allows the wavepacket to gain momentum as it traverses down the potential, consequently scattering off the oscillatory structure of the PEC. At appropriate width and momenta, the consequent coherent backscattering causes the wavepacket to appear as a propagating diffraction pattern. A comprehensive analysis of this phenomenon is presented elsewhere (see Ref. [24]), including the appropriate initial parameters needed to observe this effect. Here we build upon the previous work, and take the required parameters needed to observe diffraction, as given. Our aim then, is to see how the vibronic coupling between trilobite and potential affects the previously simulated diffraction dynamics. We try to analyze the n dependence of the vibronic corrections, by contrasting the $n = 55$ case with $n = 57$, featuring the most and the least nonadiabatic coupling strength at the avoided crossing, respectively.

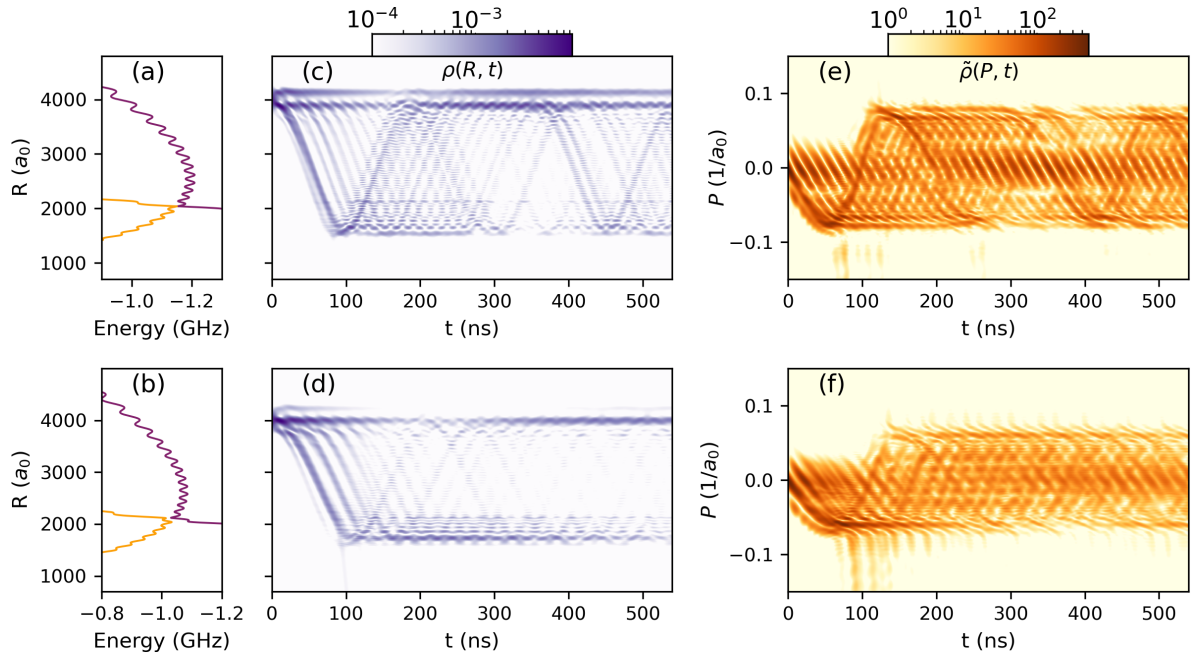


FIG. 4. Two-channel wavepacket diffraction dynamics. The potential energy structure of the $n = 55$ and $n = 57$ ULRMs in the relevant region are shown in (a), (b). The time-evolving total probability density $\rho(R, t)$ in the position representation is shown for $n = 55$ (c) and $n = 57$ (d). The corresponding total probability density in momentum representation, i.e., $\tilde{\rho}(P, t)$, is shown for $n = 55$ (e) and $n = 57$ (f).

The relevant potential energy structures of the $n = 55$ and $n = 57$ molecule are shown in Figs. 4(a) and 4(b). We choose to initialize the Gaussian wavepacket $\chi_1^a(t = 0)$ [Eq. (13)], with $\sigma = 100a_0$, and $R_0 = 4000a_0$. The width σ is chosen while taking into consideration the available initial states (vibrational ground states of low-ℓ PECs [24]) for the pump-probe experiment. At the given R_0 the diabatic and adiabatic PECs coincide and show a predominant trilobite character. Moreover, the initial configuration presented was also used in the previous single channel study [24], giving the results comparative value. Figures 4(c) and 4(d) show the resulting time-evolving probability density functions for $n = 55$ and $n = 57$, in position representation. As expected, simulations with both the n values exhibit a propagating diffraction pattern for $t < 100$ ns, until they probe the avoided crossing. We see that $n = 55$ continues to exhibit propagating wavepacket dynamics mimicking the pure trilobite case, although there is a noticeable decrease in the contrast of the pattern compared to the single channel case. This can be explained by the consistent nonadiabatic transition of the nuclear wavepacket between V_1 and V_2 PECs due to the near-exact crossing, so that the nuclear wavepacket effectively experiences a pure trilobite potential, despite the actual wavepacket dynamics occurring on coupled channels. On the other hand, the $n = 57$ case, with a wider avoided crossing, shows a much clearer diminishing of the diffraction pattern after the first crossing. As the wavepacket keeps oscillating it probes the crossing multiple times, thereby destroying the diffraction pattern. When analyzing the dynamics in the momentum space representation [see Figs. 4(e) and 4(f)], we see that the diffraction pattern is more coherent for the n value with the narrower crossing. In addition, when the wavepacket reaches the avoided crossing for the first time, we see that a considerable fraction of the wavepacket gains momentum and escape the propagating diffraction pattern. This is because the nuclei which follow the P-wave decay pathway experience a steep drop in the potential, resulting in the wavefunction gaining more momentum before it is eventually absorbed by the CAP. This phenomenon is more dramatically observed in the case of $n = 57$ due to the wider avoided crossing facilitating more adiabatic decay.

We now focus on the dynamics of the population calculated using the aforementioned formulas [Eqs. (15)–(17)]. Figures 5(a) and 5(b) show the total population (marked), as well as the channel populations in adiabatic (solid lines) and diabatic (dashed lines) representations. For both n values, the total population is constant (unit value) for the first 100 ns, until the wavefunction probes the avoided crossing. The population starts decreasing as expected, when the wavepacket is absorbed by the CAP after the avoided crossing. We also see that the populations in the adiabatic channels start mixing slightly before the total population decrease. This corresponds to the short time dynamics that characterize the transfer of population from the trilobite to the butterfly state near the avoided crossing. The diabatic channel populations, however, start mixing much before the wavepackets reach the avoided crossing, in accordance with our analysis of extended off-diagonal nonadiabatic couplings in the previous section. This hints at the non-Landau-Zener nature of the mathematical model used. Comparing Fig. 5(a) to Fig. 5(b), we see that

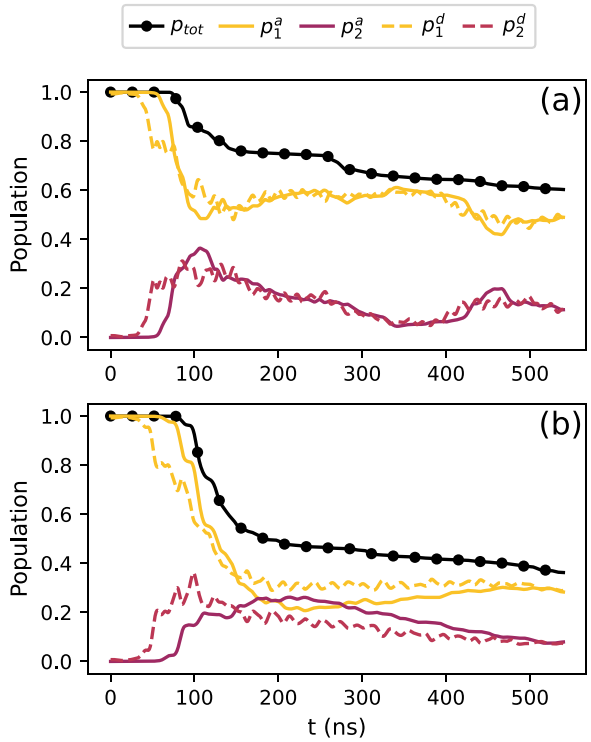


FIG. 5. Time evolution of the diabatic populations p_d (dashed curves), and the adiabatic populations p_a (solid curves) for channels 1 and 2, as well as the the total population p_{tot} (dotted curve). Panel (a) depicts the population dynamics for $n = 55$, and (b) depicts the population dynamics for $n = 57$.

the decrease in total population is indeed more prominent for $n = 57$, due to the wider avoided crossing.

C. Multiwell tunneling dynamics

Finally, we move on from higher-energy vibronic dynamics, and shift our focus to low-energy dynamics between different adjacent wells of PEC. We know that for low n values ($\leqslant 30$) vibrational ground states are generally localized in each single well of the oscillatory potential (see the Appendix of Ref. [14]). Here, narrow Gaussian wavepackets (comparable to accessible pump states) that are initialized in any particular well primarily perform intrawell oscillations. As we increase the n value, the oscillatory structure becomes more and more shallow, decreasing the potential barrier between adjacent wells. Consequently, vibrational ground states near the trilobite minima start to become delocalized across multiple adjacent wells, and corresponding wavepackets exhibit multiwell tunneling effects.

Starting from $n \geqslant 42$, the vibrational ground states can be delocalized across two wells, allowing us to engineer two-well interference effects. Figure 6(a) shows the adiabatic potential V_1 of $n = 42$, near the trilobite energetic minima. We probe this region by initializing the vibrational wavepacket (red curve) as a Gaussian centered around the midpoint of the well ($R_0 = 2064a_0$), with $\sigma = 40a_0$ for $n = 42$. The ensuing dynamics is shown in Fig. 6(b), where we see a periodic interference pattern that spans two different wells. The pattern can be explained by decomposing the wavepacket in the vibronic eigenbasis, only considering eigenstates with a large contribution [$|c_\nu|^2 = |\langle\chi(R,t)|\chi_\nu\rangle|^2$]. The vibronic spectra are plotted in Fig. 6(c), where we see that the two highlighted wavefunctions (the ground state and the first excited state of the trilobite PEC), delocalized across the two potential wells, possess the highest overlap with the initial states. The other states only marginally contribute to the dynamics (gray lines), due to negligible overlap with the initial wavefunction. One can then successfully explain the pattern as a two-well hopping dynamics, with a fixed period $\tau = 400$ ns that is the inverse of the vibrational splitting $E_2 - E_1 = 2.5$ MHz. Similarly, Figs. 6(d)–6(f) display and explain the two-well hopping for the $n = 46$ ULRM. Just like the previous case, the wavepacket is a time-evolving superposition of the two lowest-energy vibration states, localized across two wells. Their larger vibrational splitting (∼4 MHz) creates a shorter hopping period of 250 ns.

For higher n values in the range 49–52, the vibrational states can be localized across three different wells. Figure 7(a) shows the adiabatic potential V_1 of the $n = 49$ trilobite potential near its energetic minima, as well as the initial Gaussian wavepacket ($R_0 = 2450a_0$, with $\sigma = 40a_0$) of choice. The ensuing dynamics is portrayed in Fig. 7(b), where we see that pattern exhibits two different periods, with most of the population tunneling between next-nearest neighboring wells. But some of the population periodically localizes in the intermediate well with a pulsing period almost twice as large as the tunneling period. The pattern can be mainly explained using the phase relations between the responsible eigenstates [solid lines in Fig. 7(c) marked as $\nu = 0, 1, 2$] that have a high overlap with the initial Gaussian. While the highlighted bound vibronic states are centered around separate adiabatic potential wells, the wavefunction is clearly localized across other neighboring wells. This partial delocalized structure, along with very low-level splitting, leads to very interesting multiwell tunneling dynamics. The three eigenstates with the largest overlap with the initial wavepacket have energies $E_0 = -1.687$ GHz, $E_1 = -1.680$ GHz, and $E_2 = -1.678$ GHz. The slow tunneling between the two outer wells is mainly governed by the interference between the first and second excited states. Their small splitting of $E_2 - E_1 = 0.002$ GHz corresponds to an interference frequency of about 2 MHz, giving rise to a tunneling timescale of roughly 500 ns. In contrast, the faster pulsation of probability density in the central well arises mainly from the interference between the ground and second excited states. The larger splitting of $E_2 - E_0 = 0.009$ GHz corresponds to a frequency of 9 MHz, which explains the shorter modulation period of about 110 ns visible in Fig. 7(b). Figures 7(d)–7(f) present similar multiwell tunneling effects for the $n = 51$ ULRM, whose origin can be traced back to three similarly delocalized vibronic states. For even higher n values we can also see four-well and five-well dynamical effects. However, since the wavefunctions are no longer properly localized around any single well, the emerging patterns become less clear. For increasing n, the oscillatory structure eventually becomes too shallow to hold localized vibrational

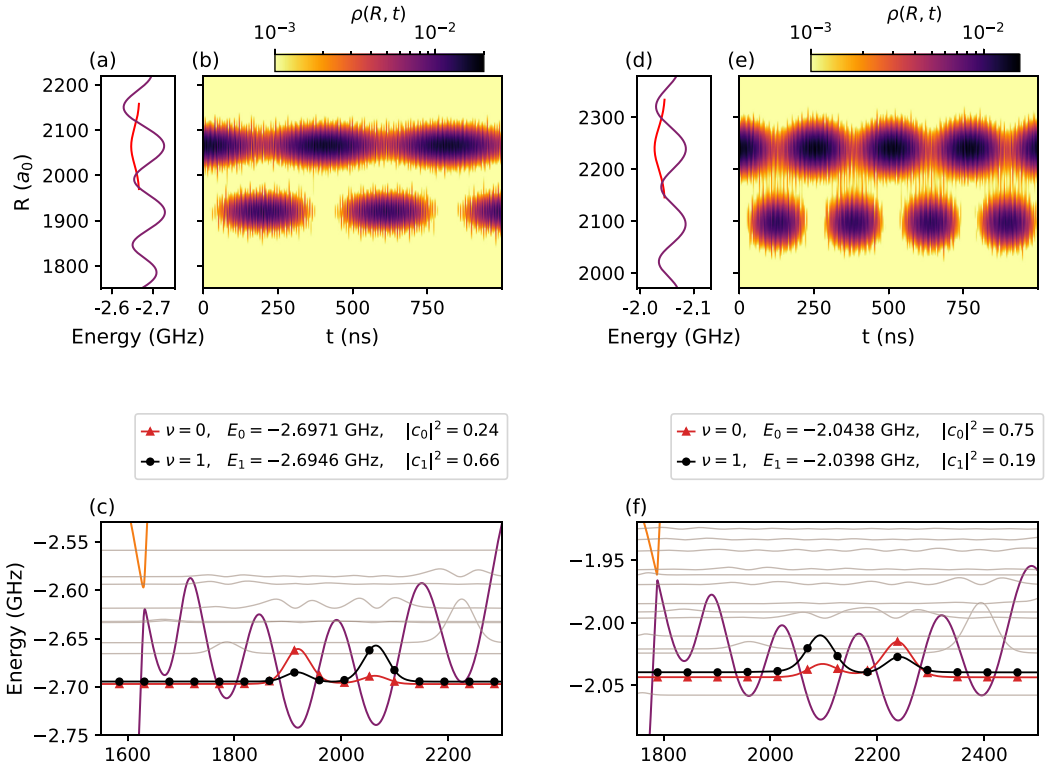


FIG. 6. Two-well interference effects in the low-energy dynamics of (a)–(c) $n = 42$, and (d)–(f) $n = 46$ ULRMs. Panels (a), (d) show the adiabatic potential energy curve V_l for the ULRM, along with the probability density of the initial Gaussian wavepacket with $\sigma = 40a_0$, centered around $R_0 = 2064a_0$ and $R_0 = 2240a_0$, respectively. Panels (b), (e) show the time-evolving total probability density $\rho(R, t)$. Panels (c), (f) display the vibronic molecular resonances. The two bound eigenstates responsible for the observed dynamics are highlighted and labeled, along with their energies E_ν, and their contribution to the wavepacket, $|c_\nu|^2 = |\langle\chi(R, t)|\chi_\nu\rangle|^2$.

states, so that multiwell tunneling effects are no longer visible.

IV. CONCLUSION AND OUTLOOK

Our work presents the first step in the study of multichannel vibronic dynamics in ULRMs. We start by constructing a two-channel diabatic model from the coupled trilobite-butterfly system, and then proceed to numerically simulate the propagation of nuclear wavepackets using a Crank-Nicolson scheme. The wavefunction is initialized as a Gaussian, with appropriate mean and variance needed to facilitate previously studied diffraction effects. Once the wavepacket escapes into the butterfly channel and reaches small R values, CAPs are used to simulate an absorbing wall (emulating internal molecular decay). We observe the two-channel analog of the diffraction effect with n-dependent nonadiabatic corrections. For n values with extremely narrow avoided crossings, the propagating diffraction pattern is nonadiabatically stabilized against decay. For n values with wide avoided crossings, larger fractions of the nuclear wavepacket are allowed to escape adiabatically. However, the high-level density and delocalized nonadiabatic coupling suggest that high-energy oscillations might need more than two channels for accurate simulation. In the case of very low-energy dynamics, accurately simulated using a few single channel vibrational states, we observe interesting multiwell interference patterns due to the partially delocalized vibronic spetrum.

In principle, the results obtained here should be experimentally observable using state of the art pump-probe schemes, as discussed in our previous work [24]. The preparation of the initial states, as well as certification of the dynamical effects can be performed using bound states in low-ℓ ULRMs. Moreover, the two-channel model provided can also be used to simulate predissociation dynamics and ℓ-changing collisions [16,41] with low-ℓ quantum defect states. With the recent advancements in optical tweezer technology that now allow the individual assembly of Rydberg molecules [72], one can also attain the ability to prepare initial states as localized ground states with tunable separation. In such cases, modern three-photon excitation schemes allow us to directly access the trilobite state [14,73] through the nf-state admixture, with MHz-scale laser linewidths. This allows us to project wavepackets directly onto the trilobite PEC, without worrying about off-resonant excitations to other potentials.

From a theoretical perspective, a more ambitious extension of this work is to develop a multichannel model, considering the effect of the quasidegenerate manifold, as well as couplings to nearby n values. This will allow us to simulate vibronic dynamics in high-ℓ and low-ℓ molecules with

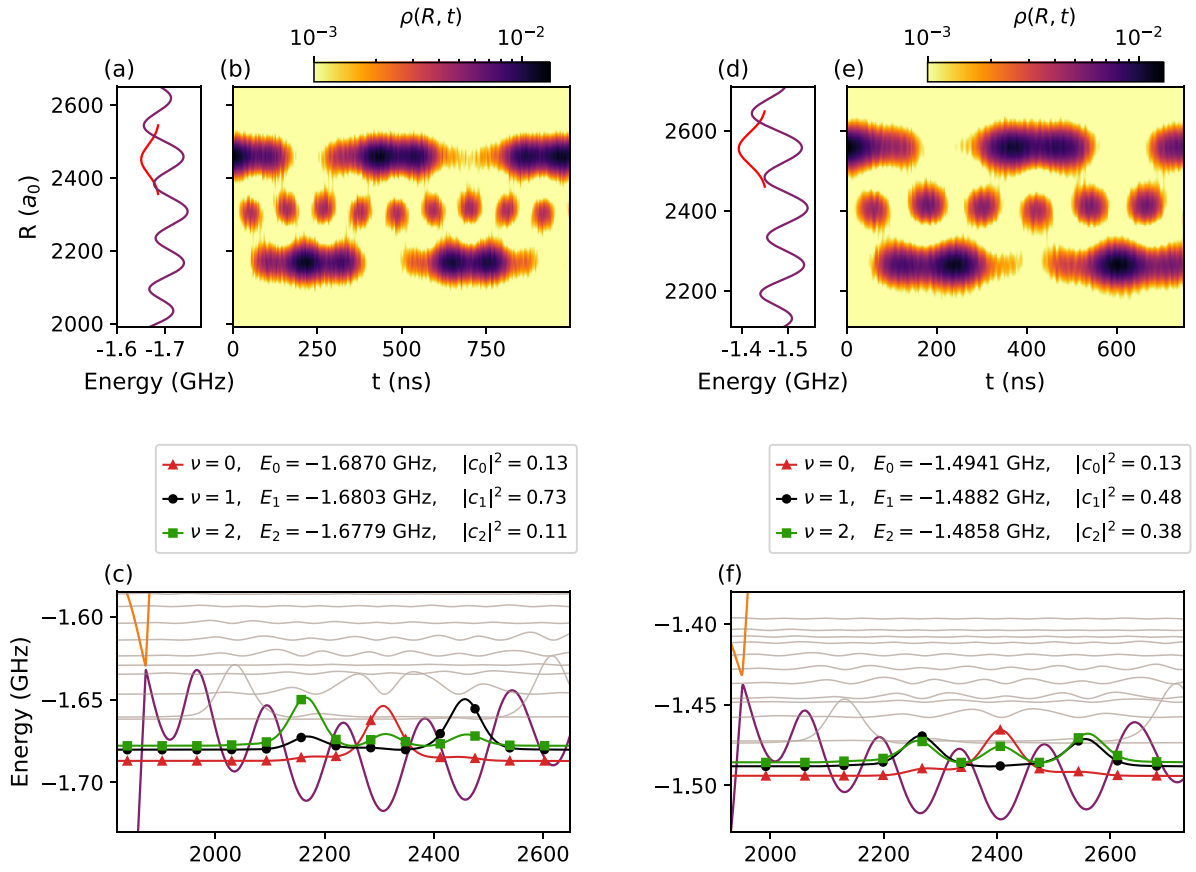


FIG. 7. Three-well interference effects in the low-energy dynamics of (a)–(c) $n = 49$, and (d)–(f) $n = 51$ ULRMs. Panels (a), (d) show the adiabatic potential energy curve V_1 for the ULRM, along with the probability density of the initial Gaussian wavepacket with $\sigma = 40a_0$, centered around $R_0 = 2450a_0$ and $R_0 = 2555a_0$, respectively. Panels (b), (e) show the time-evolving total probability density $\rho(R, t)$. Panels (c), (f) display the vibronic molecular resonances. The two bound eigenstates responsible for the observed dynamics are highlighted and labeled, along with their energies E_ν, and their contribution to the wavepacket, $|c_\nu|^2 = |\langle\chi(R, t)|\chi_\nu\rangle|^2$.

quantitative rigor. Future theoretical investigations can also consider introducing an external electric or magnetic field, breaking the spherical symmetry of the systems and facilitating conical intersections. This could possibly result in interesting dynamical effects induced by geometric phases.

ACKNOWLEDGMENT

R.S. is grateful to Matthew T. Eiles and Hans Dieter Meyer for helpful discussions.

DATA AVAILABILITY

The data that support the findings of this article are not publicly available. The data are available from the authors upon reasonable request.

APPENDIX A: COMPLEX ABSORBING POTENTIALS

Following the approach outlined in [70,71], the CAP is implemented as a negative imaginary potential of the form

$$V_{\mathrm{CAP}}(R) = -i\eta\, W(R), \tag{A1}$$

$$W(R) = [R - R_c]^n\, \Theta(R_c - R), \tag{A2}$$

where η denotes the absorption strength, R_c the onset position below which the CAP is active, n the polynomial order, and Θ the Heaviside step function. Typical choices of $n = 2 - 4$ yield a sufficiently smooth onset while keeping reflections minimal. Within this region, the total Hamiltonian becomes non-Hermitian,

$$H' = H - i\eta W(R), \tag{A3}$$

which causes a decay of the total norm according to [70]

$$\frac{d}{dt}\|\Psi\|^2 = -2\eta\langle\Psi|W(R)|\Psi\rangle. \tag{A4}$$

Hence the decrease of $\|\Psi\|^2$ directly reflects the loss of flux into the absorbing region.

For ultralong-range Rydberg molecules, optimal CAP parameters depend on the typical kinetic energy of the nuclear wavepacket. A sufficiently weak absorber ($\eta \sim 10^{-11}$ atomic units, or $\sim 10^{-5}$ GHz) ensures that the physical dynamics in the interaction region remain unaffected while reflections are

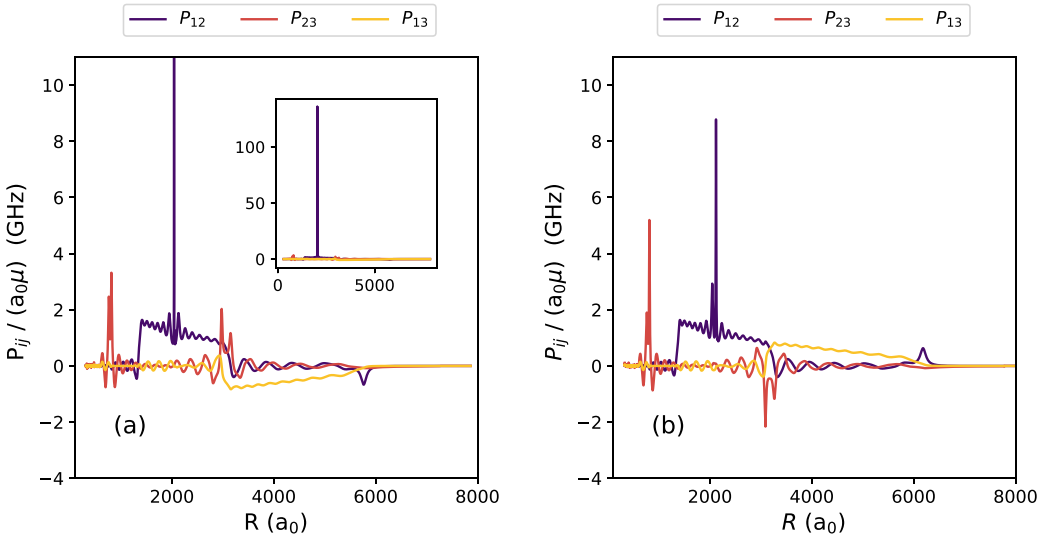


FIG. 8. The first derivative couplings $P_{ij}/(\mu a_0)$ for (a) $n = 55$ and (b) $n = 57$. The insets in (a) are meant to show the near-singular behavior of the $n = 55$ P_{12}, which is not necessary for $n = 57$.

minimized. For each n value, R_c is chosen so that the effective CAP length ($\sim 1000a_0$) far exceeds the local de Broglie wavelengths of the outgoing component to guarantee smooth absorption. In our two-channel model, the CAP is initially defined in the adiabatic representation, where it acts only within the butterfly potential channel. Upon transformation into the diabatic basis, the CAP is distributed over both diabatic components according to

$$V_{\mathrm{CAP}}^{(d)}(R) = U^{\dagger}(R)\begin{pmatrix} V_{\mathrm{CAP}}(R) & 0 \\ 0 & 0 \end{pmatrix} U(R), \qquad \text{(A5)}$$

ensuring consistent damping of the diabatic wavepacket amplitudes.

APPENDIX B: THREE-CHANNEL DERIVATIVE COUPLINGS

Figure 8 shows the off-diagonal derivative couplings between the three adiabatic states ψ_1, ψ_2, and ψ_3, with the corresponding adiabatic PECs shown in Fig. 1. The adiabatic states considered are formed by the mixing of the f state, trilobite state, and the butterfly state. All the derivative coupling elements show highly oscillatory behavior, as they are comprised of hybridized radial atomic wavefunctions and their derivatives. In the vicinity of the trilobite-butterfly avoided crossing, P_{12} dominates the other coupling terms, especially for the $n = 55$ case, where its magnitude is several orders of magnitude higher than the other coupling elements. We also see two peaks in P_{23} that correspond to the avoided crossing between trilobite and f state ($R \sim 800a_0$) as well as the avoided crossing between butterfly and f state ($R \sim 3000a_0$). Since we initialize our wavepacket in channel 1, the coupling between ψ_2 and ψ_3 is not so important for low-energy oscillations, given that the wavepacket does not reach the f state. However, we note that the coupling between channels 1 and 3 (given by P_{13}) is not negligible. In fact, P_{13} seems to dominate P_{12} at larger R values beyond the crossing between the butterfly and f states ($R \gtrsim 3000a_0$). This can be explained by the change of ψ_3 from f state to butterfly state beyond the avoided crossing, so that P_{13} represents the coupling between the trilobite and butterfly states at larger R values. Moreover, all the off-diagonal terms show GHz-scale energy structure for an extended R range away from the avoided crossing. This confirms that a quantitatively accurate treatment of the vibronic dynamics of the ULRM should definitely include three or more channels. However, it is important to note that the nonadiabatic transition probability is also dependent on the particle momentum (or derivative of the wavefunction) and the energy splitting, not just P_{ij}, so the primary correction to the adiabatic approximation, and consequently the primary cause of n-dependent nonadiabatic stabilization, is the behavior of P_{12} at the avoided crossing.

[1] C. H. Greene, A. S. Dickinson, and H. R. Sadeghpour, Creation of polar and nonpolar ultra-long-range Rydberg molecules, Phys. Rev. Lett. **85**, 2458 (2000).

[2] E. L. Hamilton, C. H. Greene, and H. R. Sadeghpour, Shape-resonance-induced long-range molecular Rydberg states, J. Phys. B: At. Mol. Opt. Phys. **35**, L199 (2002).

[3] S. Hollerith, J. Rui, A. Rubio-Abadal, K. Srakaew, D. Wei, J. Zeiher, C. Gross, and I. Bloch, Microscopic electronic structure tomography of Rydberg macrodimers, Phys. Rev. Res. **3**, 013252 (2021).

[4] S. Hollerith, J. Zeiher, J. Rui, A. Rubio-Abadal, V. Walther, T. Pohl, D. M. Stamper-Kurn, I. Bloch, and C. Gross, Quantum gas microscopy of Rydberg macrodimers, Science **364**, 664 (2019).

[5] Y.-Q. Zou, M. Berngruber, V. S. V. Anasuri, N. Zuber, F. Meinert, R. Löw, and T. Pfau, Observation of vibrational dynamics of orientated Rydberg-atom-ion molecules, Phys. Rev. Lett. **130**, 023002 (2023).

[6] N. Zuber, V. S. V. Anasuri, M. Berngruber, Y. Q. Zou, F. Meinert, R. Löw, and T. Pfau, Observation of a molecular bond between ions and Rydberg atoms, Nature (London) **605**, 453 (2022).

[7] D. J. Bosworth, F. Hummel, and P. Schmelcher, Charged ultralong-range Rydberg trimers, Phys. Rev. A **107**, 022807 (2023).

[8] R. González-Férez, J. Shertzer, and H. R. Sadeghpour, Ultralong-range Rydberg bimolecules, Phys. Rev. Lett. **126**, 043401 (2021).

[9] J. Wang, M. Gacesa, and R. Côté, Rydberg electrons in a Bose-Einstein condensate, Phys. Rev. Lett. **114**, 243003 (2015).

[10] J. Stanojevic, R. Côté, D. Tong, S. M. Farooqi, E. E. Eyler, and P. L. Gould, Long-range Rydberg-Rydberg interactions and molecular resonances, Eur. Phys. J. D **40**, 3 (2006).

[11] J. Stanojevic, R. Côté, D. Tong, E. E. Eyler, and P. L. Gould, Long-range potentials and $(n-1)d+ns$ molecular resonances in an ultracold Rydberg gas, Phys. Rev. A **78**, 052709 (2008).

[12] D. Booth, S. T. Rittenhouse, J. Yang, H. R. Sadeghpour, and J. P. Shaffer, Production of trilobite Rydberg molecule dimers with kilo-Debye permanent electric dipole moments, Science **348**, 99 (2015).

[13] W. Li, T. Pohl, J. M. Rost, S. T. Rittenhouse, H. R. Sadeghpour, J. Nipper, B. Butscher, J. B. Balewski, V. Bendkowsky, R. Löw, and T. Pfau, A homonuclear molecule with a permanent electric dipole moment, Science **334**, 1110 (2011).

[14] M. Exner, R. Srikumar, R. Blättner, M. T. Eiles, P. Schmelcher, and H. Ott, High precision spectroscopy of trilobite Rydberg molecules, Phys. Rev. Lett. **134**, 223401 (2025).

[15] F. Engel, T. Dieterle, F. Hummel, C. Fey, P. Schmelcher, R. Löw, T. Pfau, and F. Meinert, Precision spectroscopy of negative-ion resonances in ultralong-range Rydberg molecules, Phys. Rev. Lett. **123**, 073003 (2019).

[16] F. Hummel, P. Schmelcher, H. Ott, and H. R. Sadeghpour, An ultracold heavy Rydberg system formed from ultra-long-range molecules bound in a stairwell potential, New J. Phys. **22**, 063060 (2020).

[17] S. K. Kanungo, Y. Lu, F. B. Dunning, S. Yoshida, J. Burgdörfer, and T. C. Killian, Measuring nonlocal three-body spatial correlations with Rydberg trimers in ultracold quantum gases, Phys. Rev. A **107**, 033322 (2023).

[18] C. Fey, J. Yang, S. T. Rittenhouse, F. Munkes, M. Baluktsian, P. Schmelcher, H. R. Sadeghpour, and J. P. Shaffer, Effective three-body interactions in Cs(6*s*)–Cs(*nd*) Rydberg trimers, Phys. Rev. Lett. **122**, 103001 (2019).

[19] C. Fey, F. Hummel, and P. Schmelcher, Ultralong-range Rydberg molecules, Mol. Phys. **118**, e1679401 (2020).

[20] J. P. Shaffer, S. T. Rittenhouse, and H. R. Sadeghpour, Ultracold Rydberg molecules, Nat. Commun. **9**, 1965 (2018).

[21] M. T. Eiles, Trilobites, butterflies, and other exotic specimens of long-range Rydberg molecules, J. Phys. B: At. Mol. Opt. Phys. **52**, 113001 (2019).

[22] F. Hummel, K. Keiler, and P. Schmelcher, Electric-field-induced wave-packet dynamics and geometrical rearrangement of trilobite Rydberg molecules, Phys. Rev. A **103**, 022827 (2021).

[23] C. Fey, M. Kurz, and P. Schmelcher, Stretching and bending dynamics in triatomic ultralong-range Rydberg molecules, Phys. Rev. A **94**, 012516 (2016).

[24] R. Srikumar, S. T. Rittenhouse, and P. Schmelcher, Internal diffraction dynamics of trilobite molecules, Phys. Rev. A **110**, 062808 (2024).

[25] I. Lesanovsky, P. Schmelcher, and H. R. Sadeghpour, Ultralong-range Rydberg molecules exposed to a magnetic field, J. Phys. B: At. Mol. Opt. Phys. **39**, L69 (2006).

[26] T. Niederprüm, O. Thomas, T. Eichert, C. Lippe, J. Pérez-Ríos, C. H. Greene, and H. Ott, Observation of pendular butterfly Rydberg molecules, Nat. Commun. **7**, 12820 (2016).

[27] M. Kurz and P. Schmelcher, Electrically dressed ultra-long-range polar Rydberg molecules, Phys. Rev. A **88**, 022501 (2013).

[28] M. Born and R. Oppenheimer, Zur Quantentheorie der Molekeln, Ann. Phys. **389**, 457 (1927).

[29] F. Hummel, P. Schmelcher, and M. T. Eiles, Vibronic interactions in trilobite and butterfly Rydberg molecules, Phys. Rev. Res. **5**, 013114 (2023).

[30] R. Srikumar, F. Hummel, and P. Schmelcher, Nonadiabatic interaction effects in the spectra of ultralong-range Rydberg molecules, Phys. Rev. A **108**, 012809 (2023).

[31] F. Hummel, M. T. Eiles, and P. Schmelcher, Synthetic dimension-induced conical intersections in Rydberg molecules, Phys. Rev. Lett. **127**, 023003 (2021).

[32] M. T. Eiles and F. Hummel, Kato's theorem and ultralong-range Rydberg molecules, Phys. Rev. A **109**, 022811 (2024).

[33] B. Butscher, V. Bendkowsky, J. Nipper, J. B. Balewski, L. Kukota, R. Löw, T. Pfau, W. Li, T. Pohl, and J. M. Rost, Lifetimes of ultralong-range Rydberg molecules in vibrational ground and excited states, J. Phys. B: At. Mol. Opt. Phys. **44**, 184004 (2011).

[34] V. Bendkowsky, B. Butscher, J. Nipper, J. B. Balewski, J. P. Shaffer, R. Löw, T. Pfau, W. Li, J. Stanojevic, T. Pohl, and J. M. Rost, Rydberg trimers and excited dimers bound by internal quantum reflection, Phys. Rev. Lett. **105**, 163201 (2010).

[35] R. Srikumar, M. Exner, R. Blättner, P. Schmelcher, M. T. Eiles, and H. Ott, Vibrationally highly excited trilobite molecules stabilized by nonadiabatic coupling, Phys. Rev. Res. **7**, 043103 (2025).

[36] A. Duspayev and G. Raithel, Nonadiabatic decay of Rydberg-atom–ion molecules, Phys. Rev. A **105**, 012810 (2022).

[37] N. Samboy, J. Stanojevic, and R. Côté, Formation and properties of Rydberg macrodimers, Phys. Rev. A **83**, 050501(R) (2011).

[38] D. Mellado-Alcedo, A. Guttridge, S. L. Cornish, H. R. Sadeghpour, and R. González-Férez, Ultralong-range Cs-RbCs Rydberg molecules: Nonadiabaticity of dipole moments, Phys. Rev. A **110**, 013314 (2024).

[39] F. M. Gambetta, C. Zhang, M. Hennrich, I. Lesanovsky, and W. Li, Exploring the many-body dynamics near a conical intersection with trapped Rydberg ions, Phys. Rev. Lett. **126**, 233404 (2021).

[40] J. W. P. Wilkinson, W. Li, and I. Lesanovsky, Spectral signatures of vibronic coupling in trapped cold ionic Rydberg systems, Phys. Rev. Lett. **132**, 223401 (2024).

[41] M. Schlagmüller, T. C. Liebisch, F. Engel, K. S. Kleinbach, F. Böttcher, U. Hermann, K. M. Westphal, A. Gaj, R. Löw, S. Hofferberth, T. Pfau, J. Pérez-Ríos, and C. H. Greene, Ultracold chemical reactions of a single Rydberg atom in a dense gas, Phys. Rev. X **6**, 031020 (2016).

[42] F. Engel, S. K. Tiwari, T. Pfau, S. Wüster, and F. Meinert, *In situ* observation of chemistry in Rydberg molecules within a Bose-Einstein-condensate, Phys. Rev. Res. **6**, 033150 (2024).

[43] A. A. T. Durst, M. Simić, N. Abraham, and M. T. Eiles, Nonadiabatic couplings as a stabilization mechanism in long-range Rydberg molecules, Phys. Rev. A **111**, 032811 (2025).

[44] A. Marciniak, V. Despré, T. Barillot, A. Rouzée, M. C. E. Galbraith, J. Klei, C.-H. Yang, C. T. L. Smeenk, V. Loriot, S. N. Reddy, A. G. G. M. Tielens, S. Mahapatra, A. I. Kuleff, M. J. J. Vrakking, and F. Lépine, XUV excitation followed by ultrafast non-adiabatic relaxation in PAH molecules as a femto-astrochemistry experiment, Nat. Commun. **6**, 7909 (2015).

[45] H. Köppel, Ultrafast non-radiative decay via conical intersections of molecular potential-energy surfaces: $C_2H_4^+$, Chem. Phys. **77**, 359 (1983).

[46] W. Domcke, A. Sobolewski, and C. Woywod, Internal conversion funnel in benzene and pyrazine: adiabatic and diabatic representation, Chem. Phys. Lett. **203**, 220 (1993).

[47] M. F. Herman, Nonadiabatic semiclassical scattering. I. Analysis of generalized surface hopping procedures, J. Chem. Phys. **81**, 754 (1984).

[48] M. Barbatti, Nonadiabatic dynamics with trajectory surface hopping method, WIREs Comput. Mol. Sci. **1**, 620 (2011).

[49] O. K. Rice, Predissociation and the crossing of molecular potential energy curves, J. Chem. Phys. **1**, 375 (1933).

[50] R. A. Harris, Predissociation, J. Chem. Phys. **39**, 978 (1963).

[51] P. Zhang, A. Dalgarno, R. Côté, and E. Bodo, Charge exchange in collisions of beryllium with its ion, Phys. Chem. Chem. Phys. **13**, 19026 (2011).

[52] M. Born and K. Huang, *Dynamical Theory of Crystal Lattices* (Oxford University Press, Oxford, 1954).

[53] M. Baer, *Beyond Born-Oppenheimer: Electronic Non-Adiabatic Coupling Terms and Conical Intersections* (John Wiley & Sons, Ltd, Bognor Regis, UK, 2006).

[54] W. Domcke, D. R. Yarkony, and H. Köppel, *Conical Intersections* (World Scientific, Singapore, 2004).

[55] F. Hummel, C. Fey, and P. Schmelcher, Alignment of s -state Rydberg molecules in magnetic fields, Phys. Rev. A **99**, 023401 (2019).

[56] H. Köppel, W. Domcke, and L. S. Cederbaum, *Advances in Chemical Physics* (John Wiley & Sons, Ltd, Bognor Regis, UK, 1984), pp. 59–246.

[57] E. Fermi, Sopra lo spostamento per pressione delle righe elevate delle serie spettrali, Nuovo Cim. **11**, 157 (1934).

[58] A. Omont, On the theory of collisions of atoms in Rydberg states with neutral particles, J. Phys. France **38**, 1343 (1977).

[59] W. Li, I. Mourachko, M. W. Noel, and T. F. Gallagher, Millimeter-wave spectroscopy of cold Rb Rydberg atoms in a magneto-optical trap: Quantum defects of the ns, np, and nd series, Phys. Rev. A **67**, 052502 (2003).

[60] V. M. Borodin and A. K. Kazansky, The adiabatic mechanism of the collisional broadening of Rydberg states via a loosely bound resonance state of ambient gas atoms, J. Phys. B: At. Mol. Opt. Phys. **25**, 971 (1992).

[61] M. Chibisov, A. M. Ermolaev, F. Brouillard, and M. H. Cherkani, New summation rules for Coulomb wave functions, Phys. Rev. Lett. **84**, 451 (2000).

[62] M. H. Cherkani, F. Brouillard, and M. Chibisov, Summation rules for Coulomb wavefunction products, J. Phys. B: At. Mol. Opt. Phys. **34**, 49 (2001).

[63] C. H. Greene and M. T. Eiles, Green's-function treatment of Rydberg molecules with spins, Phys. Rev. A **108**, 042805 (2023).

[64] M. T. Eiles and C. H. Greene, Hamiltonian for the inclusion of spin effects in long-range Rydberg molecules, Phys. Rev. A **95**, 042515 (2017).

[65] D. A. Anderson, S. A. Miller, and G. Raithel, Angular-momentum couplings in long-range Rb_2 Rydberg molecules, Phys. Rev. A **90**, 062518 (2014).

[66] S. E. Koonin, D. C. Meredith, and W. H. Press, Computational physics: Fortran version, 1990.

[67] J. Thomas, *Numerical Partial Differential Equations: Finite Difference Methods*, Texts in Applied Mathematics Vol. 22 (Springer New York, New York, 2013).

[68] G. C. Groenenboom and H. M. Buck, Solving the discretized time-independent Schrödinger equation with the Lanczos procedure, J. Chem. Phys. **92**, 4374 (1990).

[69] M. Feit, J. Fleck, and A. Steiger, Solution of the Schrödinger equation by a spectral method, J. Comput. Phys. **47**, 412 (1982).

[70] H. D. Meyer, Introduction to MCTDH, Lecture Notes, Heidelberg University, 2010.

[71] U. V. Riss and H. D. Meyer, Calculation of resonance energies and widths using the complex absorbing potential method, J. Phys. B: At. Mol. Opt. Phys. **26**, 4503 (1993).

[72] A. Guttridge, T. R. Hepworth, D. K. Ruttley, A. A. T. Durst, M. T. Eiles, and S. L. Cornish, Individual assembly of two-species Rydberg molecules using optical tweezers, Phys. Rev. Lett. **134**, 133401 (2025).

[73] M. Althön, M. Exner, R. Blättner, and H. Ott, Exploring the vibrational series of pure trilobite Rydberg molecules, Nat. Commun. **14**, 8108 (2023).

PHYSICAL REVIEW LETTERS **134,** 223401 (2025)

Editors' Suggestion | Featured in Physics

High Precision Spectroscopy of Trilobite Rydberg Molecules

Markus Exner,[1,*] Rohan Srikumar,[2,*] Richard Blättner,[1] Matthew T. Eiles,[3] Peter Schmelcher,[2,4] and Herwig Ott[1,†]

[1]*Department of Physics and Research Center OPTIMAS, Rheinland-Pfälzische Technische Universität Kaiserslautern-Landau, 67663 Kaiserslautern, Germany*

[2]*Zentrum für Optische Quantentechnologien, Universität Hamburg, Luruper Chaussee 149, 22761 Hamburg, Germany*

[3]*Max Planck Institute for the Physics of Complex Systems, Nöthnitzer Strasse 38, 01187 Dresden, Germany*

[4]*The Hamburg Centre for Ultrafast Imaging, Universität Hamburg, Luruper Chaussee 149, 22761 Hamburg, Germany*

(Received 1 January 2025; revised 27 March 2025; accepted 17 April 2025; published 4 June 2025)

We perform three-photon photoassociation to obtain high resolution spectra of ^{87}Rb trilobite dimers for the principal quantum numbers $n = 22$, 24, 25, 26, and 27. The large binding energy of the molecules in combination with a relative spectroscopic resolution of 10^{-4} provides a rigorous benchmark for existing theoretical models. A recently developed Green's function framework, which circumvents the convergence issues that afflicted previous studies, is employed to theoretically reproduce the vibrational spectrum of the molecule with high accuracy. The relatively large molecular binding energy is primarily determined by the low-energy S-wave electron-atom scattering length, thereby allowing us to extract the $^3S_1$ scattering phase shift with unprecedented accuracy, at low-energy regimes inaccessible to free electrons.

DOI: 10.1103/PhysRevLett.134.223401

Introduction—The ability to introduce Rydberg excitations in ultracold atomic gases has set in motion a new branch of molecular physics, wherein atoms are bound over large distances via unconventional binding mechanisms [1–7]. Trilobite molecules are a peculiar category of such ultralong-range Rydberg molecules (ULRMs) [1,8–11], bound by a ground-state atom scattering off a Rydberg electron with high angular momentum ℓ. These homonuclear dimers, which exhibit permanent electric dipole moments in the kilo-Debye range [12–15] and have bond lengths of the order of micrometers, promise dynamical effects and field control not typical of conventional molecules [16–18]. Although the first experimental evidence for the trilobite dimer was obtained by mixing the trilobite wave function to low-ℓ Rydberg states [14,19], it was only very recently that direct photoassociation of the molecule, accessing the trilobite potential energy curves (PECs), was made possible [15]. For more than a decade, numerous spectroscopic studies have been performed on ULRMs [20–28] providing detailed insights into the spin structure, potential energy landscape, and rovibronic spectra of these dimers. Since the low-energy scattering of the Rydberg electron forms the binding mechanism of the molecule, the depth of the potential wells and the vibrational binding energies are directly dependent on the size of the scattering partial wave L. In turn, high resolution spectroscopic data can provide precise values of the spin-dependent scattering lengths, ultimately testing the validity of the underlying interaction mechanism. Consequently, the ULRM has been used as a laboratory to extract electron-atom scattering lengths and resonance positions at low-energy regimes inaccessible with free electrons [21].

In this work, we combine the newly formulated Green's function method [29] with the advantages of pure trilobite photoassociation spectroscopy. Because of the large molecular binding energies and the high precision of spectroscopic measurement, we determine the potential energy depth with unprecedented accuracy, and extract the energy-dependent $e^- - \mathrm{Rb}$, $^3S_1$ scattering length. At the same time, we find indications that the predictive power of the underlying molecular Hamiltonian is being challenged, and further insight in the direction of nonadiabatic physics [30–32] and/or higher order scattering terms is necessary before we can unravel agreement between experiment and theory data within the resolution achieved.

Interactions and methodology—The Born-Oppenheimer PECs $U_i(R)$ and the associated electronic states $\phi_i(\vec{r};R)$ are obtained by solving $H\phi_i(\vec{r};R) = U_i(R)\phi_i(\vec{r};R)$, where the electronic Hamiltonian H incorporates the fine structure of the Rydberg electron, hyperfine structure of the ground-state atom (with a total spin $F = 1$, 2 for ^{87}Rb), and the six different electron-atom scattering channels ($^1S_0$,$^3S_1$,$^1P_1$,$^3P_{0,1,2}$). Until recently, the standard method

*These authors contributed equally to this work.

†Contact author: ott@physik.uni-kl.de

Published by the American Physical Society under the terms of the Creative Commons Attribution 4.0 International license. Further distribution of this work must maintain attribution to the author(s) and the published article's title, journal citation, and DOI.

for determining the PECs was the diagonalization of H in a truncated basis [33]. Here, the scattering interaction between the Rydberg electron and perturber is characterized by a Fermi-type pseudopotential in S-wave [34] and P-wave channels [35]. While providing a valid semiquantitative description of the system, the Dirac-delta form of the pseudopotential introduces unphysical basis size dependence of the PECs obtained utilizing diagonalization schemes [36]. Furthermore, the approach suffers from diverging scattering volumes in the ${}^3P_J$ scattering channels introduced by negative ion resonances. For this reason, the scattering phase shift extracted by comparing experimental and theoretical binding energies obtained utilizing this method needs to be handled with care. Alternative approaches have been developed, but as these do not include all spin interactions, they are not sufficiently accurate to meet high-precision spectroscopy [37,38]. However, the recently developed nonperturbative Green's function formulation (see [29] for detailed explanation) accounts for all spin interactions, and circumvents the aforementioned convergence issues.

Figure 1 shows the Born-Oppenheimer potential energy landscape of the ULRM obtained using the Green's function calculation for principal quantum number $n = 27$, with the projection of total angular momentum along the internuclear axis taken to be $M = 1/2$. The zero frequency is the asymptotic pair state $\mathrm{Rb}(27f_{7/2}) + \mathrm{Rb}(5s, F = 1)$,

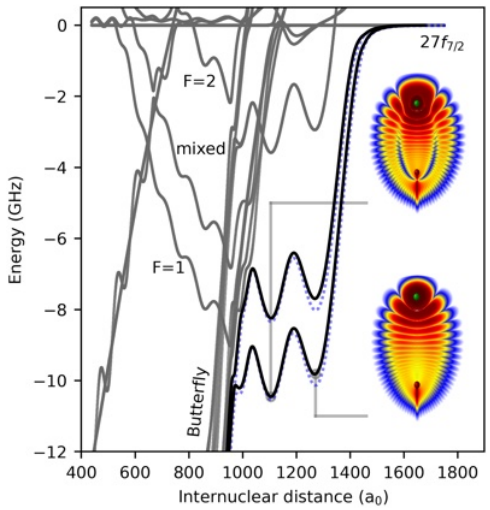


FIG. 1. Rydberg $n = 27$, $M = 1/2$ molecular Born-Oppenheimer potential curves obtained using the Green's function treatment (gray curves). The black curves highlight the trilobite potentials we experimentally probe, and for comparison the blue curves are potentials calculated by numerical diagonalization (using $n \in [25, 29]$ basis). On the right are two density plots of the Coulomb Green's function which represents the Rydberg electron distribution. Because of the S-wave scattering and the admixture of high angular momentum states, the probability of the electron staying at the position of the ground-state atom is maximized.

from which the two potential curves emerge (black curves), corresponding to the pure triplet scattering channel (lower PEC), and a singlet-triplet mixed channel (upper PEC). For illustration the same two potentials were calculated with the diagonalization method (blue dotted curves), which leads to 10% deviation in the binding energy. At 1050 a_0 the trilobite levels interact with the plummeting "butterfly" potential curves resulting from the shape resonance in the P-wave scattering, of which there are five of predominantly ${}^3P_2$ configuration, three of ${}^3P_1$, and a single ${}^3P_0$. In this work we experimentally access the vibrational bound states in the highlighted trilobite curves (hereby referred to as triplet trilobite and mixed trilobite PEC) for $n = 22$, 24, 25, 26, and 27.

Experimental setup—We prepare the atomic sample starting from a magneto-optical trap of ^{87}Rb atoms, which are subsequently transferred into a crossed dipole trap operating at $\lambda = 1064$ nm. The spherical atomic ensemble has a temperature of 40 μK, a diameter of 40 μm and a peak density of 4×10^{13} cm^{-3}. The atoms are prepared in the $F = 1$ hyperfine ground state. Employing a three-photon excitation scheme $(5s_{1/2} \rightarrow 5p_{3/2} \rightarrow 5d_{5/2} \rightarrow nf_{7/2})$ at wavelengths of 780, 776, and 1276–1288 nm, we can photoassociate pure trilobite Rydberg molecules utilizing its f-state admixture. For precise frequency control, all three excitation lasers are frequency stabilized to an ultra-low expansion cavity using a Pound-Drevel-Hall locking technique. Immediately following the excitation, the Rydberg atoms are ionized using a CO_2 laser. The resulting ions are guided by an electric field in a Wiley-McLaren configuration onto a time- and position-resolved multi-channel plate detector, enabling the direct measurement of the momentum distribution prior to ionization. Hence, we are able to distinguish the ions that have zero momentum, and consequently detect long-lived stable molecular states [15]. The full momentum signal, however, contains the signatures of both long-lived and short-lived molecular resonances. The generated ions are counted for each detuning step (2 MHz) and averaged over typically 10 experimental runs. To estimate the maximum error for the frequency, we use the accuracy of the free spectral range of 100 kHz, resulting in an error for the lowest trilobite state of $(21\ \mathrm{GHz}/1.4978\ \mathrm{GHz}) \times 100\ \mathrm{kHz} \approx 1.4$ MHz. On the other hand, we use the frequency step size of 2 MHz as the readout error. This results in a frequency uncertainty of 3.4 MHz, which corresponds to a deviation smaller than 0.01% at a binding energy of 21 GHz and thus illustrates the excellent accuracy of the experiment.

Spectral analysis—Figure 2 shows the observed spectra for all measured n, which are several gigahertz red detuned from the $nf_{7/2}$ atomic resonance. Two different vibrational series can be identified, which still overlap at the principal quantum number of 22 but are clearly separated at $n = 25$. These originate from the mixed and the triplet $F = 1$ PECs, respectively. The vertical lines show the calculated binding energies for the triplet $F = 1$ (green lines) and the mixed

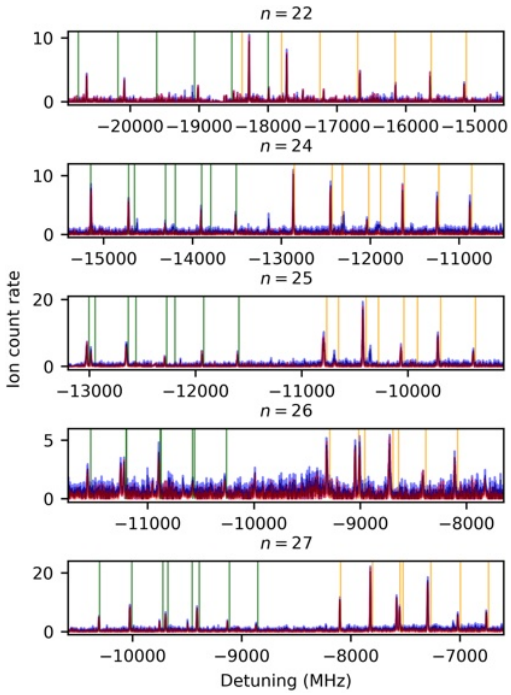


FIG. 2. The zero momentum (red) and full momentum (blue) ion signals as a function of the frequency detuning from the $nf_{7/2}$ atomic resonance, for all measured n values. The calculated eigenenergies are shown as vertical lines for the triplet $F = 1$ (green) and the mixed (orange) potential.

(orange lines) trilobite states. The number of vibrational states in each potential is limited by the position of the crossing with the butterfly PECs, as tunneling toward shorter internuclear distances occurs, leading to state-changing collisions or associative ionization [15,39]. For $n < 24$, there is a single outer well beyond the P-wave crossing, whereas for $n = 24$ and above, there is a second potential well. This explains the presence of double peaks in the spectrum for $n = 24$–27 that are absent in the $n = 22$ spectra (see End Matter for more details). The presence of the second potential well renders the assignment of the vibrational states challenging. Here, knowledge of the permanent dipole moment helps in the identification of states, as the dipole moment of the vibrational state increases with bond length. To determine the dipole moment, a weak electric field is applied and the broadening of the state is measured [15]. The measured dipole moments for different vibrational states of the $n = 27$ mixed trilobite potential is shown in Fig. 3. Their magnitudes accumulate around two different values, which clearly allows the assignment of the vibrational states to the two calculated potential wells with minima at 1100 a_0 and 1275 a_0. Note that the relative motional state of two ground-state atoms in our setup varies slowly over the extent of the molecular vibrational states, implying minimal

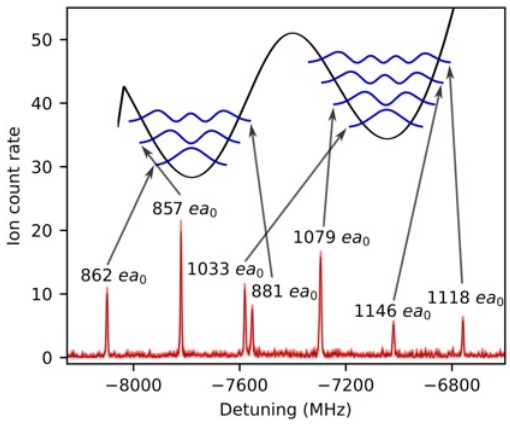


FIG. 3. The trilobite spectrum (red) for the energy range of the mixed potential for a principal quantum number of $n = 27$ with the potential energy curve (black) above including vibrational probability densities (blue, not to scale). The observed dipole moments of each measured peak are shown and assigned to the corresponding vibrational state.

Franck-Condon overlap for odd molecular vibrational states. However, the molecular spectra shows that both odd and even vibrational states have comparable signal strength. This phenomenon is explained by considering the oscillations of the $nf_{7/2}$ admixture in the trilobite state (responsible for the dipole transition from $5d_{5/2}$) that violates the Franck-Condon approximation that electronic transitions are independent of the nuclear coordinates and facilitates the photoassociation of odd vibrational states.

Phase shift extraction—We now discuss the extraction of the low-energy S-wave scattering phase shift from the high resolution data experimentally obtained. By solving the unphysical basis dependencies that afflicted other calculations, we are able to modify and correct previous phase shifts in such a way that it reproduces the observed resonances more precisely, without dependence on any external model parameters. For this, we added a ninth order polynomial to the phase shifts fitted in [21] and treated the coefficients as fit parameters. These were varied until the total difference between the theoretical and experimental bound state spectra from all n were simultaneously minimized, while avoiding any unphysical oscillatory behavior. Figure 4(a) illustrates the trilobite potential energy curves as a function of the semiclassical electron momentum k. Note that $k(R) = \sqrt{2U_n(R) + 1/R}$ is calculated separately for each particular PEC $U_n(R)$, and the curves are vertically offset for an easier visual comparison. The overlapping k ranges for multiple n values provide several data points (vibrational states) in each k window whose energetic positions are sensitive to the changes in phase shift. By minimizing the error between the computed and observed binding energies for the vibrational ground states localized in the outer well, for all values of n simultaneously,

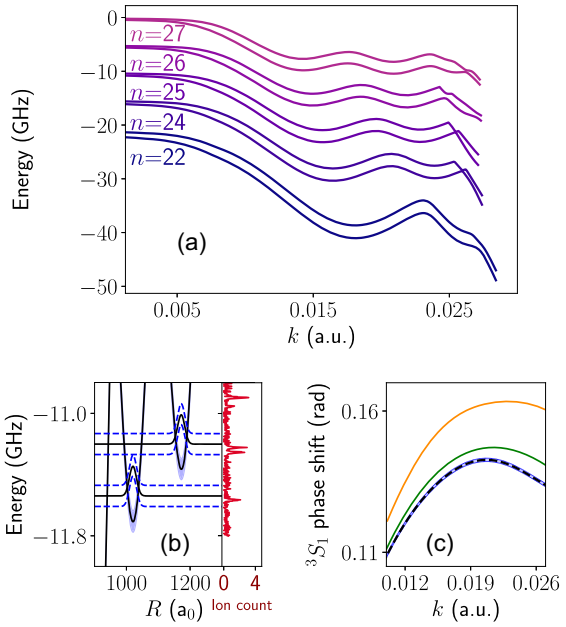


FIG. 4. Potential energy structure and extracted S-wave phase shifts. (a) Illustrative sketch of the probed trilobite PECs as a function of k, limited between the energy zeros ($k = 0$) and the P-wave crossings ($k \sim 0.025$) for each PEC. (b) The PECs (solid blue and black lines) and the ground vibrational states (dashed lines) of the molecule, for $n = 26$, in comparison with the ion-count spectra (red). (c) The dashed black curve shows the $^3S_1$ phase shifts fitted anew, with the shaded blue region in the background portraying the uncertainty in the fitting of phase shifts (see text), leading to corresponding deviations in binding energy as shown in (b). The green curve is the phase shift taken from the previous fit (from Ref. [21]), and the orange curve is the *ab initio* calculation of the phase shift (from Ref. [42]).

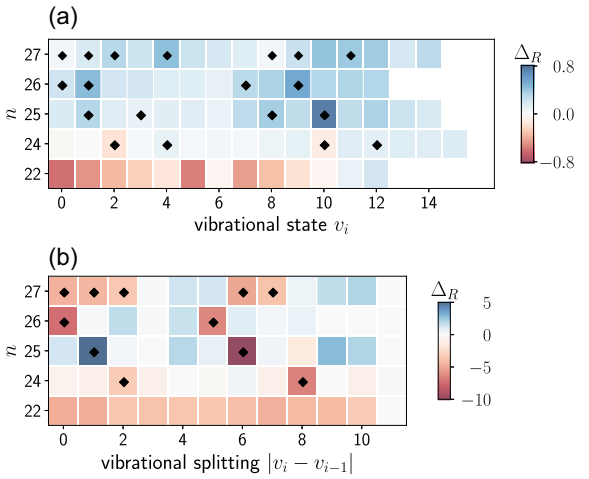


FIG. 5. The percentage relative difference of the experimental results with respect to the numerical calculations given by $\Delta_R = 100\% \times (\epsilon_e - \epsilon_t)/\epsilon_t$, where ϵ_e and ϵ_t represent the experimental and theoretical data, respectively, for (a) the calculated vibrational binding energies and (b) the splitting between vibrational states localized in separate wells. The states localized in the inner well are marked with diamonds.

we prevent possible overfits in our phase shift calculations (see End Matter for more details). Figure 4(b) shows the trilobite potential energy curves for $n = 26$, calculated utilizing the phase shifts shown in Fig. 4(c). The newly fit S-wave scattering phase shift [dashed black line, Fig. 4(c)] differs considerably from those previously determined by Ref. [21] or calculated *ab initio* by Refs. [40–42]. The shaded blue region in Figs. 4(b) and 4(c) is used to illustrate the sensitivity of the molecular binding energy on the $^3S_1$ scattering length. A 0.8% change in the S-wave phase shift in the relevant k range [Fig. 4(c)] induces an error of ~138 MHz in the binding energy of the $n = 26$ vibrational ground state [dashed lines Fig. 4(b)], nearly 2 orders of magnitude larger than the experimental resolution. The uncertainty of 0.7% in the $^3S_1$ phase shift is barely visible in comparison to the large deviation from the previously fitted or calculated phase shifts. Apart from illustrating the sensitivity of our calculations, the shaded region also shows the range of S-wave phase shifts within which the theoretical and experimental data can be selectively matched perfectly for each n value (case of overfitting). The inability to match observed and calculated binding energies simultaneously for all values of n, within experimental error bars, implies that there might be limitations in the description of the molecular interactions in the Hamiltonian. This necessitates a quantitative analysis of the error between the observed spectra and the numerical spectra calculated with the optimized phase shifts.

Figure 5(a) portrays the relative error of the binding energies of all the measured vibrational states with respect to their theoretical counterparts. The vibrational states localized in the outer wells of the $n \geq 24$ trilobite PECs are uniquely S-wave dominant and show an excellent maximum relative error $\lesssim 0.4\%$. Although the inner-well states (marked by diamonds) are also S-wave dominant, the exact positions of the $^3P_{0,1,2}$ crossings finely affect the number of bound states observed. However, we see that their binding energies are also largely dependent on the $^3S_1$ phase shift, and were reproduced with a relative error $\lesssim 0.8\%$. The average of the absolute values of all error values shown in Fig. 5(a) was calculated to be only 0.23%, validating and quantifying the high accuracy of the calculated potential energy depth and the extracted $^3S_1$ phase shift. Furthermore, in Fig. 5(b) we show the relative error between the experimental and theoretical estimates of vibrational energy splitting for both the inner-well states (marked by diamonds) and the outer-well states. This serves as a better estimate for the accuracy with which we probe the shape of the potential well. The difference between adjacent energy levels in both the triplet and the

mixed PECs are obtained separately and the relative error is shown for each n value. States localized in the outer wells (for $n = 24$–27) exhibit maximal relative error 2.7%, with the inner-well counterparts featuring error rates less than 10%. The states localized in the single well of the $n = 22$ trilobite potential exhibit error rates less than 5%. Further improvements in the molecular Hamiltonian would be necessary to produce numerical results that reproduce the experimental data within the resolution achieved.

Conclusion—To summarize, we have measured pure trilobite Rydberg series for five different principal quantum numbers at a resolution of 10^{-4}. Permanent electric dipole moments of almost 3000 D were measured and it was shown that this allows an unambiguous assignment of vibrational states in multiwell potentials. Furthermore, the recently developed Green's function method was used to analyze the most extensive experimental study of the trilobite ULRM to date. This allowed the binding energies and vibrational splittings to be theoretically reproduced with a relative error less than 0.8% and 10% respectively, providing us with an accurate estimate of the depth and shape of the potential energy curves. The vibrational ground states measured have large binding energies in comparison to the resolution, and are exceedingly S-wave dominant. This allowed for the extraction of low-energy $^3S_1$-wave scattering phase shift for ^{87}Rb with unprecedented accuracy in the relevant k range. We argue that the accuracy achieved is largely limited by the predictive power of the Hamiltonian and an enhanced understanding of the molecular interactions is necessary to proceed further. The high resolution data provided are a strong benchmark to test future theoretical models of the ULRM, and can potentially lead to an even deeper insight into low-energy electron-atom scattering.

Acknowledgments—We would like to thank Max Althön for helpful discussions. This project is funded by the German science foundation DFG, Projects No. 460443971, No. 316211972, and No. INST 248/268-1.

Data availability—The data that support the findings of this Letter are not publicly available. The data are available from the authors upon reasonable request.

[1] C. H. Greene, A. S. Dickinson, and H. R. Sadeghpour, Creation of polar and nonpolar ultra-long-range Rydberg molecules, Phys. Rev. Lett. **85**, 2458 (2000).
[2] J. A. Fernández, H. R Sadeghpour, P. Schmelcher, and R. G Férez, Ultralong-Range Rb-KRb Rydberg molecules: Selected aspects of electronic structure, orientation and alignment, J. Phys. Conf. Ser. **635**, 012023 (2015).
[3] M. Mayle, S. T. Rittenhouse, P. Schmelcher, and H. R. Sadeghpour, Electric field control in ultralong-range triatomic polar Rydberg molecules, Phys. Rev. A **85**, 052511 (2012).
[4] J. Zeiher and S. Hollerith, Rydberg macrodimers: Diatomic molecules on the micrometer scale, J. Phys. Chem. A **127**, 3925 (2023).
[5] A. Duspayev, X. Han, M. A. Viray, L. Ma, L. Zhao, and G. Raithel, Long-range Rydberg-atom–ion molecules of Rb and Cs, Phys. Rev. Res. **3**, 023114 (2021).
[6] N. Zuber, V. S. V. Anasuri, M. Berngruber, Y. Q Zou, R. Löw, and T. Pfau, Observation of a molecular bond between ions and Rydberg atoms, Nature (London) **52**, 453 (2022).
[7] D. Bosworth, F. Hummel, and P. Schmelcher, Charged ultralong-range Rydberg trimers, Phys. Rev. A **107**, 022807 (2023).
[8] M. T. Eiles, Trilobites, butterflies, and other exotic specimens of long-range Rydberg molecules, J. Phys. B **52**, 113001 (2019).
[9] C. Fey, F. Hummel, and P. Schmelcher, Ultralong-range Rydberg molecules, Mol. Phys. **118**, e1679401 (2020).
[10] F. B. Dunning, S. K. Kanungo, and S. Yoshida, Ultralong-range Rydberg molecules, J. Phys. B **57**, 212002 (2024).
[11] E. L. Hamilton, C. H. Greene, and H. R. Sadeghpour, Shape-resonance-induced long-range molecular Rydberg states, J. Phys. B **35**, L199 (2002).
[12] W. Li, T. Pohl, J. M. Rost, Seth T. Rittenhouse, H. R. Sadeghpour, J. Nipper, B. Butscher, J. B. Balewski, V. Bendkowsky, R. Löw, and T. Pfau, A homonuclear molecule with a permanent electric dipole moment, Science **334**, 1110 (2011).
[13] M. I. Chibisov, A. A. Khuskivadze, and I. I. Fabrikant, Energies and dipole moments of long-range molecular Rydberg states, J. Phys. B **35**, L193 (2002).
[14] D. Booth, S. T. Rittenhouse, J. Yang, H. R. Sadeghpour, and J. P. Shaffer, Production of trilobite Rydberg molecule dimers with kilo-Debye permanent electric dipole moments, Science **348**, 99 (2015).
[15] M. Althön, M. Exner, R. Blättner, and H. Ott, Exploring the vibrational series of pure trilobite Rydberg molecules, Nat. Commun. **14**, 8108 (2023).
[16] F. Engel, S. K. Tiwari, T. Pfau, S. Wüster, and F. Meinert, In situ observation of chemistry in Rydberg molecules within a coherent solvent, Phys. Rev. Res. **6**, 033150 (2024).
[17] F. Hummel, K. Keiler, and P. Schmelcher, Electric-field-induced wave-packet dynamics and geometrical rearrangement of trilobite Rydberg molecules, Phys. Rev. A **103**, 022827 (2021).
[18] R. Srikumar, S. T. Rittenhouse, and P. Schmelcher, Internal diffraction dynamics of trilobite molecules, Phys. Rev. A **110**, 062808 (2024).
[19] K. S. Kleinbach, F. Meinert, F. Engel, W. J. Kwon, R. Löw, T. Pfau, and G. Raithel, Photoassociation of trilobite Rydberg molecules via resonant spin-orbit coupling, Phys. Rev. Lett. **118**, 223001 (2017).
[20] V. Bendkowsky, B. Butscher, J. Nipper, J. P. Shaffer, R. Löw, and T. Pfau, Observation of ultralong-range Rydberg molecules, Nature (London) **458**, 1005 (2009).
[21] F. Engel, T. Dieterle, F. Hummel, C. Fey, P. Schmelcher, R. Löw, T. Pfau, and F. Meinert, Precision spectroscopy of negative-ion resonances in ultralong-range Rydberg molecules, Phys. Rev. Lett. **123**, 073003 (2019).

[22] T. Niederprüm, O. Thomas, T. Eichert, and H. Ott, Rydberg molecule-induced remote spin flips, Phys. Rev. Lett. **117**, 123002 (2016).

[23] T. Niederprüm, O. Thomas, T. Eichert, C. Lippe, J. Pérez-Ríos, C. H. Greene, and H. Ott, Observation of pendular butterfly Rydberg molecules, Nat. Commun. **7**, 12820 (2016).

[24] M. Deiß, S. Haze, J. Wolf, L. Wang, F. Meinert, C. Fey, F. Hummel, P. Schmelcher, and J. H. Denschlag, Observation of spin-orbit-dependent electron scattering using long-range Rydberg molecules, Phys. Rev. Res. **2**, 013047 (2020).

[25] H. Saßmannshausen, F. Merkt, and J. Deiglmayr, Experimental characterization of singlet scattering channels in long-range Rydberg molecules, Phys. Rev. Lett. **114**, 133201 (2015).

[26] M. Peper and J. Deiglmayr, Photodissociation of long-range Rydberg molecules, Phys. Rev. A **102**, 062819 (2020).

[27] M. Peper and J. Deiglmayr, Heteronuclear long-range Rydberg molecules, Phys. Rev. Lett. **126**, 013001 (2021).

[28] J. L. MacLennan, Y.-J. Chen, and G. Raithel, Deeply bound $(24D_J + 5S_{1/2})$ ^{87}Rb and ^{85}Rb molecules for eight spin couplings, Phys. Rev. A **99**, 033407 (2019).

[29] C. H. Greene and M. T. Eiles, Green's-function treatment of Rydberg molecules with spins, Phys. Rev. A **108**, 042805 (2023).

[30] F. Hummel, P. Schmelcher, and M. T. Eiles, Vibronic interactions in trilobite and butterfly Rydberg molecules, Phys. Rev. Res. **5**, 013114 (2023).

[31] R. Srikumar, F. Hummel, and P. Schmelcher, Nonadiabatic interaction effects in the spectra of ultralong-range Rydberg molecules, Phys. Rev. A **108**, 012809 (2023).

[32] M. T. Eiles and F. Hummel, Kato's theorem and ultralong-range Rydberg molecules, Phys. Rev. A **109**, 022811 (2024).

[33] M. T. Eiles and C. H. Greene, Hamiltonian for the inclusion of spin effects in long-range Rydberg molecules, Phys. Rev. A **95**, 042515 (2017).

[34] E. Fermi, Sopra lo Spostamento per Pressione delle Righe Elevate delle Serie Spettrali, Nuovo Cimento **11**, 157 (1934).

[35] A. Omont, On the theory of collisions of atoms in Rydberg states with neutral particles, J. Phys. France **38**, 1343 (1977).

[36] C. Fey, M. Kurz, P. Schmelcher, S. T. Rittenhouse, and H. R. Sadeghpour, A comparative analysis of binding in ultralong-range Rydberg molecules, New J. Phys. **17**, 055010 (2015).

[37] M. Tarana, Long-range Rydberg molecule Rb_2: Two-electron R-matrix calculations at intermediate internuclear distances, Phys. Rev. A **102**, 062802 (2020).

[38] P. Giannakeas, M. T. Eiles, F. Robicheaux, and J. M. Rost, Generalized local frame-transformation theory for ultralong-range Rydberg molecules, Phys. Rev. A **102**, 033315 (2020).

[39] P. Geppert, M. Althön, D. Fichtner, and H. Ott, Diffusive-like redistribution in state-changing collisions between Rydberg atoms and ground state atoms, Nat. Commun. **12**, 3900 (2021).

[40] C. Bahrim and U. Thumm, Low-lying $^3P^o$ and $^3S^e$ states of Rb^-, Cs^-, and Fr^-, Phys. Rev. A **61**, 022722 (2000).

[41] C. Bahrim, U. Thumm, and I. I. Fabrikant, Negative-ion resonances in cross sections for slow-electron–heavy-alkali-metal-atom scattering, Phys. Rev. A **63**, 042710 (2001).

[42] A. A. Khuskivadze, M. I. Chibisov, and I. I. Fabrikant, Adiabatic energy levels and electric dipole moments of Rydberg states of Rb_2 and Cs_2 dimers, Phys. Rev. A **66**, 042709 (2002).

End Matter

All bound states localized in the trilobite potential energy curves are predominantly of S-wave character and can be used to extract $^3S_1$ phase shifts. However, near the avoided crossing with the butterfly potential curve, the electronic state of the molecule acquires some amount of ^3P_J character. Hence, large changes in the ^3P_J phase shifts change the exact position of the avoided crossing, thereby limiting the number of bound states observed in the inner well. Since the outermost well of the trilobite molecule for $n \geq 24$ is much less affected by large changes in the P-wave phase shifts, we first fit the $^3S_1$ phase shift in the range $k \in [0.01, 0.018]$. Subsequently, we simultaneously change the S-wave and P-wave phase shifts to minimize the errors in the inner-well states in the range $k \in [0.018, 0.025]$, while avoiding unphysical oscillatory behavior in the $^3S_1$ phase shift.

Figure 6 shows the extracted ^3P_J phase shifts (black curve) and the sensitivity of the potential energy structure to large changes in the P-wave phase shifts. For comparison, we show the potential energy curve of the $n = 24$ trilobite utilizing different sets of P-wave phase shifts. We see that the outer-well bound states are very insensitive to even large changes in P-wave phase shifts, as expected from their nearly pure $^3S_1$ character. However, the P-wave phase shifts by Ref. [21] (green curve) do not accurately

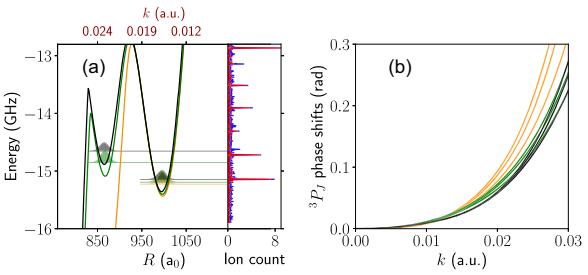


FIG. 6. The potential energy structure of the $n = 24$ trilobite molecule (a) calculated with the newly extracted $^3S_1$ phase shifts with varying ^3P_J phase shifts (b). The orange lines are the ^3P_J phase shifts taken from *ab initio* calculation, the green lines are phase shifts taken from the previous fit, and the black lines are the newly extracted phase shifts.

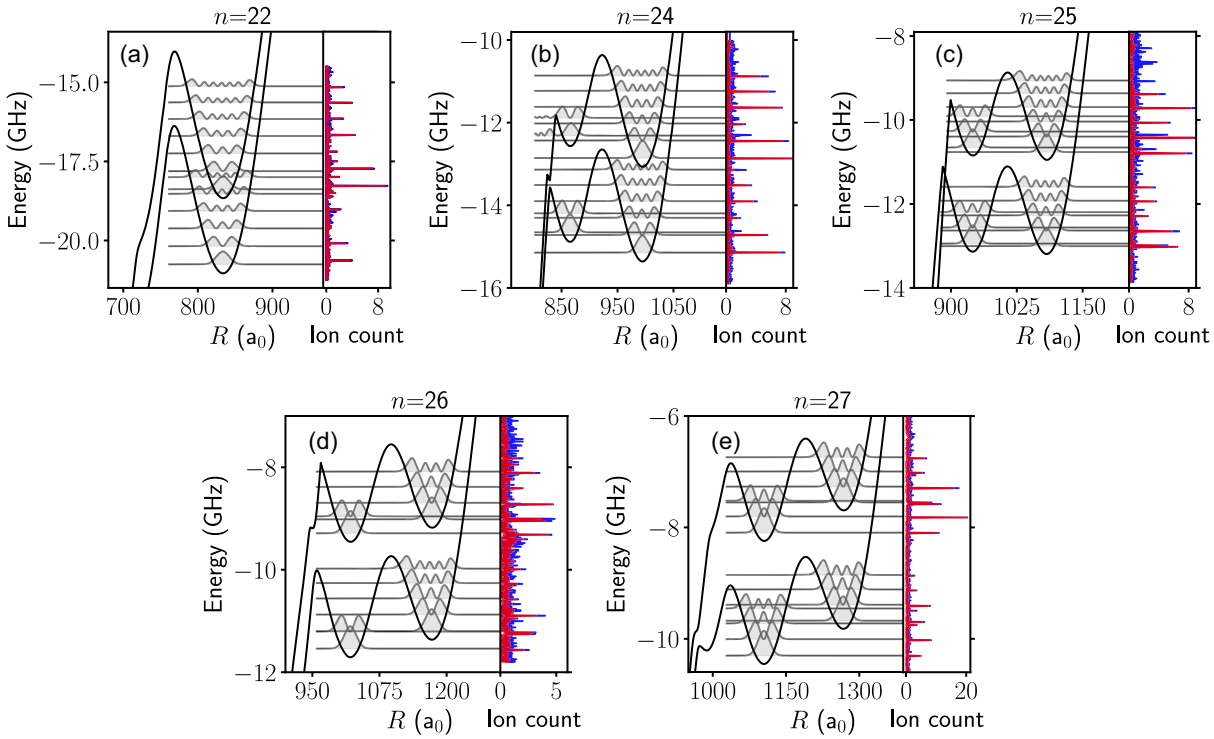


FIG. 7. The vibrational spectra of the trilobite molecule (black) for all the measured n values, from $n = 22$ to 27 plotted in (a)–(e), respectively. The blue (red) lines represent the full (zero) momentum ion counts.

predict the inner-well bound states, while the phase shifts by Ref. [42] (orange curve) renders the inner well and the observed inner-well bound state completely absent. The newly extracted set of phase shifts (black curve) not only accurately predict the positions of the inner-well and outer-well bound states for $n = 24$, it also reproduces the double-well structure for $n = 24$–27 and explains all the double peak structures quite well (see Fig. 7).

Figure 7 shows the vibrational spectra of the trilobite molecule for all n values observed. The vibrational states calculated using the newly extracted phase shifts are plotted adjacent to the observed ion count signal, making the assignment of peaks to the inner or outer well straightforward. The zero momentum spectra (red) helps us identify stable bound states and accurately depicts almost all fully bound states in the outer well. The full momentum spectra, on the other hand, also contain the zero momentum signal, as well as signals from unstable molecular resonances. Signals that are present in the full momentum spectra but absent in the zero momentum spectra represent these unstable states, either highly excited states in the outer well [see Fig. 7(c)] or states localized in the inner wells of the $n = 24$, 25 molecule near the avoided crossings [see Figs. 7(c) and 7(d)]. Note that some of these unstable states might be significantly affected by nonadiabatic coupling, explaining the relatively larger error in the numerical prediction of their vibrational splittings (∼10%). Since large changes in the ^3P_J phase shifts are necessary to affect the binding energies of the inner-well states, the exact form of the ^3P_J phase shifts extracted have limited accuracy. Nevertheless, the binding energies of all bound states (in the inner and outer wells) are reproduced very accurately (error ∼0.8%; see Fig. 5) as is visible in Fig. 7.

PHYSICAL REVIEW LETTERS 136, 243002 (2026)

Observation of Spin-Singlet Butterfly Rydberg Molecules in an Ultracold Atomic Rb Gas

Markus Exner,[1] Rohan Srikumar,[2] Richard Blättner,[1] Peter Schmelcher,[2,3] H. R. Sadeghpour,[4] Matthew T. Eiles,[5,6] and Herwig Ott[1,*]

[1]Department of Physics and Research Center OPTIMAS, Rheinland-Pfälzische Technische Universität Kaiserslautern-Landau, 67663 Kaiserslautern, Germany

[2]Zentrum für Optische Quantentechnologien, Universität Hamburg, Luruper Chaussee 149, 22761 Hamburg, Germany

[3]The Hamburg Centre for Ultrafast Imaging, Universität Hamburg, Luruper Chaussee 149, 22761 Hamburg, Germany

[4]ITAMP, Center for Astrophysics | Harvard and Smithsonian, Cambridge, Massachusetts 02138, USA

[5]Max Planck Institute for the Physics of Complex Systems, Nöthnitzer Straße 38, 01187 Dresden, Germany

[6]Department of Physics and Astronomy, Purdue University, West Lafayette, Indiana 47907, USA

(Received 30 November 2025; accepted 4 May 2026; published 18 June 2026)

We report the observation of spin-singlet ultralong-range Rydberg butterfly molecules consisting of a ground-state atom bound to a Rydberg atom by P-wave scattering of ^{87}Rb Rydberg electrons from ^{87}Rb(5 s) atoms. A three-photon excitation scheme enables the photoassociation of these molecules by weakly admixing Rb$(18f_{7/2})$ states. The measured binding energies, kilo-Debye permanent electric dipole moments, and lifetimes are in excellent agreement with theory. Two long-lived vibrational levels, red detuned from the Rb$(18f_{7/2})$ threshold, are observed. This experiment is a foundational step in the production of ultracold anions and heavy Rydberg ion-pair systems.

DOI: 10.1103/q5r1-whjr

The zoology of ultra-long-range Rydberg molecules (ULRMs) categorizes its subjects by the orbital angular momentum (ℓ) of the Rydberg electron [1–4]. Generally, low-ℓ Rydberg states with nonzero quantum defects scatter off perturbing ground-state atoms to form nonpolar ULRMs [5–7], while nearly degenerate Rydberg states with high ℓ hybridize in interaction with perturbers to form polar ULRMs [8–11]. These molecules, known colloquially as trilobites and butterflies, possess large permanent electric dipole moments and have been observed in ultracold gases of alkali atoms in predominantly spin-triplet configurations [12–16]. Spin-singlet configurations lead to much shallower, or even repulsive, molecular potentials, and thus to date have only played an indirect role through the mixing of singlet and triplet states via the hyperfine structure of the ground-state atom [17–19].

Ultracold neutral plasmas have been created [20–23], sparking the exploration of exotic phases such as the frozen-Rydberg gas [24–26] and Coulomb crystal [27] in ultracold gases. While there may be a diverse selection of systems that can be used to create pair-ion plasmas [28–30], two component cold plasmas created by ionizing ultracold atoms suffer from a variety of heating mechanisms mainly because one component (electron) is always much lighter and faster, thus leading to heating and spontaneous three-body recombination and Rydberg formation [31]. In 2013, it was proposed to create an ultracold two-component plasma in a magneto-optical trap utilizing charge transfer to form ion pairs out of Feshbach molecules [32,33]. Recently, a scheme utilizing the spin-singlet ($^1P_1$) butterfly ULRM as a central step to form heavy Rydberg states has been proposed [34].

Heavy Rydberg states, the molecular analogs of Rydberg atoms, can dissociate into positive and negative atomic ions, thus providing a pathway toward production of ultracold anions that avoids known challenges posed by the lack of laser-cooling transitions in typical anions or difficulties with sympathetic cooling [35,36]. Therefore, the production of singlet ULRM states is an important first step toward the creation of strongly coupled two-component plasmas and ultracold anions. While such singlet ULRM potentials were first predicted in 2002 [10], bound molecules in the singlet butterfly molecule have not been observed for more than two decades.

In this Letter, we report the observation of a ^{87}Rb butterfly long-range Rydberg molecule in the spin-singlet ($^1P_1$) configuration. We use a three-photon excitation scheme to photoassociate the $n = 18$ singlet butterfly molecule via the small f-state admixture in its electronic state. Two long-lived vibrational states bound within a well lying about 5 GHz below the $18f_{7/2}$ atomic resonance are detected. The measured binding energies, dipole moments

*Contact author: ott@physik.uni-kl.de

Published by the American Physical Society under the terms of the Creative Commons Attribution 4.0 International license. Further distribution of this work must maintain attribution to the author(s) and the published article's title, journal citation, and DOI.

and lifetimes of these levels are in excellent agreement with theoretical predictions, confirming the $^1P_1$ characterization of the molecule.

The binding mechanism of an ultra-long-range Rydberg molecule is mediated by the scattering of the Rydberg electron from the ground-state atom a distance of R. Scattering via S and P partial waves dominates because of the Rydberg electron's low kinetic energy. The phase shifts in these partial waves are sensitive to both the spin configuration (singlet and triplet) and, for heavy atoms such as Rb and Cs, the fine structure in the P-wave channel. We include the six dominant scattering channels $^{2S+1}L_J$: $^1S_0$, $^1P_1$, $^3S_1$, and $^3P_{0,1,2}$. The resulting high-ℓ molecular states are largely decoupled from one another.

We obtain the adiabatic potential energy curves from the R-dependent eigenvalues of the electronic Hamiltonian, including the full spin-dependent structure of both Rb atoms [37], computed using a Green's function treatment [38].

Figure 1(a) shows the adiabatic potential energy curves (PECs) for $\Omega = 3/2$, where Ω is the projection of the total angular momentum onto the internuclear axis. The dissociation threshold corresponds to the $(|18f_{7/2}\rangle + |5s_{1/2}, F = 1\rangle)$ pair state. The $^1P_1$ scattering

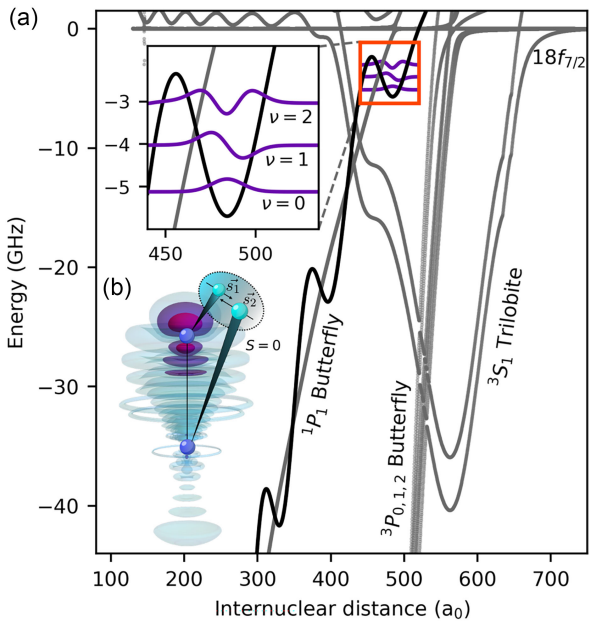


FIG. 1. (a) Born-Oppenheimer potential energy curves for the $n = 18$, $\Omega = 3/2$ $^{87}Rb_2$ ULRM. The black curve highlights the potential curve with $M_L \approx 0$, whose oscillations are deep enough to support vibrational states. The red box marks the first butterfly well, magnified in the inset with the calculated vibrational states. (b) Electron density distribution of the spin-singlet butterfly molecule.

produces the oscillating "stairwell" potential highlighted in black as well as the nonoscillating potential slicing through the stairwell. At the equilibrium point of the highlighted potential well, the electronic state has a 98.6% spin-singlet admixture [39]. Although the projection of the orbital angular momentum M_L is not separately conserved, these two potentials are predominantly of $M_L = 0$ and $|M_L| = 1$ character, respectively, due to the very weak spin-orbit coupling [44,45]. There is no appreciable change in the stairwell potential for different values of Ω, given that the $M_L = 0$ configuration is not forbidden. Unlike the $^3S_1$ and ^3P_J phase shifts, the $^1P_1$ phase is a monotonic and concave function of the electron momentum k. Hence the PECs exhibit local minima only due to the oscillatory Rydberg electronic density.

The first well in this stairwell potential supports three bound vibrational states [see inset of Fig. 1(a)]. Their energetic proximity to the $18f_{7/2}$ resonance, and the f-state electronic admixture they possess make it possible to access these vibrational states via three-photon excitation. To observe these states, we prepare ^{87}Rb atoms in a crossed dipole trap operating at $\lambda = 1064$ nm with a temperature of 40 μK, a diameter of 40 μm, and a peak density of 4×10^{13} cm^{-3}. Initially, the atoms are in the $F = 1$ ground state and photoassociation in the molecular state is achieved by a three-photon excitation scheme $(5s_{1/2} \rightarrow 5p_{3/2} \rightarrow 5d_{5/2} \rightarrow 18f_{7/2})$ at 780, 776, and 1308 nm, where the first two lasers are blue detuned to the intermediate states. After excitation, the Rydberg atoms are ionized by a CO_2 laser and the ions are detected in a reaction microscope. The experimental sequence consists of 1100 excitation and ionization pulses with a duration of $t_{\mathrm{exc}} = 3$ μs. During excitation, the dipole trap is turned off to avoid ionization from the $5d_{5/2}$ state. Because of the high field sensitivity of the molecules, the electric extraction field is switched off during photoassociation, while a residual field remains.

Figure 2 shows the spectrum with energies measured relative to the $18f_{7/2}$ atomic resonance. The solid black curve shows a fit of eight Lorentzian peaks, binned over the raw signal (gray markers). The spectrum clearly exhibits two narrow main peaks, with a full width at half maximum (FWHM) of about 7 MHz. Compared to the pure trilobite resonances observed in Refs. [15,16], the FWHM is the same, but the signal strength is significantly lower. We attribute the lower signal strength to the smaller molecular bond length, which reduces the Franck-Condon factor due to the reduced probability of finding two atoms at the correct separation in the ultracold gas. These resonances can be assigned to the ground and first-excited vibrational states in the first well of the stairwell potential, below the $18f_{7/2}$ atomic resonance [Fig. 1(a)]. The red curve shows the theoretical photoassociation spectra, with the relative signal heights showing a good match between experiment and theory [39].

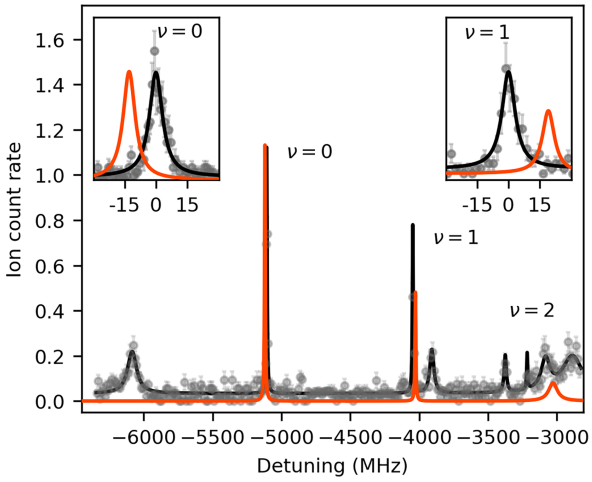


FIG. 2. Binned ion Rb^+ signal (gray markers), the Lorentzian fits (black curve), and calculated photoexcitation signal profile (red curve) are plotted as a function of detuning from the $Rb(18f_{7/2})$ threshold. The first two molecular singlet butterfly resonances are magnified in the two insets. On the horizontal axes in the insets, the molecular resonances are at zero energy, whereas on the main figure, the zero is at the atomic Rydberg resonance.

Note that the signal strengths do not follow the Franck-Condon behavior [46,47], which would predict a much weaker signal for the odd-parity vibrational state, due to the strong R dependence of the $18f_{7/2}$ state admixture in the singlet butterfly state. Finally, the observed splitting between the two resonances, $\Delta E_\nu = 1.06$ GHz, is in excellent agreement with the calculated vibration splitting, $\Delta E_\nu = 1.09$ GHz.

The spectrum also contains several peaks with substantially lower signal strength. These resonances have a high FWHM that is more than twice as large as that of the two larger peaks. One of these peaks fits well with the second excited vibrational state ($\nu = 2$) at a detuning of about -3 GHz, with an FWHM of 76 MHz. The lower signal strength can be attributed to a shorter lifetime due to molecular decay; this state has a much higher tunneling rate through the potential barrier separating it from the short-range region where ℓ-changing predissociating collisions become dominant.

The origin of the other low signal peaks is not well understood. While highly excited trilobite states (stabilized through nonadiabatic effects [48,49]) can exist for $n = 18$ in this energy range, the computed level spacing ($\sim$550 MHz) of these states is substantially smaller than that seen between the observed resonances. There are additional molecular potential curves associated with higher partial wave ($L \geq 2$) scattering present in this energy range at still smaller internuclear distances [11], and thus a possible candidate for these features could be "dragonfly" Rydberg molecules. A quantitative calculation to verify this requires the extension of the spin-coupled Green's function treatment to include $L = 2$ partial waves, and thus further characterization of these states remains the subject of future work.

Recent works have elaborated on the extraction of $^3S_1$ phase shifts [16] and ^3P_J resonance positions [40] using spectral analysis of the ULRM. In the present calculation, we use the energy-dependent $^3S_1$ and ^3P_J phase shifts fitted to trilobite spectra in Ref. [16], as they accurately describe the $S = 1$ trilobite and butterfly curves. The $^1P_1$ phase shift for Rb were taken from Ref. [50], which is in good agreement with that calculated by Ref. [51]. The $^1P_1$ phase shift was modified by an energy-independent factor of 1.02, which shifts the well depth by around -435 MHz and leads to the excellent match between theoretically predicted and observed molecular resonances seen in Fig. 2. A perturbative estimate shows that contributions from $L = 2$ scattering could have an effect on the level of several tens of MHz.

We next characterize the two main peaks by their electric dipole moments and lifetimes to confirm that they correspond to singlet butterfly molecules. Since the butterfly potential originates from the degenerate hydrogen manifold and couples high angular momentum states with different parities, these high-ℓ ULRM exhibit linear Stark shifts. To determine the dipole moment, the broadening of the molecular resonance is measured for different electric fields and fitted with a convolution of a Lorentzian and two step functions of width $2dE$ [see Fig. 3(a)]. Figure 3(b) shows the fitted dE as a function of the electric field, which leads to nearly identical dipole moments of 851 and 857 Debye, for the $n_v = 0$ and $n_v = 1$ levels, respectively. The theoretical dipole moments were calculated using electronic states obtained by diagonalizing the electronic Hamiltonian in a truncated basis of Rydberg states after benchmarking the basis size using the Green's function results [37]. The results are summarized in Table I and show an excellent agreement with the measured dipole moments, with less than 3% relative error between theory and experiment. The values of the dipole moments rule out the possibility that these states have been misclassified as singlet butterfly states, as other high-ℓ ULRMs in this same energy range, either the $L = 0$ (trilobite) or $L = 2$ (dragonfly) states, possess smaller dipole moments [2,10,11].

Figure 3(b) also shows the theoretical Stark broadening map as a function of the applied electric field E, while considering a residual field E_0. We see that the theory and observation matches well when we take E_0 to be 1 V/m, corresponding to a Stark broadening of 5 MHz. The Stark broadening of the polar molecule due to the residual stray field is thus the main contributor to the observed resonance widths, followed by the finite laser linewidth.

Finally, we measured the lifetime of the butterfly molecules by reducing the pulse duration to 1 μs and varying the time of ionization. We only count Rb^+ ions with zero momentum as ℓ-changing collisions lead to ions with large momentum. The ion counts are then fitted with

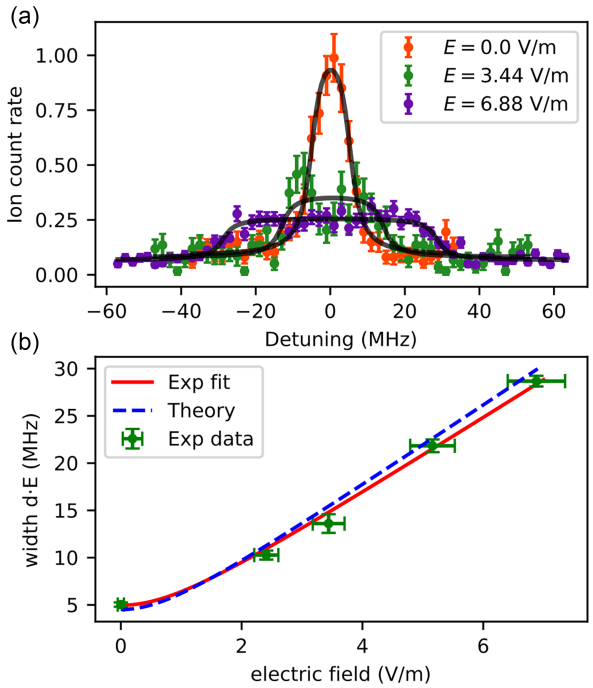


FIG. 3. Measurement of the dipole moment for the $\nu = 0$ butterfly state. (a) Spectrum of the molecular resonance for different electric fields fitted with a convolution of a Lorentzian and two step functions of width $2dE$. (b) The stark broadening map of the $\nu = 0$ state with the measured resonance widths (green markers) plotted as a function of applied electric field E_a. The dashed blue curve is the calculated width dE as a function of the total electric field $E = \sqrt{E_a^2 + E_0^2}$. The red curve is a fit over the observed data used to obtain the dipole moment of $d = 851 \pm 104$ Debye.

an exponential function as shown in Fig. 4. The vibrational ground state shows a longer lifetime than the corresponding atomic resonance. This is a signature of the high-ℓ admixture of the molecular state, as the lifetime increases with angular momentum. This was also observed in previous trilobite studies [15]. Additionally, we find that the $\nu = 1$ vibrational state has a significantly shorter lifetime than does the ground state. This can be attributed

TABLE I. Binding energies, full width at half maximum (FWHM), dipole moments, and lifetimes of the butterfly molecules.

	$\nu = 0$	$\nu = 1$	$18f_{7/2}$
$E_{b,Exp}$ (MHz)	5107 ± 2	4047 ± 2	
$E_{b,Theo}$ (MHz)	5119	4027	
FWHM (MHz)	7.2 ± 0.4	7.1 ± 0.9	
d_{Exp} (Debye)	851 ± 104	857 ± 104	
d_{Theo} (Debye)	852.5	832.6	
Lifetime (μs)	6.31 ± 0.67	1.79 ± 0.19	4.15 ± 0.06

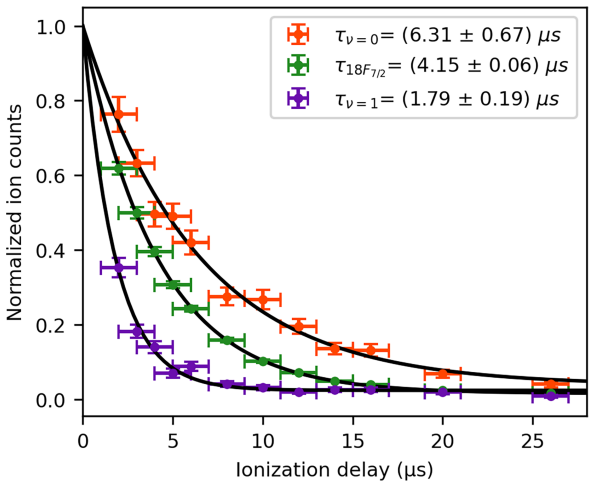


FIG. 4. Normalized ion counts as a function of the delay between excitation and ionization for the two molecular and the atomic $18f_{7/2}$ state. The high-ℓ admixture leads to an increased lifetime of the molecule. The shorter lifetime for the $\nu = 1$ state is likely due to the avoided crossings with $M_L = \pm 1$ potentials.

to its energetic proximity to the avoided crossings between the $M_L = 0$ and $M_L = \pm 1$ curves, leading to increased nonadiabatic decay to smaller internuclear distances, consequently resulting in ℓ-changing collisions or associative ionization. However, the computed lifetimes of these states are substantially longer than those measured [39], suggesting that effects outside the scope of this calculation, such as three-body collisions or additional potential curve coupling to higher partial wave states, may play a role in reducing the lifetime.

The work presented here constitutes the first observation of a Rydberg butterfly molecule where the Rydberg electron and the valence electron of the ground-state atom are in a spin-singlet configuration. The observed level spacing and dipole moments are incompatible with any other vibrational states (e.g., highly excited trilobites) that could be present in this energy range, and are in excellent agreement with the properties of singlet butterfly molecules predicted by theory. This also verifies the accuracy of the theoretical description based on the energy-dependent scattering phase shifts for the $^1P_1$ channel calculated in Refs. [10,50]. The unassigned peaks visible in the spectrum point toward the importance of including higher-order partial wave scattering in the theoretical description and, given the smaller internuclear distances and low principal quantum number at play in this experiment, possible improvements to the underlying Fermi model.

The successful preparation of such singlet character-dominated molecular states is a key stepping stone toward the production of heavy Rydberg ion-pair states. Dissociation of such ion-pair states will lead to the creation of ultracold Rb anions, which have not been observed to date

in ultracold atomic traps, and potentially to the formation of strongly coupled two component plasmas [52].

Acknowledgments—We would like to thank Max Althön for helpful discussions. This project is funded by the German science foundation DFG, Projects No. 460443971, No. 316211972, and No. INST 248/268-1. H. R. S. acknowledges funding at ITAMP through the NSF. P. S. acknowledges support by the cluster of excellence CUI: Advanced Imaging of Matter of the Deutsche Forschungsgemeinschaft (DFG) EXC-2056 Project ID—309715994.

Data availability—The data that support the findings of this article are not publicly available upon publication because it is not technically feasible and/or the cost of preparing, depositing, and hosting the data would be prohibitive within the terms of this research project. The data are available from the authors upon reasonable request.

[1] J. P. Shaffer, S. T. Rittenhouse, and H. R. Sadeghpour, Nat. Commun. **9**, 1965 (2018).
[2] M. T. Eiles, J. Phys. B **52**, 113001 (2019).
[3] C. Fey, F. Hummel, and P. Schmelcher, Mol. Phys. **118**, e1679401 (2020).
[4] F. B. Dunning, S. K. Kanungo, and S. Yoshida, J. Phys. B **57**, 212002 (2024).
[5] V. Bendkowsky, B. Butscher, J. Nipper, J. P. Shaffer, R. Löw, and T. Pfau, Nature (London) **458**, 1005 (2009).
[6] B. J. DeSalvo, J. A. Aman, F. B. Dunning, T. C. Killian, H. R. Sadeghpour, S. Yoshida, and J. Burgdörfer, Phys. Rev. A **92**, 031403(R) (2015).
[7] M. Peper and J. Deiglmayr, Phys. Rev. Lett. **126**, 013001 (2021).
[8] C. H. Greene, A. S. Dickinson, and H. R. Sadeghpour, Phys. Rev. Lett. **85**, 2458 (2000).
[9] E. L. Hamilton, C. H. Greene, and H. R. Sadeghpour, J. Phys. B **35**, L199 (2002).
[10] A. A. Khuskivadze, M. I. Chibisov, and I. I. Fabrikant, Phys. Rev. A **66**, 042709 (2002).
[11] P. Giannakeas, M. T. Eiles, F. Robicheaux, and J. M. Rost, Phys. Rev. Lett. **125**, 123401 (2020).
[12] W. Li, T. Pohl, J. M. Rost, S. T. Rittenhouse, H. R. Sadeghpour, J. Nipper, B. Butscher, J. B. Balewski, V. Bendkowsky, R. Löw, and T. Pfau, Science **334**, 1110 (2011).
[13] D. Booth, S. T. Rittenhouse, J. Yang, H. R. Sadeghpour, and J. P. Shaffer, Science **348**, 99 (2015).
[14] T. Niederprüm, O. Thomas, T. Eichert, C. Lippe, J. Pérez-Ríos, C. H. Greene, and H. Ott, Nat. Commun. **7**, 12820 (2016).
[15] M. Althön, M. Exner, R. Blättner, and H. Ott, Nat. Commun. **14**, 8108 (2023).
[16] M. Exner, R. Srikumar, R. Blättner, M. T. Eiles, P. Schmelcher, and H. Ott, Phys. Rev. Lett. **134**, 223401 (2025).
[17] H. Saßmannshausen, F. Merkt, and J. Deiglmayr, Phys. Rev. Lett. **114**, 133201 (2015).
[18] K. S. Kleinbach, F. Meinert, F. Engel, W. J. Kwon, R. Löw, T. Pfau, and G. Raithel, Phys. Rev. Lett. **118**, 223001 (2017).
[19] F. Böttcher, A. Gaj, K. M. Westphal, M. Schlagmüller, K. S. Kleinbach, R. Löw, T. C. Liebisch, T. Pfau, and S. Hofferberth, Phys. Rev. A **93**, 032512 (2016).
[20] T. Killian, T. Pattard, T. Pohl, and J. M. Rost, Phys. Rep. **449**, 77 (2007).
[21] T. C. Killian, S. Kulin, S. D. Bergeson, L. A. Orozco, C. Orzel, and S. L. Rolston, Phys. Rev. Lett. **83**, 4776 (1999).
[22] B. B. Zelener, E. V. Vilshanskaya, N. V. Morozov, S. A. Saakyan, A. A. Bobrov, V. A. Sautenkov, and B. V. Zelener, Phys. Rev. Lett. **132**, 115301 (2024).
[23] R. S. Fletcher, X. L. Zhang, and S. L. Rolston, Phys. Rev. Lett. **96**, 105003 (2006).
[24] W. Li, M. W. Noel, M. P. Robinson, P. J. Tanner, T. F. Gallagher, D. Comparat, B. Laburthe Tolra, N. Vanhaecke, T. Vogt, N. Zahzam, P. Pillet, and D. A. Tate, Phys. Rev. A **70**, 042713 (2004).
[25] M. P. Robinson, B. Laburthe Tolra, M. W. Noel, T. F. Gallagher, and P. Pillet, Phys. Rev. Lett. **85**, 4466 (2000).
[26] W. Li, P. J. Tanner, and T. F. Gallagher, Phys. Rev. Lett. **94**, 173001 (2005).
[27] T. Pohl, T. Pattard, and J. M. Rost, Phys. Rev. Lett. **92**, 155003 (2004).
[28] W. Oohara and R. Hatakeyama, Phys. Rev. Lett. **91**, 205005 (2003).
[29] W. Oohara, R. Hatakeyama, and S. Ishiguro, Phys. Rev. E **68**, 066407 (2003).
[30] N. Sato, T. Mieno, T. Hirata, Y. Yagi, R. Hatakeyama, and S. Iizuka, Phys. Plasmas **1**, 3480 (1994).
[31] T. Pohl, D. Vrinceanu, and H. R. Sadeghpour, Phys. Rev. Lett. **100**, 223201 (2008).
[32] A. Kirrander, S. Rittenhouse, M. Ascoli, E. E. Eyler, P. L. Gould, and H. R. Sadeghpour, Phys. Rev. A **87**, 031402(R) (2013).
[33] S. Markson and H. R. Sadeghpour, J. Phys. B **49**, 114006 (2016).
[34] F. Hummel, P. Schmelcher, H. Ott, and H. R. Sadeghpour, New J. Phys. **22**, 063060 (2020).
[35] C. W. Walter, N. D. Gibson, D. J. Matyas, C. Crocker, K. A. Dungan, B. R. Matola, and J. Rohlén, Phys. Rev. Lett. **113**, 063001 (2014).
[36] R. Tang, R. Si, Z. Fei, X. Fu, Y. Lu, T. Brage, H. Liu, C. Chen, and C. Ning, Phys. Rev. Lett. **123**, 203002 (2019).
[37] M. T. Eiles and C. H. Greene, Phys. Rev. A **95**, 042515 (2017).
[38] C. H. Greene and M. T. Eiles, Phys. Rev. A **108**, 042805 (2023).
[39] See Supplemental Material A and B at http://link.aps.org/supplemental/10.1103/q5r1-whjr for a detailed explanation of the singlet spin admixture in molecular states, which includes Ref. [37]; for a detailed explanation of the signal profile calculation, which includes Refs. [5,40–43]; for an estimation of the radiative lifetime of these high-ℓ molecules.
[40] F. Engel, T. Dieterle, F. Hummel, C. Fey, P. Schmelcher, R. Löw, T. Pfau, and F. Meinert, Phys. Rev. Lett. **123**, 073003 (2019).

[41] M. Peper, M. Trautmann, and J. Deiglmayr, Phys. Rev. A **107**, 012812 (2023).
[42] J. Tallant, S. T. Rittenhouse, D. Booth, H. R. Sadeghpour, and J. P. Shaffer, Phys. Rev. Lett. **109**, 173202 (2012).
[43] G. Breit and E. Wigner, Phys. Rev. **49**, 519 (1936).
[44] M. Deiß, S. Haze, J. Wolf, L. Wang, F. Meinert, C. Fey, F. Hummel, P. Schmelcher, and J. Hecker Denschlag, Phys. Rev. Res. **2**, 013047 (2020).
[45] H. Rivera-Rodríguez and R. Jáuregui, Phys. Rev. Res. **6**, 013173 (2024).
[46] A. S. Coolidge, H. M. James, and R. D. Present, J. Chem. Phys. **4**, 193 (1936).
[47] E. U. Condon, The Franck-Condon principle and related topics, in *Selected Scientific Papers of E.U. Condon*, edited by A. O. Barut, H. Odabasi, and A. van der Merwe (Springer, New York, 1991), pp. 515–529.
[48] R. Srikumar, M. Exner, R. Blättner, P. Schmelcher, M. T. Eiles, and H. Ott, Phys. Rev. Res. **7**, 043103 (2025).
[49] M. T. Eiles and F. Hummel, Phys. Rev. A **109**, 022811 (2024).
[50] M. T. Eiles, Phys. Rev. A **98**, 042706 (2018).
[51] M. I. Chibisov, A. A. Khuskivadze, and I. I. Fabrikant, J. Phys. B **35**, L193 (2002).
[52] M. S. Murillo, Phys. Plasmas **11**, 2964 (2004).

Supplementary Material

Spin singlet admixture in ULRM

In this section we briefly study the singlet admixture in the R -dependent potential energy structure of the ULRM. Using the Born-Oppenheimer approximation, the wavefunction of the ULRM can be written as $|\psi_{el}(r,R)\rangle|\chi_\nu(R)\rangle$, where $\psi_{el}(r,R)$ is the electronic wavefunction obtained via the diagonalization of the spin-coupled electronic Hamiltonian [1], and $\chi_\nu(R)$ are the vibrational wavefunctions localized in the corresponding singlet ULRM potential well. Then, the given electronic wavefunction can be expanded in the diatomic basis $\{|n,l,s_1,j,mj\rangle_r \otimes |s_2,ms_2,I,mI\rangle_g\}$, where the first vector denotes the Rydberg atomic orbitals, and the second vector denotes the electronic and nuclear spin structure of the ground state atom [1]. The total spin operator is then given by $\hat{s} = \hat{s}_1 + \hat{s}_2$, and the total spin polarization $ms = ms1 + ms2$. Note that $ms1$ is not a good quantum number in the Rydberg atom basis due to spin-orbit coupling. In a Rubidium dimer $s_1 = s_2 = 0.5$, hence s has to be 0 or 1, namely the spin singlet or triplet configuration. The electron-perturber scattering interaction mixes these singlet and triplet channels as a function of R. The spin-singlet admixture in any electronic state ψ_{el} can be found by projecting the wavefunction onto the singlet subspace, i.e $\zeta\,(R) = |\langle\psi_{el}(R)|s=0, ms=0\rangle|^2$.

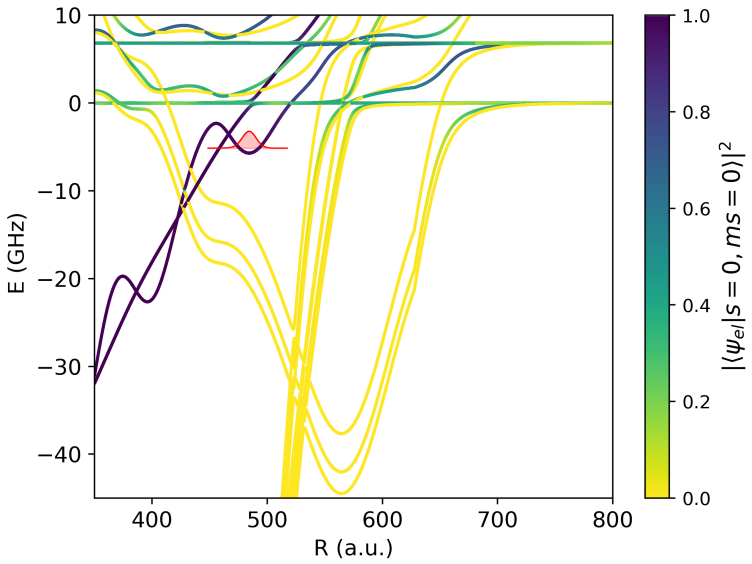


FIG. 1. The potential energy curves of the ULRM for $\Omega = 1/2$. The colorbar indicates the R-dependent spin-singlet admixture in the Born-Oppenheimer electronic states, corresponding to each potential. The stairwell potentials are highlighted due to their predominantly spin singlet nature. The $\nu = 0$ vibrational state localized in the singlet well is plotted in red.

Figure 1 show the molecular potential energy curves of the ULRM for $\Omega = 1/2$, colored according to the spin-singlet admixture $\zeta\,(R)$ in their electronic wavefunctions. We see that the stairwell potential that holds the observed vibrational state (plotted in red) are of predominantly spin-singlet character whereas the trilobite potentials and the P-wave butterfly potentials are of strong

spin-triplet character. At the equilibrium point of the potential well $R_{eq} = 463.7$ a.u., $\zeta(R_{eq}) = 0.986$. To look at the average spin-character of the observed $\nu = 0$ vibrational state, we can taken an average of $\zeta(R)$ with respect to the vibrational ground state, i.e., $\zeta_\nu = \int \zeta(R)|\chi_{\nu=0}(R)|^2 dR$. We see that $\zeta_{\nu=0} = 0.982$, proving that the observed molecule exhibits an almost completely spin-singlet character.

Photoexcitation of ULRM

We find that the observed signal profile of the singlet ULRM in the main text does not follow the expected suppression of odd vibrational states, typical in other experimental studies of ULRM [2–5]. Here, we explain this phenomenon by calculating the rate at which a pair of atoms in the atomic gas is coherently photo-excited to each vibrational state, and compare the calculated relative excitation rates to the relative line heights in the experimental data (figure 2 in the main text).

The wavefunction of the ULRM is taken to be $|\psi_{el}(r,R)\rangle|\chi_\nu(R)\rangle$, where $\psi_{el}(r,R)$ is the electronic wavefunction obtained, and $\chi_\nu(R)$ are the vibrational wavefunctions localized in the singlet ULRM potential well. The dipole transition probability to each of the vibrational state χ_ν is given by

$$\Gamma_\nu = |\int D(R)\chi_\nu(R)\chi_i(R)dR|^2\,, \tag{1}$$

where $D(R)$ is the electronic dipole transition function, proportional to the $18f_{7/2}$-state admixture in the ULRM electronic state. The initial state of the two atoms in the relative coordinate R, $\chi_i(R)$, has a large de Broglie wavelength at the ultracold temperature of the experiment and is thus effectively constant over the extent of the molecular wavefunction. If we use the Franck Condon principle, we ignore the R-dependence of D, and the transition strength is decided by the overlap of the vibrational wavefunctions $|\langle\chi_\nu|\chi_i\rangle|^2$. This would imply a vanishingly small transition strength to odd-parity vibrational states from the even-parity initial state. However, we see that our observation does not exhibit this behavior. Hence a beyond Frank-Condon calculation, explicitly considering the R-dependence of the electronic dipole transition function is necessary to understand the observed spectrum.

To circumvent the complexities in initial state characterization, polarization and Ω dependent branching ratios, we approximate the dipole transition function to just be the $18f_{7/2}$-state admixture that facilitates the dipole transition. The dipole transition function is then given by:

$$D(R) \sim \sum_{m_j} |\langle 18f_{7/2}, m_j|\psi_{el}(r,R)\rangle|^2\,. \tag{2}$$

Then we model the photo-excitation line shape using a Breit-Wigner profile [6],

$$\sigma_\nu(\omega) = \Gamma_\nu \frac{\Delta_\nu/2}{(\omega-\omega_\nu)^2 + (\Delta_\nu/2)^2} \tag{3}$$

with ω denoting the laser detuning, ω_ν denoting the energy of the vibrational state, and Δ_ν denoting the resonance width of the vibrational state. Here, we take both the Δ_ν and ω_ν from the experimental values given in the main text.

Figure 2 shows the calculated signal profile $\Gamma(\omega)$ (red line) in comparison with the Lorentzian fit (black curve) of the ion count spectra. The height of the signal profiles were scaled to match

3

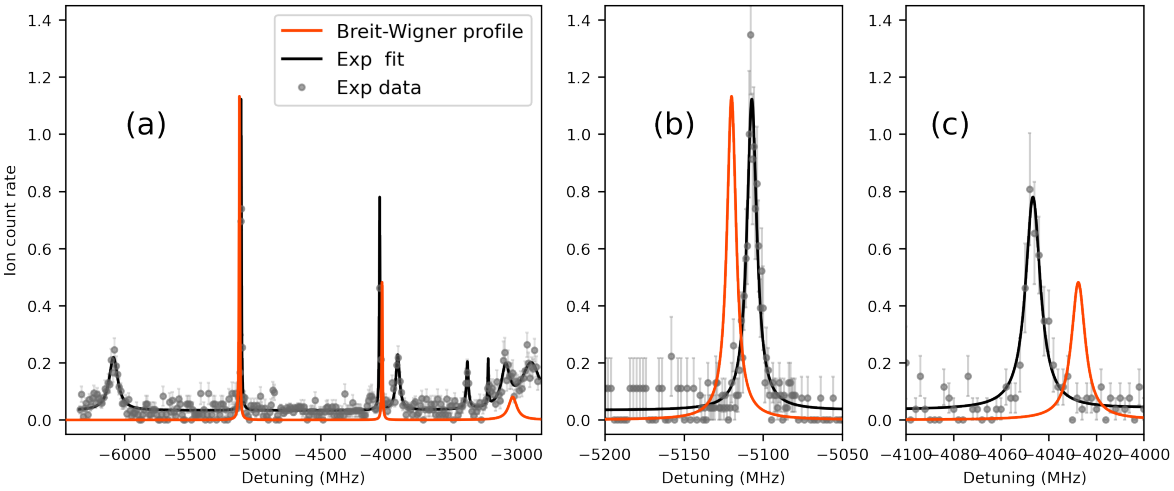


FIG. 2. (a) The calculated signal profiles of the singlet ULRM (red curve) in comparison with the measured Ion counts (grey markers) and Lorentzian fit of the experimental spectra (black curve). (b) and (c) Show magnified view of the signal near the resonance energies of the $\nu = 0$ and $\nu = 1$ vibrational states, respectively.

the ion count rate for the $\nu = 0$ vibrational state,i.e. ground state. We see that the calculated relative signal heights match the observation very well, deviating from the Franck-Condon result. This indicates that the R-dependence of the dipole transition element is necessary to explain the observed phenomena, i.e. increased excitation strength of odd vibrational states.

Radiative lifetimes

The radiative lifetimes of high-ℓ ULRMs are generally larger than that of their low -l counterparts due to the larger admixture of Rydberg states with higher angular momentum (and lower decay rates). Our observations also show that the ground-state of the singlet butterfly molecule has a 6.31 μs lifetime, in comparison to the 4.15 μs lifetime of the $18f_{7/2}$ atomic resonance. Here, we do a qualitative estimation of the increase in radiative lifetime due to the high-ℓ admixture in the singlet butterfly electronic state.

The radiative lifetime τ of an atom in an electronic state $|\psi_i\rangle$ is calculated as the inverse of the total spontaneous decay rate:

$$\tau_i = 1/\gamma_i \,, \tag{4}$$

$$\gamma_i = \frac{1}{3\pi\epsilon_0\hbar c} \sum_f |\langle\psi_i|\vec{d}|\psi_f\rangle|^2 \, \omega_{i\to f}^3 \tag{5}$$

summed over all possible states $|\psi_f\rangle$ accessible via spontaneous emission (dipole transition). Here, $\omega_{i\to f}$ is the transition frequency between the initial and final state, and $\vec{d}$ is the dipole transition operator. For the $18f_{7/2}$ atomic state, we calculate a lifetime of ~ 4.06 μs, consistent with our observation (Table 1 in main text).

4

For the singlet butterfly molecule, the total molecular wavefunction is given by $|\psi_{mol}\rangle = |\psi_{el}(r,R)\rangle|\chi_\nu(R)\rangle$, where $\psi_{el}(r,R)$ is the electronic wavefunction, and $\chi_\nu(R)$ is the vibrational wavefunction. We can expand the electronic state in the diatomic basis as $|\psi_{el}(r,R)\rangle = \sum_i c_i(R)|\psi_i\rangle|g_i\rangle$, where ψ_i is the electronic wavefunction of the Rydberg atom that undergoes radiative decay, and g_i is the ground-state atom wavefunction that does not undergo decay. Note that this R-dependency of the high-ℓ ULRM complicates the calculation of dipole transition elements to all possible $|\psi_f\rangle$ states. Hence, we make an adiabatic approximation that electronic and vibrational degrees of freedom are completely decoupled, allowing us to calculate the radiative decay rates at each R separately. Moreover, since spontaneous decay is an incoherent process we further ignore the phase relations between different Rydberg orbitals in $|\psi_{el}\rangle$, and sum over the spontaneous decay rates from each Rydberg atomic state $|\psi_i\rangle$, weighed by its population $|c_i|^2$. The radiative decay rate at any given R is given by:

$$\gamma(R) = \sum_i |c_i(R)|^2 \gamma_i \,. \tag{6}$$

The singlet butterfly molecules we observe are bound in a potential well with a local minima near $R_{eq} \sim 484$a.u. This would correspond to an approximate radiative lifetime of $\tau = 1/\gamma(R_{eq})$ $= 11.09$ μs.

If we calculate the average of this observable with respect to the vibrational wavefunction $\chi_\nu(R)$, we can make a qualitative estimate of the radiative decay rates of the vibrational state as:

$$\gamma_\nu = \int |\chi_\nu(R)|^2 \gamma(R) dR \,. \tag{7}$$

Using this equation, we calculate the radiative lifetimes of the vibrational states to be $\tau_{\nu=0} =$ 10.97 μs. If we assume that the electronic state of the ULRM is just the $18f_{7/2}$ state (all other populations are zero), then Eq. 6 and Eq. 7 will reduce to Eq. 5, wherein we will obtain the original natural lifetime $\sim 4\mu$s.

Hence the population of high-ℓ states have the effect of increasing the total radiative lifetime, by decreasing the average decay rates. Of course, the methodology used here is purely of qualitative nature and does not give us an accurate theoretical estimate that reflects our experimental observations ($\tau_{\nu=0} = 6.31$ μs). As explained in the main text, effects such as vibronic decay, three-body collisions or couplings to higher partial wave states, can all reduce the lifetime of these states.

[1] M. T. Eiles and C. H. Greene, Hamiltonian for the inclusion of spin effects in long-range Rydberg molecules, Phys. Rev. A **95**, 042515 (2017).

[2] M. Peper, M. Trautmann, and J. Deiglmayr, Role of coulomb antiblockade in the photoassociation of long-range rydberg molecules, Phys. Rev. A **107**, 012812 (2023).

[3] F. Engel, T. Dieterle, F. Hummel, C. Fey, P. Schmelcher, R. Löw, T. Pfau, and F. Meinert, Precision spectroscopy of negative-ion resonances in ultralong-range Rydberg molecules, Phys. Rev. Lett. **123**, 073003 (2019).

[4] J. Tallant, S. T. Rittenhouse, D. Booth, H. R. Sadeghpour, and J. P. Shaffer, Observation of blueshifted ultralong-range cs_2 rydberg molecules, Phys. Rev. Lett. **109**, 173202 (2012).

[5] V. Bendkowsky, B. Butscher, J. Nipper, J. P. Shaffer, R. Löw, and T. Pfau, Observation of ultralong-range Rydberg molecules, Nature **458**, 1005 (2009).

[6] G. Breit and E. Wigner, Capture of slow neutrons, Phys. Rev. **49**, 519 (1936).

Chapter 6

Conclusions

This final section presents the comprehensive conclusion of all the research work published in the course of this thesis. The common goal of these projects was to extend our understanding of the ultralong-range Rydberg molecule, and in doing so reveal new unique physical effects, while also improving our ability to engineer custom states of quantum matter. In this regard, we were able to expose new nonadiabatic effects and dynamical effects in ULRM, and enable precision spectroscopy of electron-atom scattering. Below, we provide brief conclusionary remarks and perspectives on our work in three separate themes, and end our dissertation with a discussion on future research possibilities.

Vibronic structure and nonadiabatic resonances: Our works study the breakdown of the Born-Oppenheimer approximation in the ULRM, especially in the context of high-ℓ trilobite and butterfly molecules. In Ref. [P1] we analyze the vibronic coupling between trilobite and d-states in ^{23}Na dimers. To do so, we developed analytical two-channel models that give us the diabatic potentials for any general coupled low-ℓ - trilobite system. We solve this model in an (n, R)-grid by using the principal quantum number as a synthetic dimension, observing the existence of synthetic Conical Intersections. Near these CIs, we see a complete breakdown of the adiabatic approximation, necessitating a coupled-channel approach to actually study the physics of ULRM. Our calculations predicted the existence multichannel resonance states stabilized by nonadiabatic interactions, in energy ranges where the adiabatic picture does not predict stable states. Moreover, we also see that the vibronic spectra is significantly altered from its BO counterpart, exhibiting nonadiabatic localizations and MHz-scale energy shifts. In parallel, similar works for coupled trilobite-butterfly states are performed by our collaborators [101, 238].

The work [P2] reports the first experimental observation of these predicted resonances, that are stabilized by nonadiabatic interactions. Our investigations focus on high-lying trilobite ($\nu \geq 80$) states close to the $nf_{7/2}$ atomic resonance, where the adiabatic picture does not allow stable bound states due to the avoided crossing with the butterfly PEC. The momentum resolved spectra obtained from the reactance microscope allows us to distinguish stable bound states and short lived resonances that probe internal decay channels. Depending on the n-value, the high lying states are protected against the internal decay due to nonadiabatic

couplings that facilitate surface hopping. This n-dependent diabaticity of the avoided crossings are explained using the synthetic CI picture for the coupled trilobite-butterfly system, and the surface hopping rates and lifetimes are explained with semiclassical Landau-Zener calculations. In essence, this publication reports the first ever spectral signature of the breakdown of Born-Oppenheimer approximation in the ULRM, as foreseen in [P1, 101].

The next important step in this line of research is to develop multi-channel numerical models that can include the degenerate hydrogenic manifolds, as well as hyperfine and fine structure splitting. While the two-channel models presented give us excellent qualitative results that can be experimentally verified, quantitative studies necessitates the inclusion of all underlying spin-effects. Perhaps more important is an accurate characterization of the degenerate manifold and its vibronic coupling with high-ℓ states, due to very high level densities. We find that the diabatization transform is easily altered by including more channels, which is explained by the strong nonadiabatic coupling of the trilobite and butterfly states with all $n\ell$ states nearby, hinting at the possibility of revealing interesting multichannel (≥ 3) phenomena. In the case of low-ℓ molecules, it is possible to resolve the rovibrational structure and experimentally observe complex angular momentum couplings [243–245] that cause energy corrections of the order of 100s of KHz. Since avoided crossings between high-ℓ and low-ℓ states are commonplace, the influence of nonadiabatic couplings in the rotational structure of these molecules also presents an interesting problem.

Quantum dynamics: We investigate exciting dynamical effects that emerge in the internal motion of high-ℓ dimers, due to their highly oscillatory potential structure and high level densities. Our first study [P3] explores single-channel adiabatic dynamics in pure trilobite states. Here, we report that trilobite potentials of appropriate n (≥ 50) can act as a molecular diffraction grating due to its quasi-periodic oscillatory structure in limited R-ranges. Hence, nuclear wavepackets with appropriate initial widths (similar to PEC period) can undergo continuous backscattering as they traverse the potential. We explain the results on the basis of elementary Fourier analysis, and present the ideal initial conditions necessary to observe this internal diffraction. In addition, we observe that wider initial wavepackets can trigger dynamical effects that resemble propagating Dirac comb-like structures. Fortunately, we find that the necessary initial state conditions can be readily achieved by selecting vibrational ground states in low-ℓ ULRM, particularly the dipole-allowed d-state. These states also allow us to perform projective transitions that can be used to calculate two-point correlation functions. Hence, we propose a pump-probe experiment utilizing d-states of a wide variety of n-values, to create and detect the diffraction pattern.

The most obvious extension to this work is to include the coupling between trilobite and butterfly states, and analyze how the emergent vibronic effects change the dynamics. Our second dynamical study [P4] explores the vibronic quantum dynamics that arises in this situation, utilizing a coupled trilobite-butterfly channel framework. We obtain adiabatic

potentials and states by diagonalizing the electronic Hamiltonian with both S-wave and P-wave scattering terms. Subsequently, we study the derivative nonadiabatic couplings and avoided crossings between these BO states for various n-values, reaffirming the n-dependent behaviour previously studied. The parts of the wavepacket that decay to the butterfly state via the avoided crossing are absorbed by a complex potential that simulates internal molecular decay, and prevents unphysical reflection. This also allows us to study the evolution of channel populations and total populations, and see how vibronic couplings change the dynamics and the different state populations. The work presents a two-channel analog of the diffraction effect, where the stability and population of the pattern depends on n. As expected, n-values with wider avoided crossings cause higher population decay that destabilizes the dynamics, while highly nonadiabatic n-values sustain the diffraction phenomena. Additionally, we also observe interesting multi-well tunneling effects in the low-energy dynamics of ULRM. Similar to the perspectives on spectral signatures presented before, an important quantitative step is to develop numerical methods to perform multichannel (≥ 3) dynamics in ULRM. Particularly, to see how couplings to the degenerate manifold change the results presented. Additionally, such a multichannel framework can include spin effects, thereby allowing us to study how collisional dynamics in ULRM change internal spin states.

Precision spectroscopy: Firstly, we report on the precision spectroscopy of trilobite states for five different n-values [P5], giving us access to the $^3S_1$ scattering channel. A Green's function approach that circumvents finite-basis convergence issues while also considering the underlying spin structure of the molecule, is used to quantitatively analyze the most expansive set of experimental data on trilobite molecules to date. In doing so, we were able to theoretically reproduce the observed vibrational binding energies and spacings with relative errors of 0.8% and 10%, respectively. The large binding energies of these molecules (10-20 MHz) in comparison with the experimental resolution (2-4 MHz) allows us to obtain highly precise insights on the the nature of electron-atom scattering at extremely low energies, not typically done with free electrons. The extracted $^3S_1$-scattering phases have a relative error of 0.7%, reporting excellent accuracy in the limited k-range. This high-resolution study provides an excellent benchmark for future theoretical investigations that might also consider higher order terms in the Hamiltonian, like $L \geq 2$ electron-atom partial waves, or vibronic couplings in the full-spin picture.

Secondly, we present the first ever measurement of the spin-singlet butterfly ULRM, giving us direct access to the $^1P_1$ scattering channel. The theoretical calculations performed show an excellent match with the experimentally observed binding energies, vibrational spacing, dipole moments and signal profiles, undoubtedly certifying the $^1P_1$ origin of the observed peaks. We also identify the potential energy curves that hold these bound states, and theoretically study their R-dependent spin-singlet admixture. The successful creation of the long-range $^1P_1$ finally satisfies a key step in the production of heavy Rydberg states [109], and ultracold anions.

A key extension of this work is to proceed with the creation of long-range ion pair states by radiative transition. From a theoretical perspective, this would need a rigorous study of the radiative transition strengths of the ULRM - anion transition, analyzing important branching ratios. One would also need to characterize the stability of the ion pair dimer against other radiative decay channels, and verify how a finite-width laser transition would trigger the internuclear dynamics of the Coulombic system. Very recent works also advertise the use of ULRMs to study electron-atom scattering in Ytterbium [73], revealing the complexities of electron scattering with a divalent atom. There is then the general prospect of extending ULRMs beyond alkali and alkali-earth elements, with the fundamental idea of studying high-precision low-energy electron scattering against atoms with many valence electrons.

Future research possibilities: Apart from the obvious extensions to the works in each theme listed above, here we discuss the next possible frontiers of ULRM research. While the synthetic dimension provides an exciting avenue to explore nonadiabatic physics, one could introduce real conical intersections in the nuclear coordinate space by simply introducing an external electric field, E. The external field breaks the spherical symmetry of the system and facilitates dynamics in the (R,θ) two-dimensional surface, where θ is the angle between the internuclear axis and the electric field. The polar high-ℓ states offer extensive tunability via weak electric fields [57, 66], allowing us to engineer interference/diffractive effects in a two-dimensional surface, as well as coherently control the geometric orientation and field alignment of the molecule [105].

Moreover, the exact crossing point between the butterfly PEC with the trilobite and the low-ℓ PECs can be independently controlled via changing n and E, giving us the ability to engineer conical intersections and avoided crossings, as well as tune their (R,θ)-location. The ability to engineer CIs would naturally present us with the capacity to control and study radiationless decay processes between electronic states. In principle we should also be able to observe exciting geometric phase effects [96] in ULRM dynamics.

Another equally exciting direction of research is the quantum dynamics and vibronics of triatomic Rydberg molecules [246, 247]. These trimers constituting one Rydberg atom and two ground-state atoms, support a diverse assortment of geometrical arrangements with varying R and θ. Polyatomic low-ℓ Rydberg molecules like trimers and tetramers have been theorized [248] and their spectral signatures observed [64, 249] in dense cold gases. They have been effectively utilized to study three-body correlations [69, 250], and their adiabatic dynamics have been exposed [106]. However, the quantum dynamics of high-ℓ trilobite and butterfly trimers promise completely new physics not yet observed. Triatomic systems also exhibit conical intersections in real space without external fields, possibly showcasing Jahn Teller effects [93, 94] similar to recent discoveries in triatomic Rydberg tweezer arrays [251].

Appendix A

Finite difference methods

In the course of this thesis, finite difference (FD) methods have been used consistently to obtain numerical solutions to the Schrödinger equation. Fundamentally, FD-methods aim to solve differential equations by discretizing the function domain into finite-dimensional grids, and approximating the constituent derivatives as ratio of differences [252]. The value of the solution at any point is then approximated by algebraic equations involving nearby values. The solution for the differential equation, can then be obtained by solving a system of linear equations, by known matrix manipulation techniques. Here, we give a brief overview of the numerical technique, focussing first on single channel Schrödinger equations in section. A.1, and coupled multi-channel Schrödinger equation in section A.2. In view of the scope of this thesis, our discussions are limited to one dimensional systems.

A.1 Single channel Schrödinger equation

Consider the one-dimensional Schrödinger equation discussed in section. 2.2.2, that describes the vibrational structure of the ULRM:

$$\left[-\frac{1}{2\mu}\frac{\partial^2}{\partial R^2}+\varepsilon(R)\right]\chi(R)=E\chi(R)\,. \tag{A.1}$$

We start by discretizing the domain R into a grid of size K, i.e. $[R_k]=R_0+k\Delta R$, $k=[0,1,2,...,K]$. Here $\Delta R=h$ is the constant finite-difference between any two adjacent grid points. The wavefunction is defined over this grid as $\chi_k=\chi(R_k)$, and the potential energy function is defined as $\varepsilon_k=\varepsilon(R_k)$. To represent the kinetic energy operator, we use the *central finite difference* form for the second-derivative of the wavefunction, so that

$$-\frac{1}{2\mu}\frac{\partial^2}{\partial R^2}\chi(R)|_{R=R_i}=-\frac{\chi_{i+1}-2\chi_i+\chi_{i-1}}{2\mu h^2}+O(h^2)\,, \tag{A.2}$$

where $O(h^2)$ implies that the numerical error, i.e. the deviations of the FD-form from the exact solution, scales with respect to h^2. The accuracy of the FD-representation therefore hinges on an extremely low grid-spacing h, requiring increasingly large grid-size K for fixed grid boundaries. However, one can increase the accuracy of the FD-representation (while grid size and spacing remains the same) by using a higher-order approximation for the derivative,

given by [253]

$$-\frac{1}{2\mu}\frac{\partial^2}{\partial R^2}\chi(R)|_{R=R_k} = -\frac{1}{2\mu h^2}\left[c_0\chi_k + \sum_{j=1}^{N} c_j(\chi_{j-k} + \chi_{j+k})\right] + O(h^{2N})\,, \tag{A.3}$$

where the relative error scales with respect to h^{2N}. The coefficients of expansion c_j for different orders of approximation are given in table A.1.

TABLE A.1: Coefficients c_j for central finite difference approximation of the second-derivative operator, up to the 10th order. The data is taken from [253].

Order = $2N$	c_0	c_1	c_2	c_3	c_4	c_5
2	-2	1	0	0	0	0
4	$-5/2$	$4/2$	$-1/12$	0	0	0
6	$-49/18$	$3/2$	$-3/20$	$1/90$	0	0
8	$-205/72$	$8/5$	$-1/5$	$8/315$	$-1/560$	0
10	$-5269/1800$	$5/3$	$-5/21$	$5/126$	$-5/1008$	$1/3150$

By plugging in the finite difference representations of the wavefunctions, second-derivative, and potential into the differential equation A.1, one can obtain coupled linear equations that can be written in matrix form as:

$$\underbrace{\left[-\frac{1}{2mh^2}\begin{pmatrix} c_0 & c_1 & c_2 & \cdots & 0 & 0 \\ c_1 & c_0 & c_1 & \cdots & 0 & 0 \\ c_2 & c_1 & c_0 & \cdots & 0 & 0 \\ \vdots & \vdots & \vdots & \ddots & \ddots & c_1 \\ 0 & 0 & 0 & \cdots & c_1 & c_0 \end{pmatrix} + \begin{pmatrix} \varepsilon_1 & 0 & 0 & \cdots & 0 \\ 0 & \varepsilon_2 & 0 & \cdots & 0 \\ 0 & 0 & \varepsilon_3 & \cdots & 0 \\ \vdots & \vdots & \ddots & \ddots & \vdots \\ 0 & 0 & \cdots & 0 & \varepsilon_K \end{pmatrix}\right]}_{H=T+\varepsilon} \begin{pmatrix} \chi_1 \\ \chi_2 \\ \vdots \\ \chi_K \end{pmatrix} = E \begin{pmatrix} \chi_1 \\ \chi_2 \\ \vdots \\ \chi_K \end{pmatrix}, \tag{A.4}$$

where H is the $K \times K$ hamiltonian matrix, and χ are the discretized eigenvectors in $K \times 1$ column format. One can obtain both χ and E by constructing H and then numerically diagonalizing it. Note that the potential energy matrix is diagonal in space, whereas the kinetic energy matrix is a band diagonal matrix, whose non-zero elements are confined to a narrow band of size $(2N+1)$ around the main diagonal. The Hamiltonian itself is a sparse matrix with $(2N+1)$ diagonal bands with $N \ll K$, and can be diagonalized efficiently using `LAPACK/BLAS` based modules like `numpy` or `scipy`.

A.2 Multi-channel Schrödinger equation

The state of a nuclei cannot always be represented as vibrations on a single potential curve, as discussed in section 2.2. The FD-formalism discussed above is specifically based on the discretization of Eq. A.1, representing systems that only contain a single channel. However, FD-methods can also be employed in *multi-channel* formulations described by coupled differential equations. Within the molecular physics community, the diabatic basis (sec.2.2.4)

is often employed to represent these coupled equations, to bypass badly behaved off-diagonal kinetic operator terms. For an M-channel system, the Schrödinger equation is described by a diabatic Hamiltonian

$$\hat{H} = -\frac{1}{2\mu}\sum_{m}^{M} |m\rangle\langle m| \frac{\partial^2}{\partial R^2} + \sum_{m,m'}^{M,M} |m\rangle\langle m'| \, \varepsilon^{mm'}(R) \,, \tag{A.5}$$

acting on a wavefunction

$$|\boldsymbol{\chi}(R)\rangle = \sum_{m}^{M} |m\rangle \chi^{m}(R) \,, \tag{A.6}$$

with each channel $|m\rangle$ corresponding to an electronic configuration. We see from the Hamiltonian that the kinetic energy term is diagonal in the channel-space. Moreover, the electronic channels form a complete orthonormal basis $\langle m'|m\rangle = \delta_{m'm}$, hence the second-derivative term acts on each $\chi_m(R)$ separately. Now, following the aforementioned procedure (in A.1), we can discretize the R into a grid of size K with $\Delta R = h$, and represent the wavefunction $|\boldsymbol{\chi}(R_k)\rangle = |\boldsymbol{\chi}_k\rangle = \sum_m^M |m\rangle \chi_k^m$, as a column vector of size MK. The finite difference representation of the second-derivative operator in Eq. A.5 is obtained by using a $2N$-order discretization as given in Eq. A.3. The complete discretized Hamiltonian can be represented as an $MK \times MK$ matrix, expanded in the basis $|m, k\rangle$ as

$$\langle m, k|\hat{H}|m', k'\rangle = -\frac{1}{2\mu h^2}\delta_{mm'} \, c_{|k-k'|} \, + \, \delta_{kk'} \, \varepsilon_k^{mm'} \,, \tag{A.7}$$

with m denoting the channel number, and k the R-grid position. The coefficients $c_{|k-k'|}$ can be taken from A.1, and is only non-zero if $|k - k'| \leq N$. Understandably, we see that the potential energy operator is diagonal in the k-space, but has off-diagonal terms in the m-space. The kinetic energy term on the other hand, is diagonal in the m-space but has band structure of size $2N + 1$ in the k-space. The matrix constructed using Eq. A.7 can be visualized as:

$$\begin{bmatrix} [T + \varepsilon^{11}] & [\varepsilon^{12}] & \cdots & [\varepsilon^{1M}] \\ [\varepsilon^{21}] & [T + \varepsilon^{22}] & \cdots & [\varepsilon^{2M}] \\ \vdots & \ddots & \ddots & \vdots \\ [\varepsilon^{M1}] & \cdots & \cdots & [T + \varepsilon^{MM}] \end{bmatrix} , \tag{A.8}$$

which are $M \times M$ blocks of $\left[T\delta_{mm'} + \varepsilon^{mm'}\right]$ sub-matrices, each with size $K \times K$. While more complex than its single channel counterpart, the multichannel FD-Hamiltonian is also an extremely sparse matrix (for $K \gg N$) and can be diagonalized efficiently.

Appendix B

Complex Absorbing Potentials

While numerically solving differential equations using grid-based methods, one has to limit the size of the domain to a finite range $R \in [R_0, R_k]$, imposing a fixed boundary condition. In the case of the Schrödinger equation, one typically imposes a Dirichlet condition that forces the wavefunction to be zero at the grid endpoints, i.e. $\psi(R_0) = \psi(R_k) = 0$, imitating the effects of an infinite potential barrier that does not exist in the real physical system. When calculating the spectrum of a Hamiltonian, we make sure that the end of the grid points are placed much farther away than the relevant area of interest, where the potential can hold bound states or resonances. However, scattering states and quasi-bound states often have non-vanishing wave functions that extend till the grid endpoints, where they interact with non-physical boundary conditions that alter their energy and structure. Similarly, when performing quantum dynamics, faster components of the wavepacket can leave the region of interest, be artificially reflected by the grid boundaries and return to form interference effects. These numerical artifacts with no physical analog will modify the wavefunction and the extracted observables. It is popular to solve these problems by introducing a complex absorbing potential (CAP) [198, 199] to the Hamiltonian such that

$$\hat{H}' = \hat{H} - iW(r)\,, \tag{B.1}$$

where $W(r)$ is a non-negative real function, making the modified Hamiltonian non-hermitian. The negative imaginary part of the new Hamiltonian should be designed such that it absorbs the wavefunctions before it reaches the grid endpoints, without altering the structure and dynamics of the molecule in the region of interest. For CAPs near R_0, one can achieve this by taking

$$W(r) = \eta[R - R_c]^n\,\Theta(R - R_c)\,, \tag{B.2}$$

where η is denotes the CAP strength, n is the CAP order, and Θ is the step function which ensures that the CAP vanishes for $R > R_c$ [‡]. So R_c becomes the critical domain value beyond which the Hamiltonian reverts back to its original hermitian form, and $L = R_c - R_0$ can be called the CAP length. By taking R_c to be far way from the region of interest, one can make sure that only the outgoing parts of the wavefunction are absorbed. In such a scenario, the

[‡]One can also use the step down function to ensure that the CAP vanishes for $R < R_c$

norm of the wavefunction decreases as

$$\frac{d}{dt}\|\Psi\|^2 = -2\eta\langle\Psi|W(R)|\Psi\rangle\,, \tag{B.3}$$

reflecting the loss of flux. However, unless properly designed, a CAP can also reflect an incoming/outgoing wavepacket. A simplified form of the reflection and transmission coefficients of a CAP can be derived [198, 199] as

$$|\mathcal{R}|^2 = |\frac{n!}{2^{n+2}}|^2\,\frac{\eta^2}{k^{2n}}\,, \tag{B.4}$$

$$|\mathcal{T}|^2 = \exp(\frac{-\eta W(L)kL}{E(n+1)})\,, \tag{B.5}$$

respectively, with k and E denoting the momentum and kinetic energy of the wavepacket being absorbed. It is clear from Eq. B.5 that high-energy wavepackets naturally have vanishing $|\mathcal{R}|^2$, and are hence absorbed smoothly. However, low-energy wavepackets (as well as low-energy quasi-stable states in the eigenspectra) need to be handled with care. To achieve $|\mathcal{R}|^2 + |\mathcal{T}|^2 \ll 1$, i.e. near complete absorption, one needs to minimize the strength η and increase L to be much larger than the deBroglie wavelength, i.e. $L \gg 1/k$. In our simulations, optimal results were achieved when η is taken to be around 10^{-10} to 10^{-12} atomic units (10^{-4} to 10^{-6} GHz), the CAP order is $n = 2$, and the CAP length is between 100 to 1000 a_0.

In the case of multichannel systems, certain channels can be considered open-channels when they allow for decay pathways, and certain channels are called closed-channels as there is no relevant decay mechanism. Here, one can selectively use CAPs in the open-channels, while leaving the closed channels hermitian, so that multichannel decay pathways are emulated. The open and closed channel behaviors manifest differently in the diabatic and adiabatic representations, hence one can define a CAP in a particular open channel and then utilize the diabatic transform to obtain the multi-channel diabatic absorption potential.

Bibliography

[1] NIST, in *NIST Reference on Constants, Units, and Uncertainty* (National Institute of Standards and Technology, 2024).

[2] P. D. Lett, R. N. Watts, C. I. Westbrook, W. D. Phillips, P. L. Gould, and H. J. Metcalf, *Observation of Atoms Laser Cooled below the Doppler Limit*, Phys. Rev. Lett. **61**, 169 (1988).

[3] J. Dalibard and C. Cohen-Tannoudji, *Laser cooling below the Doppler limit by polarization gradients: simple theoretical models*, J. Opt. Soc. Am. B **6**, 2023 (1989).

[4] W. D. Phillips, *Nobel Lecture: Laser cooling and trapping of neutral atoms*, Rev. Mod. Phys. **70**, 721 (1998).

[5] C. N. Cohen-Tannoudji, *Nobel Lecture: Manipulating atoms with photons*, Rev. Mod. Phys. **70**, 707 (1998).

[6] H. J. Metcalf and P. van der Straten, *Laser Cooling and Trapping* (Springer-Verlag, New York, 1999).

[7] D. Jaksch, J. I. Cirac, P. Zoller, S. L. Rolston, R. Côté, and M. D. Lukin, *Fast Quantum Gates for Neutral Atoms*, Phys. Rev. Lett. **85**, 2208 (2000).

[8] C. H. Greene, A. S. Dickinson, and H. R. Sadeghpour, *Creation of Polar and Nonpolar Ultra-Long-Range Rydberg Molecules*, Phys. Rev. Lett. **85**, 2458 (2000).

[9] L. Santos, G. V. Shlyapnikov, P. Zoller, and M. Lewenstein, *Bose-Einstein Condensation in Trapped Dipolar Gases*, Phys. Rev. Lett. **85**, 1791 (2000).

[10] C. Ates, T. Pohl, T. Pattard, and J. M. Rost, *Antiblockade in Rydberg Excitation of an Ultracold Lattice Gas*, Phys. Rev. Lett. **98**, 023002 (2007).

[11] I. I. Ryabtsev, D. B. Tretyakov, I. I. Beterov, and V. M. Entin, *Observation of the Stark-Tuned Förster Resonance between Two Rydberg Atoms*, Phys. Rev. Lett. **104**, 073003 (2010).

[12] Y. Chew, T. Tomita, T. P. Mahesh, S. Sugawa, S. de Léséleuc, and K. Ohmori, *Ultrafast energy exchange between two single Rydberg atoms on a nanosecond timescale*, Nat. Photon. **16**, 724 (2022).

[13] C. S. E. van Ditzhuijzen, A. F. Koenderink, J. V. Hernández, F. Robicheaux, L. D. Noordam, and H. B. v. L. van den Heuvell, *Spatially Resolved Observation of Dipole-Dipole Interaction between Rydberg Atoms*, Phys. Rev. Lett. **100**, 243201 (2008).

[14] G. Giudici, S. Veroni, G. Giudice, H. Pichler, and J. Zeiher, *Fast Entangling Gates for Rydberg Atoms via Resonant Dipole-Dipole Interaction*, PRX Quantum **6**, 030308 (2025).

[15] S. Zhang, F. Robicheaux, and M. Saffman, *Magic-wavelength optical traps for Rydberg atoms*, Phys. Rev. A **84**, 043408 (2011).

[16] M. Saffman, T. G. Walker, and K. Mølmer, *Quantum information with Rydberg atoms*, Rev. Mod. Phys. **82**, 2313 (2010).

[17] M. Saffman, *Quantum computing with atomic qubits and Rydberg interactions: progress and challenges*, J. Phys. B: At. Mol. Opt. Phys. **49**, 202001 (2016).

[18] S. de Léséleuc, V. Lienhard, P. Scholl, D. Barredo, S. Weber, N. Lang, H. P. Büchler, T. Lahaye, and A. Browaeys, *Observation of a symmetry-protected topological phase of interacting bosons with Rydberg atoms*, Science **365**, 775 (2019).

[19] R. Samajdar, W. W. Ho, H. Pichler, M. D. Lukin, and S. Sachdev, *Quantum phases of Rydberg atoms on a kagome lattice*, Proc. Natl. Acad. Sci. U. S. A. **118**, e2015785118 (2021).

[20] R. Verresen, M. D. Lukin, and A. Vishwanath, *Prediction of Toric Code Topological Order from Rydberg Blockade*, Phys. Rev. X **11**, 031005 (2021).

[21] O. Firstenberg, T. Peyronel, Q.-Y. Liang, A. V. Gorshkov, M. D. Lukin, and V. Vuletić, *Attractive photons in a quantum nonlinear medium*, Nature **502**, 71 (2013).

[22] O. Firstenberg, C. S. Adams, and S. Hofferberth, *Nonlinear quantum optics mediated by Rydberg interactions*, J. Phys. B: At. Mol. Opt. Phys. **49**, 152003 (2016).

[23] R. Heidemann, U. Krohn, V. Bendkowsky, B. Butscher, R. Löw, L. Santos, and T. Pfau, *Evidence for Coherent Collective Rydberg Excitation in the Strong Blockade Regime*, Phys. Rev. Lett. **99**, 163601 (2007).

[24] A. Paris-Mandoki, C. Braun, J. Kumlin, C. Tresp, I. Mirgorodskiy, F. Christaller, H. P. Büchler, and S. Hofferberth, *Free-Space Quantum Electrodynamics with a Single Rydberg Superatom*, Phys. Rev. X **7**, 041010 (2017).

[25] D. Petrosyan and K. Mølmer, *Deterministic Free-Space Source of Single Photons Using Rydberg Atoms*, Phys. Rev. Lett. **121**, 123605 (2018).

[26] T. Peyronel, O. Firstenberg, Q.-Y. Liang, S. Hofferberth, A. V. Gorshkov, T. Pohl, M. D. Lukin, and V. Vuletić, *Quantum nonlinear optics with single photons enabled by strongly interacting atoms*, Nature **488**, 57 (2012).

[27] S. Baur, D. Tiarks, G. Rempe, and S. Dürr, *Single-Photon Switch Based on Rydberg Blockade*, Phys. Rev. Lett. **112**, 073901 (2014).

[28] L. Zhang, F. Yang, K. Mølmer, and T. Pohl, *Chiral Quantum-Optical Elements for Waveguide-QED with Sub-wavelength Rydberg-Atom Arrays*, 2024.

[29] O. A. Iversen and T. Pohl, *Self-ordering of individual photons in waveguide QED and Rydberg-atom arrays*, Phys. Rev. Res. **4**, 023002 (2022).

[30] C. Boisseau, I. Simbotin, and R. Côté, *Macrodimers: Ultralong Range Rydberg Molecules*, Phys. Rev. Lett. **88**, 133004 (2002).

[31] K. R. Overstreet, A. Schwettmann, J. Tallant, D. Booth, and J. P. Shaffer, *Observation of electric-field-induced Cs Rydberg atom macrodimers*, Nat. Phys. **5**, 581 (2009).

[32] S. Hollerith, J. Zeiher, J. Rui, A. Rubio-Abadal, V. Walther, T. Pohl, D. M. Stamper-Kurn, I. Bloch, and C. Gross, *Quantum gas microscopy of Rydberg macrodimers*, Science **364**, 664 (2019).

[33] S. Hollerith, J. Rui, A. Rubio-Abadal, K. Srakaew, D. Wei, J. Zeiher, C. Gross, and I. Bloch, *Microscopic electronic structure tomography of Rydberg macrodimers*, Phys. Rev. Res. **3**, 013252 (2021).

[34] S. T. Rittenhouse and H. R. Sadeghpour, *Ultracold Giant Polyatomic Rydberg Molecules: Coherent Control of Molecular Orientation*, Phys. Rev. Lett. **104**, 243002 (2010).

[35] M. Deiß, S. Haze, and J. Hecker Denschlag, *Long-Range Atom–Ion Rydberg Molecule: A Novel Molecular Binding Mechanism*, Atoms **9** (2021).

[36] Y. Q. Zou, M. Berngruber, V. S. V. Anasuri, N. Zuber, F. Meinert, R. Löw, and T. Pfau, *Observation of Vibrational Dynamics of Orientated Rydberg-Atom-Ion Molecules*, Phys. Rev. Lett. **130**, 023002 (2023).

[37] N. Zuber, V. S. V. Anasuri, M. Berngruber, Y. Q. Zou, F. Meinert, R. Löw, and T. Pfau, *Observation of a molecular bond between ions and Rydberg atoms*, Nature **605**, 453 (2022).

[38] R. Schmidt, H. R. Sadeghpour, and E. Demler, *Mesoscopic Rydberg Impurity in an Atomic Quantum Gas*, Phys. Rev. Lett. **116**, 105302 (2016).

[39] F. Camargo et al., *Creation of Rydberg Polarons in a Bose Gas*, Phys. Rev. Lett. **120**, 083401 (2018).

[40] A. A. T. Durst and M. T. Eiles, *Phenomenology of a Rydberg impurity in an ideal Bose-Einstein condensate*, Phys. Rev. Res. **6**, L042009 (2024).

[41] M. Gievers, M. Wagner, and R. Schmidt, *Probing polaron clouds by Rydberg atom spectroscopy*, Physical Review Letters **132**, 053401 (2024).

[42] J. Sous, H. R. Sadeghpour, T. C. Killian, E. Demler, and R. Schmidt, *Rydberg impurity in a Fermi gas: Quantum statistics and rotational blockade*, Phys. Rev. Res. **2**, 023021 (2020).

[43] E. L. Hamilton, C. H. Greene, and H. R. Sadeghpour, *Shape-resonance-induced long-range molecular Rydberg states*, J. Phys. B: At. Mol. Opt. Phys. **35**, L199 (2002).

[44] R. Fortey, *Trilobite!: Eyewitness to Evolution* (HarperCollins, London, 2000).

[45] J. Wudarczyk, G. Papamokos, V. Margaritis, D. Schollmeyer, F. Hinkel, M. Baumgarten, G. Floudas, and K. Müllen, *Hexasubstituted Benzenes with Ultrastrong Dipole Moments*, Angewandte Chemie International Edition **55**, 3220 (2016).

[46] H. R. Sadeghpour and S. T. Rittenhouse, *How do ultralong-range homonuclear Rydberg molecules get their permanent dipole moments?*, Molecular Physics **111**, 1902 (2013).

[47] D. Booth, S. T. Rittenhouse, J. Yang, H. R. Sadeghpour, and J. P. Shaffer, *Production of trilobite Rydberg molecule dimers with kilo-Debye permanent electric dipole moments*, Science **348**, 99 (2015).

[48] M. T. Eiles, *Formation of long-range Rydberg molecules in two-component ultracold gases*, Phys. Rev. A **98**, 042706 (2018).

[49] M. Peper and J. Deiglmayr, *Heteronuclear Long-Range Rydberg Molecules*, Phys. Rev. Lett. **126**, 013001 (2021).

[50] J. D. Whalen, S. K. Kanungo, Y. Lu, S. Yoshida, J. Burgdörfer, F. B. Dunning, and T. C. Killian, *Heteronuclear Rydberg molecules*, Phys. Rev. A **101**, 060701 (2020).

[51] D. A. Anderson, S. A. Miller, and G. Raithel, *Angular-momentum couplings in long-range* Rb_2 *Rydberg molecules*, Phys. Rev. A **90**, 062518 (2014).

[52] H. Saßmannshausen, F. Merkt, and J. Deiglmayr, *Experimental Characterization of Singlet Scattering Channels in Long-Range Rydberg Molecules*, Phys. Rev. Lett. **114**, 133201 (2015).

[53] K. S. Kleinbach, F. Meinert, F. Engel, W. J. Kwon, R. Löw, T. Pfau, and G. Raithel, *Photoassociation of Trilobite Rydberg Molecules via Resonant Spin-Orbit Coupling*, Phys. Rev. Lett. **118**, 223001 (2017).

[54] S. Markson, S. T. Rittenhouse, R. Schmidt, J. P. Shaffer, and H. R. Sadeghpour, *Theory of ultralong-range Rydberg molecule formation incorporating spin-dependent relativistic effects: Cs(6s)-Cs(np) as case study*, Chemphyschem **17**, 3683 (2016).

[55] M. T. Eiles and C. H. Greene, *Hamiltonian for the inclusion of spin effects in long-range Rydberg molecules*, Phys. Rev. A **95**, 042515 (2017).

[56] M. Deiß, S. Haze, J. Wolf, L. Wang, F. Meinert, C. Fey, F. Hummel, P. Schmelcher, and J. Hecker Denschlag, *Observation of spin-orbit-dependent electron scattering using long-range Rydberg molecules*, Phys. Rev. Res. **2**, 013047 (2020).

[57] M. Kurz and P. Schmelcher, *Electrically dressed ultra-long-range polar Rydberg molecules*, Phys. Rev. A **88**, 022501 (2013).

[58] M. Kurz and P. Schmelcher, *Ultralong-range Rydberg molecules in combined electric and magnetic fields*, J. Phys. B: At. Mol. Opt. Phys. **47**, 165101 (2014).

[59] I. Lesanovsky, P. Schmelcher, and H. R. Sadeghpour, *Ultra-long-range Rydberg molecules exposed to a magnetic field*, J. Phys. B: At. Mol. Opt. Phys. **39**, L69 (2006).

[60] A. T. Krupp, A. Gaj, J. B. Balewski, P. Ilzhöfer, S. Hofferberth, R. Löw, T. Pfau, M. Kurz, and P. Schmelcher, *Alignment of D-State Rydberg Molecules*, Phys. Rev. Lett. **112**, 143008 (2014).

[61] F. Hummel, C. Fey, and P. Schmelcher, *Alignment of s-state Rydberg molecules in magnetic fields*, Phys. Rev. A **99**, 023401 (2019).

[62] M. Kurz, M. Mayle, and P. Schmelcher, *Ultra-long-range giant dipole molecules in crossed electric and magnetic fields*, Europhys. Lett. **97**, 43001 (2012).

[63] V. Bendkowsky, B. Butscher, J. Nipper, J. P. Shaffer, R. Löw, and T. Pfau, *Observation of ultralong-range Rydberg molecules*, Nature **458**, 1005 (2009).

[64] V. Bendkowsky et al., *Rydberg Trimers and Excited Dimers Bound by Internal Quantum Reflection*, Phys. Rev. Lett. **105**, 163201 (2010).

[65] B. Butscher, V. Bendkowsky, J. Nipper, J. B. Balewski, L. Kukota, R. Löw, T. Pfau, W. Li, T. Pohl, and J. M. Rost, *Lifetimes of ultralong-range Rydberg molecules in vibrational ground and excited states*, J. Phys. B: At. Mol. Opt. Phys. **44**, 184004 (2011).

[66] T. Niederprüm, O. Thomas, T. Eichert, C. Lippe, J. Pérez-Ríos, C. H. Greene, and H. Ott, *Observation of pendular butterfly Rydberg molecules*, Nat. Commun. **7**, 12820 (2016).

[67] M. Althön, M. Exner, R. Blättner, and H. Ott, *Exploring the vibrational series of pure trilobite Rydberg molecules*, Nat. Commun. **14**, 8108 (2023).

[68] J. Tallant, S. T. Rittenhouse, D. Booth, H. R. Sadeghpour, and J. P. Shaffer, *Observation of Blueshifted Ultralong-Range Cs_2 Rydberg Molecules*, Phys. Rev. Lett. **109**, 173202 (2012).

[69] C. Fey, J. Yang, S. T. Rittenhouse, F. Munkes, M. Baluktsian, P. Schmelcher, H. R. Sadeghpour, and J. P. Shaffer, *Effective Three-Body Interactions in $\mathrm{Cs}(6s)-\mathrm{Cs}(nd)$ Rydberg Trimers*, Phys. Rev. Lett. **122**, 103001 (2019).

[70] B. J. DeSalvo, J. A. Aman, F. B. Dunning, T. C. Killian, H. R. Sadeghpour, S. Yoshida, and J. Burgdörfer, *Ultra-long-range Rydberg molecules in a divalent atomic system*, Phys. Rev. A **92**, 031403 (2015).

[71] F. Camargo, J. D. Whalen, R. Ding, H. R. Sadeghpour, S. Yoshida, J. Burgdörfer, F. B. Dunning, and T. C. Killian, *Lifetimes of ultra-long-range strontium Rydberg molecules*, Phys. Rev. A **93**, 022702 (2016).

[72] R. Ding, S. K. Kanungo, J. D. Whalen, T. C. Killian, F. B. Dunning, S. Yoshida, and J. Burgdörfer, *Creation of vibrationally-excited ultralong-range Rydberg molecules in polarized and unpolarized cold gases of 87Sr*, J. Phys. B: At. Mol. Opt. Phys **53**, 014002 (2019).

[73] T. Legrand, X. Wang, M. Simić, F. Pausewang, W. Alt, E. Uruñuela, M. T. Eiles, and S. Hofferberth, *Revealing Electron-Ytterbium Interactions through Rydberg Molecular Spectroscopy*, arXiv.2512.20609 (2025).

[74] A. Wojciechowska, M. Tomza, and M. T. Eiles, *Ultralong-range Rydberg molecules of Hg atoms*, Phys. Rev. A **111**, 042816 (2025).

[75] J. P. Shaffer, S. T. Rittenhouse, and H. R. Sadeghpour, *Ultracold Rydberg molecules*, Nat. Commun. **9**, 1965 (2018).

[76] C. Fey, F. Hummel, and P. Schmelcher, *Ultralong-range Rydberg molecules*, Mol. Phys. **118**, e1679401 (2020).

[77] F. B. Dunning, S. K. Kanungo, and S. Yoshida, *Ultralong-range Rydberg molecules*, J. Phys. B: At. Mol. Opt. Phys. **57**, 212002 (2024).

[78] M. T. Eiles, *Trilobites, butterflies, and other exotic specimens of long-range Rydberg molecules*, J. Phys. B: At. Mol. Opt. Phys. **52**, 113001 (2019).

[79] M. Born and R. Oppenheimer, *Zur Quantentheorie der Molekeln*, Ann. Phys. (Leipzig) **389**, 457 (1927).

[80] M. Schlagmüller et al., *Ultracold Chemical Reactions of a Single Rydberg Atom in a Dense Gas*, Phys. Rev. X **6**, 031020 (2016).

[81] H. Köppel, W. Domcke, and L. S. Cederbaum, *Multimode Molecular Dynamics Beyond the Born-Oppenheimer Approximation* (John Wiley & Sons, Ltd, 1984), pp. 59–246.

[82] F. Agostini and B. F. E. Curchod, *Different flavors of nonadiabatic molecular dynamics*, Wiley Interdiscip. Rev. Comput. Mol. Sci. **9**, e1417 (2019).

[83] M. Baer, *Beyond Born-Oppenheimer: Electronic Non-adiabatic Coupling Terms and Conical Intersections* (John Wiley & Sons, Ltd, 2006).

[84] C. Arnold, O. Vendrell, R. Welsch, and R. Santra, *Control of Nuclear Dynamics through Conical Intersections and Electronic Coherences*, Phys. Rev. Lett. **120**, 123001 (2018).

[85] N. Mabrouk, W. Zrafi, and H. Berriche, *Theoretical study of the LiNa molecule beyond the Born–Oppenheimer approximation: adiabatic and diabatic potential energy curves, radial coupling, adiabatic correction, dipole moments and vibrational levels*, Mol. Phys. **118**, e1605098 (2020).

[86] T. J. Martinez, *Seaming is believing*, Nature **467**, 412 (2010).

[87] H. Köppel, W. Domcke, and L. S. Cederbaum, *Conical Intersections and Ultrafast Radiationless Decay* (Springer Netherlands, Dordrecht, 1987), pp. 217–231.

[88] B. G. Levine and T. J. Martínez, *Isomerization Through Conical Intersections*, Annu. Rev. Phys. Chem. **58**, 613 (2007).

[89] D. Polli et al., *Conical intersection dynamics of the primary photoisomerization event in vision*, Nature **467**, 440 (2010).

[90] L. Hammarström and S. Styring, *Coupled electron transfers in artificial photosynthesis*, Philos. Trans. R. Soc. B **363**, 1283 (2008).

[91] M. Barbatti, A. J. A. Aquino, J. J. Szymczak, D. Nachtigallová, P. Hobza, and H. Lischka, *Relaxation mechanisms of UV-photoexcited DNA and RNA nucleobases*, Proc. Natl. Acad. Sci. U.S.A. **107**, 21453 (2010).

[92] H. Kang, K. T. Lee, B. Jung, Y. J. Ko, and S. K. Kim, *Intrinsic Lifetimes of the Excited State of DNA and RNA Bases*, J. Am. Chem. Soc. **124**, 12958 (2002).

[93] H. A. Jahn, E. Teller, and F. G. Donnan, *Stability of polyatomic molecules in degenerate electronic states - I—Orbital degeneracy*, Proc. R. Soc. A **161**, 220 (1937).

[94] H. C. Longuet-Higgins, U. Öpik, M. H. L. Pryce, and R. A. Sack, *Studies of the Jahn-Teller effect .II. The dynamical problem*, Proc. R. Soc. A **244**, 1 (1958).

[95] F. Hummel, M. T. Eiles, and P. Schmelcher, *Synthetic Dimension-Induced Conical Intersections in Rydberg Molecules*, Phys. Rev. Lett. **127**, 023003 (2021).

[96] F. M. Gambetta, C. Zhang, M. Hennrich, I. Lesanovsky, and W. Li, *Exploring the Many-Body Dynamics Near a Conical Intersection with Trapped Rydberg Ions*, Phys. Rev. Lett. **126**, 233404 (2021).

[97] J. W. P. Wilkinson, W. Li, and I. Lesanovsky, *Spectral Signatures of Vibronic Coupling in Trapped Cold Ionic Rydberg Systems*, Phys. Rev. Lett. **132**, 223401 (2024).

[98] A. Duspayev and G. Raithel, *Nonadiabatic decay of Rydberg-atom–ion molecules*, Phys. Rev. A **105**, 012810 (2022).

[99] D. Mellado-Alcedo, A. Guttridge, S. L. Cornish, H. R. Sadeghpour, and R. González-Férez, *Ultralong-range Cs-RbCs Rydberg molecules: Nonadiabaticity of dipole moments*, Phys. Rev. A **110**, 013314 (2024).

[100] A. A. T. Durst, M. Simi ć, N. Abraham, and M. T. Eiles, *Nonadiabatic couplings as a stabilization mechanism in long-range Rydberg molecules*, Phys. Rev. A **111**, 032811 (2025).

[101] F. Hummel, P. Schmelcher, and M. T. Eiles, *Vibronic interactions in trilobite and butterfly Rydberg molecules*, Phys. Rev. Res. **5**, 013114 (2023).

[102] U. Manthe and H. Köppel, *New method for calculating wave packet dynamics: Strongly coupled surfaces and the adiabatic basis*, J. Chem. Phys. **93**, 345 (1990).

[103] W. Domcke, D. R. Yarkony, and H. Köppel, *Conical Intersections* (WORLD SCIENTIFIC, 2004).

[104] T. Pacher, L. S. Cederbaum, and H. Köppel, *Approximately diabatic states from block diagonalization of the electronic Hamiltonian*, J. Chem. Phys. **89**, 7367 (1988).

[105] F. Hummel, K. Keiler, and P. Schmelcher, *Electric-field-induced wave-packet dynamics and geometrical rearrangement of trilobite Rydberg molecules*, Phys. Rev. A **103**, 022827 (2021).

[106] C. Fey, M. Kurz, and P. Schmelcher, *Stretching and bending dynamics in triatomic ultralong-range Rydberg molecules*, Phys. Rev. A **94**, 012516 (2016).

[107] C. H. Greene and M. T. Eiles, *Green's-function treatment of Rydberg molecules with spins*, Phys. Rev. A **108**, 042805 (2023).

[108] C. Fey, M. Kurz, P. Schmelcher, S. T. Rittenhouse, and H. R. Sadeghpour, *A comparative analysis of binding in ultralong-range Rydberg molecules*, New J. Phys. **17**, 055010 (2015).

[109] F. Hummel, P. Schmelcher, H. Ott, and H. R. Sadeghpour, *An ultracold heavy Rydberg system formed from ultra-long-range molecules bound in a stairwell potential*, New J. Phys. **22**, 063060 (2020).

[110] C. W. Walter, N. D. Gibson, D. J. Matyas, C. Crocker, K. A. Dungan, B. R. Matola, and J. Rohlén, *Candidate for Laser Cooling of a Negative Ion: Observations of Bound-Bound Transitions in* La^-, Phys. Rev. Lett. **113**, 063001 (2014).

[111] R. Tang, R. Si, Z. Fei, X. Fu, Y. Lu, T. Brage, H. Liu, C. Chen, and C. Ning, *Candidate for Laser Cooling of a Negative Ion: High-Resolution Photoelectron Imaging of* Th^-, Phys. Rev. Lett. **123**, 203002 (2019).

[112] T. Pohl, D. Vrinceanu, and H. R. Sadeghpour, *Rydberg Atom Formation in Ultracold Plasmas: Small Energy Transfer with Large Consequences*, Phys. Rev. Lett. **100**, 223201 (2008).

[113] T. F. Gallagher, *Rydberg Atoms*, Cambridge Monographs on Atomic, Molecular and Chemical Physics (Cambridge University Press, 1994).

[114] A. Browaeys and T. Lahaye, *Many-body physics with individually controlled Rydberg atoms*, Nat. Phy. **16**, 132 (2020).

[115] D. Bluvstein et al., *A quantum processor based on coherent transport of entangled atom arrays*, Nature **604**, 451 (2022).

[116] T. M. Graham et al., *Multi-qubit entanglement and algorithms on a neutral-atom quantum computer*, Nature **604**, 457 (2022).

[117] J. A. Sedlacek, A. Schwettmann, H. Kübler, R. Löw, T. Pfau, and J. P. Shaffer, *Microwave electrometry with Rydberg atoms in a vapour cell using bright atomic resonances*, Nat. Phys. **8**, 819 (2012).

[118] H. Fan, S. Kumar, J. Sedlacek, H. Kübler, S. Karimkashi, and J. P. Shaffer, *Atom based RF electric field sensing*, J. Phys. B: At. Mol. Opt. Phys. **48**, 202001 (2015).

[119] J. A. Gordon, C. L. Holloway, A. Schwarzkopf, D. A. Anderson, S. Miller, N. Thaicharoen, and G. Raithel, *Millimeter wave detection via Autler-Townes splitting in rubidium Rydberg atoms*, Appl. Phys. Lett. **105**, 024104 (2014).

[120] J. R. Rydberg, *Recherches sur la constitution des spectres d'émission des éléments chimiques*, Vol. 23, Kungliga Vetenskapsakademiens Handlingar 11 (Kungliga Vetenskapsakademien, 1890).

[121] F. B. Dunning, J. J. Mestayer, C. O. Reinhold, S. Yoshida, and J. Burgdörfer, *Engineering atomic Rydberg states with pulsed electric fields*, J. Phys. B: At. Mol. Opt. Phys **42**, 022001 (2009).

[122] E. Fermi, *Sopra lo Spostamento per Pressione delle Righe Elevate delle Serie Spettrali*, Nuovo Cim. **11**, 157 (1934).

[123] E. Amaldi and E. Segrè, *Effetto della Pressione Sui Termini Elevati Degli Alcalini*, Nuovo Cimento **11**, 145 (1934).

[124] Omont, A., *On the theory of collisions of atoms in Rydberg states with neutral particles*, J. Phys. France **38**, 1343 (1977).

[125] M. Hugon, F. Gounand, P. R. Fournier, and J. Berlande, *Collisional properties of highly excited rubidium atoms*, J. Phys. B: At. Mol. Opt. Phys **12**, 2707 (1979).

[126] K. A. Safinya, J. F. Delpech, F. Gounand, W. Sandner, and T. F. Gallagher, *Resonant Rydberg-Atom-Rydberg-Atom Collisions*, Phys. Rev. Lett. **47**, 405 (1981).

[127] S. Haroche, *Measuring Photons Non-Destructively*, Europhys. news **24**, 51 (1993).

[128] J. M. Raimond, M. Brune, and S. Haroche, *Manipulating quantum entanglement with atoms and photons in a cavity*, Rev. Mod. Phys. **73**, 565 (2001).

[129] S. Haroche, *Nobel Lecture: Controlling photons in a box and exploring the quantum to classical boundary*, Rev. Mod. Phys. **85**, 1083 (2013).

[130] M.-J. Giannoni, A. Voros, and J. Zinn-Justin, *Chaos and quantum physics* (North-Holland, 1991).

[131] H. Friedrich and H. Wintgen, *The hydrogen atom in a uniform magnetic field — An example of chaos*, Phys. Rep. **183**, 37 (1989).

[132] M. Lakshmanan and K. Ganesan, *Rydberg atoms and molecules – Testing grounds for quantum manifestations of chaos*, Curr. Sci. **68** (1995).

[133] T. S. Monteiro and G. Wunner, *Analysis of quantum manifestations of chaos in general Rydberg atoms in strong magnetic fields*, Phys. Rev. Lett. **65**, 1100 (1990).

[134] S. Ma, A. P. Burgers, G. Liu, J. Wilson, B. Zhang, and J. D. Thompson, *Universal Gate Operations on Nuclear Spin Qubits in an Optical Tweezer Array of* $^{171}\mathrm{Yb}$ *Atoms*, Phys. Rev. X **12**, 021028 (2022).

[135] A. Jenkins, J. W. Lis, A. Senoo, W. F. McGrew, and A. M. Kaufman, *Ytterbium Nuclear-Spin Qubits in an Optical Tweezer Array*, Phys. Rev. X **12**, 021027 (2022).

[136] J. T. Wilson, S. Saskin, Y. Meng, S. Ma, R. Dilip, A. P. Burgers, and J. D. Thompson, *Trapping Alkaline Earth Rydberg Atoms Optical Tweezer Arrays*, Phys. Rev. Lett. **128**, 033201 (2022).

[137] M. A. Norcia et al., *Iterative Assembly of ^{171}Yb Atom Arrays with Cavity-Enhanced Optical Lattices*, PRX Quantum **5**, 030316 (2024).

[138] M. Peper et al., *Spectroscopy and Modeling of ^{171}Yb Rydberg States for High-Fidelity Two-Qubit Gates*, Phys. Rev. X **15**, 011009 (2025).

[139] M. A. Norcia, A. W. Young, and A. M. Kaufman, *Microscopic Control and Detection of Ultracold Strontium in Optical-Tweezer Arrays*, Phys. Rev. X **8**, 041054 (2018).

[140] A. J. Daley, *Quantum computing and quantum simulation with group-II atoms*, Quantum Information Processing **10**, 865 (2011).

[141] M. Aymar, C. H. Greene, and E. Luc-Koenig, *Multichannel Rydberg spectroscopy of complex atoms*, Rev. Mod. Phys. **68**, 1015 (1996).

[142] H. Friedrich, *Theoretical Atomic Physics*, 3rd (Springer-Verlag Berlin Heidelberg, Berlin, Heidelberg, 2006).

[143] U. Fano, *Atomic Collisions and Spectra* (Academic Press, 2012).

[144] M. Marinescu, H. R. Sadeghpour, and A. Dalgarno, *Dispersion coefficients for alkali-metal dimers*, Phys. Rev. A **49**, 982 (1994).

[145] B. H. Bransden and C. J. Joachain, *Physics of atoms and molecules*, 2003.

[146] E. Hairer, S. P. Nørsett, and G. Wanner, *Solving Ordinary Differential Equations I: Nonstiff Problems*, 2nd (Springer-Verlag, Berlin, Heidelberg, 1993).

[147] B. Numerov, *Note on the numerical integration of d2x/dt2 = f(x, t)*, Astron. Nachr. **230**, 359 (1927).

[148] M. Kurz, *Ultralong-range Diatomic Molecules in External Electric and Magnetic Fields*, PhD thesis (Universität Hamburg, 2014).

[149] M. J. Seaton, *Quantum defect theory*, Rep. Prog. Phys. **46**, 167 (1983).

[150] E. Whittaker and G. Watson, *A Course of Modern Analysis* (Cambridge University Press, 1996).

[151] A. B. O. Daalhuis, in *NIST Handbook of Mathematical Functions*, edited by F. W. J. Olver, D. M. Lozier, R. F. Boisvert, and C. W. Clark (Cambridge University Press, New York, NY, 2010) Chap. 13.

[152] M. Abramowitz and I. A. Stegun, *Handbook of Mathematical Functions with Formulas, Graphs, and Mathematical Tables* (Dover, New York, 1965).

[153] J. J. Sakurai and J. Napolitano, *Modern Quantum Mechanics*, 3rd ed. (Cambridge University Press, 2020).

[154] D. J. Griffiths and D. F. Schroeter, *Introduction to quantum mechanics*, Third edition (Cambridge University Press, Cambridge ; New York, NY, 2018).

[155] P. Goy, J. Liang, M. Gross, and S. Haroche, *Quantum defects and specific-isotopic-shift measurements in ns and np highly excited states of lithium: Exchange effects between Rydberg and core electrons*, Phys. Rev. A **34**, 2889 (1986).

[156] C.-J. Lorenzen and K. Niemax, *Quantum Defects of the n2P1/2,3/2 Levels in 39K I and 85Rb I*, Physica Scripta **27**, 300 (1983).

[157] W. Li, I. Mourachko, M. W. Noel, and T. F. Gallagher, *Millimeter-wave spectroscopy of cold Rb Rydberg atoms in a magneto-optical trap: Quantum defects of the ns, np, and nd series*, Phys. Rev. A **67**, 052502 (2003).

[158] J. Han, Y. Jamil, D. V. L. Norum, P. J. Tanner, and T. F. Gallagher, *Rb nf quantum defects from millimeter-wave spectroscopy of cold ^{85}Rb Rydberg atoms*, Phys. Rev. A **74**, 054502 (2006).

[159] N. Šibalić, J. Pritchard, C. Adams, and K. Weatherill, *ARC: An open-source library for calculating properties of alkali Rydberg atoms*, Computer Physics Communications **220**, 319 (2017).

[160] E. Robertson, N. Šibalić, R. Potvliege, and M. Jones, *ARC 3.0: An expanded Python toolbox for atomic physics calculations*, Computer Physics Communications **261**, 107814 (2021).

[161] R. Cardman and G. Raithel, *Hyperfine structure of $nP_{1/2}$ Rydberg states in ^{85}Rb*, Phys. Rev. A **106**, 052810 (2022).

[162] T. A. Johnson, E. Urban, T. Henage, L. Isenhower, D. D. Yavuz, T. G. Walker, and M. Saffman, *Rabi Oscillations between Ground and Rydberg States with Dipole-Dipole Atomic Interactions*, Phys. Rev. Lett. **100**, 113003 (2008).

[163] Y. Miroshnychenko, A. Gaëtan, C. Evellin, P. Grangier, D. Comparat, P. Pillet, T. Wilk, and A. Browaeys, *Coherent excitation of a single atom to a Rydberg state*, Phys. Rev. A **82**, 013405 (2010).

[164] D. P. Fahey and M. W. Noel, *Excitation of Rydberg states in rubidium with near infrared diode lasers*, Opt. Express **19**, 17002 (2011).

[165] C. E. Theodosiou, *Lifetimes of alkali-metal—atom Rydberg states*, Phys. Rev. A **30**, 2881 (1984).

[166] F. Gounand, *Calculation of radial matrix elements and radiative lifetimes for highly excited states of alkali atoms using the Coulomb approximation*, J. Phys. France **40**, 10.1051/jphys:01979004005045700 (1979).

[167] D. B. Branden, T. Juhasz, T. Mahlokozera, C. Vesa, R. O. Wilson, M. Zheng, A. Kortyna, and D. A. Tate, *Radiative lifetime measurements of rubidium Rydberg states*, **43**, 015002 (2009).

[168] D. Kleppner, *Inhibited Spontaneous Emission*, Phys. Rev. Lett. **47**, 233 (1981).

[169] H. Wu, R. Richaud, J.-M. Raimond, M. Brune, and S. Gleyzes, *Millisecond-Lived Circular Rydberg Atoms in a Room-Temperature Experiment*, Phys. Rev. Lett. **130**, 023202 (2023).

[170] C. Hölzl, A. Götzelmann, E. Pultinevicius, M. Wirth, and F. Meinert, *Long-Lived Circular Rydberg Qubits of Alkaline-Earth Atoms in Optical Tweezers*, Phys. Rev. X **14**, 021024 (2024).

[171] T. L. Nguyen et al., *Towards Quantum Simulation with Circular Rydberg Atoms*, Phys. Rev. X **8**, 011032 (2018).

[172] S. R. Cohen and J. D. Thompson, *Quantum Computing with Circular Rydberg Atoms*, PRX Quantum **2**, 030322 (2021).

[173] I. I. Beterov, I. I. Ryabtsev, D. B. Tretyakov, and V. M. Entin, *Quasiclassical calculations of blackbody-radiation-induced depopulation rates and effective lifetimes of Rydberg nS, nP, and nD alkali-metal atoms with $n \leq 80$*, Phys. Rev. A **79**, 052504 (2009).

[174] J. W. Farley and W. H. Wing, *Accurate calculation of dynamic Stark shifts and depopulation rates of Rydberg energy levels induced by blackbody radiation. Hydrogen, helium, and alkali-metal atoms*, Phys. Rev. A **23**, 2397 (1981).

[175] G. Fields, F. B. Dunning, S. Yoshida, and J. Burgdörfer, *Destruction of high-n ($n \sim 300$) Rydberg atoms in Rydberg-Rydberg collisions*, Phys. Rev. A **99**, 022710 (2019).

[176] P. Geppert, M. Althön, D. Fichtner, and H. Ott, *Diffusive-like redistribution in state-changing collisions between Rydberg atoms and ground state atoms*, Nat. Commun. **12**, 3900 (2021).

[177] (John Wiley & Sons, Ltd, 2005).

[178] M. Born and K. Huang (Oxford University Press, 1954).

[179] M. F. Herman, *Nonadiabatic semiclassical scattering. I. Analysis of generalized surface hopping procedures*, J. Chem. Phys. **81**, 754 (1984).

[180] M. Barbatti, *Nonadiabatic dynamics with trajectory surface hopping method*, Wiley Interdiscip. Rev. Comput. Mol. Sci. **1**, 620 (2011).

[181] J. von Neumann and E. P. Wigner, *Über merkwürdige diskrete Eigenwerte* (Springer Berlin Heidelberg, Berlin, Heidelberg, 1993), pp. 291–293.

[182] E. C. Alguire, Q. Ou, and J. E. Subotnik, *Calculating Derivative Couplings between Time-Dependent Hartree–Fock Excited States with Pseudo-Wavefunctions*, J. Phys. Chem. B **119**, 7140 (2015).

[183] I. Lengsfield Byron H., P. Saxe, and D. R. Yarkony, *On the evaluation of nonadiabatic coupling matrix elements using SA-MCSCF/CI wave functions and analytic gradient methods. I*, J. Chem. Phys. **81**, 4549 (1984).

[184] Z. Top and M. Baer, *Nonadiabatic transitions in chemical reactions: A quantum mechanical study*, Chem. Phys. **10**, 95 (1975).

[185] B. D. Esry and H. R. Sadeghpour, *Split diabatic representation*, Phys. Rev. A **68**, 042706 (2003).

[186] F. Gatti, B. Lasorne, H.-D. Meyer, and A. Nauts, Vol. 98, Lecture Notes in Chemistry (Springer International Publishing, Cham, Switzerland, 2017).

[187] R. Kosloff, *Time-dependent quantum-mechanical methods for molecular dynamics*, J. Phys. Chem. **92**, 2087 (1988).

[188] R. Kosloff, *Propagation Methods for Quantum Molecular Dynamics*, Annu. Rev. Phys. Chem. **45**, 145 (1994).

[189] A. Fioretti, D. Comparat, A. Crubellier, O. Dulieu, F. Masnou-Seeuws, and P. Pillet, *Formation of Cold Cs_2 Molecules through Photoassociation*, Phys. Rev. Lett. **80** (1998).

[190] C. M. Dion, C. Drag, O. Dulieu, B. Laburthe Tolra, F. Masnou-Seeuws, and P. Pillet, *Resonant Coupling in the Formation of Ultracold Ground State Molecules via Photoassociation*, Phys. Rev. Lett. **86** (2001).

[191] R. Schinke, *Photodissociation Dynamics: Spectroscopy and Fragmentation of Small Polyatomic Molecules*, Cambridge Monographs on Atomic, Molecular and Chemical Physics (Cambridge University Press, 1993).

[192] G. G. Balint-Kurti and M. Shapiro, "Quantum Theory of Molecular Photodissociation", in *Advances in Chemical Physics* (John Wiley & Sons, Ltd, 1985).

[193] G. C. Schatz and A. Kuppermann, *Quantum mechanical reactive scattering for planar atom plus H2 * diatom systems. II. Accurate cross sections for H+H2 **, J. Chem. Phys. **65**, 4624 (1976).

[194] M. Hankel, G. G. Balint-Kurti, and S. K. Gray, *Quantum Mechanical Calculation of Reaction Probabilities and Branching Ratios for the O(1D) + HD → OH(OD) + D(H) Reaction on the XÃ‘ and 11A" Adiabatic Potential Energy Surfaces*, J. Phys. Chem. A **105** (2001).

[195] D. Craig and T. Thirunamachandran, *Molecular Quantum Electrodynamics*, Dover Books on Chemistry (Dover Publications, 2012).

[196] S. E. Koonin, D. C. Meredith, and W. H. Press, *Computational Physics: Fortran Version* (1990).

[197] J. Thomas, *Numerical Partial Differential Equations: Finite Difference Methods*, Texts in Applied Mathematics (Springer New York, 2013).

[198] H.-D. Meyer, *Introduction to MCTDH: Lecture Notes*, LATEX version by Daniel Peláez-Ruiz. Revised: October 2018 (2018).

[199] U. V. Riss and H. D. Meyer, *Calculation of resonance energies and widths using the complex absorbing potential method*, J. Phys. B: At. Mol. Opt. Phys **26**, 4503 (1993).

[200] W. F. Holmgren, M. C. Revelle, V. P. A. Lonij, and A. D. Cronin, *Absolute and ratio measurements of the polarizability of Na, K, and Rb with an atom interferometer*, Phys. Rev. A **81**, 053607 (2010).

[201] A. Miffre, M. Jacquey, M. Büchner, G. Trénec, and J. Vigué, *Atom interferometry measurement of the electric polarizability of lithium*, Eur. Phys. J. D. **38**, 353 (2006).

[202] J. Mitroy, M. S. Safronova, and C. W. Clark, *Theory and applications of atomic and ionic polarizabilities*, J. Phys. B: At. Mol. Opt. Phys. **43**, 202001 (2010).

[203] E. Karule, *Elastic scattering of low-energy electrons by alkali atoms*, Phys. Lett. **15**, 137 (1965).

[204] D. W. Norcross, *Low energy elastic scattering of electrons by Li and Na*, J. Phys. B: At. Mol. Opt. Phys **4**, 1458 (1971).

[205] I. I. Fabrikant, *Interaction of Rydberg atoms and thermal electrons with K, Rb and Cs atoms*, J. Phys. B: At. Mol. Opt. Phys **19**, 1527 (1986).

[206] C. Bahrim, U. Thumm, and I. I. Fabrikant, *3Se and 1Se scattering lengths for e- + Rb, Cs and Fr collisions*, J. Phys. B: At. Mol. Opt. Phys. **34**, L195 (2001).

[207] M. Tarana and R. Čurík, *R-matrix calculations of electron collisions with a lithium atom at low energies*, Phys. Rev. A **99**, 012708 (2019).

[208] A. R. Johnston and P. D. Burrow, *Shape resonances in electron scattering from metal atoms*, J. Phys. B: At. Mol. Opt. Phys. **15**, L745 (1982).

[209] D. L. Moores, *The scattering of electrons by potassium atoms*, J. Phys. B: At. Mol. Opt. Phys. **9**, 1329 (1976).

[210] V. M. Borodin, I. I. Fabrikant, and A. K. Kazansky, *Collisional broadening of Rydberg atoms perturbed by ground-state sodium atoms*, Z. Phys. D – Atoms, Mol. Clusters **27**, 45 (1993).

[211] A. A. Khuskivadze, M. I. Chibisov, and I. I. Fabrikant, *Adiabatic energy levels and electric dipole moments of Rydberg states of Rb_2 and Cs_2 dimers*, Phys. Rev. A **66**, 042709 (2002).

[212] M. Tarana and R. Čurík, *Adiabatic potential-energy curves of long-range Rydberg molecules: Two-electron R-matrix approach*, Phys. Rev. A **93**, 012515 (2016).

[213] C. Laughlin and G. A. Victor, *Model Potential Calculations for Two-Valence Electron Systems*, edited by S. J. Smith and G. K. Walters (1973).

[214] U. Thumm and D. W. Norcross, *Relativistic R-matrix calculations for electron–alkali-metal-atom scattering: Cs as a test case*, Phys. Rev. A **45**, 6349 (1992).

[215] C. Bahrim, U. Thumm, and I. I. Fabrikant, *Negative-ion resonances in cross sections for slow-electron–heavy-alkali-metal-atom scattering*, Phys. Rev. A **63**, 042710 (2001).

[216] F. Engel, T. Dieterle, F. Hummel, C. Fey, P. Schmelcher, R. Löw, T. Pfau, and F. Meinert, *Precision Spectroscopy of Negative-Ion Resonances in Ultralong-Range Rydberg Molecules*, Phys. Rev. Lett. **123**, 073003 (2019).

[217] L. Spruch, T. F. O'Malley, and L. Rosenberg, *Modification of Effective-Range Theory in the Presence of a Long-Range Potential*, Phys. Rev. Lett. **5**, 375 (1960).

[218] T. F. O'Malley, L. Rosenberg, and L. Spruch, *Low-Energy Scattering of a Charged Particle by a Neutral Polarizable System*, Phys. Rev. **125**, 1300 (1962).

[219] E. de Prunelé, *Coulomb and Coulomb-Stark Green-function approach to adiabatic Rydberg energy levels of alkali-metal–helium systems*, Phys. Rev. A **35**, 496 (1987).

[220] P. Valiron, A. L. Roche, F. Masnou-Seeuws, and M. E. Dolan, *Molecular treatment of collisions between a Rydberg sodium atom and a rare-gas perturber*, J. Phys. B: At. Mol. Opt. Phys. **17**, 2803 (1984).

[221] V. M. Borodin and A. K. Kazansky, *The adiabatic mechanism of the collisional broadening of Rydberg states via a loosely bound resonance state of ambient gas atoms*, J. Phys. B: At. Mol. Opt. Phys. **25**, 971 (1992).

[222] B. E. Granger, E. L. Hamilton, and C. H. Greene, *Quantum and semiclassical analysis of long-range Rydberg molecules*, Phys. Rev. A **64**, 042508 (2001).

[223] V. Kanellopoulos, M. Kleber, and T. Kramer, *Use of Lambert's theorem for the n-dimensional Coulomb problem*, Phys. Rev. A **80**, 012101 (2009).

[224] M. I. Chibisov, A. A. Khuskivadze, and I. I. Fabrikant, *Energies and dipole moments of long-range molecular Rydberg states*, J. Phys. B: At. Mol. Opt. Phys. **35**, L193 (2002).

[225] T. Niederprüm, O. Thomas, T. Eichert, and H. Ott, *Rydberg Molecule-Induced Remote Spin Flips*, Phys. Rev. Lett. **117**, 123002 (2016).

[226] E. Arimondo, M. Inguscio, and P. Violino, *Experimental determinations of the hyperfine structure in the alkali atoms*, Rev. Mod. Phys. **49**, 31 (1977).

[227] J. Persson, *Table of hyperfine anomaly in atomic systems*, Atomic Data and Nuclear Data Tables **99**, 62 (2013).

[228] L. Hostler and R. H. Pratt, *Coulomb Green's Function in Closed Form*, Phys. Rev. Lett. **10**, 469 (1963).

[229] V. A. Davydkin, B. A. Zon, N. L. Manakov, and L. P. Rapoport, *Quadratic Stark Effect on Atoms*, J. Exp. Theor. Phys. **33**, 70 (1971).

[230] I. I. Fabrikant, *Theory of negative ion decay in an external electric field*, J. Phys. B: At. Mol. Opt. Phys **26**, 2533 (1993).

[231] M. Exner, *High-l Rydberg molecules: From trilobites to singlet butterflies*, PhD thesis (Rheinland-Pfälzischen Technischen Universität, Kaiserslautern Landau, 2025).

[232] E. L. Raab, M. Prentiss, A. Cable, S. Chu, and D. E. Pritchard, *Trapping of Neutral Sodium Atoms with Radiation Pressure*, Phys. Rev. Lett. **59**, 2631 (1987).

[233] J. Weiner, V. S. Bagnato, S. Zilio, and P. S. Julienne, *Experiments and theory in cold and ultracold collisions*, Rev. Mod. Phys. **71**, 1 (1999).

[234] S. Chu, L. Hollberg, J. E. Bjorkholm, A. Cable, and A. Ashkin, *Three-dimensional viscous confinement and cooling of atoms by resonance radiation pressure*, Phys. Rev. Lett. **55**, 48 (1985).

[235] C. S. Adams, H. J. Lee, N. Davidson, M. Kasevich, and S. Chu, *Evaporative Cooling in a Crossed Dipole Trap*, Phys. Rev. Lett. **74**, 3577 (1995).

[236] R. Grimm, M. Weidemüller, and Y. B. Ovchinnikov, in , Vol. 42, edited by B. Bederson and H. Walther, Advances In Atomic, Molecular, and Optical Physics (Academic Press, 2000), pp. 95–170.

[237] S. H. Autler and C. H. Townes, *Stark Effect in Rapidly Varying Fields*, Phys. Rev. **100**, 703 (1955).

[238] M. T. Eiles and F. Hummel, *Kato's theorem and ultralong-range Rydberg molecules*, Phys. Rev. A **109**, 022811 (2024).

[239] A. Córdoba, *Dirac combs*, Lett. Math. Phys. **17**, 191 (1989).

[240] S. A. Diddams, L.-S. Ma, J. Ye, and J. L. Hall, *Broadband optical frequency comb generation with a phase-modulated parametric oscillator*, Opt. Lett. **24**, 1747 (1999).

[241] J. Deiglmayr, H. Saßmannshausen, and F. Merkt, *Observation of singlet-scattering channels in long-range Rydberg dimers*, J. Phys.: Conf. Ser. **635**, 022075 (2015).

[242] F. Böttcher, A. Gaj, K. M. Westphal, M. Schlagmüller, K. S. Kleinbach, R. Löw, T. C. Liebisch, T. Pfau, and S. Hofferberth, *Observation of mixed singlet-triplet* Rb_2 *Rydberg molecules*, Phys. Rev. A **93**, 032512 (2016).

[243] O. Thomas, C. Lippe, T. Eichert, and H. Ott, *Photoassociation of rotating ultra-long range Rydberg molecules*, J. Phys. B: At. Mol. Opt. Phys. **51**, 155201 (2018).

[244] C. Wang, Y. Lu, A. Li, S. K. Kanungo, T. C. Killian, F. B. Dunning, and S. Yoshida, *Anomalies in the rotational spectra of* $^{86}\mathrm{Sr}$ *ultralong-range Rydberg molecule dimers*, Phys. Rev. A **111**, 052811 (2025).

[245] C. Wang, A. Li, S. K. Kanungo, T. C. Killian, F. B. Dunning, and S. Yoshida, *Photoassociation of* $^{84}\mathrm{Sr}$ $n\,^1D_2$ *ultralong-range Rydberg dimers*, Phys. Rev. A **113**, 052802 (2026).

[246] C. Fey, F. Hummel, and P. Schmelcher, *Building principle of triatomic trilobite Rydberg molecules*, Phys. Rev. A **99**, 022506 (2019).

[247] M. T. Eiles, C. Fey, F. Hummel, and P. Schmelcher, *Triatomic butterfly molecules*, J. Phys. B: At. Mol. Opt. Phys. **53**, 084001 (2020).

[248] I. C. Liu, J. Stanojevic, and J. M. Rost, *Ultra-long-range Rydberg trimers with a repulsive two-body interaction*, Physical review letters **102**, 173001 (2009).

[249] A. Gaj, A. T. Krupp, J. B. Balewski, R. Löw, S. Hofferberth, and T. Pfau, *From molecular spectra to a density shift in dense Rydberg gases*, Nat. Commun. **5**, 4546 (2014).

[250] S. K. Kanungo, Y. Lu, F. B. Dunning, S. Yoshida, J. Burgdörfer, and T. C. Killian, *Measuring nonlocal three-body spatial correlations with Rydberg trimers in ultracold quantum gases*, Phys. Rev. A **107**, 033322 (2023).

[251] M. Magoni, R. Joshi, and I. Lesanovsky, *Molecular Dynamics in Rydberg Tweezer Arrays: Spin-Phonon Entanglement and Jahn-Teller Effect*, Phys. Rev. Lett. **131**, 093002 (2023).

[252] K. W. Morton and D. F. Mayers, *Numerical Solution of Partial Differential Equations: An Introduction*, 2nd ed. (Cambridge University Press, 2005).

[253] G. C. Groenenboom and H. M. Buck, *Solving the discretized time-independent Schrödinger equation with the Lanczos procedure*, J. Chem. Phys. **92**, 4374 (1990).

Acknowledgements

I would like to express my sincere gratitude to everyone who has supported me and wished me well during the course of my doctoral studies. I was able to pursue my passion for theoretical physics, overcoming various professional and personal challenges, only because of the help of many people around me.

First and foremost, I would like to thank my supervisor Prof. Peter Schmelcher, for accepting me as a doctoral candidate and providing me the opportunity and the resources to complete this dissertation. He has provided me with mentorship and guidance in scientific thinking, academic writing, as well as the fundamental physics of the projects I worked on. He facilitated various collaborations and projects that allowed me to perform frontier research, and also made it possible for me to be a part of various discussions, conferences and workshops, encouraging me to share my work. He has also encouraged the development of my conceptual and physical intuition by timely appreciations. I am also grateful to Prof. Peter Schauß for agreeing to examine and correct my thesis, undoubtedly increasing its written quality.

Next, I would like to thank Prof. Matthew Eiles for his help throughout the course of my doctorate. He has consistently managed several of our collaborations, offering technical and conceptual assistance, in methodology, writing, and analysis. He has also personally contributed to many of the results that were obtained in our collaborative works, often performing calculations and simulations himself, while also being a senior investigator. The many discussions, scientific arguments, and combined error correction definitely shaped my growth.

I extend my gratitude to Dr. Frederic Hummel, for providing me close mentorship for my first project and kickstarting my PhD. I wrote my first ever peer-reviewed work under his guidance, and I really appreciate his patience in dealing with the novice that I was. I am also grateful to my theory collaborators Prof. Seth Rittenhouse and Prof. Hossein Sadeghpour, for their wonderful ideas that turned into two successful projects. I enjoyed their creative outlook, and learned a lot from the many discussions I shared with them.

The most exciting part of my work came through the collaborations with the experimental group led by Prof. Herwig Ott. It was a privilege to immerse myself in the scientific experience of developing theory and experiment together, and I am grateful to Prof. Ott for this opportunity. I have to thank Dr. Markus Exner and Richard Blättner for the many hours they spent in the lab obtaining valuable data, despite all the technical difficulties they faced. Markus was also constantly helpful in the preparation of multiple manuscripts we wrote together.

It is not just the people that mentored me, but also the ones that I mentored, that contributed to much of my growth as a physicist and a person. I was very happy to co-supervise the Bachelor's project, and the consequent HiWi position of Felix Giering, as well as the Master's project of Dimitris Tridimas. Helping them realize their potential as physics students, and watching their progress, reassured my love for physics education.

My peers in Hamburg deserve special appreciation for the many memories, that I will fondly take with me. I must start with Zeki, my friend from day one, having witnessed each other grow in matters of science, math, relationships, and ambitions. I am fortunate to have friends like Dan and Zeki, with whom I share the enthusiasm for Rydberg physics, sports, workouts, and late-night adventures. I must also thank all my peers in the group: Judith, Fabian, Kapil, Georgious, George, Ilias, Maxim, Dimitrios, André, Ansgar, Alejandro and Friethjof. The many lunches, dinners, and coffee break discussions made my days more worthwhile and enjoyable. I wish them all the very best in their future endeavors. I should thank André specifically for patiently helping me with German translations for a good two years. I thank Anja for all her professional help, solving umpteen bureaucratic barriers on a regular basis. Outside work, I have to thank Rahul, one of my longstanding friendships in Hamburg, for the many stimulating conversations regarding physics, life, philosophy, and whatnot.

The people who have been my personal support system, and enriched my life outside work deserve a lot of credit. I was only able to push through professional challenges due to their continued love and kindness. I am grateful to Annika for being by my side and helping me and supporting my emotional growth.

I thank my alma mater, Sri Sathya Sai Institute of Higher Learning, for their efforts and goodwill towards my human development.

Lastly, and most importantly, I thank my family back home in Kerala. For raising me and supporting my passions from an early age. I would not have been able to come to Germany, or pursue a PhD, if not for the sacrifices they have made. I cannot be more indebted to my mother Preetha, father Srikumar, sister Vijeta, as well as my grandparents Bhaskaran, Vijayakumari, Gopinathan, and Harivallabha, to whom I dedicate whatever little success I have achieved in my pursuits.

Declaration of authorship / Eidesstattliche Versicherung

I hereby declare and affirm that this doctoral dissertation is my own work and that I have not used any aids and sources other than those indicated.

If electronic resources based on generative artificial intelligence (gAI) were used in the course of writing this dissertation, I confirm that my own work was the main and value-adding contribution and that complete documentation of all resources used is available in accordance with good scientific practice. I am responsible for any erroneous or distorted content, incorrect references, violations of data protection and copyright law or plagiarism that may have been generated by the gAI.



Hamburg, 22.06.2026

Rohan Srikumar

Hiermit versichere ich an Eides statt, die vorliegende Dissertationsschrift selbst verfasst und keine anderen als die angegebenen Hilfsmittel und Quellen benutzt zu haben.

Sofern im Zuge der Erstellung der vorliegenden Dissertationsschrift generative Künstliche Intelligenz (gKI) basierte elektronische Hilfsmittel verwendet wurden, versichere ich, dass meine eigene Leistung im Vordergrund stand und dass eine vollständige Dokumentation aller verwendeten Hilfsmittel gemäß der Guten wissenschaftlichen Praxis vorliegt. Ich trage die Verantwortung für eventuell durch die gKI generierte fehlerhafte oder verzerrte Inhalte, fehlerhafte Referenzen, Verstöße gegen das Datenschutz- und Urheberrecht oder Plagiate.



Hamburg, den 22.06.2026

Rohan Srikumar

Declaration of Conformity for Printed Copy / Konformitätserklärung für die gedruckte Ausgabe

I, the undersigned, declare that this bound copy of the dissertation and the dissertation submitted in electronic form (via the Docata upload) and the printed bound copy of the dissertation submitted to the faculty (responsible Academic Office or the Doctoral Office Physics) for archiving are identical.



Hamburg, den 22.06.2026

Rohan SRIKUMAR

Ich versichere, dass dieses gebundene Exemplar der Dissertation und das in elektronischer Form eingereichte Dissertationsexemplar (über den Docata-Upload) und das bei der Fakultät (zuständiges Studienbüro bzw. Promotionsbüro Physik) zur Archivierung eingereichte gedruckte gebundene Exemplar der Dissertationsschrift identisch sind.



Hamburg, den 22.06.2026

Rohan SRIKUMAR